Search for an electron electric dipole moment with trapped molecular ions

by

Huanqian Loh

B.Sc., Massachusetts Institute of Technology, 2006

A thesis submitted to the

Faculty of the Graduate School of the

University of Colorado in partial fulfillment

of the requirements for the degree of

Doctor of Philosophy

Department of Physics

2013

This thesis entitled:
Search for an electron electric dipole moment with trapped molecular ions
written by Huanqian Loh
has been approved for the Department of Physics

Eric Cornell

Jun Ye

Date _____

The final copy of this thesis has been examined by the signatories, and we find that both the content and the form meet acceptable presentation standards of scholarly work in the above mentioned discipline.

Loh, Huanqian (Ph.D., Physics)

Search for an electron electric dipole moment with trapped molecular ions

Thesis directed by Prof. Eric Cornell

The search for a permanent electron electric dipole moment (eEDM) serves as a test of fundamental symmetry violations and of physics beyond the Standard Model. Trapped molecular ions in the $^3\Delta_1$ metastable electronic state are suitable candidates for an eEDM search due to their large effective electric fields and long electron spin coherence times. This thesis presents the quantum state manipulation and coherent spectroscopy of trapped HfF^+ molecular ions in rotating bias fields for an eEDM search. The quantum state manipulation, which involves preparation of a large fraction of molecular ions in a single desired quantum state as well as rotational-state-resolved detection, is complicated by the lack of HfF^+ spectroscopic information prior to the start of this thesis. We performed state preparation by first state-selectively autoionizing neutral HfF such that 35% of the HfF^+ are formed in a single rovibrational level of the electronic ground state $^1\Sigma^+$, and then transferring those ions into the desired Stark levels of a single hyperfine-rovibrational manifold of the $^3\Delta_1$ state. Rotational-state-resolved detection is accomplished by both laser-induced fluorescence and resonance-enhanced multi-photon photodissociation, where the latter is preferred as the state detection method of choice because its efficiency is two orders of magnitude higher compared to fluorescence. With the quantum state manipulation techniques developed, we performed Ramsey spectroscopy of the trapped HfF^+ ions in the presence of rotating bias electric and magnetic fields, demonstrating electron spin coherence times as long as 150 ms. Finally, we present a preliminary measurement of the eEDM at the $|d_e| < 10^{-25}$ e cm level.

Dedication

To Wah Sing, Hui Sok, Zhi Heng, and Travis.

Acknowledgements

This thesis work could not have been completed without the help of many people, most of whom are at JILA. JILA houses a wonderful scientific community, which I am fortunate to be a part of for my graduate school.

Of the people at JILA, I would first like to thank my graduate school advisor, Eric Cornell. From painting intuitive pictures to calling us out on software issues, Eric is a boundless source of creative ideas, an effective problem-solver, and a gifted teacher. I will miss his motivational emails explaining the merits of higher data-collection efficiency in terms of spending less time in the lab and more time skiing. As a mentor, Eric also cares deeply about his students. I am immensely grateful to his concern and advice on issues ranging from health to career.

Jun Ye has been a fantastic co-advisor, injecting a healthy amount of enthusiasm into the eEDM experiment. His wealth of technical expertise on all things lasers, experience with molecules, and persistent demand for scientific rigor have contributed to my growth as a scientist.

From the conception of this experiment, John Bohn and his former student Ed Meyer have provided both extensive theory support and a lively dose of humor. Chris Greene and his former student Jia Wang taught us about angular momentum in the autoionization of Rydberg molecules. We have also had many fruitful collaborations with Bob Field from MIT, who shared with us the finer points of diatomic molecular structure and with whom we co-authored several papers.

Through the regular Cornell-Jin group meetings, Debbie Jin has offered much physical insight into our problems and has a knack for asking questions that keep our minds focused on the big picture. I would also like to thank the rest of the Cornell-Jin group members for their friendship,

their patience, and their magnanimity in lending us various kinds of equipment. Similarly, our experiment has also benefited from our interactions with the Ye group, the Lewandowski group, the Thompson group, the Nesbitt group and the Lineberger group. Our access to so many groups of expertise within a single building — be it securing the last-minute loan of a servo loop filter or obtaining technical advice on pulsed Nd:YAG lasers — has been instrumental to our experimental progress.

JILA's collaborative environment goes beyond the interactions between the research groups. The technical staff in the instrument shop, electronics shop and computing department have provided critical support for our experiment, for which I am very grateful. Special mention goes to Todd Ascinar for machining our ion trap, to Hans Green and Blaine Horner for many creative vacuum-compatible solutions, to Terry Brown and Carl Sauer for advice on all things electronics, and to J. R. Raith for his computer wizardry. Pam Leland and Krista Beck also made sure that we never had to worry about administrative issues.

Much of the work in this thesis was performed together with my fellow eEDM labmates, whom I have had the pleasure to work with at one point or another. Russ Stutz showed me the ropes on the eEDM experiment and left the experiment in excellent running condition when he graduated. Kang-Kuen Ni was one of my first friends in Boulder and joined the eEDM effort as our powerhouse postdoc in the last 14 months. She has always encouraged me to push myself to greater heights, be it making a run for an eEDM measurement before graduating or convincing me to ski through glades. Matt Grau and I have spent many late nights taking data or bolting vacuum chambers, and over the years I think I may have learned more from him than I have taught him. Kevin Cossel's expertise on cavities, molecular spectroscopy and baked treats have greatly benefited our experiment from his involvement in the comb spectroscopy setup and more recently, the ion trap setup. With Kevin and Matt taking over the experiment, I am sure many exciting results will soon be forthcoming. I would also like to thank Tyler Yahn, Laura Sinclair, Dan Gresh, Herbert Looser, Tyler Coffey, Trent Fridey and Yiqi Ni for their impactful contributions to the JILA eEDM effort. Tyler Yahn was a very talented machinist and keen learner; Laura Sinclair led the initial

effort to perform comb spectroscopy on HfF^+; Dan Gresh has made a huge impact on the molecular spectroscopy of both HfF^+ and ThF^+; Herbert Looser was both a very patient physics teacher and an avid Labview programmer; Tyler Coffey, Trent Fridey and Yiqi Ni are undergraduates who have built all sorts of useful apparatus for the experiment.

My graduate school career was partly financed by A*STAR, for which I am grateful.

Prior to my time at JILA, Vladan Vuletić, James Thompson and Jon Simon have been instrumental in stoking my love for atomic, molecular and optical physics. I thank them for their honest advice and kind words of encouragement from my undergraduate days through the end of graduate school.

My parents have always been very supportive of my decisions, and I thank them for their boundless love and their regular visits to Boulder. To my brother, thank you for being my role model and for all the stimulating discussions we have had in life. I am excited to share this thesis with you. To my sister in-law, thank you for your invaluable friendship and advice.

I have been extremely lucky to pick up a second family while in graduate school. I am indebted to Johannah Nicholson and Jeff Nicholson for loving me like their own daughter. To Joe Cohen and the rest of the Nicholson family, thank you for the memorable times we spent outside of JILA.

It is hard to imagine the completion of this thesis without the love and support of my husband, Travis Nicholson. His non-judgmental character, combined with his extensive technical experience, has rendered him almost always the first person with whom I bounce ideas off. From lending an extra hand to tighten vacuum bolts at midnight to taking me on a lovely hike through fields of Colorado wildflowers, Travis has been responsible for keeping me sane and happy through the many ups and downs of graduate school. Travis is my inspiration in his dedication to physics and to his loved ones, and I look forward to our many adventures in life together.

Contents

Chapter

Tables

Table

Figures

Figure

Chapter 1

Introduction

1.1 Motivation for an electron electric dipole moment (eEDM) search

The electron is a fundamental particle of mass m_e, charge $-e$ and spin $S = \hbar/2$. The electron spin and charge give rise to a magnetic moment $\boldsymbol{\mu}_e = g_e \mu_B \mathbf{S}/\hbar$, where $\mu_B = e\hbar/(2m_e)$ is the Bohr magneton and g_e is the magnetic g-factor. According to relativistic quantum mechanics as described by the Dirac equation, $g_e = 2$. Quantum electrodynamics (QED), however, predicts that g_e deviates slightly from 2, i.e.

$$\frac{g_e}{2} = 1 + C_2 \left(\frac{\alpha}{\pi}\right) + C_4 \left(\frac{\alpha}{\pi}\right)^2 + \dots \quad , \tag{1.1}$$

where α is the fine-structure constant, the coefficients C_n are calculated from the QED Feynman diagrams of order n depicting an electron being scattered by a static magnetic field [14]. A precise measurement of the electron magnetic g-factor provides a stringent test on QED; in fact, with the current precision on the g-factor to 13 decimal places [33], QED has been tested out to the eighth order term $C_8 \left(\frac{\alpha}{\pi}\right)^4$ in Eq. (1.1). [2, 3].

What about an electron electric dipole moment (eEDM)? If the center of mass and center of charge of the electron are slightly displaced (see Fig. 1.1), the displacement would give rise to an eEDM. Such a permanent electric dipole moment is fundamentally different from that induced by a finite external electric field, for example in a polar molecule like OH. In this thesis, we only consider the case where the eEDM points only either along or against the direction of electron spin: if the eEDM is to point along a different direction (such that it can be expressed as a linear combination

of directions parallel and orthogonal to the electron spin), quantum mechanics would have required additional quantum numbers beyond m_s to describe the electron [44].

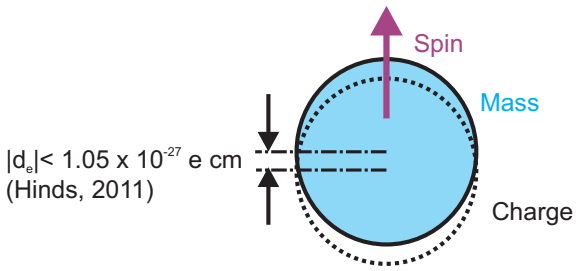

Figure 1.1: A displacement between the electron's center of mass and center of charge gives the electron an electric dipole moment.

To date, no eEDM has been observed. More precisely, the current experimental limit on the eEDM is $|d_e| < 1.05 \times 10^{-27}$ e cm [36]. The observation of an eEDM would have profound implications on both fundamental symmetries and grand unified theories of physics. Fig. 1.2a illustrates how the presence of an eEDM implies a direct violation of both time-reversal (T) symmetry and parity (P) symmetry. Under time-reversal (parity inversion), the electron spin (eEDM) flips direction while the eEDM (electron spin) remains unchanged. In either operation, the relative direction between the spin and EDM are different compared to the initial configuration, implying direct T and P violation. By the CPT theorem, direct T violation implies CP violation and vice versa. While CP violation has already been observed in neutral kaon decay in 1964 [13], direct T violation has only been observed in the B^0 meson decay experiment as recently as 2012 [47]. The observation of an eEDM would be another experiment that directly confirms the violation of T symmetry.

As explained above, the eEDM arises from CP violation. In the Standard Model, the CP-violating terms are calculated to be so small that the eEDM is predicted to be $< 10^{-38}$ e cm [70]. CP- and T-violating terms in the Standard Model also predict that the amount of matter and anti-matter in the early universe should have been approximately equal, in which case the two kinds of matter should annihilate such that the universe has almost no remaining matter.

Nevertheless, the fact that there is an asymmetry between the amount of matter and anti-matter in the universe is one of the key weaknesses of the Standard Model. Theories beyond the Standard Model (e.g. supersymmetry) allow for CP-violating terms of much larger magnitudes than that in the Standard Model. These theories predict an eEDM in the range of 10^{-29}–10^{-26} e cm [9, 7, 69]. If we can probe eEDM more precisely at a level that is one to two orders of magnitude beyond the current experimental limit, we can either validate or constrain more rigorously the various theories beyond the Standard Model (Fig. 1.2b). Of note is the fact that the electric dipole moment of the electron as predicted by the Standard Model is several orders of magnitude smaller than that predicted by the other extension theories. Such a low "Standard Model background" facilitates the discrimination of these extension theories from the Standard Model should an eEDM be observed.

1.2 Measuring the eEDM

1.2.1 Figure-of-merit

How would one measure the eEDM? In the presence of an external electric field $\boldsymbol{\mathcal{E}}$ and magnetic field $\boldsymbol{B}$, the Hamiltonian for an electron with eEDM d_e is:

$$\mathcal{H}_e(\boldsymbol{\mathcal{E}}, \boldsymbol{B}) = -\left(d_e \boldsymbol{\mathcal{E}} + \mu_e \boldsymbol{B}\right) \cdot \frac{\boldsymbol{\sigma}}{|\boldsymbol{\sigma}|} \quad . \tag{1.2}$$

The frequency difference between an electron in its state of spin-down versus spin-up (and assuming d_e aligned parallel to the spin) is then given by

$$\omega_e(\mathcal{E}, B) = -\frac{2}{\hbar}\left(d_e \mathcal{E} + \mu_e B\right) . \tag{1.3}$$

The measurement of the transition frequency between the spin-up and spin-down states is known as electron spin resonance (ESR) spectroscopy. To attribute the ESR frequency to d_e only, the electron spin-flip frequency is measured with a fixed external magnetic field and the external electric field $\boldsymbol{\mathcal{E}}$ first applied parallel to $\boldsymbol{B}$ and then anti-parallel to $\boldsymbol{B}$. The difference in the two measured frequencies then gives $4 d_e \mathcal{E}$ (Fig 1.3a). (One may question the necessity of applying a magnetic field to measure d_e; after all, the electron frequency shift from d_e can be obtained from only reversing

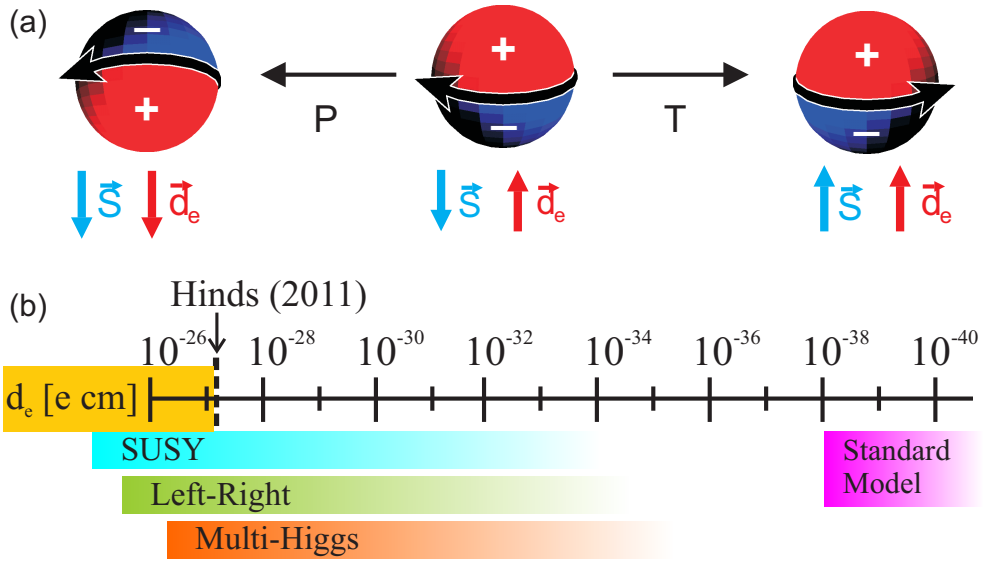

Figure 1.2: (a) The presence of an eEDM implies the direct violation of time reversal (T) symmetry and parity inversion (P) symmetry. As depicted, under either time reversal or parity inversion, the electron's spin and eEDM change from being anti-aligned to aligned. Although the electron spin and eEDM are illustrated to be initially anti-aligned, the same argument of T and P violation holds if the electron spin and eEDM are initially aligned. (b) Theories extending physics beyond the Standard Model predict eEDM values much higher than that predicted by the Standard Model [9, 7, 69]. These theories can be tested more rigorously by pushing the current eEDM experimental limit down by another one to two orders of magnitude.

the electric field direction. The magnetic field is useful for biasing the measurement frequency away from 0 Hz, so that the eEDM shift is insensitive to noise sources near DC.) Conversely, one may add the two transition frequencies measured in a fixed electric field but with the magnetic field applied aligned and anti-aligned to $\mathcal{E}$ (Fig. 1.3b). Whether the magnetic field or electric field direction is being reversed, the deliberate change should be performed relatively quickly (so that one is insensitive to drifts in the other experimental parameters) and is henceforth referred to as a 'chop'. Combining the measured transition frequencies from the four chops, we get

$$\omega_e(\mathcal{E}, B) + \omega_e(\mathcal{E}, -B) - \big(\omega_e(-\mathcal{E}, B) + \omega_e(-\mathcal{E}, -B)\big) = 8 d_e \mathcal{E} \,. \tag{1.4}$$

The statistical sensitivity of an eEDM measurement is governed by three quantities: the magnitude of the electric field $\mathcal{E}$ experienced by the electron spin, the coherence time τ, and the square root of the number of spin-flip transitions $\sqrt{N}$ detected in a given integration time, say, of one day. Fig. 1.4a–c shows how each quantity affects the eEDM measurement, where the eEDM measurement is depicted in each of these cases as a chop in only the external electric field direction and the statistical distribution of measured transition frequencies for a given electric field direction manifests as a spectral line. Firstly, the higher the electric field $\mathcal{E}$ experienced by the electron spin, the larger the separation between the center of each spectral line. Secondly, the longer the coherence time of the measurement, the narrower the linewidth of each frequency and the better the two spectral lines can be resolved. Thirdly, each spectral line is composed of a large number of trials detecting the spin-flip transition, each of which is independent and therefore the result follows a Poisson distribution. The signal-to-noise ratio of each spectral line is hence given by the square root of the number of spin-flip transitions. The higher the signal-to-noise ratio, the better the determination of each spectral line center. The combination of $\mathcal{E}, \tau$ and $\sqrt{N}$ forms the figure-of-merit for determining the statistical limit of an eEDM measurement:

$$\delta d_e = \frac{\hbar}{2e\mathcal{E}\tau\sqrt{N}} \,. \tag{1.5}$$

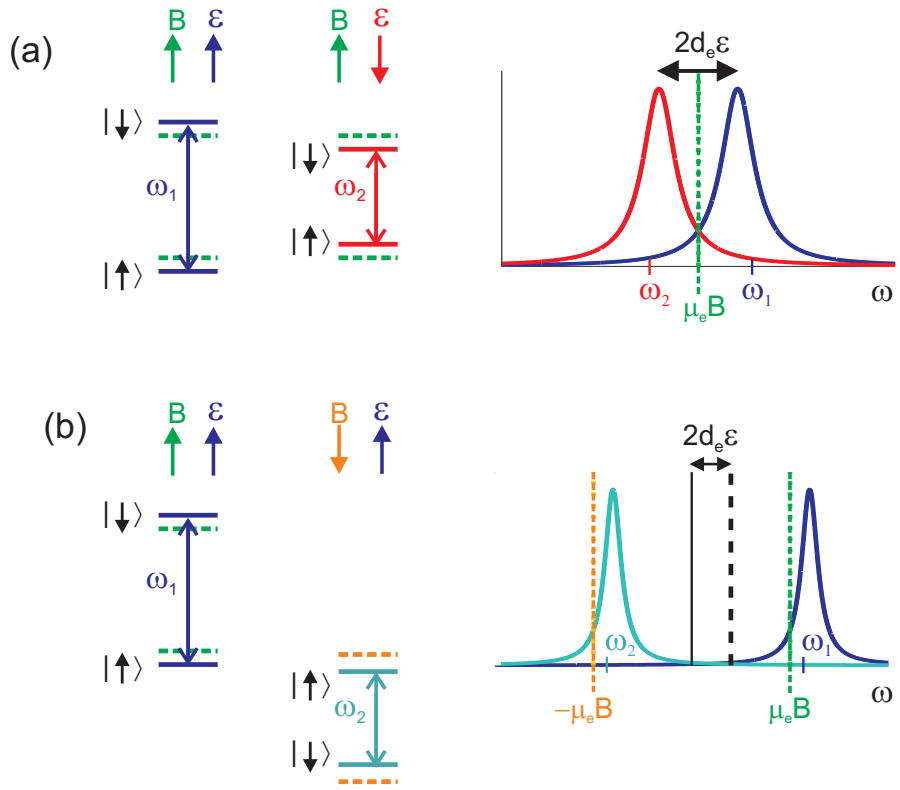

Figure 1.3: (The eEDM may be determined by measuring the electron spin-flip transition frequency in the presence of an external electric and magnetic field aligned parallel to each other, and then (a) reversing the direction of the electric field and taking the difference of the two transition frequencies, or (b) reversing the direction of the magnetic field and summing the two transition frequencies.

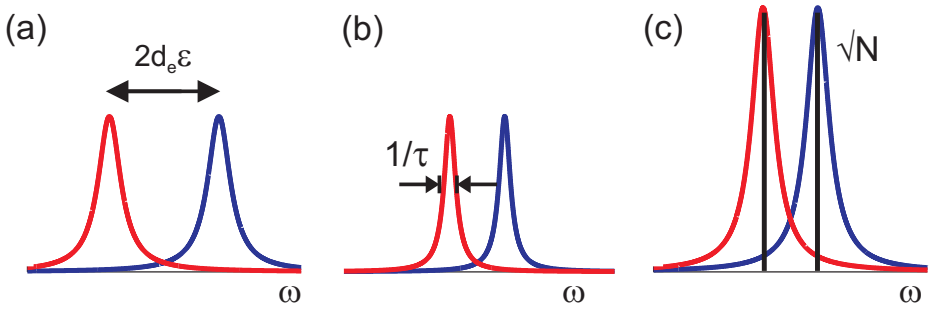

Figure 1.4: The eEDM measurement figure-of-merit, which is inversely proportional to the statistical uncertainty on the eEDM, is proportional to (a) the electric field $\mathcal{E}$ experienced by the electron, (b) the coherence time τ, and (c) the square root of the number of spin flips detected $\sqrt{N}$.

1.2.2 HfF^+ molecular ions for an eEDM measurement

While the discussion of the eEDM measurement so far focuses on a single unpaired electron, the eEDM measurement is never carried out on a bare electron, as the application of a large electric field would invariably cause the electron to fly away. Sandars [72, 73, 74, 75] suggested the use of electrons in atoms and molecules for probing the eEDM, where the valence electron's energy level can be shifted by the electric field $\mathcal{E}_{\mathit{eff}}$ induced in the polarized atom or molecule upon the application of an external electric field $\mathcal{E}_{ext}$. The induction of an effective internal electric field from $\mathcal{E}_{ext}$ can be accounted for using a loophole of Schiff's theorem [76, 15], a discussion of which is beyond the scope of this thesis. For atoms, the scale of the internal electric field goes as the cube of the nuclear charge times the applied external field $Z^3\mathcal{E}_{ext}$, such that the electric field experienced by the unpaired electron of interest can be as high as 72 MV/cm in a heavy atom like thallium [71]. In this case, $\mathcal{E}_{ext}$ was already maximized at about 100 kV/cm, above which arcing between the plates can occur in vacuum. To obtain a higher internal electric field, one would either have to go to an atom of even higher Z or turn to polar molecules.

For polar molecules, the internal effective electric field saturates at a specific value $\mathcal{E}_{\mathit{eff}}^{max}$, unlike in atoms where the internal electric field continues to be proportional to the applied field for obtainable laboratory electric fields. The saturation occurs when the applied electric field is large enough to fully mix adjacent molecular states of opposite parity. In the $^2\Sigma^+$ state of YbF, the closest two states of opposite parity are adjacent rotational levels spaced by $\sim (2\pi)40$ GHz, so the applied electric field of 10 kV/cm was able to induce an effective electric field of 14.5 GV/cm but not as large as the maximum possible value of 26 GV/cm [39]. Nonetheless, the effective electric field obtained was already two orders of magnitude higher than that in thallium. Ideally, one would like to be able to obtain similarly high an effective electric field with a polar molecule with an external electric field as small as 10 V/cm, so as to access $\mathcal{E}_{\mathit{eff}}^{max}$ more easily and to reduce systematic effects from, say, leakage currents from the electric field plates; for this purpose, the $^3\Delta_1$ electronic state, present in a class of molecules such as ThO [55, 87], WC [46], HfF^+ and ThF^+

[56, 62, 55, 45], is a suitable candidate. The $^3\Delta_1$ configuration in those species comes from an s and a d valence electron. The diffuse d electron gives rise to an Ω-doublet of opposite parity levels spaced as closely as $(2\pi)1$ MHz, such that as little as 2 V/cm is required to fully polarize the molecule. The s electron experiences relativistic effects near the nucleus of the heavy atom (e.g. Th, W, Hf), such that once the molecule is polarized, the internal electric field can be as high as 90 GV/cm!

Of the molecules with the $^3\Delta_1$ state, some are neutral molecules whereas others are molecular ions. Trapping neutral molecules is difficult to date, so all the eEDM neutral molecule experiments work with molecular beams. The coherence time of the eEDM measurement is then limited to that taken for the molecules to traverse the electric field plates (i.e. $\sim$1 ms). Molecular ions, on the other hand, can be easily trapped with electric fields in an ion trap. It is fortuitous that the molecular ions proposed for the eEDM measurement such as HfF^+ and ThF^+ tend to have $^3\Delta_1$ lifetimes of at least three orders of magnitude longer than 1 ms, so we can take advantage of the ion trap to perform an eEDM with much longer coherence times ($\sim$300 ms) than for the neutral molecules. The downside to using molecular ions, however, is that the density of molecular ions tends to be limited by space-charge repulsion between multiple ions, so the number of spin-flip transitions in an eEDM experiment can be orders of magnitude smaller for molecular ions than for neutral molecules. Since the eEDM figure-of-merit is proportional to $\mathcal{E}_{eff}\tau\sqrt{N}$, for similar effective electric fields, there is no obvious winner between neutral molecules and molecular ions, and each experimental group simply has to work as hard as they can on both τ and $\sqrt{N}$ to achieve the better statistical sensitivity!

For this thesis work, the species of choice is the molecular ion HfF^+. Among the different eEDM experimental groups, the JILA group is the only one employing molecular ions. Beyond a discussion of the statistical limit to d_e, molecular ions have the advantage that the longer τ leads to a narrower spectral linewidth, which makes us less vulnerable to systematic errors that affect the lineshape.

Fig. 1.5a–c shows the $^3\Delta_1, \nu = 0, J = 1$ energy level structure for $^{180}Hf^{19}F$ for three different

cases: (a) in the absence of any external fields, (b) with an external electric field but ignoring the effect of an eEDM, and (c) with both an external electric and magnetic field and accounting for the eEDM. Since the nuclear spin of fluorine is 1/2 and ^{180}Hf has no nuclear spin, the $J = 1$ rotational level has two hyperfine levels, $F = 3/2$ and 1/2. Without any external fields, the states of well-defined parity are given by $|\pm\rangle = (|\Omega = +1\rangle \pm |\Omega = -1\rangle)/\sqrt{2}$. For $F = 3/2$, each state of well-defined parity has four degenerate levels, which are the four m_F projections of the hyperfine angular momentum onto a quantization axis. In the eEDM experiment, the external electric field serves as the quantization axis. When present, the external electric field mixes the states of opposite parity to give states where Ω, which is the total projection of orbital and electron spin angular momentum onto the internuclear axis $\hat{n}$, is a good quantum number. The $F = 3/2$ and 1/2 levels split into four and two Stark manifolds, respectively, while states of the same $m_F\Omega$ remain degenerate. Finally, in the presence of an external magnetic field colinear with the external electric field, the stretch states of the same $m_F\Omega$ in the $F = 3/2$ hyperfine level are split by the frequencies

$$\omega^u = 3g_F^u \mu_B B + 2d_e \mathcal{E}_{eff}, \tag{1.6a}$$

$$\omega^\ell = 3g_F^\ell \mu_B B - 2d_e \mathcal{E}_{eff}, \tag{1.6b}$$

where $g_F^{u/\ell}$ is the magnetic g-factor of the upper and lower Stark manifolds. The sign of the eEDM transition frequency shift can be understood as the following: for the upper manifold $\{|a\rangle, |b\rangle\}$, the effective electric field points parallel to B. Assuming that d_e is aligned with the electron spin, state $|a\rangle$ ($|b\rangle$), which has been shifted upwards (downwards) by the Zeeman effect, is displaced further up (down) by the effective electric field, giving an extra energy splitting of $2d_e\mathcal{E}_{eff}$ on top of the usual Zeeman splitting. Conversely, for the lower manifold $\{|c\rangle, |d\rangle\}$, $\mathcal{E}_{eff}$ points in the opposite direction as B. The sign of the energy splitting $2d_e\mathcal{E}_{eff}$ is then opposite to that of the Zeeman splitting. The magnetic g-factors of the upper and lower Stark manifolds are predicted to be very similar, such that a chop of the electric field amounts to performing the electron spin resonance on the upper versus lower Stark manifold. The ability to sample the magnetic field using the same molecular species as a co-magnetometer is another advantage of using an $\Omega = 1$ level such as the $^3\Delta_1$ level

[18, 23]. Analogous to Eq. (1.4), the eEDM signal is then given by the four-way chop:

$$\omega^u(\mathcal{E}_{ext}, B) + \omega^u(\mathcal{E}_{ext}, -B) - \left(\omega^\ell(\mathcal{E}_{ext}, B) + \omega^\ell(\mathcal{E}_{ext}, -B)\right) = 8 d_e \mathcal{E}_{\mathit{eff}}. \tag{1.7}$$

In HfF^+, $\mathcal{E}_{\mathit{eff}}$ saturates at 24 GV/cm [62]. From Eq. (1.7), a determination of d_e at the level of 1×10^{-28} e cm — about an order of magnitude better than the present experimental limit — then demands that the sum frequency shift of $8 d_e \mathcal{E}_{\mathit{eff}}$ be measured to as precisely as $(2\pi)5$ mHz! At this point, three commonly asked questions may arise in the reader's head:

(1) How does one measure such a small frequency shift as $(2\pi)5$ mHz?

(2) How does one experimentally determine $\mathcal{E}_{\mathit{eff}}$?

(3) How can one, in the first place, apply an external bias electric field without ejecting the HfF^+ ions from their ion trap?

The answer to the first question is that the absolute frequency to be measured in any given chop of $\mathcal{E}_{\mathit{eff}}$ and B is only $\omega^u/(2\pi) \approx$100 Hz, and for an estimated spectral linewidth of 2 Hz, the spectral line center only needs to be determined to a precision of 1/2000 to measure a shift of of the line center by 1 mHz. The absolute frequency measurement for a particular chop is in turn given by Ramsey spectroscopy. Instead of using a narrow laser or radiofrequency source to probe the eEDM transition (say, ω^u), we first populate all the ions in $|a\rangle$ (with none in $|b\rangle$). We then apply a $\pi/2$ pulse to create an equal superposition of the two stretch states (i.e. $|b\rangle + |a\rangle$), wait for some duration T over which $|a\rangle$ dephases relative to $|b\rangle$ (i.e. $|b\rangle + e^{-i\omega^u T}|a\rangle$), and finally apply another $\pi/2$ pulse to read out the relative phase $\omega^u T$ as a fraction of ions in state $|a\rangle$. As T is varied such that the relative phase changes from 0 to 2π, the final fraction of ions in state $|a\rangle$ oscillates from 0 to 1, and the frequency of oscillation then gives ω^u.

The need to obtain a reliable value for $\mathcal{E}_{\mathit{eff}}$ is important because d_e can only be extracted from a measured frequency after having knowledge of $\mathcal{E}_{\mathit{eff}}$. All the values for $\mathcal{E}_{\mathit{eff}}$ for the different molecules listed earlier in this chapter come from ab-initio calculations of the molecular potentials, which therefore motivates the second question. Unfortunately, there is no way to experimentally

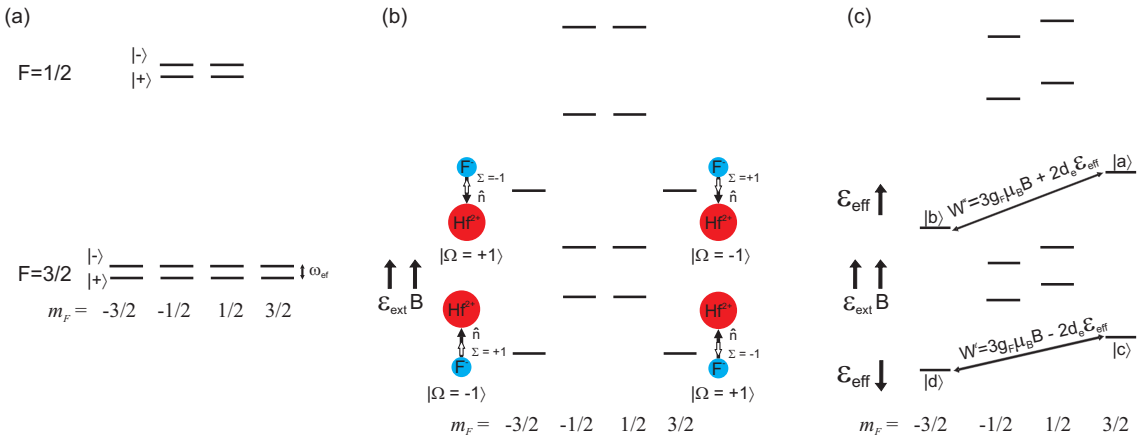

Figure 1.5: HfF^+ energy levels within the $^3\Delta_1, \nu = 0, J = 1$ state. This figure is adapted from [45], with the energy ordering of the hyperfine levels switched to reflect the results experimentally obtained in this thesis. (a) In the absence of an external electric field, each hyperfine level possesses two closely-spaced states of opposite parity $\{|+\rangle, |-\rangle\}$, while the hyperfine m_F projections are degenerate. (b) With an external electric field (that also sets the quantization axis), the states of opposite parity are mixed and the hyperfine levels are split into $(2F+1)/2$ Stark manifolds, where the molecule internuclear axis $\hat{n}$ is aligned parallel (anti-parallel) to the external electric field for the lower (upper) Stark manifold. (c) In the presence of a magnetic field parallel to $\mathcal{E}_{ext}$, the m_F sublevels undergo a Zeeman shift. The eEDM-sensitive transitions are denoted by $\omega^{u/\ell}$, with the eEDM having oppositely signed contributions to ω^u and ω^ℓ (see text).

measure $\mathcal{E}_{eff}$. For the case of YbF, several different calculations were performed to obtain $\mathcal{E}_{eff}$, amongst which the agreement was valid to within 10% [39]. The 10% error on $\mathcal{E}_{eff}$ ultimately had almost no bearing on the eEDM result reported [36]. For HfF^+, we hope to check the validity of the ab-initio calculations by measuring other important experimental parameters such as the hyperfine structure of $^{179}Hf^{19}F$ and $^{177}Hf^{19}F$ and comparing against the predicted values, thereby indirectly giving confidence to the calculated value of $\mathcal{E}_{eff}$.

The issue raised by the last question comes from the fact that a DC bias electric field is either smaller than the trapping fields, such that the HfF^+ ions will simply be displaced to a new position in the trap, or larger than the trapping fields, such that the HfF^+ ions will be ejected from the trap. For a bias field of $\mathcal{E}_{ext}$ =10 V/cm, the latter case applies. The trick is to apply the bias electric field in a rotating manner, where the rotation frequency ω_{rot} is fast enough for the ions to remain trapped but slow enough for the ions' internuclear axis to track the electric field direction adiabatically. In fact, the application of a rotating quantization axis is unique to our experiment amongst trapped ion experiments.

1.2.3 Challenges of using HfF^+

Unlike atoms, molecules have many more quantum states: besides electronic, hyperfine and Zeeman sublevels, molecules also have vibrational and rotational levels. As explained in the description of the Ramsey time-of-flight spectroscopy, full quantum control of the Zeeman-hyperfine-rovibronic states of HfF^+ is needed to carry out the eEDM measurement. The implementation of quantum state preparation, state manipulation and state readout at the level of $(2\pi)100$ Hz was complicated by the fact that no spectroscopic information on HfF^+ was available when our experiment first began. Some theoretical calculations of the low-lying states were performed [62, 63], but those had uncertainties as large as 30 THz (i.e. 50 nm uncertainty for a transition centered at 700 nm), such that theorists could not agree on whether the ground state of HfF^+ was $^1\Sigma^+$ or $^3\Delta_1$ [54]. There was a lot of work to do!

In general, spectroscopy of molecular ions is a lot more challenging than spectroscopy of

neutral molecules because of the much lower density (by three orders of magnitude in typical setups) of molecular ions. Along our journey towards precision spectroscopy of HfF^+ in the $^3\Delta_1$ state, we were fortunately aided by the low-lying electronic state assignments that came out of Heaven et. al.'s experiments [4] and by a parallel JILA experiment performing velocity modulation spectroscopy in a discharge tube [82, 16].

Beyond assigning the energy levels, we had to create a large fraction of HfF^+ ions in a single desired quantum state. While a high ion number was important to increasing the spin-flip detection count rate, more ions also meant more ion-ion collisions that could also lead to decoherence on our Ramsey measurements, so efficient state preparation was key to maximizing the former while minimizing the latter constraint. One method to state-selectively create HfF^+ was to photoionize neutral HfF using two resonant photons, which meant that we needed to first find the ionization energy of neutral HfF as well as vibronic states of neutral HfF that could serve as intermediate states for two-photon photoionization. The eEDM-sensitive transitions lay in the $^3\Delta_1$ metastable state, so special effort (such as combining photoionization with stimulated Raman transfer) was needed to populate that electronic state.

For state detection, a popular atomic physics technique is laser-induced fluorescence (LIF), where the number of fluorescence photons is proportional to the number of molecular ions excited by a laser addressing a particular transition. Unlike atoms, molecules generally have no cycling transitions, which makes LIF a rather painful way of probing the molecules. Photodissociation, where the HfF^+ molecule is state-selectively broken up into Hf^+ and a fluorine atom, promised a much higher detection efficiency by counting ions. However, to enable photodissociation as a state readout technique, we had to perform UV spectroscopy of high-lying bound and dissociating states of HfF^+ in our ion trap.

Finally, the manipulation of molecular ions with a rotating bias electric field meant non-trivial physics to be explored, which was in itself a very happy problem to have, since it finally signified our departure from "shot-in-the-dark" survey spectroscopy!

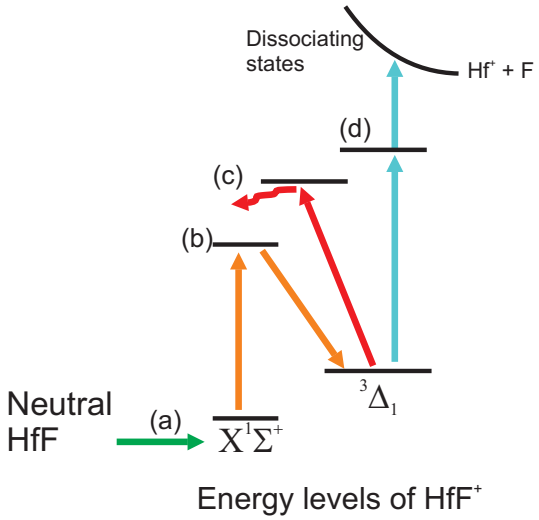

Figure 1.6: Major state manipulation steps that had to be performed to enable to eEDM measurement: state preparation of HfF^+ in a single desired quantum level using (a) photoionization and (b) Raman transfer, and state detection using either (c) laser-induced fluorescence or (d) photodissociation. This figure has been adapted from [81, 16].

1.3 Overview of thesis

Unlike many physics theses, there is no single "experiment setup" chapter that can adequately summarize the experiment setup used in this thesis work. From neutral HfF molecules to a molecular ion beam to trapped molecular ions, the experiment setup is constantly changing (with many vacuum breaks!) and is thus described in its appropriate chapter. Chapter 2 presents the spectroscopy of neutral HfF performed using resonance-enhanced multiphoton ionization (REMPI), with the goal of identifying suitable vibronic states at 30000–33000 cm^{-1} that can be used as intermediate states in two-photon autoionization to create HfF^+. The state-selective nature of two-photon autoionization is probed by performing LIF on a beam of HfF^+ ions, as described in chapter 3, where we show that as much as 30% of the total ion yield can be formed in a particular $|J, m_J\rangle$ state. For the remainder of the thesis, the HfF^+ ions are trapped in a radiofrequency Paul trap, whose design and associated electronics particular to the eEDM experiment are given in chapter 4. Chapter 4 also discusses various techniques that have been used to characterize the ions' in-trap behavior. Chapter 5 revisits the implementation of LIF, this time with trapped HfF^+ ions. Beyond chapter 5, we abandon LIF as a technique for state detection and turn instead to photodissociation, for which the spectroscopy of high-lying HfF^+ states and usefulness of photodissociation as a readout tool are illustrated in chapter 6. In chapter 7, the stimulated Raman transfer of HfF^+ ions from the ground $^1\Sigma^+$ state to the desired quantum states in $^3\Delta_1$ is described, and we experimentally map out, for the first time, the level structure presented in Fig. 1.5a–b. Finally, chapter 8 discusses the implementation and physics of coherent Ramsey spectroscopy with trapped HfF^+ ions in a rotating bias field and closes with a preliminary measurement of the eEDM at the 10^{-25} e cm level.

Chapter 2

REMPI spectroscopy of neutral HfF [51]

The first stage of preparing HfF^+ ions in a single desired ro-vibronic level is to state-selectively autoionize neutral HfF prepared using the optical-optical double resonance (OODR) technique [52]. In OODR, two ultraviolet (UV) photons of different frequencies are used, where the first photon is tuned to an intermediate state of neutral HfF and the second photon further excites HfF to a Rydberg state above the lowest ionization threshold at 59462(2) cm^{-1} [4, 52]. Since the final state of the autoionized product depends strongly on the intermediate state accessed by the first UV photon, there is a need to characterize and understand the neutral HfF states that lie in the vicinity of and above 30000 cm^{-1}, some of which may hold promise as intermediate states for HfF^+ ion-creation in the desired $^3\Delta_1$ state.

The HfF spectroscopy published to date includes transitions to excited states as high as 28600 cm^{-1}, detected by laser-induced fluorescence [1, 30], and resonance-enhanced multi-photon ionization (REMPI) [4]. This chapter[1] presents HfF spectroscopy performed in the 30000–33000 cm^{-1} range, using both 1+1 REMPI and 1+1′ REMPI, which complements the previously published spectroscopic results.

2.1 Experiment setup

Figure 2.1 shows a schematic of the experimental setup used to ionize a HfF molecular beam via (1+1) REMPI. The source and time-of-flight mass spectrometry (TOFMS) chambers are

[1] Most of this chapter has already appeared in Reference [51].

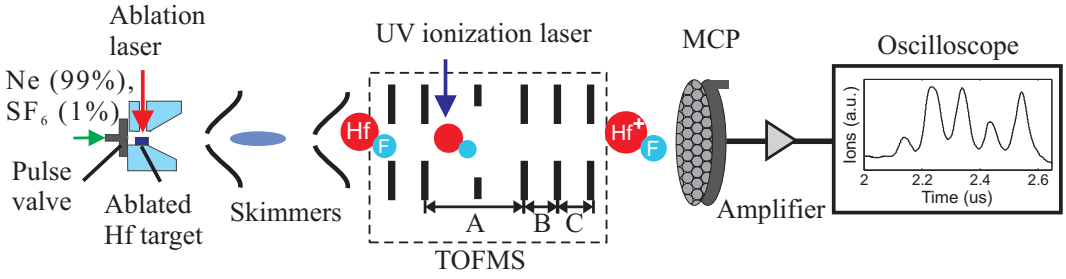

Figure 2.1: Schematic of the resonance-enhanced multiphoton ionization (REMPI) experiment.

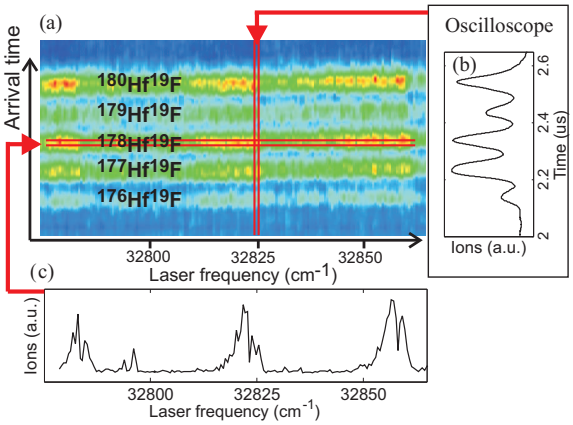

Figure 2.2: (a) A pictorial summary of the oscilloscope traces taken over multiple vibronic bands. (b) A sample of the oscilloscope trace shows the capability of the time-of-flight mass spectrometry (TOFMS) apparatus to separate the spectra arising from each of the five isotopologues of HfF^+. (c) (1+1) REMPI spectrum of $^{178}Hf^{19}F$.

separately pumped. A gas comprising 1% SF_6 and 99% Ar is released into the source chamber through the opening of a pulsed valve (800 μm orifice, 120 psi backing pressure) for 150 μs. In the presence of SF_6, the ablation of a Hf rod by the fundamental of a Nd:YAG pulsed laser (5–7 ns, 25 mJ/pulse, focused beam diameter 230 μm) creates HfF. We can also use the second harmonic of the Nd:YAG laser to perform the ablation; both cases gave no difference to the number of HfF molecules created. The HfF molecular beam is cooled through supersonic expansion to a rotational temperature of ~ 10 K. The beam is collimated by two skimmers (1 mm orifice diameter, separation distance 29 cm) before passing through a home-built TOFMS, which is a series of six disks arranged along a common axis [83].

In the TOFMS chamber, a UV laser, tuned such that two photons are required to ionize HfF, intersects the molecular beam perpendicularly in the TOFMS region A. The resultant HfF^+ ions drift under an electric field of 1 V/cm toward region B. Regions B and C of the TOFMS are operated in the Wiley-McLaren mode [88]: when in region B, the ions are spatially focused by a small electric field of 0.25 V/cm until they reach region C, in which the ions are velocity-focused, by a transient electric field of 1 kV/cm for 500 ns, toward a microchannel plate assembly (MCP) positioned 56 cm away. The ion signal is enhanced by a transimpedance amplifier and read out by an oscilloscope. The TOFMS has a fractional mass resolution of at least 1/200, allowing us to resolve individual isotopologues of HfF^+ that differ by 1 amu (natural relative abundances in parentheses): $^{176}Hf^{19}F$ (5.2%), $^{177}Hf^{19}F$ (18.6%), $^{178}Hf^{19}F$ (27.3%), $^{179}Hf^{19}F$ (13.6%) and $^{180}Hf^{19}F$ (35.1%). Figure 2.2(a) gives a pictorial summary of all the oscilloscope traces recorded over multiple vibronic bands, while Fig. 2.2(b) shows a sample of an oscilloscope trace for a particular wavelength of the UV laser. All five isotopologues of HfF^+, well-separated in arrival time on the MCP, appear as laser frequency striations of different intensities.

As detailed in Ref. [52], cold (~ 10 K rotational temperature) HfF molecules are created by ablating a Hf target in the presence of 1% SF_6 and 99% Ne (690 kPa backing pressure), followed by supersonic expansion through a 800 μm diameter nozzle. The molecular beam is collimated by two 1 mm diameter skimmers separated by 29 cm before passing through a home-built time-of-flight

mass spectrometer (TOFMS), which is a series of six disks arranged along a common axis [83].

Most of the HfF spectra presented in this chapter are recorded using (1+1) REMPI, in which the spectral resolution is limited to 0.1 cm^{-1} (FWHM), the linewidth of the UV laser. The UV photoionization radiation comes from a 532 nm-pumped dye laser operating with DCM dye, frequency doubled in a KDP crystal (100-200 μJ/pulse, 10 ns, 0.1 cm^{-1} FWHM). Its wavelength is continuously monitored by a wavemeter calibrated against Ne spectral lines.

Two of the HfF vibronic bands are recorded with high spectral resolution (0.003 cm^{-1}) using (1+1′) REMPI, where two co-propagating laser pulses simultaneously intersect the molecular beam at the same intersection point. The first photon (3 μJ/pulse, 10 ns, 150 MHz FWHM) is the frequency doubled output of a home-built two-stage Rhodamine 101 dye cell amplifier. The dye cell amplifier is seeded by a continuous-wave ring dye laser operating with Rhodamine 610 Chloride dye. It is pumped by the second harmonic of a Nd:YAG laser. The seed laser frequency is monitored by a high-precision wavemeter that is regularly calibrated against the ^{87}Rb D_2 transition. The second photon in (1+1′) REMPI, held at a fixed wavelength of 351.5 nm, is provided by the same dye laser as that used in the (1+1) REMPI setup, but operating with LDS722 dye.

In this chapter, transitions between energy levels of HfF are labeled as $\{\nu_0/10^3\}$, where ν_0 is the vibronic band origin in cm^{-1} [5].

2.2 HfF spectra in the range 30000–33000 cm^{-1}

A survey scan of HfF transitions was conducted over the frequency range 30000–33000 cm^{-1} (Fig. 2.3(a)), which is the range encompassed by the frequency doubled output of the DCM dye. Most of the strong transitions were scanned in detail and were found to belong to either an $\Omega' = 3/2 \leftarrow \Omega'' = 3/2$ transition (Fig. 2.3(b)) or a $\Pi_{1/2} \leftarrow \Omega'' = 3/2$ transition (Fig. 2.3(c)).

The REMPI spectra were modeled by the following Hamiltonian for the $\Omega = 3/2$ states [35]:

$$E(J) = T_e + G_\nu + BJ(J+1)\,, \tag{2.1}$$

where T_e is the electronic energy (difference in energy between the extrapolated minima of the

$X^2\Delta_{3/2}$ and electronically excited states) and G_ν is the energy of the vibrational level ν. For the $\Pi_{1/2}$ states, there is strong Λ-doubling and transitions from the Λ-doubled $X^2\Delta_{3/2}$ ground state into both Λ-doublets of a given rotational level can be resolved, even in the low-resolution spectra. Since no prior information is known about the parity of a given member of a Λ-doublet, the doublets are assigned 'a'/'b' instead of the usual spectroscopic notation 'e'/'f' [11]. Their energy levels can be modeled by the following polynomial [48]:

$$E^{a/b}(J) = T_e + G_\nu + BJ(J+1) - / + \frac{(-1)^{(J+\frac{1}{2})}}{2}(p+2q)\left(J+\frac{1}{2}\right). \tag{2.2}$$

Following Ref. [1], we assume that the $^2\Pi$ spin-orbit splitting is large enough for us to consider only the diagonal matrix element $\left\langle {}^2\Pi_{1/2}\left|\mathcal{H}\right|^2\Pi_{1/2}\right\rangle$ in our description of the Λ-doublets. Among the $\Pi_{1/2}$ states, the $^4\Pi_{1/2}$ states can borrow oscillator strength from the $^2\Pi_{1/2}$ states via spin-orbit coupling. Since transitions into the $^4\Pi_{1/2}$ upper levels would look very similar to those into $^2\Pi_{1/2}$, we have left out the superscript in the term symbol for the $\Pi_{1/2}$ levels. Based on the Λ-doubling, none of the observed spectra belong to excited states of Σ character, which have been previously reported in the ranges 13800–14400 cm^{-1} [30] and 19700–20000 cm^{-1} [1]. For both $\Pi_{1/2}$ and $\Omega' = 3/2$ types of excited electronic states, the centrifugal distortion term, $DJ^2(J+1)^2$, is neglected because the supersonic HfF molecular beam is too cold to populate rotational levels beyond $J = 21/2$, which would be required for an accurate determination of D.

Although all five isotopologues were observed, only the two most abundant (^{178}Hf^{19}F and ^{180}Hf^{19}F) were analyzed. (In Section 2.5, we extend for selected bands our analysis to the ^{177}Hf^{19}F and ^{179}Hf^{19}F isotopologues.) For a given transition, the two isotopologues' REMPI spectra are simultaneously fit to a contour described by a common set of fit parameters: temperature, intensity, band origin for ^{180}Hf^{19}F ($^{180}\nu_0 = {}^{180}T'_e - {}^{180}T''_e + {}^{180}G'_{\nu'} - {}^{180}G''_{\nu''}$), band origin for ^{178}Hf^{19}F ($^{178}\nu_0$), lower state rotational constant (B''), excited state rotational constant (B') and, where applicable, the Λ-doubling constant $(p+2q)/2$. Since the rotational constants of a given state for the two isotopologues are related to each other by the inverse ratio of their reduced masses μ (e.g., $^{180}B/{}^{178}B = {}^{178}\mu/{}^{180}\mu$), the B-value ratios are held fixed for the simultaneous contour fit. The

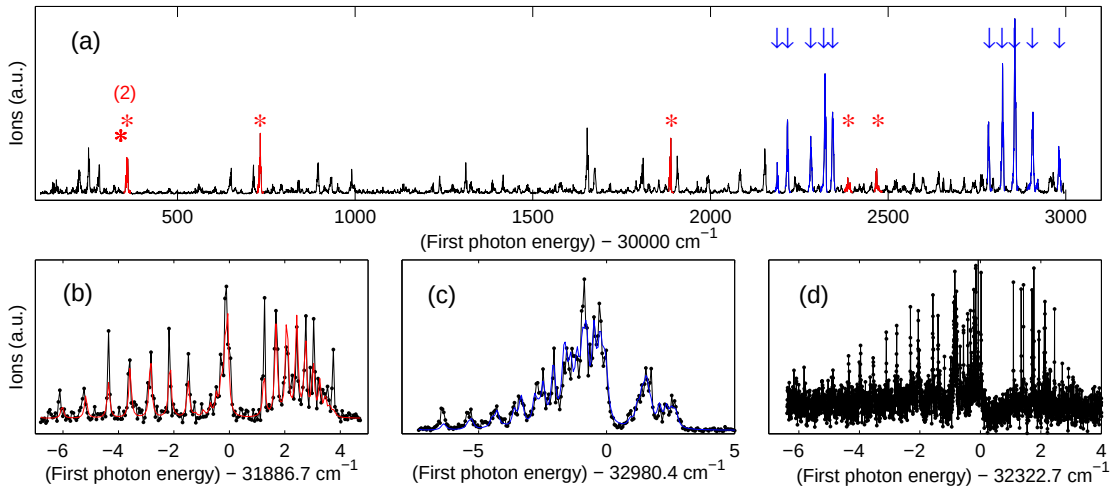

Figure 2.3: (a) Coarse (1+1) REMPI scan of excited HfF states near 30000 cm^{-1}. The ion signal shown is the integrated ion signal for all five HfF isotopologues. Two main types of transitions have been identified in this survey scan: $\Omega' = 3/2 \leftarrow \Omega'' = 3/2$ (marked by asterisks, typical spectrum shown in (b)) and $\Pi_{1/2} \leftarrow \Omega'' = 3/2$ (marked by arrows, typical spectrum shown in (c)). (b) Detailed (1+1) REMPI scan of the {31.89} vibronic band. The red smooth curve is a contour fit to the data shown as connected black dots. (c) Detailed (1+1) REMPI scan of the {32.98} vibronic band. The blue smooth curve is a contour fit to the data shown as connected black dots. (d) High resolution (1+1′) REMPI spectrum of the {32.32} vibronic band. Individual upper state rotational levels of opposite parity can be resolved.

resolution of our data is insufficient to detect a difference between the $(p+2q)/2$ terms for different isotopologues.

The molecular constants for the observed HfF transitions are summarized in Table 2.1. The numbers in parentheses indicate the 1σ-standard deviation in the last digit. The standard deviation for each fit parameter was calculated from a histogram of fit parameters obtained by bootstrapping the residuals of the fit [24]. The bootstrapping process adds the residuals, obtained after a single fit iteration, randomly to the fitted data to form a new data set, which is then re-fit against the model; this process is repeated a hundred times to get a hundred sets of fit parameters for the histogram. For the bands examined in high-resolution (1+1′) REMPI scans, (1+1) REMPI data for the same bands was also available for comparison. We find good agreement between the values of ν_0 from the coarse (1+1) REMPI spectra and from the (1+1′) REMPI spectra, where the uncertainty in ν_0 is the specified accuracy of the wavemeter, i.e. 0.1 cm^{-1}. The global systematic error of 0.1 cm^{-1} is determined by how often the wavemeter is calibrated against the Ne spectral lines. For each vibronic band, because the spectra of all isotopologues are simultaneously recorded, the isotope shifts from the (1+1) REMPI scans and (1+1′) REMPI scans agree well when the error calculated by the bootstrap method is at least 0.01 cm^{-1}. Similarly, the uncertainties in B' and B'' appear to be dominated by the bootstrap statistics when they are at least as large as 0.001 cm^{-1}. When the purely statistical standard deviations in the isotope shift or $\{B', B''\}$ fall below 0.01 cm^{-1} and 0.001 cm^{-1} respectively, the uncertainties reported in Table 2.1 have been increased to reflect an estimate of the corresponding systematic errors. We find that the purely statistical uncertainty estimated using the bootstrap method accounts well for the uncertainty in the Λ-doubling parameter.

2.3 Lower states of observed transitions

From previous work, the electronic ground state of HfF is $^2\Delta_{3/2}$ and for $\nu = 0$, the rotational constants are B =0.284 001(7) cm^{-1} and 0.283 668(6) cm^{-1} for the ^{178}Hf^{19}F and ^{180}Hf^{19}F isotopologues respectively [1]. From our own laser-induced fluorescence studies [30], we get the

Table 2.1: Summary of molecular constants (all in cm^{-1}) for observed transitions. The numbers in parentheses denote the 1σ uncertainties, assigned as explained in the text.

Ω'	$^{180}\widetilde{T}'_e$	$^{180}\nu_0 - {}^{178}\nu_0$	$^{180}Hf^{19}F$			$^{178}Hf^{19}F$			$(p+2q)/2$
			ν_0	B''	B'	ν_0	B''	B'	
3/2	27165(74)	-1.67(4)	30272.97(10)	0.282(3)	0.249(3)	30274.63(10)	0.283(3)	0.249(3)	-
	27307(19)	-1.838(10)	30731.53(10)	0.2864(01)	0.2532(10)	30733.37(10)	0.2867(10)	0.2535(10)	-
	28137(19)	-1.150(10)	30277.59(10)	0.2859(10)	0.2596(10)	30278.74(10)	0.2862(10)	0.2599(10)	-
	31831(19)	-0.030(10)	31886.71(10)	0.2832(10)	0.2638(10)	31886.74(10)	0.2835(10)	0.2641(10)	-
	31833(19)	-0.335(10)	32466.00(10)	0.2852(10)	0.2630(10)	32466.34(10)	0.2855(10)	0.2633(12)	-
	32385(56)	0.00(3)	32384.89(10)	0.2810(10)	0.2625(12)	32384.88(10)	0.2813(10)	0.2628(10)	-
1/2	27471(19)	-2.962(12)	32980.34(10)	0.2823(10)	0.2503(10)	32983.31(10)	0.2826(10)	0.2506(10)	0.0735(9)
	29565(19)	-1.464(12)	32282.12(10)	0.2849(10)	0.2586(10)	32283.58(10)	0.2852(10)	0.2589(10)	0.0176(6)
	29682(37)	-1.43(2)	32343.44(10)	0.2843(10)	0.2623(10)	32344.87(10)	0.2846(10)	0.2626(10)	0.0787(7)
	29723(37)	-1.71(2)	32905.78(10)	0.2800(12)	0.2499(12)	32907.5(2)	0.2803(12)	0.2502(11)	0.0159(7)
	31276(37)	-0.49(2)	32188.26(15)	0.280(2)	0.257(2)	32188.75(15)	0.281(2)	0.257(2)	0.057(2)
	31349(37)	-0.81(2)	32856.7(2)	0.2841(13)	0.2568(12)	32857.5(2)	0.2844(13)	0.2571(11)	0.054(3)
	31485.1(5)	-0.4503(3)	32322.7375(2)	0.28364(2)	0.25667(2)	32323.1878(2)	0.28395(2)	0.25695(2)	0.04252(3)
	31629(37)	-0.62(2)	32782.57(11)	0.2832(10)	0.2573(10)	32783.2(2)	0.2835(10)	0.2576(10)	0.074(2)
	31690.0(4)	-0.2834(2)	32217.15454(14)	0.28378(2)	0.26019(2)	32217.43796(14)	0.28409(2)	0.26047(2)	0.08537(2)
	31799(19)	-0.553(14)	32822.37(12)	0.2814(10)	0.2553(10)	32822.93(10)	0.2817(10)	0.2556(10)	0.0879(12)

isotope-averaged rotational constants to be $B_{\nu=0} = 0.2836(4)$ cm^{-1}, $B_{\nu=1} = 0.2822(10)$ cm^{-1} and $B_{\nu=2} = 0.2791(12)$ cm^{-1}. We found [30] that in our apparatus a majority of the HfF molecules are created in the ground vibronic state, although populations in multiple lower vibrational levels can be retained, athermally, in the supersonic expansion.

In this chapter, all characterized transitions appear to originate from the $^2\Delta_{3/2}$ ground state of HfF. In principle, the vibrational assignment of the lower state can be inferred from a precise fit to the lower state's rotational constant and comparison against the values obtained in Ref. [30]. The vibrational quantum number of the lower state was indeed obtained from our high-resolution (1+1′) REMPI data (Fig. 2.3(d)), which shows that some bands we observe come from the ground vibronic state. However, the (1+1) REMPI data are too noisy, too broad in linewidth, and have population in too few rotational states to permit a precise enough determination of B''.

2.3.1 A tool for understanding vibronic bands

The spectra of HfF in the vicinity of 30000 cm^{-1} are complicated; tools are needed to sort out the spectra and to group together excited states that belong to the same electronic orgin. For most of the vibronic bands, we did not have available to us sufficiently precise determinations of both B' and B'' to determine the vibrational numbering of upper and lower state levels. Instead, we used the isotope shift, $\Delta\nu \equiv {}^{180}\nu_0 - {}^{178}\nu_0$, to determine an estimate of the electronic energy, $\widetilde{T}'_e$, for each excited vibrational level.

Assuming that the electronic and vibrational energies are separable, we can write the vibronic band origin for the isotopologue ${}^i\mathrm{Hf}^{19}\mathrm{F}$ as

$$ {}^{(i)}\nu_0 = {}^{(i)}T'_e - {}^{(i)}T''_e + {}^{(i)}G'_{\nu'} - {}^{(i)}G''_{\nu''} \,, \tag{2.3} $$

and, assuming an approximately harmonic potential, we can write

$$ {}^{180}G'_{\nu'} - {}^{(i)}G'_{\nu'} = \left(\frac{\sqrt{{}^{(i)}\mu} - \sqrt{{}^{180}\mu}}{\sqrt{{}^{(i)}\mu}} \right) {}^{180}G'_{\nu'} \,, \tag{2.4} $$

where ${}^{(i)}\mu$ is the reduced mass for isotope (i). A similar relation applies for $G''_{\nu''}$, thus if we define ${}^{180}T''_e \equiv 0$, we combine Eqs. (2.3) and (2.4) to give an estimated value of the electronic energy,

${}^{180}\widetilde{T}_e$:

$$\begin{aligned} {}^{180}\widetilde{T}_e &\equiv {}^{180}T'_e - {}^{180}T''_e \\ &= {}^{180}\nu_0 + \eta\left[\Delta\nu - \left({}^{180}T'_e - {}^{178}T'_e\right) + \left({}^{180}T''_e - {}^{178}T''_e\right)\right] , \end{aligned} \tag{2.5}$$

where $\eta \equiv \sqrt{{}^{178}\mu}/(\sqrt{{}^{180}\mu} - \sqrt{{}^{178}\mu}) \approx 1861$. Then, assuming that the electronic contribution to the isotope shift is much smaller than the vibrational contribution [35],

$${}^{180}\widetilde{T}'_e = {}^{180}\nu_0 + \eta\Delta\nu\,. \tag{2.6}$$

Even in the case that the electronic contribution to the isotope shift $({}^{180}T'_e - {}^{178}T'_e - {}^{180}T''_e + {}^{178}T''_e)$ is *not* much smaller than the vibrational contribution $({}^{180}G'_{\nu'} - {}^{178}G'_{\nu'} - {}^{180}G''_{\nu''} + {}^{178}G''_{\nu''})$, two bands that share common upper and lower electronic states should get, from Eq. 2.6, very similar values for ${}^{180}\widetilde{T}'_e$, even if ν'' and ν' are different for the two bands. Again, this depends on the assumption of harmonic potentials and of separable electronic and vibrational contributions to the band energy.

Figure 2.4 is a graphical summary of the observed $\Omega' = 3/2 \leftarrow X^2\Delta_{3/2}$ bands and $\Pi_{1/2} \leftarrow X^2\Delta_{3/2}$ bands in HfF. Part (a) of the figure shows the isotope shifts, where an isotope shift is estimated to be about -0.3 cm^{-1} for a change in vibrational quanta of $\nu' - \nu'' = +1$. Some isotope shifts of anomalously large magnitude (1.5 cm^{-1} to 3 cm^{-1}) are further discussed in Section 2.5. Part (b) shows the estimated electronic energy versus band origin, in which transitions that share the same pair of lower and upper electronic states are expected to line up horizontally. In Fig. 2.4(b) we see two bands {31.89} and {32.47} that, while their band origins are separated by 579 cm^{-1}, have ${}^{180}\widetilde{T}'_e$ values that differ by only 13 cm^{-1} (identical within measurement uncertainty). It is likely that these two bands share a common electronic transition with ${}^{180}\widetilde{T}'_e \approx 31840$ cm^{-1}, as indicated by the y-axis. We note that 579 cm^{-1} would be a reasonable excited state vibrational spacing. We can see, from the spacing of data points in the y-direction in Fig. 2.4(b), that there are at least four distinct $\Omega' = 3/2$ electronic levels: near 27200, 28150, 31850 and 32400 cm^{-1}. As a caveat, we note that several of the bands have unreasonably large isotope shifts. We discuss possible causes for anomalous isotope shifts in Section 2.5 below.

For the $\Pi_{1/2} \leftarrow X^2\Delta_{3/2}$ transitions, from Fig. 2.4(b) we can see immediately that there are multiple distinct $\Pi_{1/2}$ electronic levels: one with ${}^{180}\widetilde{T}_e' \approx 27500$ cm^{-1}, at least one with ${}^{180}\widetilde{T}_e' \approx 29600$ cm^{-1}, and multiple levels with ${}^{180}\widetilde{T}_e'$ in the range 31500 ± 300 cm^{-1}. One cannot say for certain that the three bands with ${}^{180}\widetilde{T}_e' \approx 29600$ cm^{-1} share a common electronic transition. With reference to Table I, we see the {32.34} band has a Λ-doubling constant quite distinct from that of the {32.91} band, which suggests either two distinct electronic transitions or, more likely, a local perturbation of one of the bands. For the cluster of six $\Omega' = 1/2$ bands with ${}^{180}\widetilde{T}_e'$ between 31200 and 31800 cm^{-1}, the spread in ${}^{180}\widetilde{T}_e'$ is too large for the bands to share a common electronic transition. Moreover, the respective rotational constants for the bands {32.22} and {32.32} are determined so precisely that we can say with some confidence that these two bands share a common lower level vibrational level ($\nu'' = 0$), but belong to distinct upper vibrational levels. Since the values of ν_0 are too close together to make it likely that the upper levels are adjacent vibrational levels of the same electronic state, it seems quite likely that the two bands terminate in distinct electronic upper levels. For the bands {32.19} and {32.86}, the vibronic band origins differ by 668.41(14) cm^{-1}, which is within 2σ of the 1–0 vibrational energy splitting of the $X^2\Delta_{3/2}$ ground state [30]. Further, both bands fit to the same B' whereas one band fits to a value of B'' that is consistently smaller than that of the other band. This strongly suggests that the bands {32.19} and {32.86} arise from the $\nu'' = 1$ and $\nu'' = 0$ ground vibrational levels, respectively.

2.4 Rotational line strengths

In the (1+1) REMPI experiments, the transition excited by the second photon is typically left unsaturated, so the observed REMPI line strengths are actually a convolution of the line strengths for both the first and second step in REMPI. We have observed in other work [52] that the above-threshold ionization spectrum is highly structured. This structure corresponds to $\nu_{\mathrm{Ryd}} > 0$ levels that autoionize into $\nu^+ = 0$ vibrational levels of HfF^+. Qualitatively, the Hönl-London expressions for Hund's case (a) molecules work well to describe the observed rotational line intensities. This is the case for all observed bands except two $\Omega' = 3/2 \leftarrow X^2\Delta_{3/2}$ bands: {30.73} and {32.47}.

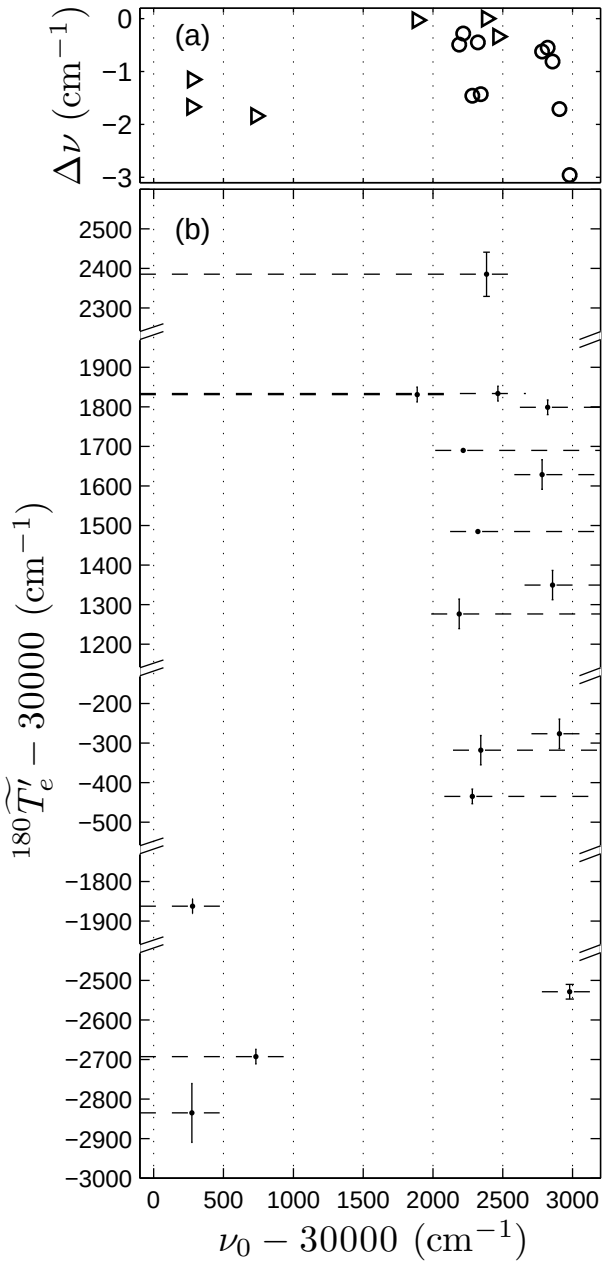

Figure 2.4: (a) Isotope shifts (triangles denoting $\Omega' = 3/2 \leftarrow X^2\Delta_{3/2}$ transitions and circles denoting $\Pi_{1/2} \leftarrow X^2\Delta_{3/2}$ transitions) and (b) calculated electronic energies for the $\Omega' = 3/2 \leftarrow X^2\Delta_{3/2}$ transitions (dashed lines terminating on the left axis) and $\Pi_{1/2} \leftarrow X^2\Delta_{3/2}$ transitions (dashed lines terminating on the right axis). The spread in $^{180}\widetilde{T}'_e$ values indicates at least four distinct $\Omega' = 3/2$ electronic states and at least six distinct $\Pi_{1/2}$ electronic states.

To fit the line intensities in a given vibronic band, we included terms that described possible interference effects between parallel ($\Omega' - \Omega'' = 0$) and perpendicular ($\Omega' - \Omega'' = \pm 1$) transitions [48]. For example, a nominal $\Omega' = 3/2$ (for clarity, also denoted here as Ω'_N) excited state could also possess some $\Omega' = 1/2$ ($= \Omega'_N - 1$) and/or $\Omega' = 5/2$ ($= \Omega'_N + 1$) character from mixing (via the Hamiltonian term -$B\mathbf{J}^{\mp}\mathbf{L}^{\pm}$) with nearby "dark" states. When the excited state is no longer a good Hund's case (a) state due to these admixtures, transitions between the $^2\Delta_{3/2}$ ground state and all three admixed Ω' components are allowed. The line strength $S(J', \Omega'_N; J''\Omega'')$ for a given rotational line is given by:

$$S(J', \Omega'_N; J''\Omega'') \propto \left| \mu_\alpha \begin{pmatrix} J' & 1 & J'' \\ -\Omega'_N & (\Omega'_N - \Omega'') & \Omega'' \end{pmatrix} + \mu_\beta \begin{pmatrix} J' & 1 & J'' \\ -(\Omega'_N + 1) & (\Omega'_N + 1 - \Omega'') & \Omega'' \end{pmatrix} + \mu_\gamma \begin{pmatrix} J' & 1 & J'' \\ -(\Omega'_N - 1) & (\Omega'_N - 1 - \Omega'') & \Omega'' \end{pmatrix} \right|^2, \quad (2.7)$$

where μ_α, μ_β, and μ_γ refer to the transition dipole matrix elements between the ground state and the admixed excited states (of Ω'_N, $\Omega'_N + 1$, and $\Omega'_N - 1$ character, correspondingly). Note that, since the $\mu_\alpha, \mu_\beta, \mu_\gamma$ amplitudes are summed and then squared, interference effects are present. These matrix elements are allowed to vary in the contour fits. If the second and third terms are ignored, the line strength expression reduces to the normal Hönl-London factor [94].

For the $\Pi_{1/2}$ excited states, the $\Delta\Omega = \pm 1, 0$ transition selection rule requires the last term to be zero. Between the two remaining transition dipole matrix elements, μ_α tends to dominate for all of the observed $\Pi_{1/2} \leftarrow X^2\Delta_{3/2}$ bands. Similarly, μ_α tends to be the dominant dipole matrix element for all of the $\Omega' = 3/2 \leftarrow X^2\Delta_{3/2}$ bands except for two, {30.28} and {32.47}. Figure 2.5 compares the contour fits performed using the Hönl-London expressions versus Eq. (2.7) to describe rotational line intensities for each of the anomalous bands. In both cases, the incorporation of interference effects in Eq. (2.7) gives rise to a better fit. In particular, the contour fits indicate an admixture from a nearby $\Omega' = 1/2$ state (where μ_γ is dominant), which suggests that the observed

upper state is of nominal $^2\Pi_{3/2}$ character, the transition "brightness" from the ground state has been lent to it from a nearby $\Pi_{1/2}$ state. In fact, the rotational line strengths imply that at least one of the two bands ($\{32.47\}$) is located very close to a $\Pi_{1/2} \leftarrow X^2\Delta_{3/2}$ band, as seen in Fig. 2.4. The observed admixture of electronic states is the reason for using Hund's case (c) notation to specify the $\Omega' = 3/2$ excited states.

2.5 Large isotope shifts

As shown in part (a) of Fig. 2.4, several bands were observed to have isotope shifts more negative than -1.6 cm^{-1}, which would correspond to the upper state of the transition having vibrational energy that exceeds the lower state vibrational energy by more than 3000 cm^{-1}. If we assume a typical upper-state vibrational spacing of $\sim$ 600 cm^{-1}, a 3000 cm^{-1} vibrational change implied a change in vibrational quanta, $\Delta\nu \sim 5$. Deriving bond lengths from observed rotational constants, one calculates extremely small Franck-Condon factors for such transitions. This poses a mystery: how were we able to excite these transitions? One possible explanation could be that interactions between potential curves, say an anticrossing of some sort, generate a few levels described by anomalously large vibrational constants, as depicted in Fig. 2.6(a). An upper-state vibrational constant as large as 1000 cm^{-1}, for instance, could yield an acceptably large Franck-Condon overlap for the corresponding $\Delta\nu = 3$ transition. But it seems unlikely there would be multiple electronic states with such exotically large curvatures in their potential curves. Moreover, in Fig. 2.4, the x-axis spacing between some pairs of points that are clumped along the y-axis suggests that at least some of the large-isotope-shift bands have relatively modest upper-state vibrational spacing, perhaps 450–600 cm^{-1}.

As an alternative hypothesis to the picture of transitions involving large changes in the number of vibrational quanta, the anomalous isotope shifts could arise from isotope-specific accidental degeneracies between two mutually perturbing excited states, each of which have, in the absence of perturbation, smaller isotope shifts (Fig. 2.6(b)). In this case, the perturbing state would not only cause the $^{178}Hf^{19}F$ and $^{180}Hf^{19}F$ states to split apart from each other, but also cause all of

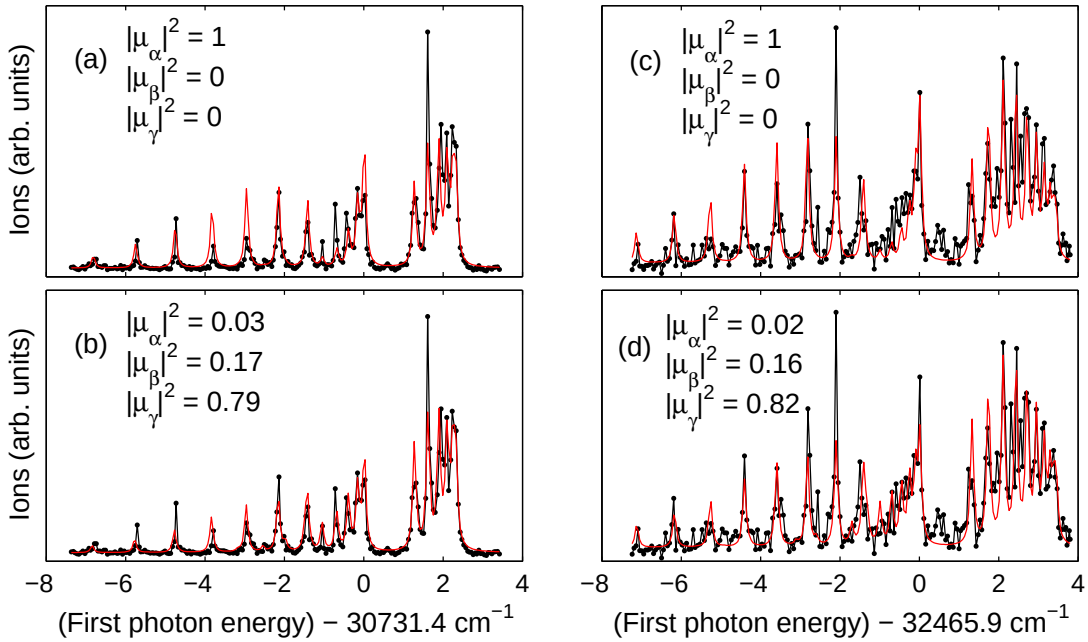

Figure 2.5: Contour fits (red) to the $\Omega' = 3/2 \leftarrow X^2\Delta_{3/2}$ {30.73} and {32.47} bands (data shown as connected black dots). In (a, c), the contour fits are constrained to use Hönl-London expressions for the rotational line strengths, which are shown here to be inadequate for a good description of the observed line intensities, especially for those in the Q branch. In (b, d), the contour fits are allowed to take into account possible interference effects between parallel and perpendicular transition moments. In both cases, μ_γ dominates over the other transition dipole matrix elements, indicating that the nominal $\Omega' = 3/2$ upper states in both cases appear to possess an admixture from nearby $\Omega' = 1/2$ states.

the other isotopologues to follow an irregular splitting that is not linear with $\sqrt{1/^{(i)}\mu}$. Figure 2.7 displays the isotope splitting between the four most abundant isotopologues for several bands with large isotope shifts. The isotopologues are found to follow a linear energy spacing relative to the inverse square root of their reduced masses, which is what we expect in the *absence* of such an isotopologue-specific perturbation and where the observed isotope shift is determined primarily by $\sqrt{1/^{(i)}\mu}$ vibrational energy shifts.

The high visibility of bands that had large isotope shifts could also be due to spin-orbit interactions between vibrational levels that belong to different excited states, as shown in Fig. 2.6(c). The observed excited state of a high vibrational quantum number, ν'_d, could have been an initially "dark" electronic state that became observable by spin-orbit interaction with a "bright" electronic state of much lower vibrational quantum number, ν'_b. This would provide the latter with decent Franck-Condon overlap with the lower state. Such a spin-orbit interaction would be proportional to the vibrational overlap matrix element, $\langle \nu'_d | \nu'_b \rangle$ [48], which is estimated to be large only for $\nu'_d \approx \nu'_b \pm 1$ for all the observed excited states in HfF.

One plausible explanation for the large isotope shifts is that there may be a third state that induces an indirect interaction between the observed state and another "bright" state, where the "bright" state is of a significantly lower vibrational quantum number and has large Franck-Condon overlap with the lower state (Fig. 2.6(d)). It is likely that there are other plausible explanations for the observation of such anomalously large isotope shifts, and we invite the interested spectroscopist to offer his or her ideas.

2.6 Intermediate states for OODR autoionization

Among the six $\Pi_{1/2} \leftarrow X^2\Delta_{3/2}$ bands with $^{180}\widetilde{T}'_e$ in the range 31200–31900 cm^{-1}, two of the bands ({32.22} and {32.32}) have been scanned at high resolution, using the (1+1′) REMPI technique. Their distinct Λ-doubling constants, coupled with the close proximity of the electronic energy levels, indicate that they must belong to electronically distinct states in order to exhibit such small repulsion. Their dominant electronic configurations must differ by at least two spin-orbitals,

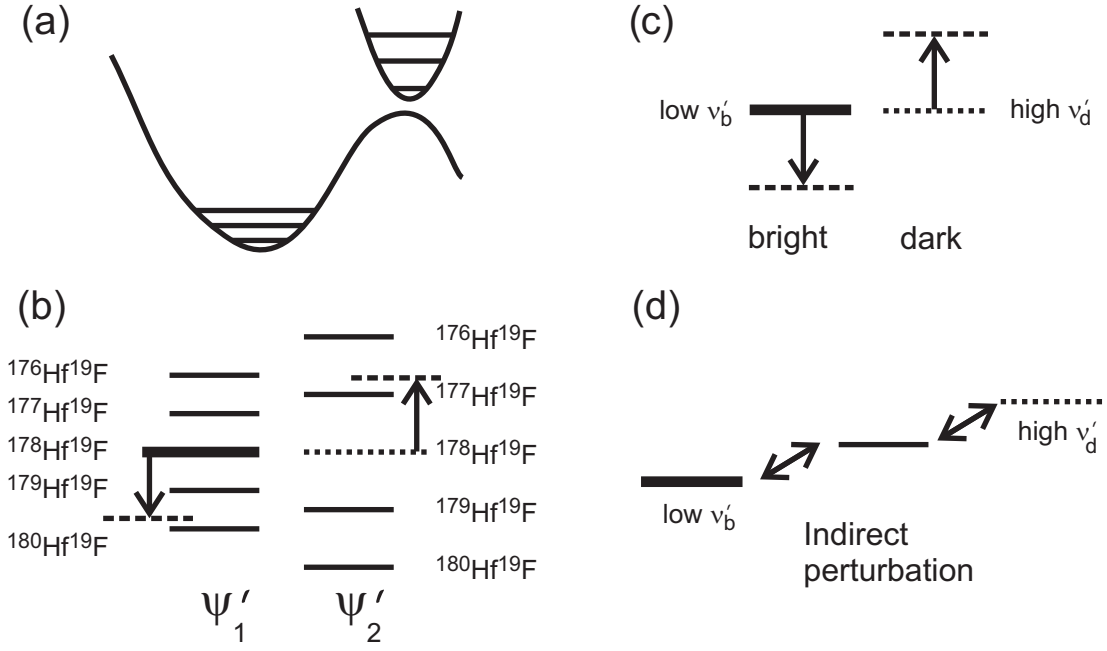

Figure 2.6: Four hypotheses for the observation of large isotope shifts. (a) Avoided crossing of potential energy curves, giving rise to anomalously large vibrational spacings. (b) Isotope-specific accidental degeneracies between two mutually perturbing excited states, ψ'_1 and ψ'_2. In this picture, the isotope splittings would not be linear in $\sqrt{1/^{(i)}\mu}$. (c) Local perturbation between a high-ν'_d level of a "dark" electronic state and a low-ν'_b level of a "bright" electronic state. The higher ν'_d level becomes observable by borrowing brightness from the low-ν'_b level, but it has the normal isotope shift of a high-ν'_d level. (d) Indirect coupling between the high-ν'_d level and low-ν'_b level.

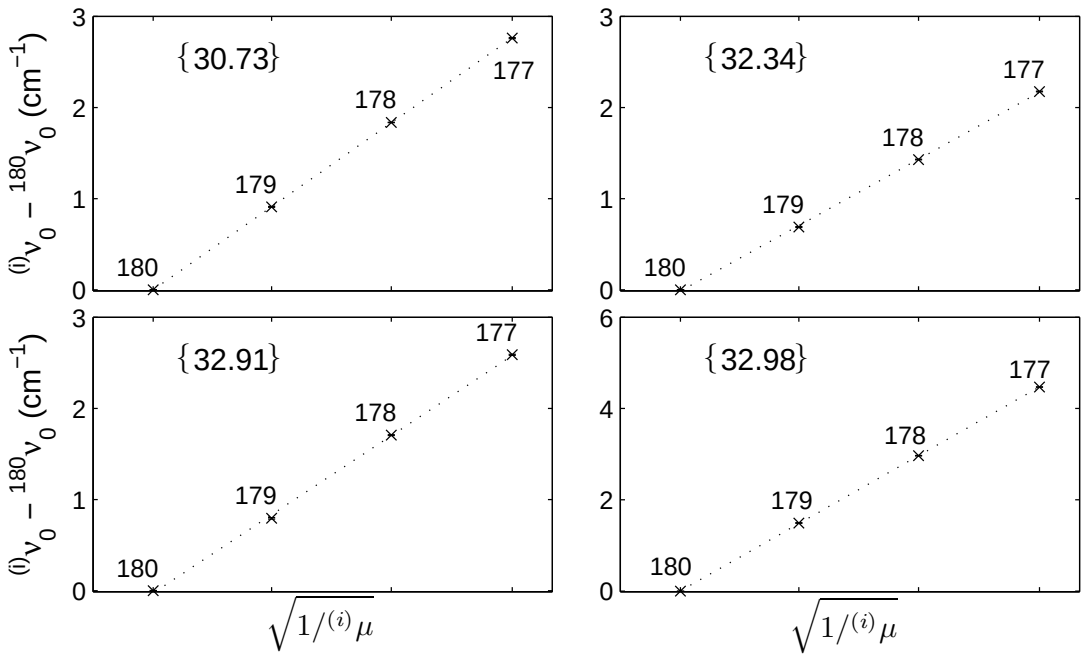

Figure 2.7: For the vibronic bands $\{30.73\}, \{32.34\}, \{32.91\}$, and $\{32.98\}$, the isotope shifts are found to vary linearly with the inverse square root of the isotopologue reduced masses, which suggests that anomalously large isotope shifts are indeed due to a large $\Delta\nu$ and not to isotope-specific perturbations.

e.g. $sd\delta(^3\Delta_1)n\ell\lambda$ versus $s^2(^1\Sigma^+)n'\ell'\lambda'$, where $sd\delta(^3\Delta_1)$ or $s^2(^1\Sigma^+)$ refers to the core configurations, and $n\ell\lambda$ or $n'\ell'\lambda'$ refers to an additional electron in a more highly excited orbital. These two configurationally distinct states could potentially be used as intermediate states to access different states of HfF^+ when performing OODR autoionization, which is relevant to our goal of preferential population of the metastable $^3\Delta_1$ state rather than $X^1\Sigma^+$ for the eEDM experiment. These two vibronic states have indeed been observed to yield very different autoionization spectra, as shown in Fig. 2.8. We are in the process of characterizing the electronic states of the ions so produced.

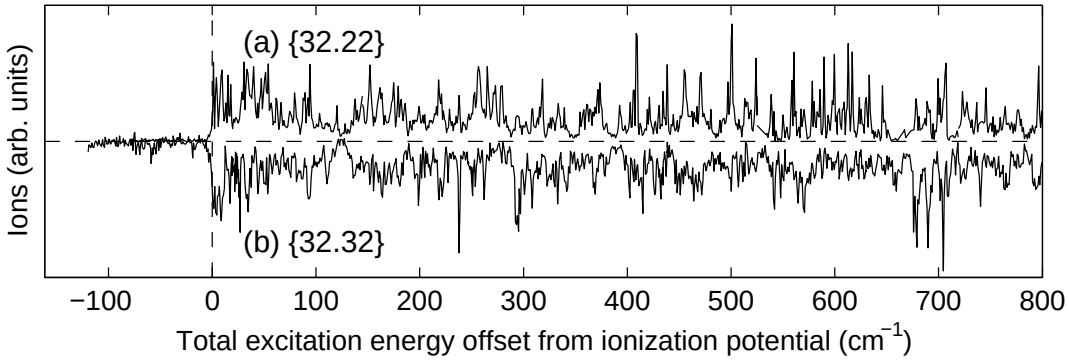

Figure 2.8: OODR autoionization spectra measured by tuning the first photon to access a particular excited rotational state ($J' = 1/2(a)$) using the vibronic bands (a) {32.22} and (b) {32.32} (ion signal inverted for clarity), then scanning the second photon to map out the spectrum of autoionizing Rydberg states accessible from that intermediate state. Each case gives a unique set of autoionization resonances, suggesting that the ionic core of the autoionizing Rydberg state differs between the two cases.

2.7 Summary

A plethora of HfF bands in the 30000–33000 cm^{-1} region have been observed using (1+1)REMPI and (1+1′) REMPI. We have characterized six $\Omega' = 3/2 \leftarrow X^2\Delta_{3/2}$ and ten $\Pi_{1/2} \leftarrow X^2\Delta_{3/2}$ vibronic bands. To sort out the spectra, we used the isotope shift for a given band to determine the electronic energy, $^{180}\widetilde{T}'_e$, for the upper electronic state. This method of grouping bands only works for bands where the potential energy curves are fairly well-approximated by a harmonic potential. Two bands exhibit interference effects between parallel and perpendicular transition moments

through their rotational line strengths. Several bands with anomalously large isotope shifts had intensities much larger than predicted based on the expected small Franck-Condon factors for transitions from the low-ν'' lower state. Among the six $\Pi_{1/2} \leftarrow X^2\Delta_{3/2}$ bands with electronic energy offsets crowded in the vicinity of 31300–31800 cm^{-1}, there are at least two electronically distinct states. When such configurationally distinct states are used as intermediate states in the OODR preparation of Rydberg states, these states provide access to at least two possible routes for creating distinct HfF^+ electronic states after autoionization decay, which will be important for the selective formation of ionic HfF^+ in the desired $^3\Delta_1$ quantum state for the eEDM experiment.

Chapter 3

Autoionization for preparing HfF^+ in a single rovibronic ($^1\Sigma^+$) state [52]

A high-precision search for the eEDM demands the preparation of as many HfF^+ ions of a single isotope as possible in a particular $|J^+, M^+\rangle$ rovibronic, Zeeman sublevel. Unwanted ions created in other states are co-trapped and can collide with the relevant ions, contributing to the dephasing of the latter species. The reduction in both the relevant sample number and coherence time can doubly hurt the sensitivity of an eEDM experiment. Hence, the state preparation of HfF^+ in a single rovibronic, Zeeman level is an important but non-trivial task.

The strategy we use to prepare HfF^+ in a state-selective manner is the autoionization of Rydberg HfF molecules excited from ground state HfF using the optical-optical double resonance (OODR) technique [48]. These autoionizing states lie above the lowest ionization threshold. Their ion-core is excited and decays after a short time, releasing energy to kick out the Rydberg electron. Will the resultant state of the ion have some memory of the state of its parent Rydberg molecule?

In principle, the above question can be answered by building a model of autoionization based on multichannel quantum defect theory (MQDT) [25, 37, 80, 31], like that performed for CaF [41]. This model calculates the quantum defect matrix elements $\mu(R, \mathcal{E})$ and their derivatives with respect to the internuclear distance R and energy $\mathcal{E}$, which can then be used to describe the Rydberg energy spectrum, dynamics of autoionization and resultant ion states. However, constructing such a quantum defect model demands extensive knowledge of Rydberg levels to provide input parameters; such knowledge is presently lacking for HfF.

Alternatively, we tackle the question of Rydberg state – ion state branching ratios by experi-

mentally probing the post-autoionization states of HfF^+ with laser-induced fluorescence (LIF). Ion LIF has been reported before by other groups as a tool to examine the states of ions created from resonance-enhanced multiphoton ionization (REMPI) [20, 27, 28, 90, 67] , electron-impact ionization [59] and ion-molecule collisions [32]. A slightly different but related form of state detection is the grating-dispersed fluorescence obtained from highly-excited ions formed by photoionization using synchrotron light sources [43, 68, 38, 17, 66]. In our experiment, the ions are formed from a Rydberg band at 54 cm^{-1} above the lowest ionization threshold. The upper levels of this Rydberg band are energetically allowed to decay only to the $X^1\Sigma^+(\nu^+ = 0)$ vibronic ground state of HfF^+, although the ions could be spread out over as many as ≈ 200 distinct $|J^+, M^+\rangle$ rotational-Zeeman sublevels. The ion distribution over the various $|J^+, M^+\rangle$ states remain to be unveiled through their LIF intensities.

To predict the ion population distributions, which are connected to the observed fluorescence intensities, we present a simplified model of autoionization that assumes: 1. the Rydberg molecule has the same electronic ion-core as its autoionization product, and 2. the Rydberg electron flies off with the same angular momentum as it possessed when it was bound to the molecule, i. e. the dynamics of autoionization are radial only. The first assumption is based on the picture that the Rydberg state undergoes vibrational autoionization as opposed to electronic autoionization; in vibrational autoionization, propensity rules tend to favor a $\nu_{Ryd} = 1 \rightarrow \nu^+ = 0$ decay process [48]. The second assumption means that unlike the quantum defect model, the simplified model neglects the matrix elements of $\partial\mu/\partial R$ that are off-diagonal in the Rydberg electron's orbital angular momentum l. We do not yet understand the HfF Rydberg spectrum sufficiently well, in fact, to independently test these two assumptions. Instead, the severe lack of information obligates us to propose an initial model that is as simple as possible. As will be seen, the model can be adjusted to give a good account of the ion rotational distributions, and with no further adjustment it does well predicting the orientation and M^+ populations of a particular J^+ level. That said, on the basis of the present work alone, we cannot rule out electronic autoionization nor the presence of

angular dynamics in the autoionization process. The remaining sections of this chapter[1] detail the experimental methods, autoionization theory and results of our LIF studies on autoionized HfF, with the primary goal toward maximizing ion creation in a desired single $|J^+, M^+\rangle$ state.

3.1 Experiment setup

Fig. 3.1 shows a schematic of the OODR-LIF experiment setup used to ionize a HfF molecular beam and probe the resultant ionic states. The source chamber is the same as that described in Section 2.1, while the OODR-LIF chamber replaces the TOFMS chamber. The two skimmers responsible for collimating the molecular beam are also now replaced by skimmers of 3 mm orifice diameter, separated by 12.5 cm. Three co-propagating lasers — two for OODR and one for LIF of the ions — enter and exit the OODR-LIF chamber through Brewster-angled windows mounted on 15-cm long tubes, in which baffles are placed to reduce scattered light. The three lasers intersect the molecular beam axis at 90° and the HfF^+ ions produced are accelerated by an electric field of 0.3 V/cm through 5 cm to two microchannel plates (MCP) stacked in a chevron configuration. The ion signal, after amplification by a transimpedance amplifier, is monitored on an oscilloscope. Fluorescence photons are collected above and below the ion beam for 2 μs after the ions are excited. The mirror on top collects most of the fluorescence photons and directs them to a parabolic mirror below, which in turn focuses them onto a photomultiplier tube (PMT). To further reduce scattered light counts, the photomultiplier tube is not gated on until 200 ns after the LIF laser fires. A bandpass filter centered at 820 nm is also placed between the top collection mirror and the parabolic mirror. The photon signals are amplified by a transimpedance amplifier, accumulated over at least 500 shots using a separate channel of the oscilloscope and counted individually using a peak-finding algorithm.

All three lasers involved in addressing the energy levels in the OODR-LIF scheme, as depicted in Fig. 3.2, are dye lasers. The first OODR laser pulse (309 nm, 1.5 μJ/pulse, 10 ns, 150 MHz FWHM) is the output of a home-built two-stage Rhodamine 101 dye cell amplifier, frequency

[1] Most of this chapter has already appeared in Reference [52].

doubled with a β-BBO crystal. The dye cell amplifier is seeded by a continuous-wave ring dye laser operating with Rhodamine 610 Chloride dye and pumped by the second harmonic of a Nd:YAG laser. The Nd:YAG second harmonic at 532 nm also pumps a dye laser operating with Pyridine 2, the output of which is frequency-doubled with a KDP crystal to produce the second OODR laser pulse (345–370 nm, 100–200 μJ/pulse, 10 ns, 0.1 cm^{-1} FWHM). The second laser pulse is delayed by 14 ns relative to the first laser. The LIF laser pulse (769 nm, 6–8 ns, 0.5 uJ/pulse, 100–200 MHz) is the output of a home-built two-stage LDS 798 dye cell amplifier, which is pumped by the second harmonic of a Nd:YAG laser and seeded by an external cavity diode laser at 769 nm to address the $[13.0]1(\nu' = 0) \leftarrow X^1\Sigma^+(\nu'' = 0)$ transition[1] [16] in ^{180}Hf^{19}F$^+$. The LIF laser is delayed by 2 μs relative to the OODR lasers. Dichroic mirrors are used to overlap the three laser beams spatially before they enter the vacuum chamber. The laser pulses are linearly polarized either by the orientation of their frequency-doubling crystals or by passing through a polarizing beam splitter. They can then be set to either left or right circular polarizations using quarter and half waveplates for the appropriate wavelength ranges. Throughout the experiment, the frequencies of the seed lasers for both the first OODR and LIF lasers are locked to a single rotational line using a high-precision wavemeter that is regularly calibrated against the ^{87}Rb D_2 transition. The frequency of the second OODR laser is monitored by both the high-precision wavemeter and a second wavemeter that is internally calibrated against Ne spectral lines.

To record OODR autoionization spectra, we fix the first OODR laser pulse on a single rotational line of a given parity of the $[31.5]1/2 \leftarrow X^2\Delta_{3/2}$ transition[2] [51] in the ^{180}Hf^{19}F isotope while scanning the second laser pulse in frequency. We use circular dichroism techniques (i.e. we compare the ion signal obtained when both lasers are polarized with the same helicity versus when polarized with opposite helicity) to identify transitions to various Rydberg rotational levels (denoted as J) in the autoionization spectra [96, 65].

[1] "$[13.0]1(\nu' = 0)$" refers to an excited state of vibrational quantum number $\nu' = 0$, total angular momentum projected on the body-fixed axis $\Omega = 1$, and at 13,0xx cm^{-1} from the vibronic ground state of HfF$^+$.

[2] Similarly, "$[31.5]1/2$" refers to an excited state of $\Omega = 1/2$, and at 31,5xx cm^{-1} from the vibronic ground state of HfF.

Rovibronic state detection of the HfF^+ ion yield is accomplished by counting fluorescence photons that are emitted down to the $X^1\Sigma^+(\nu'' = 1)$ vibronic level [63, 4] when the ions are excited by the LIF laser pulse. The frequency of the LIF laser is chopped every 100 shots between being on-resonance and 500 MHz off-resonance of a rotational line. The number of fluorescence photons detected when the horizontally-polarized LIF laser is tuned to an R(0), Q(1), Q(2), ... , Q(5) transition is related to the rotational populations in the $J^+ = 0, 1, 2, ..., 5$ levels respectively. Both OODR laser pulses are set to right circular polarizations. LIF detection is carried out when the second OODR laser pulse is tuned to both on-resonance and ± 0.35 cm^{-1} off-resonance of an autoionizing line, so as to subtract out the contribution to the measured LIF intensities from non-resonantly produced ions.

To determine the orientation of the ions formed in the $J^+ = 1$ rotational state, the LIF laser is fixed on either the Q(1) or the R(1) transition. With both OODR lasers right circularly polarized, we chop between having the LIF laser left and right circularly polarized and measure the respective fluorescence signals. Half waveplates and quarter waveplates are mounted on motorized rotation stages to perform the polarization switching.

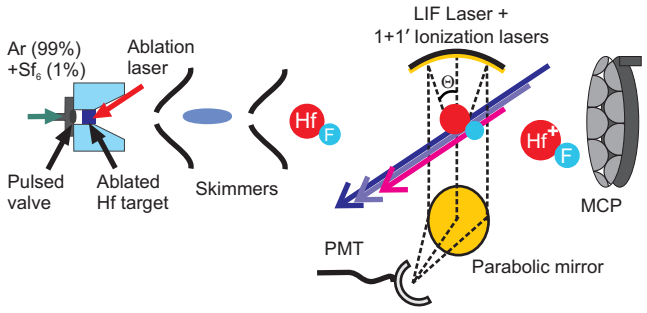

Figure 3.1: Schematic of the OODR-LIF apparatus. The molecular beam axis, the direction of propagation of the three co-propagating lasers and the axis of fluorescence photon collection are mutually perpendicular. From the ions, the fluorescence collection mirror on top subtends a polar angle of $\delta\theta = 75°$, whereas the parabolic mirror below subtends $\theta = -11.8°$ to $8.4°$. A 820nm-bandpass filter, placed between the top collection mirror and the parabolic mirror, is not shown.

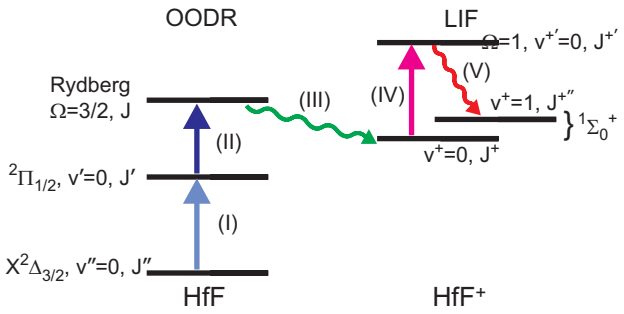

Figure 3.2: Neutral HfF and HfF^+ energy levels addressed in the OODR-LIF scheme. The quantum numbers assigned to each rotational level follow those given in Section 3.3. The transitions marked by roman numbers correspond to the following: I) first excitation photon in the OODR technique, II) second excitation photon in the OODR technique, III) autoionization, IV) laser-driven transition in LIF, and V) fluorescence photons detected by the PMT.

3.2 Autoionizing states of hafnium fluoride

Transitions to different Rydberg rotational levels can be made by tuning the first OODR laser pulse to access intermediate states of different J' and parity, as shown by the stacked plots in Fig. 3.3a. The various rotational transitions driven by the first OODR laser pulse are labeled on the top left corner of each subplot. Since the Ω-doublets of the $X^2\Delta_{3/2}$ ground state in HfF cannot be resolved by the first OODR laser, the parity of the Rydberg states can only be determined up to an overall sign and is assigned as either 'a' or 'b' instead of as 'e' or 'f'. The Rydberg rotational levels are identified using the circular dichroism technique outlined in Section 3.1; for the autoionization spectrum shown in Fig. 3.3a, both OODR lasers are chosen to be right circularly polarized to enhance the autoionization line intensity from higher J states. The level spacings arise from half-integer pattern-forming quantum numbers, which indicate that the Rydberg electron is core-penetrating, i.e. the inner lobe of its wavefunction lies inside the molecular ion-core [40]. Since no transition to the $J = 1/2$ level is observed, the Rydberg vibronic band is inferred to have $\Omega = 3/2$. The Ω-doublets of the Rydberg vibronic band have no observable energy splitting, even up to $J = 11/2$. The Rydberg rotational energies are fit to the polynomial $E(J) = T_0 + B_{Ryd}J(J+1)$, yielding a rotational constant of $B_{Ryd} = 0.2911(6)$ cm^{-1}. The $J = 7/2$ and $11/2$ levels are found to be perturbed by as much as -0.16(2) cm^{-1} and +0.27(3) cm^{-1} from the expected energy levels of a rigid rotor.

The Rydberg vibronic band characterized at 54 cm^{-1} above the lowest ionization threshold (59462(2) cm^{-1}) is part of a broader scan of the autoionization spectrum, shown in Fig. 3.3b. In contrast to the anomalously clean series of rotational lines in Fig. 3.3a, the HfF autoionization spectrum is generally cluttered. Although the pulse energy of the second OODR laser is reduced to avoid saturating the transitions to Rydberg states, the autoionization spectrum contains many broad features, the narrowest of which, at 0.3 cm^{-1}, is three times broader than the linewidth of the second OODR laser. This broadening cannot be attributed to either lifetime or hyperfine structure. The clutter of features makes it impossible for us to identify a clean Rydberg series of

lines leading to ionization thresholds [3] .

The identification of various Rydberg series and their underlying Rydberg electron character could potentially lead to predictions of ion rovibronic distributions. Alternatively, we can measure the distributions of the ions formed and work backwards to elucidate the character of the Rydberg electron. Toward this end, we developed a simplified model of autoionization, presented in the following section.

3.3 Theory

In this simplified model of autoionization, the Rydberg molecule is treated as a Rydberg electron attached to a $^1\Sigma^+$ ion-core at relatively short distances. The good quantum numbers of the resonant Rydberg state include the total angular momentum of the molecule J, its projection on the molecular z-axis Ω (approximately), its projection on the laboratory z-axis M_J, and the parity of the molecule. The quantization ($\hat{z}$) axis in the laboratory is provided by the direction of laser propagation. The anisotropic interaction between the outermost electron and the ion-core couples the orbital angular momentum l and total angular momentum j of the Rydberg electron. Neglecting the vibrational part, we write the short-range Rydberg states as a superposition of basis states having definite values of l and j:

$$\Psi_{res} = \sum_{lj} A_{lj} \psi_{lj}^{|\Omega| P} \,, \tag{3.1}$$

where A_{lj} is the probability amplitude of the corresponding $\{l, j\}$ partial wave, and where

$$\begin{aligned} \psi_{lj}^{|\Omega| P} = \; & \tfrac{1}{\sqrt{2}} \Bigg[\mathcal{R}\left(J\,|\Omega|\,M_J\right) \sum_{\Omega\sigma} C^{j|\Omega|}_{l\Omega;s\sigma} Y_{l\Omega} \chi_{s\sigma} \\ & - (-1)^{j+J-l+P} \mathcal{R}\left(J\,-\,|\Omega|\,M_J\right) \sum_{\Omega\sigma} C^{j-|\Omega|}_{l\Omega;s\sigma} Y_{l\Omega} \chi_{s\sigma} \Bigg] \,. \end{aligned} \tag{3.2}$$

In Eq. (3.2), $C, Y_{l\Omega}$, and $\chi_{s\sigma}$ denote a Clebsch-Gordan coefficient, spherical harmonic, and spinor wavefunction, respectively. $\mathcal{R}\left(J\Omega M_J\right)$ is related to the Wigner rotation matrix $D^J_{M_J\Omega}$, which is a

[3] The lowest and excited HfF ionization thresholds have been identified using pulsed field ionization – zero electron kinetic energy (PFI-ZEKE) photoelectron spectroscopy[4]

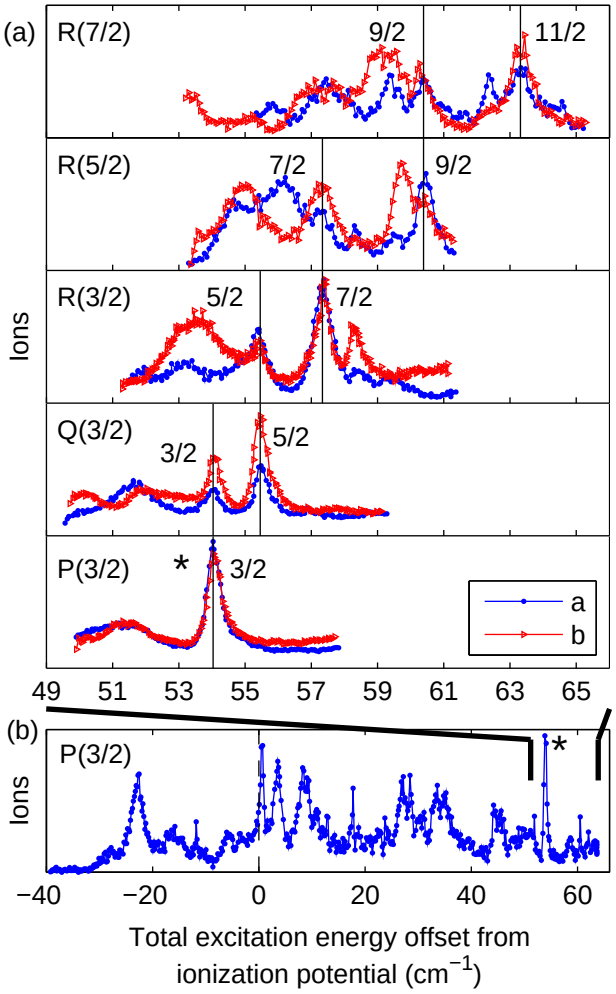

Figure 3.3: (a) Stacked plots of OODR autoionization spectra, measured by scanning the frequency of the second photon while holding the first photon fixed on different ground-intermediate transitions (denoted on the left of the figure as 'P(3/2)', etc.) to access different intermediate rotational states. The identified Rydberg rotational energy levels are marked by solid black lines with their corresponding assignments. The autoionization spectra shown as blue dots (red triangles) belong to the same parity 'a' ('b'). The ionization energy given by the x-axis is referenced to the ground rovibronic level in neutral HfF [1] and is offset from the ionization potential, 59462(2) cm^{-1}. (b) A broader scan of OODR ionization spectra is conducted in an electric field of ≈ 25 V/cm, which explains the appearance of peaks in ion creation at ~ 30 cm^{-1} below the ionization potential of HfF. The peak marked by an asterisk is the same peak as that in (a).

function of the Euler angles $\{\alpha, \beta, \gamma\}$,

$$\mathcal{R}\left(J\Omega M_J\right) = \sqrt{\frac{2J+1}{8\pi^2}}\left[D^J_{M_J\Omega}\left(\alpha\beta\gamma\right)\right]^* . \tag{3.3}$$

The parity of the molecule is given by $(-1)^P$.

After autoionization, the distance between the emitted electron and the ion-core is large. This long-range (electron +HfF^+) system is described by the total ionic angular momentum J^+, its projection M^+ on the laboratory z-axis, and its projection Ω^+ on the body-fixed z-axis. Here, $\Omega^+ = 0$ since the ion is in a $^1\Sigma^+$ state. Because the short-range states have a definite total angular momentum J and projection on the laboratory z-axis M_J, we also want to construct the long-range states with definite J and M_J. We assume that the Rydberg electron flies off with the same $\{l, j\}$ angular momenta it possessed when bound to the molecule, i.e. there are no angular dynamics in autoionization. The $\{l, j\}$ partial waves of the system after autoionization can then be written as

$$\phi^{J^+}_{lj} = \sum_{M^+ m_j} C^{JM_J}_{J^+M^+;jm_j}\mathcal{R}\left(J^+, \Omega^+ = 0, M^+\right) \times \sum_{\lambda m_s} C^{jm_j}_{l\lambda;sm_s} Y_{l\lambda}\chi_{sm_s} . \tag{3.4}$$

Eqs. (3.2) and (3.4) can be related by a rotational frame transformation,

$$\psi^{|\Omega|P}_{lj} = (-1)^{j+|\Omega|}\sum_{J^+} C^{J^+0}_{j-|\Omega|,J|\Omega|}\sqrt{1+(-1)^{l+J^++P}}\,\phi^{J^+}_{lj} . \tag{3.5}$$

Hence, after autoionization, the probability for a Rydberg state with quantum numbers J and M_J to produce an ion in the $|J^+, M^+\rangle$ state is

$$P^{J,M_J}_{J^+,M^+} = \sum_{lj} |A_{lj}|^2 \left[C^{J^+0}_{j-|\Omega|,J|\Omega|}\right]^2 \left[C^{JM_J}_{J^+M^+,jm_j}\right]^2 \left[1+(-1)^{l+J^++P}\right] . \tag{3.6}$$

In the experiment determining the ions' rotational distribution, the resonant Rydberg state is prepared by two right circularly polarized laser pulses. The OODR excitation steps are denoted as $(X^2\Delta_{3/2})J'' \rightarrow (\Pi_{1/2})J' \rightarrow$ (Rydberg $\Omega = 3/2$) J. The molecules are assumed to reside initially in a random distribution of M''_J sub-levels. The relative probability for a resonant Rydberg molecule to be prepared in a $|J, M_J\rangle$ level is then given by

$$P^J_{M_J} = \left|C^{J'M_J-1}_{J''M_J-2;11}C^{JM_J}_{J'M_J-1;11}\right|^2 , \tag{3.7}$$

where saturation effects are assumed negligible. The final (unnormalized) rotational distribution of the ions is obtained by combining Eq. (3.6) with Eq. (3.7):

$$P^{J}_{J^+M^+} = \sum_{M_J} P^{J}_{M_J} P^{M_J}_{J^+M^+} \,. \tag{3.8}$$

The rotational distribution given by Eq. (3.8), however, cannot be compared against the experiment directly. In the experiment, LIF signals for the different J^+ states are measured. The ions are excited by an x-polarized laser tuned to the rotational transition $J^+ \rightarrow J^{+'}$ and subsequently emit photons as they decay radiatively to some lower state $J^{+''}$. The x-polarized laser can be described by a linear combination of two spherical harmonics $\frac{1}{\sqrt{2}}\left(Y_{1-1} - Y_{11}\right)$. Since the photomultiplier tube collects photons of both Y_{1-1} and Y_{11} polarizations emitted in almost all directions, we can add the probabilities corresponding to each spherical harmonic incoherently. For a given spherical harmonic Y_{1q}, the relative signal strength has been adapted as a generalization of Eq. (23) in Ref. [34]:

$$\begin{aligned}
& I^{(q)}_{J^+M^+,J^{+'}} \\
= \;& \left(2J^+ + 1\right)\left(2J^{+'} + 1\right) \\
\times \;& \begin{pmatrix} J^+ & 1 & J^{+'} \\ -\Omega^+ & \Omega^{+'} - \Omega^+ & \Omega^{+'} \end{pmatrix}^2 \begin{pmatrix} J^+ & 1 & J^{+'} \\ -M^+ & -q & M^{+'} \end{pmatrix}^2 \\
\times \;& \sum_{J^{+''}=\left|J^{+'}-1\right|}^{J^{+'}+1} \; \sum_{M^{+''}=-J^{+''}}^{J^{+''}} \left(2J^{+'} + 1\right)\left(2J^{+''} + 1\right) \\
\times \;& \begin{pmatrix} J^{+'} & 1 & J^{+''} \\ -\Omega^{+'} & \Omega^{+'} - \Omega^{+''} & \Omega^{+''} \end{pmatrix}^2 \begin{pmatrix} J^{+'} & 1 & J^{+''} \\ -M^{+'} & -q' & M^{+''} \end{pmatrix}^2 .
\end{aligned} \tag{3.9}$$

The first two lines describe the laser excitation step and the last two lines describe the spontaneous emission step of the LIF process. The summation in the last two lines gives unity. Hence, for a

given $|J^+, M^+\rangle$ state, the relative LIF signal strength for an x-polarized LIF excitation is given by

$$\begin{aligned} I_{J^+M^+,J^{+\prime}} &= \frac{1}{2}\left(I^{(+1)}_{J^+M^+,J^{+\prime}} + I^{(-1)}_{J^+M^+,J^{+\prime}}\right) \\ &= \frac{1}{2}\left(2J^+ + 1\right)\left(2J^{+\prime} + 1\right) \\ \times &\quad \begin{pmatrix} J^+ & 1 & J^{+\prime} \\ -\Omega^+ & \Omega^+ - \Omega^{+\prime} & \Omega^{+\prime} \end{pmatrix}^2 \\ \times &\quad \left[\begin{pmatrix} J^+ & 1 & J^{+\prime} \\ -M^+ & -1 & M^{+\prime} \end{pmatrix}^2 + \begin{pmatrix} J^+ & 1 & J^{+\prime} \\ -M^+ & 1 & M^{+\prime} \end{pmatrix}^2\right]. \end{aligned} \tag{3.10}$$

Finally, the relative LIF signal strength, to be compared against the measured LIF intensities that trace over the M^+ levels, is given by

$$I_{J^+,J^{+\prime}} = \frac{1}{\mathcal{N}} \sum_{M^+} P^J_{J^+M^+} I_{J^+M^+,J^{+\prime}}\,, \tag{3.11}$$

where $\mathcal{N}$ is a normalization factor chosen such that $\sum_{\{J^+,J^{+\prime}\}} I_{J^+,J^{+\prime}} = 1$. We use Eq. (3.11) to fit $I_{J^+,J^{+\prime}}$ to the measured LIF signal and determine the values of $|A_{lj}|^2$. The effects of excited state ($J^{+\prime}$) alignment and orientation on the photon collection efficiency were evaluated and found to be very small.

When probing the orientation of the ions, the LIF excitation laser is either right or left circularly polarized. The LIF signals for these cases are then given by

$$\gamma_R = \sum_{M^+} P^J_{J^+M^+} I^{(1)}_{J^+M^+,J^{+\prime}}\,, \tag{3.12a}$$

$$\gamma_L = \sum_{M^+} P^J_{J^+M^+} I^{(-1)}_{J^+M^+,J^{+\prime}}\,. \tag{3.12b}$$

3.4 Rotational distributions and parity propensities in autoionization decay

The fluorescence intensities, measured by exciting ions formed in various rotational states of the $X^1\Sigma^+, \nu^+ = 0$ vibronic ground state after autoionization, are given in Fig. 3.4a. We focus on the ions produced from both parities of the $J = 3/2$ and $5/2$ rotational Rydberg levels. Although the Rydberg molecules at 54 cm^{-1} above ionization threshold are energetically allowed to decay into

many rotational levels of HfF^+, they are observed to autoionize into only a few rotational levels. The Rydberg molecules of a given parity are further observed to decay into ion rotational levels of the same parity, i.e. molecules from the 'a' ('b') Rydberg state primarily form ions in the odd (even) rotational states, as shown on the left (right) side of Fig. 3.4a. Both the rotational propensity and parity propensity observations have also been reported for near-homonuclear molecular ions like N_2^+ and NO^+ created from REMPI [27, 90, 61], and are accounted for in a theory paper by Xie and Zare [91]. For a polar molecule like CaF^+, however, the parity propensity rule tends not to hold due to extensive l-mixing for the Rydberg electron. For the HfF vibronic band reported here, the parity propensity observation indicates the release of a Rydberg electron with l of predominantly one parity. On the other hand, the non-negligible formation of ions in rotational states of both parities implies that the Rydberg electron was ejected with a superposition of orbital angular momenta.

We use Eq. (3.11) from the simplified autoionization model to generate fluorescence intensities for each allowed $\{l, j\}$ and fit them against the LIF data to obtain the angular momentum composition of the Rydberg electron. We note that since the overall parity of the Rydberg states cannot be determined *a priori*, there are two possible sets of A_{lj} to which the data could have fit. However, the fits only converged for one of the two cases, strongly suggesting that the Rydberg states denoted by 'a' ('b') should be assigned the parity $P = +1(-1)$ in Eq. (3.1). In this case, the fit results gave 67.5(3.7)% $p_{3/2}$, 9.8(4.5)% $d_{3/2}$ and 22.7(5.3)% $d_{5/2}$ character to the Rydberg electron, where the numbers in parenthesis indicate the 1σ-error. In accordance with the half-integer quantum number progression of the Rydberg rotational states, the Rydberg electron is found to be in primarily a core-penetrating state. The mixed $\{l, j\}$ character of the HfF Rydberg state has also been reported for CaF Rydberg molecules [41]. We acknowledge that in contrast to the presented model, other groups have reported significant angular dynamics in autoionization, which may be accounted for within the framework of MQDT: for example, the Rydberg electron may have only a single set of $\{l, j\}$ when bound to the molecule, but flies off with multiple $\{l, j\}$ [61], leading to the formation of ions in rotational states of both parities. Since the $\{l, j\}$ composition of the HfF Rydberg state is not known *a priori*, we cannot claim the validity of our model over others.

From the fits to the LIF intensities, the population distribution of HfF^+ ions in the various rotational states can be obtained (see Fig. 3.4b). There can be as many as 60% of the ions created in a single rovibronic state (highlighted as black solid bar plots), which is significant for the state selective creation of HfF^+ for future experiments.

3.5 Preservation of orientation in autoionization decay

Certain experiments demand not only the creation of molecular ions in a particular rovibronic state, but in a single Zeeman level of that state. To this end, we experimentally determine the orientation of HfF^+ formed in the $J^+ = 1, \nu^+ = 0, X^1\Sigma^+$ state from the Rydberg levels $J = 3/2(a)$ and $J = 5/2(a)$ prepared using two right circularly polarized OODR photons. The 'a' parity states are chosen to maximize the ion signal, given the parity propensity rule observed in the previous section. Unlike when measuring the ion rotational populations, the orientation was only determined for when the OODR lasers are tuned to the resonance of an autoionizing line, as the non-resonant ions were found to contribute to only $\approx 20\%$ of the population in $J^+ = 1$.The orientation is related to the contrast ratio $\mathcal{C}$ for the fluorescence signal (γ_R, γ_L) measured when chopping between right and left circular polarizations for the LIF laser, where $\mathcal{C}$ is defined as

$$\mathcal{C} \equiv \frac{\gamma_R - \gamma_L}{\gamma_R + \gamma_L}\,. \tag{3.13}$$

The contrast ratio is a convenient quantity immune to drifts in ion production. As a systematic check of our polarizations, we measured the contrast ratio when both OODR laser pulses are left circularly polarized and found $\mathcal{C}$ to be of the same magnitude but opposite sign as when both lasers were right circularly polarized, as expected.

The contrast ratios for the Q(1) and R(1) transitions are related to the orientation $\mathcal{O}_0$ and alignment $\mathcal{A}_0$ of the ions through the following [26]:

$$\mathcal{C}^{Q(1)} = \frac{3(1+G_1)\mathcal{O}_0}{\mathcal{A}_0 - 2(1+G_2)}\,, \tag{3.14a}$$

$$\mathcal{C}^{R(1)} = \frac{15(1+G_3)\mathcal{O}_0}{\mathcal{A}_0 + 10(1+G_4)}\,, \tag{3.14b}$$

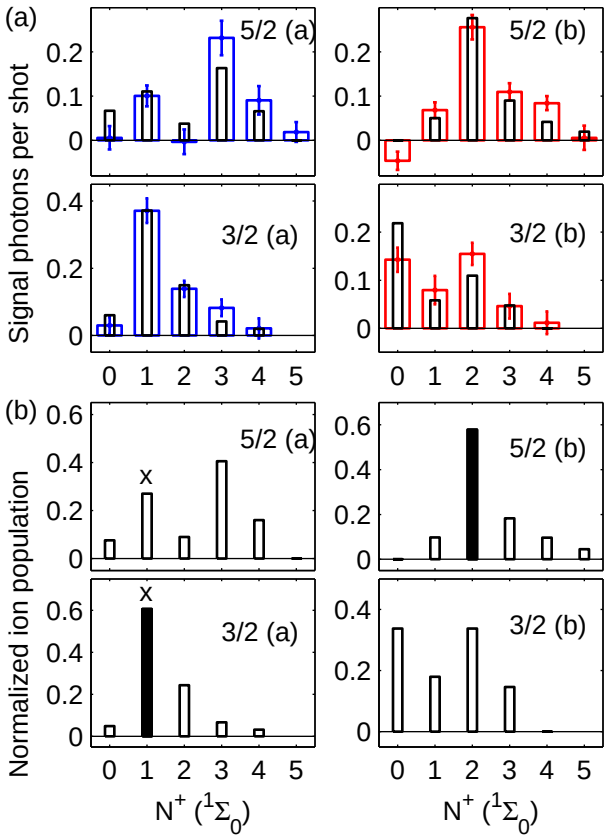

Figure 3.4: (a) The Rydberg molecules, labeled by J and parity on the top right corner, are observed to autoionize into only a few ion rotational levels. These rotational distributions are probed by measuring the number of LIF photons, as shown in blue/red with error bars. In one case ($J^+ = 0 \leftarrow J = 5/2$ (b)), the measured LIF intensity appears negative, which is a statistical artifact of the multiple signal subtractions performed to account for scattered light photons and the rotational distribution of background ions. The narrower bar plots are theory fits to the data. (b) The calculated rotational distribution of ions is obtained based on the fits to the rotational line intensities above. The creation of $\sim 60\%$ of the ions in a single rotational level, as highlighted by the solid black bars, can be a significant advantage for future experiments. The ions formed in the $J^+ = 1$ state, marked by crosses above the bar plots, have their M^+ distributions further examined (see Fig. 3.5).

where $\{G_i\} \lesssim 0.05$ are correction factors that account for the anisotropy of the fluorescence collection setup (depicted in Fig. 3.1). The orientation and alignment parameters are in turn related to the M^+ populations, which are displayed as plots with error bars in Fig. 3.5. The narrower bar plots show the contrast ratios and M^+-level distributions predicted from Eq. (3.12) of Section 3.3, using the same Rydberg electron composition of $\{l, j\}$ inferred from the rotational distributions. The agreement between theory and experiment is good for the $M^+ = 1$ population but only fair for the $M^+ = 0, -1$ populations, part of which may be attributed to the oversimplification of the model's assumptions. We note that of the decay into a single rovibronic state, the population in a single Zeeman level may be as high as 54(7)% (from $J = 3/2(a)$) or even 73(6)% (from $J = 5/2(a)$). In particular, the former number, combined with the formation of 60% of the ions in that same rovibronic state, means that as many as 30% of the HfF^+ ions created from a certain autoionizing resonance can be in a single $|J^+, M^+\rangle$ level.

Different rotational levels can have different maximal (minimal) values for their orientation, given by $\mathcal{O}_0^{\max}(= -\mathcal{O}_0^{\min}) = 1/(J+1)$. Therefore, instead of comparing the orientation parameter of the Rydberg molecule to that of the autoionized product, we compare the fractional orientation $\mathcal{O}_0'$:

$$\mathcal{O}_0' = \frac{\mathcal{O}_0 - \mathcal{O}_0^{\min}}{\mathcal{O}_0^{\max} - \mathcal{O}_0^{\min}}\,. \tag{3.15}$$

$\mathcal{O}_0'$ is 1 (0) when only the $|M^+ = +J^+\rangle$ ($|M^+ = -J^+\rangle$) states are populated and 0.5 when there is no orientation. From the values reported in Table 3.1, we find that the autoionization of HfF Rydberg molecules to the $J^+ = 1, \nu^+ = 0, X^1\Sigma^+$ rovibronic state preserves orientation qualitatively, which bodes well for the creation of HfF^+ predominantly in a single Zeeman, rovibronic level for other experiments.

3.6 Summary

We have spectroscopically characterized a vibronic band of the autoionization spectrum in HfF at 54 cm^{-1} above the lowest ionization threshold. We directly probe the decay of its Rydberg

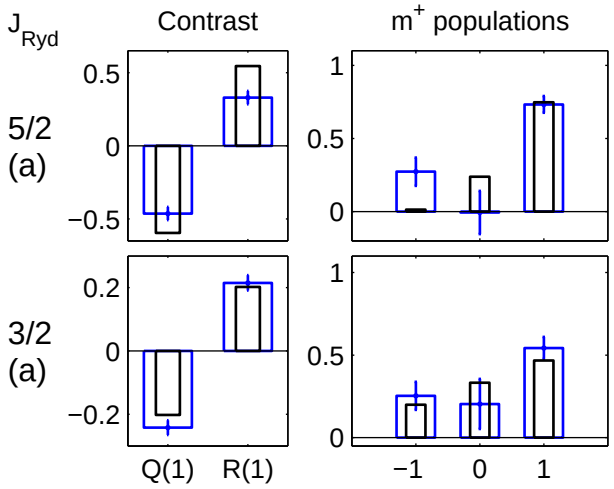

Figure 3.5: The Rydberg molecules in (top) $J = 5/2(a)$ and (bottom) $J = 3/2(a)$, prepared using two right circularly polarized photons in OODR, are observed to decay into the ion rotational level $J^+ = 1$ with a certain orientation. The ions' orientation, related to the M^+ population distribution (right), is inferred from measurements of contrast ratios (left) for the Q(1) and R(1) LIF transition. The narrower bar plots are the theory predictions for the M^+ populations.

Table 3.1: Fractional orientation $\mathcal{O}'_0$ of Rydberg HfF molecules in a given rotational level J and of the ions formed in $J^+ = 1$ after autoionization. The HfF orientation is calculated from the polarizations of the OODR lasers; the HfF^+ orientation is predicted from the simplified model of autoionization described in the text; the HfF^+ (measured) column refers to values inferred from LIF polarization contrast ratios in Fig. 3.5.

J	Fractional orientation		
	Rydberg HfF (calculated)	HfF^+ (predicted)	HfF^+ (measured)
$3/2$ (a)	0.835	0.633	0.645(62)
$5/2$ (a)	0.865	0.867	0.730(86)

states ($J = 3/2, 5/2$) into various rotational states of the $X^1\Sigma^+, \nu^+ = 0$ vibronic ground state of HfF^+ by performing laser-induced fluorescence on the ions. The measured fluorescence intensities are fit using a simplified model of autoionization that assumes no angular dynamics and that the Rydberg state has the same electronic ion-core as its autoionized state. The fit parameters imply that the Rydberg electron has dominant $p_{3/2}$ character with some mixing from the d orbitals. Using the same Rydberg electron character, the model predicts qualitative preservation of orientation when the Rydberg molecule autoionizes to the $J^+ = 1, \nu^+ = 0, X^1\Sigma^+$ state, which was corroborated by fluorescence intensity measurements carried out after excitation by a circularly polarized laser. Thanks to a combination of rotational propensity, parity propensity and preservation of orientation during autoionization, we find that we can create as many as 30% of the HfF^+ ions in a single Zeeman level of a rovibronic state. Having an initial population of 30% of the ions in a single $|J^+, M^+\rangle$ level could prove to be very advantageous for future experiments such as the eEDM search.

We note that although this work has concentrated on one vibronic band of a core-penetrating Rydberg state, there is a body of core-nonpenetrating states in HfF that has yet to be uncovered with experiment. Core-nonpenetrating states have almost pure l character. With $l \geq 2$ for HfF, the Rydberg electron hardly exerts a torque on the ion core rotational states when ejected, which means that the resultant ion rotational states are likely to follow that of the Rydberg molecules more closely. [42] This lends core-nonpenetrating Rydberg states even more promise for populating ions of a desired $|J^+, M^+\rangle$ level with high efficiency.

Chapter 4

Ion traps

The aspect that best distinguishes the JILA eEDM experiment from the other eEDM efforts is the fact that we work with molecular ions. As mentioned in the Introduction, molecular ions can be trapped easily with electric fields, whereas the trapping of neutral molecules is *d*ifficult. Trapped molecular ions offer a potentially long coherence time, which the eEDM statistical sensitivity is proportional to. Ions can be trapped using a Paul trap or a Penning trap, and the JILA eEDM experiment employs the former. In this chapter, we review the basics of a linear Paul trap, describe our own design of a linear Paul trap, and demonstrate several techniques used to characterize and diagnose the ions' in-trap behavior.

4.1 Linear Paul trap basics

4.1.1 A simple picture for the quadrupole trap

The conventional linear Paul trap consists of four radial ($\hat{x}, \hat{y}$) electrodes and two axial end cap ($\hat{z}$) electrodes (Fig. 4.1a). To confine the ions along the axial direction, one can apply a DC voltage to the end cap electrodes V_{ec}, such that the potential between the electrodes is described by $\Phi_1(x, y, z)$:

$$\begin{aligned} \Phi_1(x,y,z) &= \frac{1}{2}\frac{\partial^2 \Phi_1}{\partial z^2}\left(z^2 - \frac{x^2+y^2}{2}\right) \\ &= k_1 V_{ec}\left(z^2 - \frac{x^2+y^2}{2}\right), \end{aligned} \tag{4.1}$$

where k_1 is a geometrical term related to the end cap electrode voltages giving rise to a second derivative of the potential $\partial^2\Phi_1/\partial z^2$. The deconfining potential along the radial direction ($-(x^2+y^2)/2$) comes from Φ_1 having to satisfy Laplace's equation $\nabla^2\Phi = 0$. To confine the ions in the radial directions, one can apply an additional radiofrequency (RF) voltage to the radial electrodes, creating a time-varying quadrupole potential $\Phi_2(x,y,t)$:

$$\begin{aligned}\Phi_2(x,y,t) &= \frac{1}{2}\frac{\partial^2\Phi_2}{\partial x^2}\left(x^2-y^2\right)\cos(\omega_{rf}t) \\ &= k_2 V_{rf}\left(x^2-y^2\right)\cos(\omega_{rf}t)\,, \end{aligned} \tag{4.2}$$

where k_2 is again a geometrical factor relating the radial electrode voltages to the second derivative of Φ_2. The total ion trap potential is given by $\Phi = \Phi_1 + \Phi_2$.

At any one point in time, Eq. (4.2) describes the radial potential as a saddle, i.e. it is confining along one direction but deconfining along its perpendicular direction. Averaging over the ions' trajectory for 1 RF cycle, however, the radial potential becomes a harmonic pseudopotential well in which ions can be trapped, as depicted in Fig. 4.1b. For simplicity, Fig. 4.1b considers only the ion behavior along the $\hat{x}$ direction. Initially, the electric field (of direction and magnitude shown by the arrows) points outwards from $x = 0$ and displaces an ion from x_0 to $x_1 (> x_0)$, where the magnitude of the electric field at x_1 is larger than that at x_0. Half a RF cycle later, the electric field switches direction and the ion moves back to x_2, where $x_2 < x_0$ since $|E(x_1)| > |E(x_0)|$. Another half-cycle later, the ion is at x_3, where $x_3 < x_1$ since $|E(x_2)| > |E(x_1)|$. Continuing such analysis, one can see how the ion eventually oscillates back and forth through the origin as if it is in a harmonic potential well (i.e. secular motion), while exhibiting some "jerky motion" at a small amplitude and at the radio frequency ω_{rf} (i.e. micromotion).

4.1.2 Pseudopotential

To derive an expression for a 1-dimensional harmonic pseudopotential ψ in which a trapped ion moves, we start with the force exerted on the ion of mass m and charge e:

$$m\ddot{x} = e\mathcal{E}_0(x)\cos(\omega_{rf}t) = e\mathcal{E}(x)\,, \quad \text{where} \quad \mathcal{E}_0(x) = -2k_2\,V_{rf}\,x\,. \tag{4.3}$$

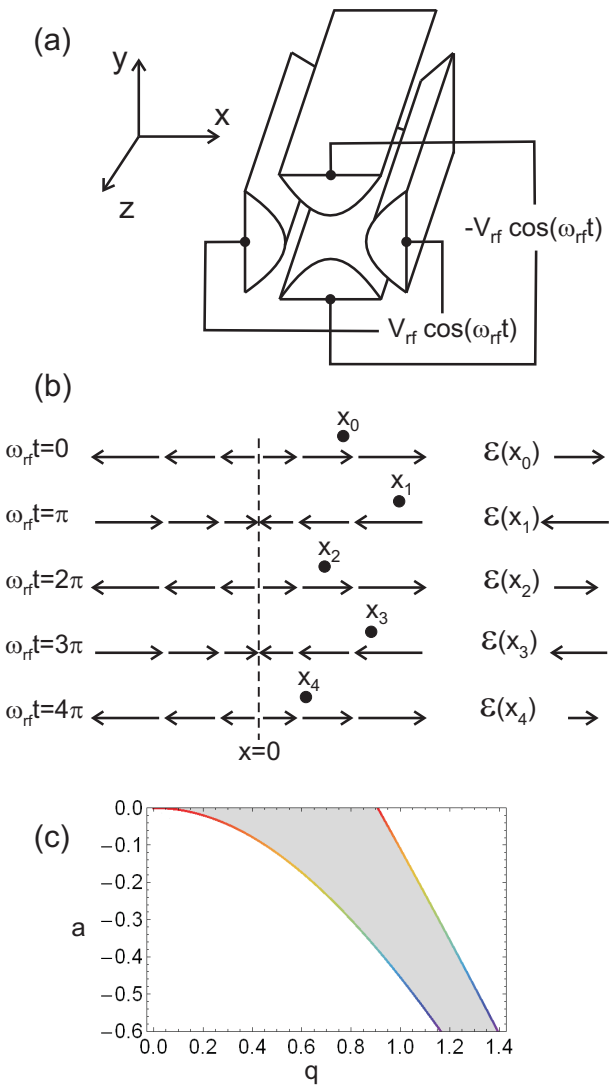

Figure 4.1: (a) Linear Paul trap with the depicted electrodes providing radial $(\hat{x}, \hat{y})$ confinement (adapted from [29]). The axially confining $(\hat{z})$ potential and axial electrodes are not shown. (b) A simple picture for the motion of an ion in a linear Paul trap. The arrows depict electric fields along the $\hat{x}$ axis of a linear Paul trap, oscillating at frequency ω_{rf}. An ion (shown as the black dot) starting at some initial position is subject to a force whose direction (along $\hat{x}$) switches sign every half RF cycle, causing the ion to exhibit micromotion whose amplitude is larger when the ion is farther from the trap center. Overall, there is a net pushing of the ion towards the trap center whenever the ion is displaced, hence the ion behaves like a harmonic oscillator with added micromotion. (c) Stability diagram for the linear Paul trap with axial confinement, expressed in terms of the trap parameters a and q, which are proportional to the axial end cap electrode voltage V_{ec} and RF voltage V_{RF}, respectively. For sets of $\{a, q\}$ within the gray shaded region, the ions can be stably trapped.

Using the simple picture given in Section 4.1.1, we assume that the ion motion can be separated into its secular motion $\bar{X}$ and a fast but small amplitude micromotion δ that occurs at the drving RF frequency ω_{rf}:

$$x = \bar{X} + \delta \quad , \quad \delta = A\cos(\omega_{rf} t)\,, \tag{4.4}$$

where $\bar{X} \gg \delta$, $\ddot{\delta} \gg \ddot{\bar{X}}$. To figure out the amplitude of micromotion A, we substitute the above expression for x and δ into Eq. (4.3). $\ddot{\bar{X}}$ and δ are subsequently neglected because the secular motion is negligible on the time scale of the micromotion and the micromotion amplitude is too small.

$$\begin{aligned} m\left(\cancel{\ddot{\bar{X}}} + \ddot{\delta}\right) &= e\mathcal{E}_0(\bar{X} + \cancel{\delta})\cos(\omega_{rf} t) \\ -m\omega_{rf}^2 A\cos(\omega_{rf} t) &= e\mathcal{E}_0(\bar{X})\cos(\omega_{rf} t) \\ A &= -\frac{e\mathcal{E}_0(\bar{X})}{m\omega_{rf}^2} \\ \Rightarrow \delta &= -\frac{e\mathcal{E}_0(\bar{X})}{m\omega_{rf}^2}\cos(\omega_{rf} t)\,. \end{aligned} \tag{4.5}$$

Eq. (4.5) shows that the amplitude of the micromotion increases as the ions move farther from the trap center.

The pseudopotential $\bar{D}$ is related to the force exerted on the ion, averaged over one micromotion cycle $\bar{F}$: $\bar{F}/e = -\vec{\nabla}\bar{D}$. Performing a Taylor expansion of $\bar{F}/e$ about the secular position $\bar{X}$ and then averaging over a cycle of the micromotion:

$$\begin{aligned} \frac{1}{e}\bar{F}(\bar{X}) &= \frac{1}{e}\left\langle \left(F(x=\bar{X}) + \frac{\partial F}{\partial x}|_{x=\bar{X}}\,(x-\bar{X})\right)\right\rangle_{\text{micromotion t}} \\ &= \left\langle \mathcal{E}(x=\bar{X}) + \frac{\partial \mathcal{E}}{\partial x}|_{x=\bar{X}}\cdot\delta \right\rangle_t \\ &= \left\langle \cancel{\mathcal{E}_0(\bar{X})\cos(\omega_{rf} t)} + \frac{\mathcal{E}_0(\bar{X})}{\bar{X}}\cos^2(\omega_{rf} t)\cdot\left(-\frac{e\mathcal{E}_0(\bar{X})}{m\omega_{rf}^2}\right)\right\rangle_t \end{aligned} \tag{4.6}$$

In the last line, we made use of the fact that $\mathcal{E}_0(x)$ is linear in x, so that $\frac{\partial \mathcal{E}}{\partial x} = \mathcal{E}/x$. Then,

$$\begin{aligned} -\vec{\nabla}\bar{D}(\bar{X}) &= -\frac{e\mathcal{E}_0(\bar{X})}{2m\omega_{rf}^2} \\ \Rightarrow \bar{D}(\bar{X}) &= \frac{e\mathcal{E}_0(\bar{X})^2}{4m\omega_{rf}^2}\,. \end{aligned} \tag{4.7}$$

Incidentally, the kinetic energy of the micromotion δ averaged over 1 RF cycle is also related to $\bar{D}(\bar{X})$:

$$\begin{aligned} \langle U_\delta \rangle &= \frac{1}{2} m\omega_{rf}^2 \langle \delta^2 \rangle \\ &= \frac{1}{4} \frac{e\mathcal{E}_0(\bar{X})^2}{m\omega_{rf}^2} \\ &= e\bar{D}(\bar{X})\,. \end{aligned} \tag{4.8}$$

4.1.3 Mathieu equations

More generally, the motion of an ion in an rf trapping potential is described by Mathieu equations. Here we derive the Mathieu equations for an ion of mass m and charge e in the ion trap described in Section 4.1.1, with the DC and radial RF potentials given by Eqs. (4.1) and (4.2), respectively.

We start with the expressions for the electric fields in all 3 directions:

$$\overrightarrow{\mathcal{E}_{rf}} = -\overrightarrow{\nabla}\Phi_2 = -2k_2V_{rf}(x\hat{x} - y\hat{y})\cos(\omega_{rf}t)\,, \tag{4.9a}$$

$$\overrightarrow{\mathcal{E}_z} = -\overrightarrow{\nabla}\Phi_1 = k_1V_{ec}(-2z\hat{z} + x\hat{x} + y\hat{y})\,, \tag{4.9b}$$

$$\overrightarrow{\mathcal{E}} = \overrightarrow{\mathcal{E}_{rf}} + \overrightarrow{\mathcal{E}_z}\,. \tag{4.9c}$$

Using Newton's second law $m\ddot{\overrightarrow{r}} = \overrightarrow{F} = e\overrightarrow{\mathcal{E}}$, we get

$$\begin{pmatrix} \ddot{x} \\ \ddot{y} \\ \ddot{z} \end{pmatrix} = \frac{e}{m} \begin{pmatrix} (-2k_2V_{rf}\cos(\omega_{rf}t) + k_1V_{ec})x \\ (+2k_2V_{rf}\cos(\omega_{rf}t) + k_1V_{ec})y \\ -2k_1V_{ec}z \end{pmatrix}\,. \tag{4.10}$$

We now make the substitutions:

$$\tau = \omega_{rf}t/2\,, \tag{4.11a}$$

$$\frac{dx}{d\tau} = \frac{dx}{dt}\frac{2}{\omega_{rf}}\,, \tag{4.11b}$$

$$\frac{d^2x}{d\tau^2} = \frac{d}{d\tau}\left(\frac{dx}{dt}\frac{2}{\omega_{rf}}\right) = \frac{4}{\omega_{rf}^2}\frac{d}{dt}\left(\frac{dx}{dt}\right) = \frac{4}{\omega_{rf}^2}\ddot{x}\,, \tag{4.11c}$$

which then give rise to

$$\frac{d^2x}{d\tau^2} + \left(-4k_1V_{ec} + 2\cdot 4k_2V_{rf}\cos(2\tau)\right)\frac{e}{m\omega_{rf}^2}x = 0 \tag{4.12}$$

$$\frac{d^2y}{d\tau^2} + \left(-4k_1V_{ec} - 2\cdot 4k_2V_{rf}\cos(2\tau)\right)\frac{e}{m\omega_{rf}^2}y = 0 \tag{4.13}$$

$$\frac{d^2z}{d\tau^2} + 8k_1V_{ec}\frac{e}{m\omega_{rf}^2}z = 0\,. \tag{4.14}$$

Now, let $a \equiv -\frac{4k_1V_{ec}e}{m\omega_{rf}^2}$, $q \equiv \frac{4k_2V_{rf}e}{m\omega_{rf}^2}$. Then, where $\ddot{r}_\tau$ now refers to $d^2r/d\tau^2$,

$$\begin{pmatrix}\ddot{x}_\tau\\ \ddot{y}_\tau\\ \ddot{z}_\tau\end{pmatrix} + \begin{pmatrix}(a+2q\cos(2\tau))x\\ (a-2q\cos(2\tau))y\\ (-2a)z\end{pmatrix} = \begin{pmatrix}0\\0\\0\end{pmatrix}\,. \tag{4.15}$$

Fig. 4.1c shows the stability diagram for the Mathieu equations. For certain values of $\{a, q\}$ (depicted as the gray regions), the ion motion is stable and the ion remains trapped. For other sets of $\{a, q\}$ (depicted as the white regions), the ion follows an unstable trajectory and is ejected from the trap.

Where a is small compared to q and where $q^2 \ll 1$, we can rederive the pseudopotential in terms of a and q by plugging Eq. (4.4) into Eq. (4.15) [29]:

$$\begin{aligned}\cancel{\ddot{\bar{X}}} + \ddot{\delta} &= -(\cancel{a} + 2q\cos(2\tau))(\bar{X} + \cancel{\delta})\\ \Rightarrow \delta &= \frac{q\bar{X}}{2}\cos(2\tau)\,,\end{aligned} \tag{4.16}$$

which is the same expression as that given in Eq. (4.5). Plugging Eq. (4.16) into the first line of Eq. (4.15) again to solve for $\bar{X}$ and averaging over one micromotion cycle, we get an equation of motion describing the secular motion:

$$\begin{aligned}\left\langle \ddot{\bar{X}}\right\rangle_\tau &= -\left\langle (a+2q\cos(2\tau))\left(\bar{X} + \frac{q\bar{X}}{2}\cos(2\tau)\right)\right\rangle_\tau\\ &= \left\langle -a\bar{X} - \cancel{2q\bar{X}\cos(2\tau)} - \cancel{\frac{q\bar{X}}{2}\cos(2\tau)} - q^2\bar{X}\cos^2(2\tau)\right\rangle_\tau\\ &= -\left(a + \frac{q^2}{2}\right)\bar{X}\,.\end{aligned} \tag{4.17}$$

Recalling that $\tau = \omega_{rf}t/2$, we can see that the ion's pseudopotential in the radial and axial directions are $\bar{D}_r = m\omega_r^2 r^2/2$ and $\bar{D}_z = m\omega_z^2 z^2/2$, where

$$\omega_r = \frac{\omega_{rf}}{2}\sqrt{\frac{q^2}{2} + a} \qquad (r = x, y)\,, \tag{4.18a}$$

$$\omega_z = \frac{\omega_{rf}}{2}\sqrt{-2a}\,. \tag{4.18b}$$

4.1.4 Multiple ions

So far, the ion motion described applies very well to that of a single trapped ion. When multiple ions are trapped, the potential felt by any given ion is modified due to space charge repulsion by other ions. The maximum ion density is set by the confining pseudopotential $\bar{D}$ being as strong as the deconfining potential from the space charge repulsion ϕ_i [29]:

$$\begin{aligned}
-\nabla^2\phi_i &= \nabla^2\bar{D} = \frac{\rho_{max}}{\epsilon_0} \\
\Rightarrow \frac{\rho_{max}}{\epsilon_0} &= \nabla^2\left(\bar{D}_x + \bar{D}_y + \bar{D}_z\right) \\
&= 2\left(m\omega_r^2 + \frac{1}{2}m\omega_z^2\right) \\
&= m\frac{\omega_{rf}^2}{4}\left(\frac{q^2}{2} + a + \frac{q^2}{2} + a - 2a\right) \\
&= m\frac{\omega_{rf}^2}{4}q^2\,.
\end{aligned} \tag{4.19}$$

For our typical trap parameters, $q = 0.59$ and $\omega_{rf} = (2\pi)50$ kHz, so the maximum number of ions that can be confined in a spherical cloud of radius $r_{2\sigma} = 3$ mm is

$$N_{max} = \frac{\rho_{max}}{e^2}\left(\frac{4}{3}\pi r_{2\sigma}^3\right) = 1.1 \times 10^5\,. \tag{4.20}$$

Another useful estimate is the following expression for the mean field space-charge repulsion energy U_{mf} of a cloud of N_{ions} ions confined in a sphere of radius r [45, 83]:

$$\frac{U_{mf}}{k_B} = \frac{N_{ions}e^2}{4\pi\epsilon_0 r k_B} \approx 3\text{K} \times \left(\frac{N_{ions}}{1000}\right)\left(\frac{r}{0.5\text{ cm}}\right)^{-1}\,. \tag{4.21}$$

Where U_{mf} is significant compared to the temperature T of trapped ions, instabilities and heating are more likely to occur.

4.1.5 Rotating field

The application of a rotating bias electric field $\vec{\mathcal{E}}_{rot}$ on top of the RF and DC voltages in the $\{\hat{x}, \hat{y}\}$ plane is a novel feature in the operation of ion traps. The rotating bias field serves to polarize the HfF^+ molecule and to provide a quantization axis for the eEDM experiment. If it were not rotating, the bias electric field would simply eject the ions out of the trap. So, $\vec{\mathcal{E}}_{rot}$ is kept rotating at a frequency slow enough for the molecular axis to track but fast enough so that the ions stay trapped as the radius of rotation remains small compared to the trap extent:

$$\vec{r}_{rot} = -\frac{e\vec{\mathcal{E}}_{rot}}{m\omega_{rot}^2}\,. \tag{4.22}$$

This circular micromotion $\vec{r}_{rot}$ is superimposed on top of the trap RF micromotion and secular motion. In contrast to the RF micromotion, $\vec{r}_{rot}$ is not a function of secular displacement. To avoid resonantly driving and heating the ions with the rotating bias field, care is taken to choose the rotating field frequency to be incommensurate with respect to ω_{rf}. The kinetic energy of the ions' circular micromotion, averaged over a rotation cycle, is much higher than the other energy scales in the ion trap:

$$U_{rot} = \frac{e^2\mathcal{E}_{rot}^2}{2m\omega_{rot}^2}\,. \tag{4.23}$$

Table 4.1 lists the typical frequencies, electric fields, length scales and kinetic energies encountered by the ions' secular motion, trap RF micromotion and rotating circular micromotion.

Table 4.1: Typical frequencies, length scales and kinetic energies for the ions' secular motion, trap RF micromotion and circular micromotion due to $\mathcal{E}_{rot}$.

Motion	$\frac{\omega}{2\pi}$ (kHz)	$\mathcal{E}$ (V/cm)	Length scale (mm)	Kinetic energy (K)
Secular motion	4	0.03	2	30
Trap RF micromotion	50	0.3	0.2	30
Rotating field micromotion	253	16	0.3	2800

4.2 JILA eEDM ion trap version 2

4.2.1 Trap construction

Equipped with the basic knowledge of ion traps and rotating bias fields, we now turn to the JILA eEDM ion trap. Prior to this thesis work, a first generation ion trap has already been built and demonstrated to trap HfF^+ ions by resolving the mass-to-charge ratios of the ion species[83]. A second generation ion trap needed to be constructed to provide both a uniform rotating field and efficient spin readout using laser-induced fluorescence. Given our ability to create HfF^+ ions of a single isotope using photoionization, there was a less pressing need for the second generation ion trap to exhibit a high mass resolution capability. Instead of isolating different HfF^+ isotopes, all we require is to isolate HfF^+ from Hf^+ (see Chapter 6).

As demonstrated in Chapter 3, laser-induced fluorescence of ions can serve as a method of state-sensitive ion detection. Fig. 4.2a and b show a schematic and photograph of the second generation ion trap, respectively. Central to the ion trap design are two ellipsoidal mirrors, each of which focuses light from the trap center to the other mirror's exit after a single reflection off the mirror. Light is then directed through light pipes to photomultiplier tubes (PMTs) outside the vacuum can. The radial extent of each mirror (177.8 mm in diameter) is chosen such that the largest angle of incidence to the light pipe is 45°. The mirrors are held at ground, whereas the light pipes, being electrically insulated from the mirrors, serve as the end cap electrodes providing axial confinement in a linear Paul trap. Both the mirrors and light pipes are machined out of aluminum, hand-polished to a mirror finish and coated with gold. The solid angle subtended by the mirrors is $0.6 \times 4\pi$ steradians and the reflectivity of gold coated on the hand-polished surface is 0.85, making the combined efficiency of both light pipes capturing light emitted from a 1 cm diameter ion cloud as high as 0.5.

The electrodes responsible for radial confinement of the ions are shaped as fins to minimize their shadow cast on the mirrors. The shaping of electrodes as narrow fins, however, may compromise the radial field homogeneity [19], thus there are six electrodes instead of four as in a usual

Paul trap so as to improve the uniformity of the rotating field in the trap center. Nevertheless, the trapping potential still mimics that of a conventional quadrupole trap, as two pairs of electrodes are tied to the same RF voltage within the pair (Fig. 4.2c). Each stainless steel, electropolished fin electrode is 8 cm apart from its diagonally opposing fin, and shaped like a parabola to obtain more uniform fields in the axial direction. The ends of each fin are machined into threaded rods with flat edges to guide the positioning of each fin at a relative angle of 60° to its adjacent fins. With this ion trap design, the rotating field is calculated to have an inhomogeneity of as small as 0.5% over a 1 cm diameter ion cloud, assuming perfect assembly and trap driver electronics.

The trap confinement coefficients $k_1 V_{ec}$ and $k_2 V_{rf}$ can be obtained by simulating the trap potential in SIMION and calculating the second derivatives of the potential. The center of the quadrupole potential can be approximated as two parabolas of opposite sign, one along $\hat{x}$ and the other along $\hat{y}$. By applying 1 V to fins 2, 3, 5 and 6, and -2 V to fins 1 and 4 while holding the end cap electrodes at ground (see Fig. 4.2c), the radial trap confinement coefficients along $\hat{x}$ and $\hat{y}$ are given by

$$k_{2x} V_{rf} = 595\,\mathrm{V/m^2}\,, \tag{4.24}$$

$$k_{2y} V_{rf} = -603\,\mathrm{V/m^2}\,. \tag{4.25}$$

Along the axial direction, applying 1 V to the end cap electrodes while holding the radial fin electrodes at ground gives the axial trap confinement coefficients

$$k_{1z} V_{ec} = 26.1\,\mathrm{V/m^2}\,. \tag{4.26}$$

4.2.2 Trap driver electronics

To drive each ion trap fin electrode, several electronic inputs are used: a quasi-DC voltage that can be gated and ramped on and off, a trapping RF voltage at 40–50 kHz, and a rotating voltage at 253 kHz, for which adjacent fins have a 60° relative phase shift. The end cap electrodes have the DC voltage component only. The DC voltages are the buffered output of a 8-channel digital-to-analog

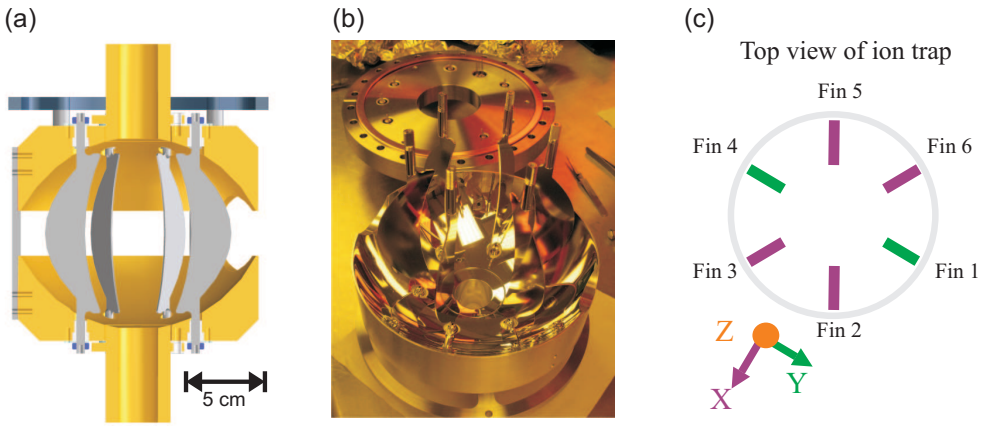

Figure 4.2: (a) Side view schematic of the ion trap. (b) Photograph of the bottom electrodes, mirror and six fins, taken during a test assembly of the ion trap. In this test assembly, the bottom end cap electrode had a different cross section profile than the electrode used in the final assembly (see also Fig. 5.1c). (c) Bird's eye view schematic of the HfF source and ion trap setup.

converter (DAC, part number NI6733), which is then passed through a multiplexer comprising a series of DG409 analog switches actuated by the TTL outputs of a Labview-controlled DIO64. The multiplexer switch enables the fins to apply either a DC shim voltage for the trap or an electric field impulse to 'stop' or 'kick' the ions as necessary. The trapping RF voltage is provided by an Agilent function generator 33220A, whose output amplitude can be amplified with a voltage-controlled gain op-amp (AD8336). The voltage-controlled gain op-amp allows the ion trap spring constants to be ramped up and down dynamically. Finally, the rotating voltages are applied by six digital delay synthesizer (DDS) channels (from two synchronized AD8429 chips), with one channel for each fin electrode. Each channel's amplitude, phase, and frequency are digitally programmed in Labview, where a ramp of any one of these attributes can be triggered dynamically using TTL. A single DDS channel output is differentially amplified by an op-amp OP-27, and then amplified with a variable gain by another OP-27 that uses a multiplying digital-to-analog converter (DAC chip AD5543) as its feedback resistor. The multiplying DAC and second OP-27 allow for dynamic ramps of the rotating voltage amplitude between several different values.

The DC voltage, trap RF voltage and AC-coupled rotating voltages are then sent to the main ion trap driver to be buffered, summed and then amplified. Fig. 4.3 shows a schematic of the main trap driver circuit. LM318N op-amps are used for buffering the DC voltages, whereas OPA627 op-amps are used for buffering the trap RF voltages and summing up all the different inputs for a given electrode. The output of each summing OPA627 op-amp is then amplified with a gain of 100 using a PA98 op-amp that is driven by a $\pm$200 V/0.1 A power supply. The PA98 op-amps are attached to a water-cooled aluminum block to manage their heat dissipated. In fact, relay switches (Meder BE05-2A85-P) ensure that the PA98 op-amps can be turned on only if the chilled water is already flowing. As connected in Fig. 4.3, the PA98 can provide an output voltage of $\pm$200 V and current of 63 mA, and with a gain of 100, its maximal slew rate is at 1000 V/μs.

To drive a large amplitude rotating field at high frequency given the limited output current, it is important to reduce the capacitive load seen by a PA98. The total capacitance load of a PA98 is 126 pF, of which 40 pF comes from a radial fin (32 pF) and its two SHV connectors (4 pF

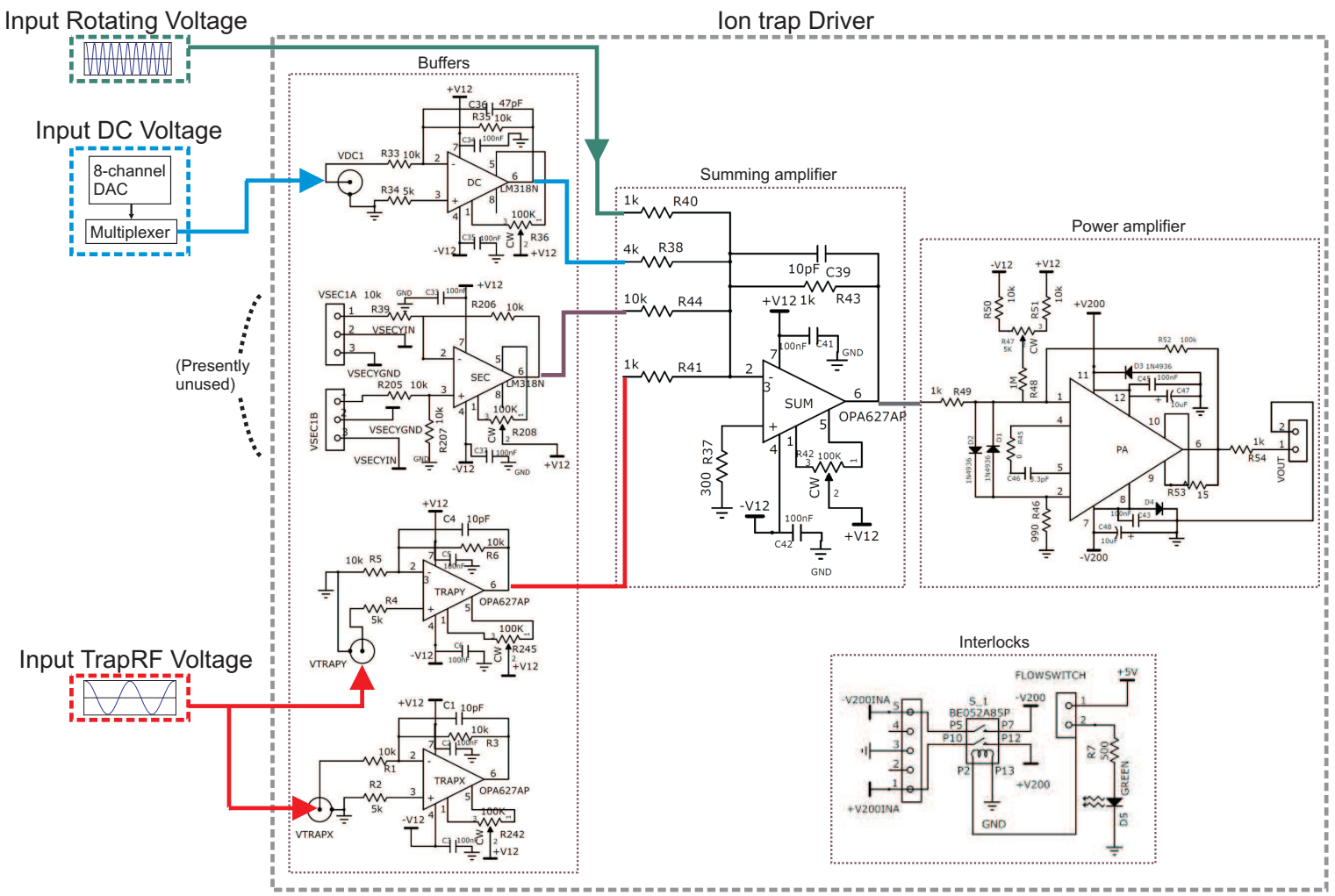

Figure 4.3: Schematic of the trap driver inputs and electronics used to generate the voltage applied to a single fin electrode. In the trap driver, the 'TRAPX' and 'TRAPY' buffer op-amp outputs are shared amongst 4 and 2 fin electrodes, whereas the 'SEC' and 'DC' buffer op-amps, summing amplifier and power amplifier are repeated 7 more times for all 6 fin electrodes and the 2 end cap electrodes.

each), whereas the remaining capacitance comes from using a 183 cm RG-62 cable to connect the PA98 output to a fin electrode. To monitor an electrode's voltage while minimizing the oscilloscope probe's capacitance seen by the PA98, 1% of each PA98 output is tapped off using a voltage divider and sent through a buffer (not shown in Fig. 4.3). With these capacitive loads, the PA98s can provide a rotating field of up to ±24 V/cm (from ±150 V applied, so that 50 V is reserved for V_{rf}) at 300 kHz without significant distortion.

4.2.3 Experiment sequence for ion trapping

Putting the trap electrodes and driver electronics altogether, the ion trap as used in the eEDM experiment is typically driven as described in the following sequence (see also Fig. 4.4a) and discussed in more detail in Section 4.3.

(1) Neutral HfF molecules are created in the source chamber, as already described in detail in Chapter 2. The neutral molecules undergo supersonic cooling to a rotational temperature of ∼10 K as they traverse a differentially pumped chamber into the ion trap chamber. The ion trap chamber does not have any vacuum pumps directly attached to it, although it is attached (with a conductance of 420 l/s) to a nearly empty adjacent six-way cross with a Varian TV551 turbo pump mounted on top.

(2) The cooled cloud of neutral HfF molecules, entrained in the argon buffer gas, are excited via optical-optical double resonance to a Rydberg state and autoionized in-trap. The ions inherit the 600 m/s center-of-mass velocity of the neutral beam.

(3) The trap electrodes apply an electric field along -$\hat{x}'$ to stop the HfF^+ ion beam in the center of the trap.

(4) The trap RF voltages (along with any DC shims for the radial fins) and end cap voltages are immediately turned on to start confining the ions.

(5) (Optional) The amplitude of the rotating field is ramped on, held fixed for a given duration,

and then ramped back down to zero.

(6) (Optional) The trap RF voltages and end cap voltages may also be ramped up over time to provide a more or less tightly confining trap as necessary.

(7) When the trap confining voltages are turned off after a given trap duration, a uniform electric field is applied along $\hat{x}$, $\hat{x'}$ or $-\hat{x}$ to 'kick' the ions onto one of the two 'fast' microchannel plate assemblies (MCPs) or onto an 'imaging' MCP, which is a phosphor screen located behind two stacked microchannel plates. These MCPs allow us to diagnose the ions' in-trap motion in the $\hat{x}, \hat{y}$ and $\hat{z}$ directions.

Fig. 4.4b shows the sequence of voltages applied to one of the fin electrodes (fin 3) for the last four steps. The following section details our efforts to optimize the trap loading and characterize the ion trap.

4.3 Trap loading and characterization

4.3.1 Basic assumptions and terminology

Before launching into a presentation of our trap optimization and characterization techniques, we first lay out the assumptions we often make when considering the ions' motion in the trap. For an individual ion, its simple harmonic motion in the trap is independent of other ions. This means that an ensemble of trapped ions behave roughly like an ideal gas, where the mean field energy and collisions are both small. The mean free path of an ion between collisions is very long compared to the size of the ion cloud, such that in a 3-dimensional harmonic trap with incommensurate trap frequencies $\omega_x \neq \omega_y \neq \omega_z$, the motion along each direction is separate.

Formally, the secular motion of the i^{th} ion in the j^{th} direction can be expressed as

$$r_j^i = A_j^i \cos(\omega_j t + \phi^i)\,, \tag{4.27}$$

where ω_j is the trap frequency along the j^{th} direction. We assume the following distributions for

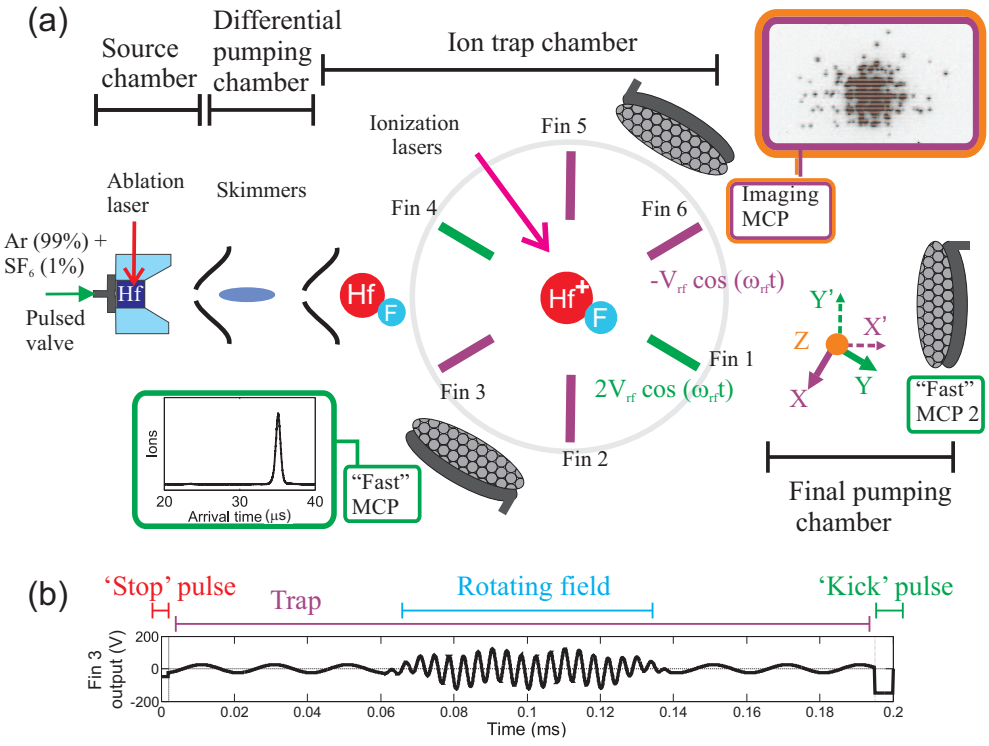

Figure 4.4: (a) Bird's eye view schematic of the HfF source and ion trap setup. In the ion trap chamber, HfF^+ are formed in-situ by autoionization, trapped, and then ejected onto one of the three diagnostic MCPs, which allows us to detect both the ion number and motion in-trap. The top and bottom end cap electrodes are not shown. (b) Voltage output on one of the radial fin electrodes (fin 3).

the phase ϕ and amplitude A for a cloud of ions:

$$\begin{aligned} &\text{(a)} \quad f(\phi) \text{ is uniform,} \\ &\text{(b)} \quad f(A) \propto A e^{-\frac{m\omega^2 A^2}{k_B T}} , \end{aligned} \tag{4.28}$$

where $m\omega^2 A^2$ is the total (kinetic and potential) energy of the ions and T is the temperature of the cloud. A note of caution is that these assumptions are not necessarily valid, but we make them for their simplicity.

The overall motion of the ion cloud can be described in terms of a 'slosh' and 'breathe' if the following occurs:

$$\begin{aligned} f(\phi) &\neq f(\phi+\pi) \quad \text{(sloshing)}\,, \\ f(\phi)+f(\phi+\pi) &\neq f(\phi+\frac{\pi}{2})+f(\phi+\frac{3\pi}{2}) \quad \text{(breathing)}\,. \end{aligned}$$

So far, we have also assumed that the trap is perfectly harmonic. In the presence of trap anharmonicities or ion-ion collisions, ϕ_j randomizes and the cloud can spread out as the sloshing and breathing can transform into a hotter cloud.

Experimentally, the slosh and breathe are characterized by motion in the center-of-mass of the cloud $(\bar{r}, \dot{\bar{r}})$ and a change in the cloud radius $(\sigma_r, \sigma_{\dot{r}})$, respectively. In the absence of breathe, $\sigma_{\dot{r}} = \omega\sigma_r$. The ion cloud temperature T_J along the j^{th} trap direction can also be inferred from the cloud width σ_j:

$$T_j = \frac{m}{k_B} v_j^2 = \frac{m}{k_B} \left(\omega_j \sigma_j\right)^2 . \tag{4.29}$$

The slosh and breathe can in turn be combined with the cloud width into an effective width $\sigma_{eff,j}$:

$$\sigma_{eff,j} = \sqrt{\sigma_j^2 + \sigma_{CM,j}^2 + \sigma_{b,j}^2}\,, \tag{4.30}$$

where σ_j is the spread of individual ions' secular motion averaged over the cloud with the distribution given by Eq. (4.28), $\sigma_{CM,j}$ is the root-mean-squared slosh amplitude, and $\sigma_{b,j}$ is the root-mean-squared breathe amplitude.

4.3.2 Trap loading

In many ion-trap experiments [29, 49], the ions are created using electron-gun ionization or photoionization, and then cooled via laser cooling or sympathetic cooling to 10–100 of μK upon being trapped. The eEDM measurement, however, can be performed with the HfF^+ ions being as hot as 10–30 K [45]. When the HfF^+ ions are initially created via autoionization, their translational temperature (in the moving frame) is the same as that of the supersonically cooled molecular beam, i.e. 10 K. No further cooling of the ions is then required during the trap duration as long as the ions can be brought to a stop from 600 m/s without additional heating, and the RF heating within the ion trap occurs on a time scale long compared to the eEDM measurement. After stopping the ions, the loading of the ion trap is considered optimal if the effective spatial width $\sigma_{eff,j}$ as described by Eq. (4.30) is dominated by σ_j. Since each contribution to the width is added in quadrature, as long as $\sigma_{CM,j}$ and $\sigma_{b,j}$ are less than a third of σ_j, their contribution to the effective width is about an order of magnitude smaller than σ_j.

All three contributions can be measured simultaneously by looking at the ions' arrival on the 'imaging' MCP (for motion along the trap axes $\hat{y}, \hat{z}$) or the 'fast' MCP housed in the same trap chamber (for motion along the trap axis $\hat{x}$) as a function of the trap duration. Measurements of the slosh and breathe tend to be made at short trap times (i.e. after only a few trap cycles), where the slosh and breathe, if their amplitudes are discernible, are expected to take place at the trap frequency and twice the trap frequency, respectively. At longer trap times, the slosh and breathe amplitudes may be diminished if the ions interact with each other or with trap anharmonicities and cause dephasing. Fig. 4.5a shows a typical set of slosh, spatial width and breathe data measured along the $\hat{x}$ axis on the 'fast' MCP over a few trap cycles, where each data point is obtained by fitting the time-of-arrival distribution of the ions on the 'fast' MCP to a Gaussian distribution and recording its center and standard deviation. In the plotted example, the trap loading is sub-optimal since the slosh amplitude is three time that of the spatial width.

To achieve optimal loading with minimal slosh, two conditions need to be met: firstly, the

ion cloud's center-of-mass velocity needs to be removed, and secondly, the position at which the ions come to a stop (from 600 m/s) needs to be the same as that when the ions are close to the trap center. More precisely, the distance between the position at which the ions come to a stop and the trap center determines the slosh amplitude. To meet the first condition, the 'stop' electric field pulse applied opposite to the center-of-mass velocity needs to give the correct impulse to the ion cloud, and can be varied by changing the amplitude-duration product of the pulse. To meet the second condition, the DC shim voltages of the ion trap center need to be adjusted. Since the principal trap axes are a linear combination of the direction of center-of-mass velocity $\hat{x'}$, the above two conditions must be fulfilled in both the $\hat{x}$ and $\hat{y}$ directions (see Fig. 4.4a). To optimize this two-dimensional walk of parameters for a given trap axis (say, $\hat{x}$), we can plot the real and imaginary parts of the ions' slosh as obtained from Fig. 4.5a as a point on a complex plane (Fig. 4.5b), where $x = A_x \cos(2\pi\phi_x), y = A_x \sin(2\pi\phi_x)$. Varying the 'stop' pulse walks the points on the complex plane along the direction $\hat{u}$, whereas adjusting the DC shims walks the points along $\hat{v}$. Using this information, once we figure out where a point describing a given slosh behavior lies on the complex plane $\overrightarrow{w} = |u|\hat{u} + |v|\hat{v}$, we can easily minimize the slosh by jumping it towards the origin of the complex plane.

The breathe of the ion cloud can be minimized by matching the in-trap temperature to the initial temperature of the moving cloud, i.e. the trapping potential energy and initial kinetic energy are close to the equal partition point. If the trap is too tightly confining for the initial temperature, the ion cloud will breathe inwards at the start of the trap. Conversely, if the trap is too weakly confining for the initial temperature, the ion cloud will initially breathe outwards. The typical trap frequencies are about $\omega = (2\pi)3$–6 kHz.

All of the above slosh and breathe measurements of the ion cloud have been taken with the RF component of the trap voltages set to a particular initial phase ϕ_{rf}, e.g. $V_{FinX} = -V_{rf}\cos(\omega_{rf}t+\phi_{rf})$. At different times within a RF cycle, the speed of the micromotion can vary between zero and $e\mathcal{E}(x_0)/(m\omega_{rf})$, where x_0 is the position of maximum displacement from the trap center. (The displacement of micromotion may be ignored because it is typically about a tenth of the secular

displacement, as shown in Table 4.1.) The RF initial phase ϕ_{rf} is then chosen such that at the start of the trap, the least amount of micromotion velocity is excited. Similarly, when the ion cloud is 'kicked' out of the trap towards one of the diagnostic MCPs, the RF end phase is chosen so that the micromotion velocity does not add to the overall velocity, and the spread of ions on the MCP is solely due to the ions' secular motion. In other words, where ϕ_{rf} is set to minimize the excitation of initial micromotion velocity, the trap duration T_{trap} is chosen such that $\omega_{rf} T_{trap} = 2\pi n$, where n is a positive integer.

4.3.3 Microchannel plate transfer matrices

In the previous section, we have only tried to minimize the slosh and breathe relative to the width of the ion cloud as detected on the MCP. Ultimately, however, we are interested in the width of the ions in-trap $\sigma_{trap,j}$. The width of ions on the detector may be scaled down or up from the in-trap width, depending on whether the ions get focused or de-focused on their way to the detector. Further, the distribution of ions on the MCP may reflect either the position or velocity distribution of ions in-trap, or some linear combination of the two, depending on how long the ions take to travel towards the detector compared to a trap oscillation. For many atomic physics experiments using time-of-flight expansion to probe the atomic cloud width, the atoms take a long time to fall to the detector, so the cloud width as seen on the detector is mainly due to the in-trap velocity distribution . Conversely, one can imagine applying a very high electric field pulse to push ions towards a nearby MCP such that the flight time T_{det} is much shorter than a trap cycle ($\omega_j T_{det} \ll 1$), in which case the in-trap position distribution gets 'frozen' out and is projected (up to some scale factor) directly onto the MCP.

To figure out how the width as seen on the detector maps onto the in-trap width, we assume that the trapped ions undergo small displacements about the trap center, so that any change in the position or velocity remains linear. We can then use the following transfer matrix formulation:

$$\begin{pmatrix} z_{det} \\ \dot{z}_{det} \end{pmatrix} = M_z \begin{pmatrix} z_{trap} \\ \dot{z}_{trap} \end{pmatrix} = \begin{pmatrix} m_{11,z} & m_{12,z}\, T_{det,z} \\ m_{21,z} & m_{22,z}\, T_{det,z} \end{pmatrix} \begin{pmatrix} z_{trap} \\ \omega_z z_{trap} \end{pmatrix} . \tag{4.31}$$

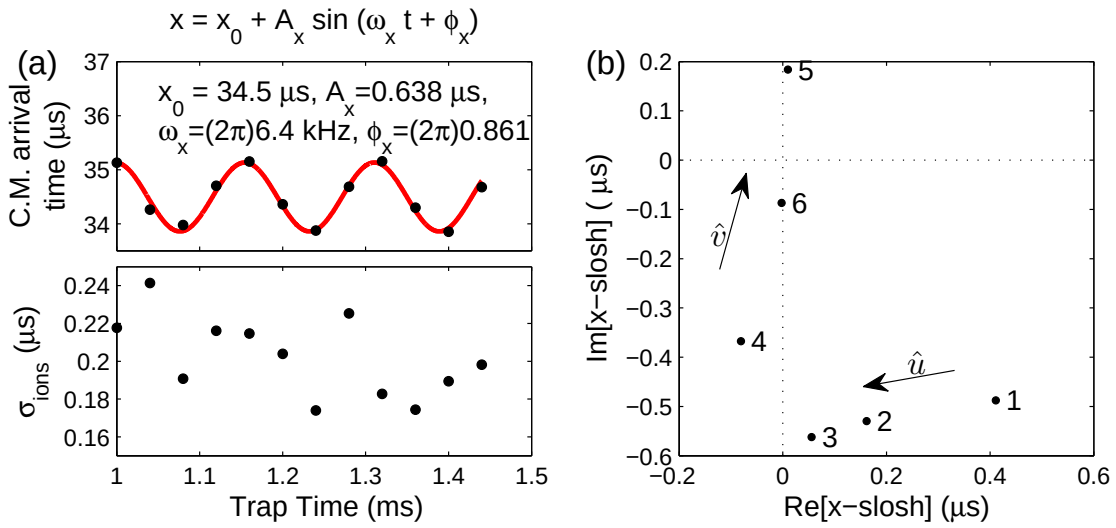

Figure 4.5: Motion of trapped HfF^+ ions along $\hat{x}$, where the position and width of the ions are mapped onto arrival time on the 'fast' MCP in microseconds. (a) (Top) The center-of-mass slosh of the ion cloud versus trap duration is fit to a sine wave, from which the trap frequency is extracted to be $(2\pi)6.4$ kHz; (bottom) standard radius of the ion cloud as a function of trap duration. While the breathe of the ion cloud is negligible in this case, the center-of-mass slosh is significant compared to the standard cloud width, indicating sub-optimal loading conditions. In fact, its slosh amplitude and phase can be summarized as a single point on a complex plane (point '1') in (b). (b) A summary of different slosh behaviors for different trap loading parameters. Varying the voltage pulse used to 'stop' the 600 m/s HfF^+ ions walked the slosh summary points along $\hat{u}$, whereas changing the position of the DC trap center moved the slosh summary points along $\hat{v}$.

By denoting $\dot{z}_{trap} = \omega_z z_{trap}$ in Eq. (4.31), we also assume that there is no breathe. The goal is to experimentally determine the matrix elements $m_{11,j}$ and $m_{12,j}$ of the transfer matrix M_j. $m_{21,j}$ and $m_{22,j}$ are not evaluated because the MCPs do not give the velocity distribution of ions upon hitting the detector. Using Eq. (4.31), the width of the ions as seen on the detector σ_{det} is then related to the in-trap width σ_{trap} via a factor $m_{\sigma,j}$:

$$\sigma_{det,j} = m_{\sigma,j}\,\sigma_{trap,j} = \sqrt{(m_{11,j})^2 + (m_{12,j}\,T_{det,j}\,\omega_j)^2}\;\sigma_{trap,j} \tag{4.32}$$

To figure out $m_{11,z}$ and $m_{12,z}$, we applied a 'kick' of known impulse to the ions along the $\hat{z}$ direction and measured the slosh response of the ions as seen on the 'imaging' MCP (Fig. 4.6). Any immediate displacement of the ions came from the change in velocity due to the impulse, as indicated by the blue dashed line ending with a blue cross in Fig. 4.6. On the other hand, the ions' displacement after a quarter of a trap cycle reflects the change in position effected by the impulse kick, as indicated by the blue dotted line ending with a blue triangle. In the depicted case, after an applied voltage kick of 120 Vμs between the top and bottom electrodes, we expected the ions to slosh with an amplitude of 1.76 mm based on SIMION calculations. Since the changes in position and velocity showed up as a displacement of 1.45 mm and 2.28 mm on the MCP respectively, the transfer matrix elements $m_{11,z}$ and $m_{12,z}$ are 0.824 and 1.30 for a flight time of $T_{det} = 0.045$ ms to the 'imaging' MCP. The above procedure of measuring the ions' response to a voltage 'kick' can also be applied to the $\hat{x}$ and $\hat{y}$ directions. Table 4.2 summarizes the transfer matrix elements and m_σ values for typical trap frequencies and detector flight times in all three directions. Equipped with the transfer matrix elements, we can then characterize the ion trap in terms of its patch charges and anharmonicities by determining how the ions respond in-trap to various voltage settings.

4.3.4 Trap characterization I: patch charges

Patch charges can be easily introduced if there was any grease left on the trap electrodes when the trap was assembled, or can develop over time if hafnium or other additional material was slowly deposited on the electrodes. Of the effects that patch charges can have on the ions, the two that we

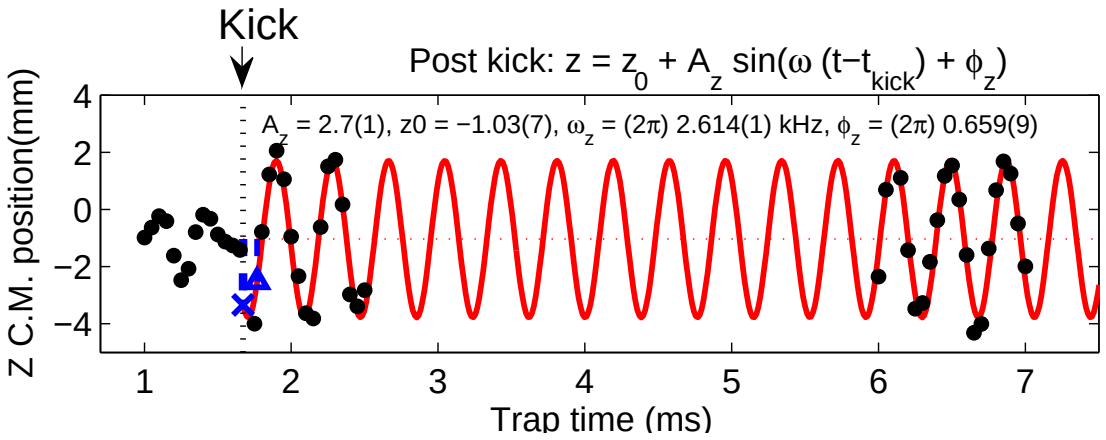

Figure 4.6: To extract the ions' motion in-trap from that on the MCP, a deliberate kick is applied to the ions (shown here in the $\hat{z}$ direction) and the resultant slosh response is fit to a sine wave. The displacement at t_{kick} and at a quarter trap cycle after t_{kick}, given by the dashed line down to the cross and the triangle, respectively) then maps onto a change in velocity and position due to the applied impulse. By comparing the expected and measured slosh response, we can deduce the MCP transfer matrix elements.

Table 4.2: Summary of MCP transfer matrix elements and m_σ values for typical trap frequencies and detector flight times in all three directions. m_{11}, m_{12} and m_σ are dimensionless for the directions $\hat{y}$ and $\hat{z}$, and have units [μs/mm] for $\hat{x}$.

	Detector	m_{11}	m_{12}	T_{det} (ms)	$\frac{\omega}{2\pi}$ (kHz)	m_σ
x	'Fast' MCP	0.129	0.093	0.021	5.9	0.148
y	'Imaging' MCP	0.412	1.60	0.045	4.2	1.94
z	'Imaging' MCP	0.824	1.30	0.045	3.7	1.59

care most about are dipolar and quadrupolar effects. Dipolar patch charges (simulated as $+V_{patch}$ and $-V_{patch}$ on two opposing electrodes) can displace ions away from the ion trap center, while quadrupolar patch charges (simulated as $+V_{patch}$ on each of the two opposing electrodes) can modify the trap frequencies relative to that expected from SIMION calculations. By characterizing patch charges, we can understand how closely the resultant ion trap potential resembles that calculated from SIMION when the effects of patch charges are accounted for, which may (or not!) indicate whether the ion trap assembly is built as a faithful realization of its design. Further, it is important to null out dipolar effects so that the ions do not shift in position over time.

Along the $\hat{z}$ direction, both dipolar and quadrupolar patch charges can be simultaneously quantified by first trapping the ions, and then adiabatically ramping up or down the axial confinement to avoid exciting a large slosh. The ions' center-of-mass motion along $\hat{z}$ is measured on the 'imaging' MCP for a few oscillation cycles and both the post-ramp offset and axial frequency are recorded. In the presence of a dipolar patch electric field $\mathcal{E}_{z,patch}$, the ions shift to a new position z_0:

$$\begin{aligned} U_z &= \frac{1}{2}m\omega_z^2 z^2 - q\mathcal{E}_{z,patch} z \\ &= \frac{1}{2}m\omega_z^2\left(z - \frac{q\mathcal{E}_{z,patch}}{m\omega_z^2}\right)^2 + \frac{1}{2}m\left(\frac{q\mathcal{E}_{z,patch}}{\omega_z}\right)^2 \\ \Rightarrow z_0 &= \frac{q\mathcal{E}_{z,patch}}{m\omega_z^2}. \end{aligned} \tag{4.33}$$

Fig. 4.7a shows how the post-ramp offset varies with axial frequency. The dipolar patch field can be extracted from the slope of the fit in Fig. 4.7a, which in this case turns out to be -0.21(3) V/m.

To elucidate the quadrupolar patch field $\partial\mathcal{E}_{z,patch}/\partial z$, we can examine the trap axial frequency instead. Fig. 4.7b shows how the square of the axial trap frequency, rescaled by ω_{rf}, varies against the trap parameter a, where a can be calculated given the specified DC voltages applied to the end cap and fin electrodes. Using Eq. 4.18b, we expect the data points to fall on a line of slope -2, and any offset is attributed to a quadrupolar patch field:

$$\begin{aligned} \omega_z &= \frac{\omega_{rf}}{2}\sqrt{-2a + a_{patch}} \\ \Rightarrow \left(\frac{2\omega_z}{\omega_{rf}}\right)^2 &= -2a + a_{patch}\,, \qquad (4.34) \\ \text{where} \quad a_{patch} &= \frac{2e}{m\omega_{rf}^2}\frac{\partial\mathcal{E}_{z,patch}}{\partial z}\,. \qquad (4.35) \end{aligned}$$

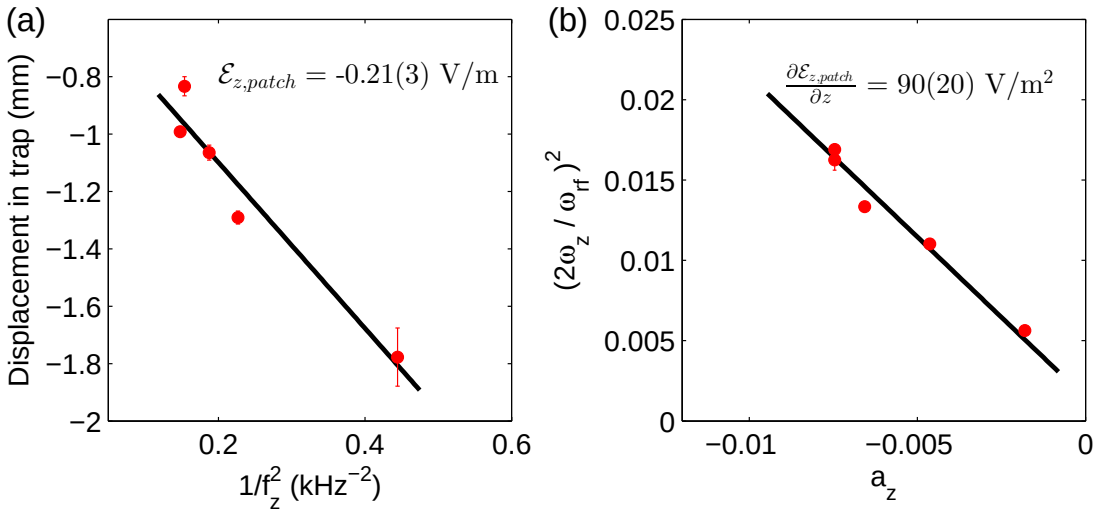

Figure 4.7: (a) The ions' in-trap displacement is measured as a function of the inverse trap frequency squared, from which the slope yields the axial dipolar patch field $\mathcal{E}_{z,patch}$. (b) The ratio of trap secular frequency to the RF frequency, squared, is plotted against the applied end cap electrode voltage (proportional to a_z). The slope is fixed to be -2, in accordance with Eq. (4.34), and the offset indicates the quadrupolar patch field $\partial\mathcal{E}_{z,patch}/\partial z$.

For the radial directions, a dipolar patch electric field would not only displace the ions (the displacement is more apparent if the DC potential is weak compared to the pseudopotential), but also induce excess micromotion arising from the non-zero RF voltages at the center of the DC

potential [8]:

$$x = (x_0 + A_x \sin(\omega_x t + \phi_x)) \left(1 + \frac{q_x}{2} \cos(\omega_{rf} t)\right) , \tag{4.36}$$

where x_0 is the displacement described by Eq. 4.33 for the patch field $\mathcal{E}_{x,patch}$. The micromotion $q_x x_0/2$ is considered to be in "excess" of the regular micromotion that has zero amplitude when the ions are at the trap center but whose amplitude increases when the ions move away from the trap center. To determine the radial dipolar patch field, we can probe the micromotion amplitude when the ions are displaced by an equal amount from the trap center. How these ion in-trap positions map onto the detector positions have already been determined from the MCP transfer functions as outlined in Sec. 4.3.3: in Fig. 4.8, for instance, ions at positions '1' and '2' correspond to ions that are displaced farthest from and nearest towards the 'fast' MCP, respectively. Where there is a dipolar patch field $\mathcal{E}_{x,patch}$ displacing the ions away from the detector, the micromotion of ions at position '1' is larger than those at position '2', as shown in Fig. 4.8a. In Fig. 4.8b, the patch field has been compensated for by applying DC shim voltages to the fin electrodes, such that the micromotion measured at the two equal displacements display the same amplitudes.

4.3.5 Trap characterization II: anharmonicities

To lowest order, the confinement of ions in an ion trap is harmonic with a trap frequency of ω_0. However, once the ions access larger displacements from the trap center, anharmonic terms (e.g. bz^4) in the trapping potential Φ start to matter. Anharmonic terms can modify the observed trap frequency ω, depending on the ions' oscillation amplitude z:

$$\begin{aligned} U &= \frac{1}{2} m\omega_0^2 z^2 + bz^4 = \frac{1}{2} m\omega_0^2 z^2 \left(1 + \frac{2bz^2}{m\omega_0^2}\right) \\ &\equiv \frac{1}{2} m\omega^2 z^2 \\ \Rightarrow \omega &= \omega_0 \sqrt{1 + \frac{2bz^2}{m\omega_0^2}} \approx \omega_0 \left(1 + \frac{bz^2}{m\omega_0^2}\right) \end{aligned} \tag{4.37}$$

The JILA eEDM ion trap was designed to have the anharmonic contribution be as small as 1.2% over a trap radius of 1 cm to minimize systematic effects in measuring the eEDM signal. An

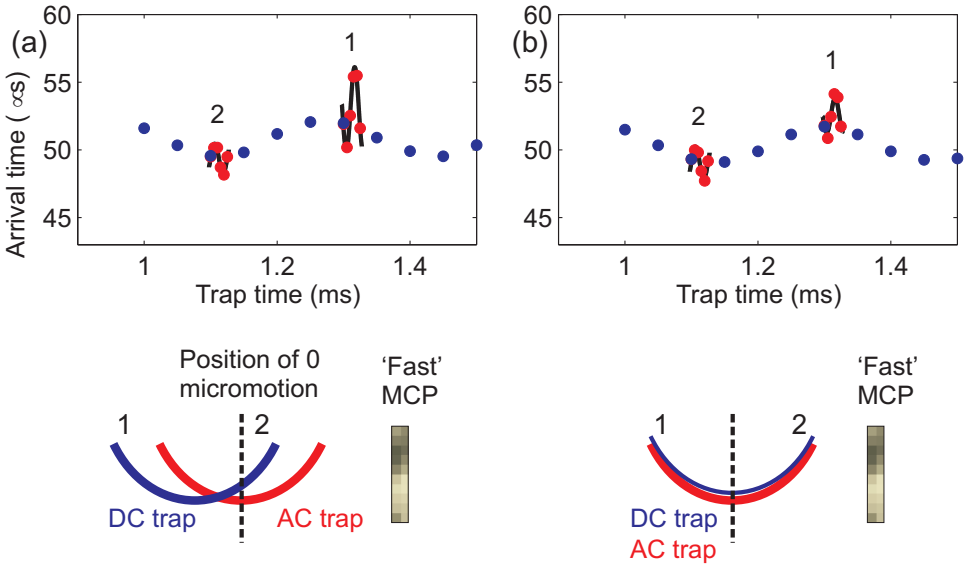

Figure 4.8: Plots of micromotion (red data points, 1 period = 25 μs) at different trap positions (secular motion shown in blue): at position '1' ('2'), the ions are displaced farther from (nearest towards) the 'fast' MCP detector. (a) A dipolar patch field has displaced the ions away from the center of the harmonic pseudopotential formed by the RF voltages (denoted as 'AC trap'), so the micromotion tends to be larger at position '1' than at '2'. (b) When the dipolar patch field is nulled out, the micromotion is equal at both positions '1' and '2'.

experimental determination of the trap anharmonicities would not only check the trap assembly configuration against its design parameters but also help us (together with other measured quantities) estimate systematic effects for the eEDM measurement. To measure the trap anharmonicity, we kicked the ions along the axial direction and measured its resultant slosh amplitude and frequency. Fig. 4.9 shows a summary of the trap frequency dependence on the slosh root-mean-square amplitude, from which the anharmonic contribution to the frequency is determined to be 1.7% over a trap radius of 1 cm.

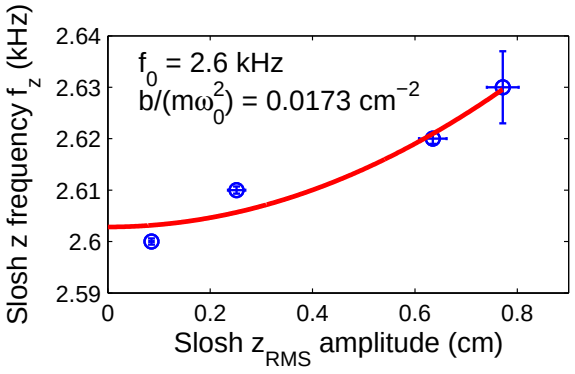

Figure 4.9: Plot of slosh frequency versus root-mean-square amplitude, where the different slosh amplitudes have been excited by kicking the ions. The blue data points are fit to a curve given by Eq. (4.37).

4.4 Rotating field characterization

Many of the tools already developed in Section 4.3 are directly applicable to the characterization of the rotating bias electric field. A characterization of the rotating field inhomogeneity is not purely an academic exercise, but has profound implications on potential systematic effects for the eEDM experiment. Briefly (see [45, 83] for details), if $\mathcal{E}_{rot}$ was always larger in the region $z > 0$ than that in $z < 0$ by 0.03%, a frequency shift of $\omega_{max} = 0.0003\,\delta m_F\,\omega_{rot}\,\frac{\mathcal{E}_{z,max}}{\mathcal{E}_{rot}} \approx (2\pi)0.23$ Hz would be added to the energy difference between the two Zeeman sublevels $|a\rangle$ and $|b\rangle$ in a single $^3\Delta_1$ Stark manifold (see Fig. 1.5). The net systematic effect after performing the four-way eEDM chop described by Eq. (1.7) is then a frequency shift of $(\delta g_F/g_F)\omega_{max} = (2\pi)0.45$ mHz, which

translates to a systematic error of $\delta d_e = 9 \times 10^{-30}$ e cm. These values assume $\omega_{rot} = (2\pi)250$ kHz, $\mathcal{E}_{z,max} = 1$ V/cm, $\mathcal{E}_{rot} = 10$ V/cm and $\delta g_F / g_F = 0.002$.

Although the rotating field is applied in the $(\hat{x}, \hat{y})$ plane, inhomogeneities in $\mathcal{E}_{rot}$ along $\hat{x}$ and $\hat{y}$ transform into an inhomogeneity along $\hat{z}$ by Laplace's equation:

$$\vec{\nabla} \cdot \vec{\mathcal{E}}_{rot} = 0 \quad \Rightarrow \quad \frac{\partial \mathcal{E}_{rot}}{\partial z} = -\frac{\partial \mathcal{E}_{rot}}{\partial x} - \frac{\partial \mathcal{E}_{rot}}{\partial y} \,. \tag{4.38}$$

Further, if the axial direction is not orthogonal to the plane of rotation, one can obtain higher-order spatial dependencies of $\mathcal{E}_{rot}$ in the axial direction, i.e. $\frac{\partial^n \mathcal{E}_{rot}}{\partial \mathcal{E}_{rot}^n} \neq 0$. Expressing the rotating field inhomogeneity as a Taylor expansion in z, we get

$$\frac{\mathcal{E}_{rot}}{\mathcal{E}^0_{rot}} = 1 + \frac{1}{\mathcal{E}^0_{rot}} \frac{\partial \mathcal{E}_{rot}}{\partial z} z + \frac{1}{2} \frac{1}{\mathcal{E}^0_{rot}} \frac{\partial^2 \mathcal{E}_{rot}}{\partial z^2} z^2 + \ldots \,, \tag{4.39}$$

where $\mathcal{E}^0_{rot}$ is the nominal value of the bias field.

In the presence of an inhomogeneous rotating field, the ions experience a ponderomotive force that causes the ions to undergo secular motion in addition to its circular micromotion, like that described in Section 4.1.2. Analogous to Eq. (4.8), the ponderomotive potential energy $e\bar{D}_{rot}(\bar{X})$ is the same as the kinetic energy U_{rot} given by Eq. (4.23). The total potential energy experienced by the trapped ions in an inhomogeneous rotating field is then

$$U = \frac{1}{2} m \omega_0^2 z^2 + \frac{e^2}{2 m \omega_{rot}^2} \mathcal{E}_{rot}^2 = \frac{1}{2} m \left(\omega_0^2 + (\Delta\omega)^2 \right) (z - z_0)^2 \,. \tag{4.40}$$

The effect of U_{rot} on the ions' secular motion is described by a mean displacement z_0 and a quadrature difference in secular frequency with and without a rotating field $(\Delta\omega)^2$. The first order gradient in $\mathcal{E}_{rot}$ can be extracted from z_0:

$$\begin{aligned} \frac{\partial U}{\partial z} &= m \omega_0^2 z + \frac{e^2}{m \omega_{rot}^2} \mathcal{E}_{rot} \frac{\partial \mathcal{E}_{rot}}{\partial z} = m \left(\omega_0^2 + (\Delta\omega)^2 \right) (z - z_0) \\ \Rightarrow \left| \frac{1}{\mathcal{E}^0_{rot}} \frac{\partial \mathcal{E}_{rot}}{\partial z} \right| &\simeq \left(\frac{m \omega_{rot} \omega_0}{e \mathcal{E}^0_{rot}} \right)^2 z_0 \\ &= 4.3 \left(\frac{\omega_{rot}}{(2\pi)253 \text{ kHz}} \right)^2 \left(\frac{\omega_0}{(2\pi)1 \text{ kHz}} \right)^2 \left(\frac{1 \text{ V/cm}}{\mathcal{E}_{rot}} \right)^2 \left(\frac{z_0}{1 \text{ cm}} \right) \quad \text{cm}^{-1} \,, \end{aligned} \tag{4.41}$$

where the $(\Delta\omega)^2$ term can be neglected. A further round of differentiation yields the expression for the second order gradient:

$$\begin{aligned}
\frac{\partial^2 \mathcal{E}_{rot}}{\partial z^2} &= m\omega_0^2 + \frac{e^2}{m\omega_{rot}^2}\left[\left(\frac{\partial \mathcal{E}_{rot}}{\partial z}\right)^2 + \mathcal{E}_{rot}^0\left(\frac{\partial^2 \mathcal{E}_{rot}}{\partial z^2}\right)^2\right] = m\left(\omega_0^2 + (\Delta\omega)^2\right) \\
\frac{1}{\mathcal{E}_{rot}^0}\frac{\partial^2 \mathcal{E}_{rot}}{\partial z^2} &\simeq \left(\frac{m\omega_{rot}}{e\mathcal{E}_{rot}^0}\right)^2 (\Delta\omega)^2 \\
&= 4.3\left(\frac{\omega_{rot}}{(2\pi)253\text{ kHz}}\right)^2\left(\frac{(\Delta\omega)^2}{((2\pi)1\text{ kHz})^2}\right)\left(\frac{1\text{ V/cm}}{\mathcal{E}_{rot}^0}\right)\quad \text{cm}^{-2}\,. \qquad (4.42)
\end{aligned}$$

To experimentally characterize the rotating field inhomogeneity, the ions' secular motion is monitored with and without a rotating field. For the case with the rotating field present, $\mathcal{E}_{rot}$ needs to be ramped on quickly compared to a cycle of secular motion but slowly compared to the rotation frequency ω_{rot} to avoid kicking the ions. $\mathcal{E}_{rot}$ is ramped off at the same speed as its turn-on ramp, at a short but fixed time interval before the end of the trap duration. Fig. 4.10 shows the ions' mean displacement and secular frequency, as detected on the 'imaging' MCP, plotted as a function of $\mathcal{E}_{rot}$. The plotted mean displacement has already been converted into the in-trap displacement using the MCP transfer matrix. Using Eq. (4.41), the first order inhomogeneity $\frac{1}{\mathcal{E}_{rot}^0}\frac{\partial \mathcal{E}_{rot}}{\partial z}z$ over a typical cloud 2σ-radius of $z = 3$ mm is $6(1) \times 10^{-5}$. Similarly, from Eq. (4.42), the second order inhomogeneity in Eq. (4.39) over $z = 3$ mm is measured to be $1.0(1) \times 10^{-4}$.

4.5 Fluorescence

So far, the trap and rotating field characterization results have implied that the JILA eEDM ion trap is fairly well-matched in its assembly compared to its design. How well the ion trap performs in terms of ion fluorescence collection, which is one of the trap's major design considerations, has yet to be seen and will be presented in the following chapter.

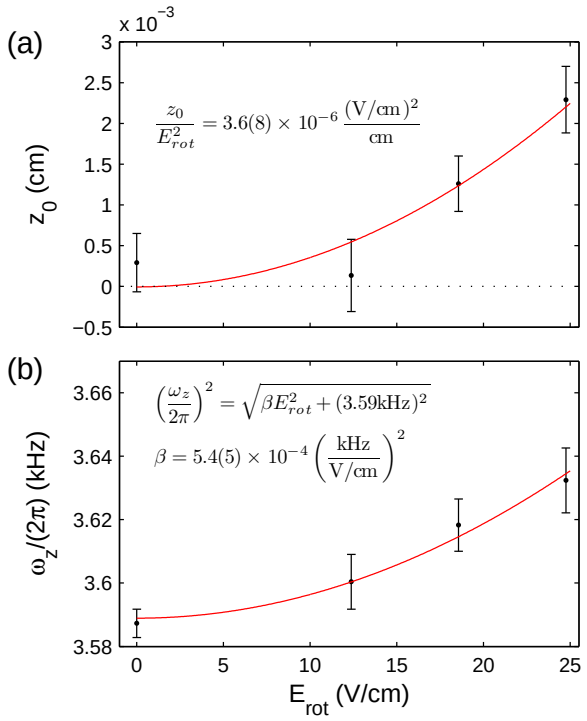

Figure 4.10: (a) Plot of mean displacement versus $\mathcal{E}_{rot}$, from which the quadratic term can be used to determine the first order gradient in $\mathcal{E}_{rot}$. (b) Plot of secular frequency versus $\mathcal{E}_{rot}$, from which the second order gradient in $\mathcal{E}_{rot}$ can be extracted.

Chapter 5

Spin readout techniques (I): fluorescence

The ability to detect HfF^+ in a state-sensitive manner is an integral part of the eEDM measurement: in the Ramsey spectroscopy of an eEDM-sensitive transition, the transition frequency is measured by counting the relative HfF^+ left in one of the two spin states as a function of the free evolution time between two $\pi/2$ pulses. In the context of Ramsey spectroscopy, the state detection process is also known as the spin readout process.

Before beginning the Ramsey pulse sequence, state-sensitive detection of HfF^+ is also used to determine the number of ions prepared in the desired state. As shown in Chapter 3, we have already demonstrated the ability to detect the rotational states of HfF^+ using laser-induced fluorescence (LIF), so it is tempting to extend that to LIF *in-trap*, as discussed in this chapter. It is important to bear in mind that LIF is not used as the final means of state detection for the eEDM experiment, especially with the development of resonance-enhanced multi-photon dissociation (REMPD) as a state detection method that is two orders of magnitude more efficient than LIF (see Chapter 6). Nevertheless, this chapter discusses the design considerations behind the incorporation of LIF with an ion trap, with the aim of maximizing fluorescence photon collection while minimizing scattered light. At the end of this chapter, we also present estimates for cavity-enhanced absorption as a plausible state detection technique.

5.1 Experiment setup

5.1.1 Fluorescence collection

The LIF that is performed on the trapped ions makes use of the same transitions as that on the molecular beam in Chapter 3: a 1 μJ/pulse laser at 769 nm (output by a dye cell amplifier seeded by a diode laser) drives a rotational transition in the $^1\Pi_1 \leftarrow ^1\Sigma^+$ ($\nu' = 0, \nu'' = 0$) band [16, 81], and fluorescence photons emitted on the $^1\Pi_1 \rightarrow ^1\Sigma^+$ (0, 1) band are detected by a photomultiplier tube (PMT). As with almost all molecular transitions, this one is non-cycling, which means that once a molecular ion gets excited by a 769 nm photon and fluoresces, it lands in a dark state and cannot be re-excited by the same laser on the LIF experiment time scale. Hence, the in-trap fluorescence collection setup, comprising two large gold mirrors as detailed in Chapter 4, was built to capture photons with as high an efficiency as possible.

By design, most of the photons exit the light pipe onto a PMT with an angle of 45°, favoring a PMT with the photosensitive material close to its flat entrance surface (e.g. Hamamatsu R7600U-20-M4) as opposed to one with a curved glass surface, from which the photosensitive material is farther recessed (e.g. Hamamatsu R3896). Since the preferred PMT (R7600U-20-M4) has a square-shaped active area (18 mm × 18 mm), the light pipe also has a matching square profile (11 mm × 11 mm) (see Fig. 5.1). The use of R7600U-20-M4 over R3896, however, comes at a price: the quantum efficiency of the photosensitive material is 5% and 15% at 818 nm for the former and latter PMT, respectively. In fact, both PMTs are specified to have the same quantum efficiency curves, but the R3896 has been measured to have an uncharacteristically high quantum efficiency. Nevertheless, the overall efficiency of fluorescence photon collection with the ion trap setup described so far in combination with two R7600U-20-M4 PMTs is still higher (2.6%) than that for the ion beam (1.2%).

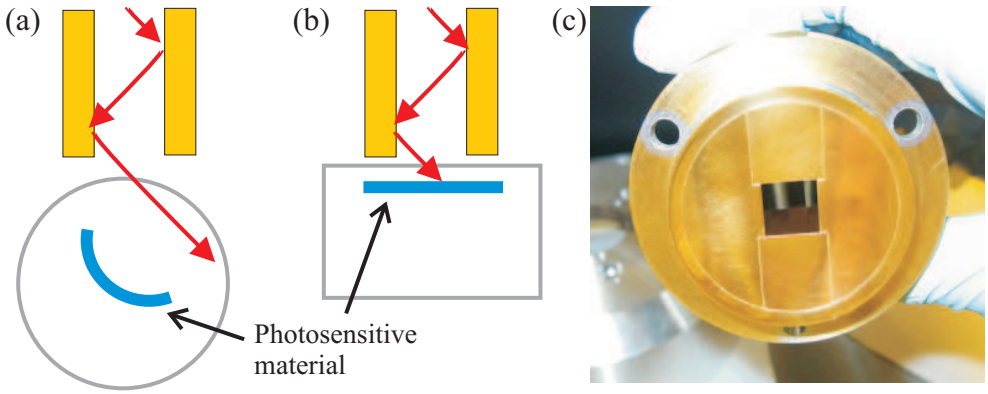

Figure 5.1: Schematic of a light pipe used in combination with (a) a PMT of curved entrance glass surface, where the photosensitive material is farther recessed, and (b) a PMT of a flat entrance surface, where the photosensitive material is nearer to the light pipe. (c) Photograph of the exit of a light pipe whose square profile matches that of the R7600U-20-M4 PMT.

5.1.2 Scattered light, the nemesis

Despite the fact that LIF had already worked for us in a molecular beam, in-trap LIF is not without its challenges. Performing LIF in the presence of a 'shiny' environment — where the trap electrodes and large gold mirrors have been polished to a highly reflective finish — means that it is also easy for scattered light to make its way to the PMT! To optimize the LIF signal-to-noise ratio, one must try to suppress the the background noise coming from scattered photons.

Scattered light is typically suppressed using three approaches: time gating, wavelength filtering, and spatial filtering. Time gating in the LIF context means that the chain of high voltages within the PMT circuit is only turned on *after* the 769 nm laser fires, so that the avalanche process converting prompt scattered light into voltage pulses is suppressed when the excitation laser fires (Fig. 5.2a). Even if HfF^+ had a cycling transition, the need for time gating also eliminates the possibility of collecting multiple photons from any single trapped ion by shining on the LIF laser continuously.

Wavelength filtering is carried out by detecting the fluorescence photons at a different wavelength (818 nm) from the excitation wavelength (769 nm). When performing LIF on a molecular ion beam, we were able to efficiently filter out 769 nm light by placing a narrowband (10 nm FWHM, 820 nm center wavelength) dichroic filter in a region where the light rays were perpendicular to the filter. With the ion trap setup, however, photons exit the light pipe at a range of angles from 0° to 45°. Since the transmission of a dichroic bandpass filter tends to be blue-shifted as the angle of incidence increases (Fig. 5.2b), the 820 nm bandpass filter would both step on the transmission of 818 nm light and ineffectively filter out 769 nm light. Unlike dichroic filters, colored glass filters do not suffer from any sensitivity to the angle of incidence and are also highly transmissive in their passband (>90%). However, they tend to refluoresce after absorbing photons in the filter stopband, and the band edge separating the stopband and passband regions is typically as broad as ≈100 nm. A hybrid of the above two types of filters is the "colored glass alternative" dichroic long-pass filter, which offers a high transmission in the passband and a relative sharp (10 nm width) band edge,

although the band edge width and position can also be tuned by the angle of incidence (Fig. 5.2c). Such a filter (Newport CGA830) with a nominal band edge at 830 nm is placed between the light pipe and the PMT to allow for high transmission (>90%) at 818 nm while stepping on scattered light at 769 nm after accounting for the distribution of angles of incidence.

Besides the 769 nm laser, the much stronger UV pulsed laser (∼1 mJ/pulse, 368 nm) used to ionize neutral HfF can also give rise to scattered light. (The other ionization laser at 309 nm has < 10 μJ/pulse.) The UV scattered light could in principle be suppressed by time gating if the ionization lasers were to fire a long time before the LIF pulse was applied. However, experiments probing the rotational lifetime of the molecules need to perform LIF starting from very short times after ionization, i.e. where time gating alone is insufficient to deal with scattered photons from the intense ionization laser pulse. Further, the stray UV photons hitting metal surfaces off the vacuum chamber or ion trap tend to be absorbed and reemitted as red-detuned photons over a large wavelength range. In this respect, the aforementioned CGA830 long-pass filter helps to filter out scatter from the UV laser, but is not aggressive enough on its own. A colored glass filter (IR-80, passband >760 nm) is inserted between the CGA830 and PMT to provide a high absorbance of any scattered light within its stop band while avoiding the refluorescence of UV light.

The last approach to deal with scattered light, spatial filtering, is typically done by carefully imaging the detection target onto the PMT, while rejecting light from other areas with the help of a pinhole. Since the light pipes of the ion trap are non-imaging, the pinhole technique does not work. Nevertheless, given the fact that a significant fraction of scattered light arises from lasers (UV, 769 nm) passing through the entrance and exit Brewster windows of the ion trap chamber, we can reduce the scattered light off of these windows with the following methods:

(1) Setting the polarization of the lasers to be p-polarized relative to the Brewster window orientation (i.e. horizontal polarization). In fact, since the fluorescence collection optics are positioned above and below the ions, the fluorescence signal is maximized for a horizontally polarized excitation laser.

(2) Using Suprasil, a fused silica material with low bubble content, in place of regular quartz or fused silica for the Brewster windows.

(3) Extending the distance between the ion trap and each Brewster window.

(4) Inserting baffles between the ion trap and each Brewster window (Fig. 5.2d). The baffles are machined out of stainless steel to a conical razor blade tip and painted with Ball Aerospace Flat Black paint. The razor blade tip limits the extent of diffraction fringes that may result if the laser beams are clipped and diffracted by the baffles. The diameter of the baffles opening, 14 mm, is chosen to be a compromise between not clipping the laser beams versus decreasing the probability of scattered light off the windows making its way into the ion trap chamber.

The above techniques of suppressing scattered light also tends to deteriorate the signal collection efficiency a little. Most notably, time gating and wavelength filtering reduces the fluorescence photon collection efficiency by 0.7 and 0.6, respectively. According to the collection efficiency budget outlined in Table 5.1, with ∼500 ions in a single rovibronic level, the total number of photons detected by a single PMT is estimated to be only 0.8 per shot, where the loss in efficiency is mostly dominated by the PMT quantum efficiency. Nevertheless, the combination of all three scattered light suppression techniques brought the scattered counts down to 0.1 photon per shot.

5.2 LIF signal

With the estimated signal-to-noise ratio optimized, we proceeded to detect the states of the trapped HfF^+ ions using LIF. Fig. 5.3a shows a LIF spectrum of ions that have been trapped for 2 ms, recorded by scanning the frequency of the 769 nm laser centered on the $Q(1)$ rotational line. The LIF signal is on the same order of magnitude as that estimated, i.e. 0.4 photons per shot. The rotational line has a full width half maximum of 240(24) MHz, which is dominated by the RF micromotion-induced Doppler effect of the trapped ions. In order to detect a LIF signal beyond 2 ms of trapping time, we needed to install a home-built fast shutter [53, 78] to block the weak

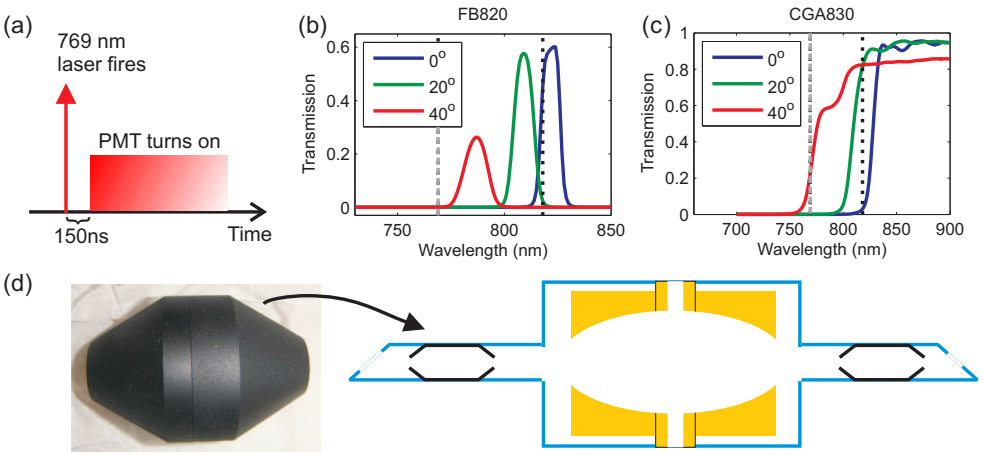

Figure 5.2: (a) Time gating of the PMT to reduce the detection of scattered light from the 769 nm excitation laser. (b) Plots of the bandpass filter FB820 transmission versus wavelength for different angles of incidence. (c) Plots of the colored glass alternative long-pass dichroic filter CGA830 transmission versus wavelength for different angles of incidence. In both (b) and (c), the gray dashed lines denote the excitation laser wavelength at 769 nm, at which scattered light is the strongest and needs to be suppressed most aggressively. The dotted black lines denote the fluorescence wavelength at 818 nm, at which the filters need to have high transmission for efficient fluorescence collection. (d) Photograph of a light baffle, which is placed in between the ion trap and Brewster window to reduce scattered light.

Table 5.1: Effects of various components of the fluorescence collection experiment on the collection efficiency.

Total number of trapped ions	800
Fraction of ions in $^1\Sigma^+, \nu'' = 0, J = 1$	0.6
Saturation	0.5
Franck-Condon overlap $\langle {}^1\Pi_1, \nu' = 0 \vert {}^1\Sigma^+, \nu = 1 \rangle$	0.3
Spatial overlap of lasers, ions and imaging axis	~ 1 (optimistic!)
Detection solid angle for 1 cm ion cloud	0.6
Reflectivity of gold mirrors	0.85
Tranmission of filters and vacuum flange window	0.6
Signal remaining after time gating	0.7
PMT efficiency at 818 nm	*0.05*
Total photons per shot on both PMTs	0.75

continuous-wave component of 769 nm light whenever the 769 nm dye cell amplified pulse was not firing, otherwise the continuous-wave component of the light (coming from the seed diode laser, transmitted through the dye cell) would pump away ions on resonance and serve as a source of LIF signal decay. Fig. 5.3b shows the LIF signal measured as a function of the trap duration with the shutter in place. There is an initial decay of the HfF^+ LIF signal over the first few milliseconds, after which the LIF signal remains constant over 40 ms. One clue to the source of initial LIF signal decay comes from how the decay amplitude is less pronounced when the ions are squeezed by ramping to tighter trap frequencies. Fig. 5.3c shows the LIF signal versus trap duration for a HfF^+ cloud that is 1.8 times smaller in area (along the radial directions $\hat{x}, \hat{y}$) compared to that in Fig. 5.3b. The LIF signal from 10–40 ms is correspondingly 1.9(4) times higher in Fig. 5.3c. It seems, then, that the LIF signal collection at long times is simply limited by the initial expansion of the HfF^+ ions in the trap, which reduces the spatial overlap between the HfF^+ ions and the imaging axis formed by the light pipes.

5.3 Estimates for cavity-enhanced detection

Let us return to the fluorescence collection efficiency budget outlined in Table 5.1, and think of possible ways to improve it. One might look at the main culprit, the quantum efficiency of the

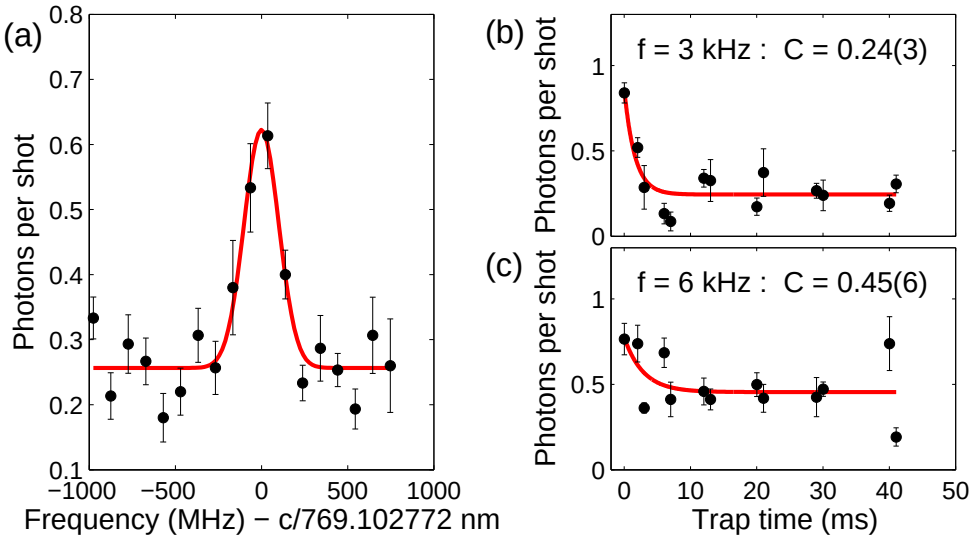

Figure 5.3: (a) Frequency scan of the $^1\Pi_1 \leftarrow^1 \Sigma^+(0,0)\,Q(1)$ transition, taken by performing LIF on ions that have been trapped for 2 ms. (b) Plot of LIF signal as a function of trap duration for a 3 kHz trap. The signal is fit to a decaying exponential with offset C. (c) Plot of LIF signal as a function of trap duration for a 6 kHz trap. The tighter trap in (c) yields a larger LIF signal C at long times compared to the weaker trap in (b).

PMT, and exclaim, "Aha! Why don't we use an avalanche photodiode instead, where the quantum efficiency is much higher in the visible red or near infrared wavelengths?" The problem with the avalanche photodiode is its high dark count rate per square millimeter of active area ($\sim 10^8$ counts per second compared to $\sim$100 counts per second for a PMT with the same active area). The dark count rate can be reduced by shrinking the size of the active area, but unfortunately, for collecting photons from a relatively diffuse cloud of ions, the signal is correspondingly compromised in a way that reduces the signal-to-noise ratio. On the other hand, the output of a single-mode cavity may be efficiently focused onto a small-area avalanche photodiode, thus it is worth considering cavity-enhanced detection techniques. For the cavity-enhanced techniques presented in this section, we refer the reader to References [84] and [95] for detailed explanations, and use the results from those two Vuletić-group papers to estimate experimental parameters particular to our trapped HfF^+ ions.

Cavity-enhanced techniques may be applied to either fluorescence or absorption for detecting the states of HfF^+. In both cases, the coupling between the cavity and a single molecular ion can be described by the cooperativity η, which is related to the ion-cavity coupling g, cavity decay linewidth κ and ion spontaneous decay linewidth Γ by

$$\eta = 4g^2/(\kappa\Gamma)\,. \tag{5.1}$$

In terms of experimental parameters like the cavity finesse $\mathcal{F}$, cavity mode waist w_c and scattering cross section σ_s, we get the expression for η to be

$$\eta = \frac{4\sigma_s\mathcal{F}}{\pi^2 w_c^2}\,. \tag{5.2}$$

For cavity-enhanced fluorescence, the ratio with which a molecular ion emits fluorescence photons into the cavity compared to that into free space is given by η. The ion number resolution ΔN one can hope to achieve with fluorescence from N ions is [84]

$$\Delta N = \sqrt{\frac{2N}{q\eta p}}\,, \tag{5.3}$$

where q is the photodiode quantum efficiency and $p = 1$ is the number of photons scattered per molecular ion. On the other hand, for cavity-enhanced absorption, the ion number resolution is

[84, 95]

$$\Delta N = \sqrt{\frac{1}{2q\eta p}}. \tag{5.4}$$

Comparing between Eqs. (5.3) and (5.4), cavity-enhanced absorption has the potential for much higher ion number resolution.

It is worth noting that there are a number of different cavity-enhanced absorption techniques, such as noise-immune cavity-enhanced optical heterodyne molecular spectroscopy (NICEOHMS) [93], where the molecular ions are modulated at a frequency that is the same as the free spectral range of the cavity. This section follows the particular experiment described in [95], where the Rb atoms are only modulated at a small fraction ($\approx 1/44$) of the cavity free spectral range. The frequency modulation of the Rb atoms is performed so as to place the first order red sideband near or on resonance with the cavity, and then the cavity reflection of that sideband is heterodyned against the carrier. The shift in cavity resonance, which shows up as a shift in the dispersive lineshape, is then proportional to the number of ions coupled to the cavity.

Suppose, then, that we are interested in using cavity-enhanced absorption to resolve up to $\Delta N \leq 10$ ions. For a sample of 50 ions in a single rovibronic state, a signal-to-noise ratio $\geq$ 5 offered by cavity absorption can only be achieved with competing spin readout methods if the total detection efficiency is as high as 50%. To achieve $\Delta N \leq 10$ with a reasonable photodiode quantum efficiency of $q = 0.5$, Eq. (5.4) dictates that $\eta > 0.01$. We now examine more closely the expression for η in Eq. (5.2) and estimate reasonable parameters needed to achieve $\eta > 0.01$.

For atoms that can be well approximated as a two-level system due to the use of a cycling transition, the scattering cross section is $\sigma_s^{atom} = 3\lambda^2/(2\pi)$. For molecules without cycling transitions, the scattering cross section is reduced from σ_s^{atom} by the Franck-Condon overlap and electronic and rotational state branching ratios. Of the HfF^+ states lying below 22000 cm^{-1} with transitions to $^3\Delta_1$, the $^3\Pi_{0-}$ states (at $\approx$10400 cm^{-1} and $\approx$19200 cm^{-1}) and $^3\Sigma_{0-}$ state (at $\approx$21700 cm^{-1}) decay only to the $^3\Delta_1$ state [86]; of these, the $[10.4]^3\Pi_{0-} \leftarrow^3 \Delta_1(\nu' = 0, \nu'' = 0)$ transition has the most favorable Franck-Condon overlap, as shown in Table 5.2. Including the rotational branching

ratio of the $|J'=0,\Omega'=0,F'=1/2\rangle \leftarrow |J''=1,\Omega''=1,F'=3/2\rangle$ transition, the best scattering cross section we can achieve is then $\sigma_s = 0.52 \times 0.5\,\sigma_s^{atom} = 0.26\,\sigma_s^{atom}$. So far, we have not yet taken into account the Doppler width of the ions. With a typical Doppler width of $\Gamma_{dopp} =$ 30 MHz along the axial direction, the scattering cross section is diluted down by $\Gamma/\Gamma_{dopp} \sim 10^4$, i.e. $\sigma_s = 2.6 \times 10^{-5}\,\sigma_s^{atom}$.

Table 5.2: Franck-Condon overlaps $|\langle \nu''=0|\nu'\rangle|^2$ between the $^3\Delta_1, \nu''=0$ state and excited states $[10.4]^3\Pi_{0-}, [19.2]^3\Pi_{0-}$ and $[21.7]^3\Sigma_{0-}$ of various vibrational levels ν'. The notation for the excited electronic states follows the same convention as that used in Chapter 2.

ν'	0	1	2	3	4	5	6
$[10.4]^3\Pi_{0-}$	0.52	0.36	0.11	< 0.01	< 0.01	< 0.01	< 0.01
$[19.2]^3\Pi_{0-}$	0.30	0.07	0.04	0.21	0.22	0.12	0.04
$[21.7]^3\Sigma_{0-}$	0.31	0.04	0.08	0.26	0.21	0.08	0.02

Given the above scattering cross section, the remaining parameters we can choose to fulfil $\eta > 0.01$ are the cavity finesse and mode waist: the lower the finesse desired, the smaller the mode waist needed. The cavity mode waist is limited by the number of ions we can squeeze radially in the trap. With the eEDM linear Paul trap presented in this thesis, the highest trap frequency we can obtain in the radial direction is $(2\pi)28$ kHz, which comes from applying $|V_{rf}| = 200$ V and $\omega_{rf} = (2\pi)60$ kHz. (Increasing ω_{rf} does not help because we are limited by V_{rf}.) Using the typical trap radius of 2 mm for a $(2\pi)4$ kHz trap, we can only get a radius of 0.76 mm with the squeezed trap. Alternatively, we can run the eEDM ion trap as a cylindrical Paul trap, i.e. $|V_{rf}|\cos(\omega_{rf}t)$ is applied to all six radial fins and a weak DC cylindrical quadrupole field that further confines the ions radially is generated by the end cap electrodes. The cylindrical Paul trap does not offer a higher trap frequency (maximum achievable $\omega = (2\pi)24$ kHz) because the end cap electrodes in the existing design are spaced too far apart. With the cavity mode waist limited to 0.76 mm, we require, for a resolution of $\Delta N \leq 10$ ions, that the cavity finesse be $\mathcal{F} \geq 10^{10}$.

State-of-the-art cavities have finesses in the range of $10^5 - 10^6$ and are dominated by losses in the cavity mirrors [92]. The required cavity finesse of 10^{10}, then, is quite impossible. The main

limitation is the small scattering cross section due to the ion cloud's large Doppler widths. With these challenges in mind, we retired the idea of implementing cavity-enhanced absorption. We may revisit it as a spin-readout technique to be used with future generations of eEDM experiments where the molecular ions may be sympathetically cooled to much lower temperatures and where the ion trap geometry is more compact.

Chapter 6

Spin readout techniques (II): photodissociation

In the previous chapter, we saw how we could detect the state of HfF^+ ions in the $^1\Sigma^+(\nu'' = 0)$ level using laser-induced fluorescence. A possible path from there to the eEDM measurement is to extend the capability of LIF to $^3\Delta_1(\nu'' = 0)$ state detection, where a known transition to the $^3\Phi_2(\nu' = 1)$ level can be excited by a 684 nm laser, and fluorescence down to the $^3\Delta_1, \nu = 2$ level at 763 nm can be measured and reasonably well-filtered from the excitation wavelength [16]. However, as shown in Table 5.1, the LIF efficiency can be easily nickled-and-dimed down to a paltry 0.18% for a single PMT, and the dominant limitation in efficiency — the quantum efficiency of the PMT at 763 nm — remains as miserly as 8%. Given these numbers, even if we were to optimistically populate 30 HfF^+ ions in a given $|F, m_F, J, \Omega\rangle$ state of the $^3\Delta_1, \nu'' = 0$ manifold, our readout signal would only be 0.05 photons per shot. With a repetition rate of 4 Hz (limited by the pumping speed in the ablation/source chamber to remove residual gas after the pulsed valve fires, also assuming a coherence time of 0.25 s), such a low readout signal would mean as long as 2.5 hours spent to reach 1×10^{-27} e cm.

Counting photons from non-cycling transitions in a diffuse cloud of molecular ions is hard. Counting ions, on the other hand, is relatively easy: the quantum efficiency of detection for a highly energetic (> 2 keV) ion hitting a single MCP channel can be on the order of unity. The overall efficiency of the ion detector is then limited by the open area ratio (ratio of active channel area to the total MCP area) and by the transparency of the ground mesh above the MCP to approximately 25%. In all the experiments discussed so far, HfF^+ ions have been counted using

the MCP in a manner indiscriminate for the ions' internal state. To be sensitive to the state of HfF^+, one can use a laser to resonantly excite HfF^+ molecules to a repulsive potential, which breaks apart the molecules into Hf^+ and F. The Hf^+ atomic ions can then be counted on a MCP. Using such a resonance-enhanced multi-photon dissociation (REMPD) scheme, the detection efficiency is potentially much higher than that for LIF: if it were higher, say, by a factor of 10, the eEDM measurement could be carried out 10 times faster to reach the same statistical sensitivity (assuming the same level of noise). To quote Eric's famous motivational refrain, this would ideally translate to "less time spent taking data, more time spent skiing".

Performing REMPD, alas, is easier said than done. Firstly, we have to find the repulsive curves, which are likely to lie > 50000 cm^{-1}. Secondly, photodissociating in a rotational state specific way means that we also have to find intermediate bound states of energy < 40000 cm^{-1}, so that we can drive a bound state-bound state transition with a weak but narrow UV/visible laser before hitting the repulsive curve. A simultaneous search for (at least) two unknown potential curves is non-trivial, especially since theoretical calculations on HfF^+ have only been performed up to 22000 cm^{-1}. This chapter presents the following: the basics of photodissociation; the experiment sequence and layout needed to prepare for a survey scan of high-lying HfF^+ states; spectroscopy of HfF^+ states at > 30000cm^{-1}; our preliminary understanding of the repulsive curve; the experimental efficiency of photodissociation as a state readout method.

6.1 Basics of photodissociation

6.1.1 Direct photodissociation

In direct photodissociation, a HfF^+ molecule is excited by a laser (or multiple lasers) to a molecular potential that is purely repulsive in nature, before breaking apart into its constituent atoms:

$$HfF^+ + h\nu \rightarrow Hf^+ + F\,. \tag{6.1}$$

Repulsive molecular potentials lie above the bond dissociation energy D_0, which is the minimum energy necessary to break apart a molecule starting in its ground rovibronic state. D_0 has been estimated from ab-initio calculations to be 51400(300) cm^{-1} [62]. As shown in Fig. 6.1a, D_0 can also be estimated from the measured bond dissociation energy of neutral HfF (55600 $\pm$ 1600 cm^{-1} [6]) and the ionization energies of HfF and Hf (59462 cm^{-1} and 55048 cm^{-1}, respectively) [4, 12] to be 51200 $\pm$ 1600 cm^{-1}:

$$D_0(\mathrm{HfF}^+) = D_0(\mathrm{HfF}) + IE(\mathrm{Hf}) - IE(\mathrm{HfF})\,. \tag{6.2}$$

If the repulsive molecular potential arises from constituent atomic orbitals that are in their ground configurations (i.e. $\mathrm{Hf}^+(^2D_{3/2})$ + $\mathrm{F}(^2P_{3/2})$), the potential energy at large internuclear separation, $D_{R\to\infty}$, asymptotes towards the bond dissociation energy (Fig. 6.1b). Conversely, if the repulsive potential is the result of anti-bonding between excited atomic orbitals, $D_{R\to\infty}$ is higher than D_0 (Fig. 6.1c).

The excitation of molecules to the repulsive potential takes place quickly compared to the motion of the constituent atomic nuclei, i.e. where the Born-Oppenheimer approximation is valid. The energy of the molecules at the point of excitation on the repulsive curve (U^*) that is in excess of $D_{R\to\infty}$ gets released as the kinetic energy of the dissociation products. For Hf^+ and F, the lighter fluorine atom flies away with 10 times as much kinetic energy compared to the Hf^+ ion. When the trap is dumped onto the MCP, the Hf^+ ion, being 10% lighter than HfF^+, is separated from any residual HfF^+ molecular ions in time-of-flight and detected on a MCP.

To figure out the position and width of the photodissociation resonance, we can use the reflection approximation [48, 35]: the repulsive potential in the vicinity of U^*, where U^* is many vibrational energies above $D_{R\to\infty}$, can be approximated as a linear negative slope. For such high-lying vibrational levels, the vibrational wavefunction amplitudes are mostly concentrated at the wavefunction turning points, i.e. at the internuclear separation where the repulsive slope lies (see Fig. 6.1d). The Franck-Condon overlap between these high-lying dissociative vibrational states and the lower vibrational state gives the probability of dissociation for a given laser frequency. Therefore,

over the range of frequencies connecting the lower state to the repulsive slope, the photodissociation resonance looks like the wavefunction of the lower state *reflected* about the negative linear slope of the repulsive potential.

As mentioned previously, there are no theoretical calculations describing HfF^+ molecular potentials lying above 22000 cm^{-1}, and certainly none above the bond dissociation energy. Nevertheless, it has been estimated, by extrapolating from the calculated molecular potential of PtH^+ [54], that a $^3\Sigma$ repulsive potential of slope 80000 $cm^{-1}/Å$ lies at 71000 cm^{-1} [83]. It is forbidden to make a transition directly from the ground $^1\Sigma^+$ state to a $^3\Sigma$ state, so one would need to go through an intermediate mixed-spin state. The photodissociation transition to the $^3\Sigma$ state is estimated to have a resonance of width 4200 cm^{-1} and cross section 3.8×10^{-19} cm^{-2} (assuming an electronic transition dipole moment of 0.3 ea_0), which requires a 266 nm laser pulse of energy ≈250 mJ to saturate an ion cloud of 2 mm radius.

6.1.2 Predissociation

A 10 ns laser pulse at 266 nm with a few hundred mJ of energy demands a rather hefty Nd:YAG laser for its source. In order to use less pulse energy for photodissociation, one can use predissociating molecular states. In pre-dissociation, the molecule is excited to a bound-state molecular potential that has an avoided crossing with a repulsive potential (see Fig. 6.2) [48, 35]:

$$HfF^+ + h\nu \rightarrow HfF^{+(*)} \rightarrow Hf^+ + F\,. \tag{6.3}$$

Comparing between predissociation and direct dissociation is analogous to comparing between autoionization and direct photoionization. Since the oscillator strength for a bound-bound transition tends to be stronger than for a bound-free transition, the laser pulse energy required to access a predissociating/autoionizing state tends to be smaller compared to that for its direct analog. The predissociation/autoionization resonances are also generally narrower, which means that they are harder to find! For predissociation, the reflection approximation does not hold because of structure in the upper bound-repulsive potential. In fact, sometimes the point of avoided crossing may occur

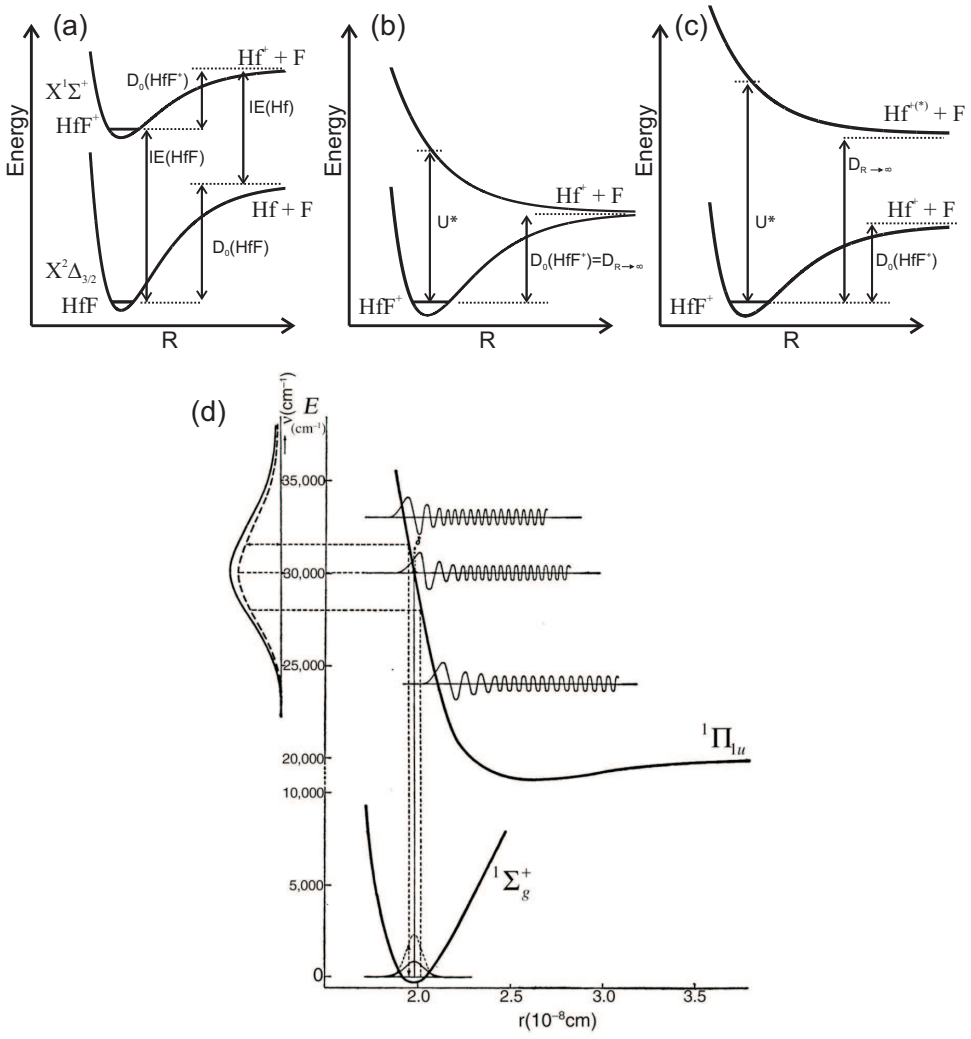

Figure 6.1: (a) Schematic of ground state molecular potentials for both neutral and ionic HfF, illustrating how to derive the bond dissociation energy of the HfF^+ molecular ion species from the ionization energies and bond dissociation energy of the neutral molecule species. (b) Schematic of ground and repulsive molecular potentials in HfF^+, where both molecular potentials come from Hf^+ and F atomic orbitals in their ground state configuration, such that the repulsive potential at large internuclear distances $D_{R\to\infty}$ tends to the bond dissociation energy D_0. U^* is the energy needed to access the repulsive potential from the ground state. (c) Schematic of ground and repulsive molecular potentials in HfF^+, where the repulsive potential is composed of atomic orbitals in an excited state configuration, i.e. $D_{R\to\infty} > D_0$. (d) Using the reflection approximation, the dissociation resonance (vertical Gaussian) is a reflection of the lower state's wavefunction (thin line) about the repulsive potential that has been approximated as a linear negative slope, as shown in the depicted example for Cl_2 [35].

such that U^* is barely above $D_{R\to\infty}$, which means that the constituent atoms fly off with a much lower kinetic energy, simplifying their detection.

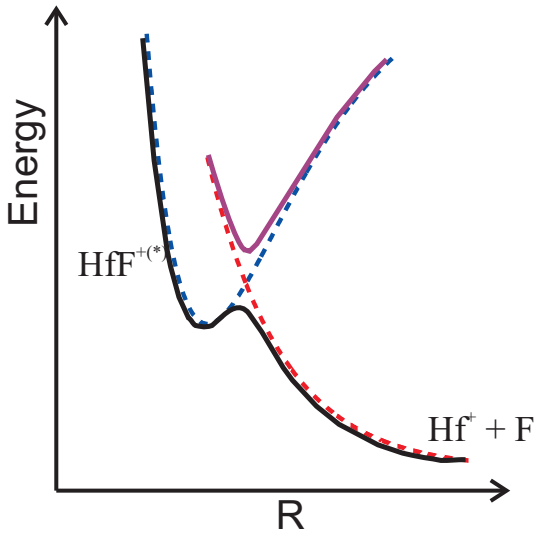

Figure 6.2: The avoided crossing of a bound state (blue dashed line) and repulsive state (red dashed line) gives rise to a predissociating potential (black line) and a more tightly confined bound state (purple line).

6.2 Practical challenges and considerations

6.2.1 HfF^+ creation

For photodissociation to work as a state detection method on the eEDM experiment, the question is not so much the nature of the molecular potential at > 50000 cm^{-1}, but *where* we need to tune our lasers to hit a repulsive/predissociating state. The best tunable laser at our disposal for performing a survey spectroscopy of HfF^+ lines — a SIRAH Precision Scan pulsed dye laser and its motorized doubling crystal setup — was already being used to deliver the second photon at 368 nm for photoionizing HfF. Since we did not know how likely we were to succeed in performing photodissociation, we were reluctant to buy another pulsed dye laser system specially for photodissociation. Instead, we freed up our existing pulsed dye laser by using 308 nm (unchanged from before) +

355 nm (the third harmonic of a Nd:YAG laser) to excite neutral HfF to the autoionizing Rydberg state. Since the total energy of a 308 nm and a 355 nm photon lies above the ionization threshold for the ionic $^3\Delta_1$ state, this autoionization scheme meant that the HfF^+ ions could be formed in the $^1\Sigma^+(\nu = 0)$, $^1\Sigma^+(\nu = 1)$ and $^3\Delta_1(\nu = 0)$ states, which would dilute the number of ions in any given quantum state and possibly reduce our chances of seeing a photodissociation signal from a particular state. We attempted to circumvent the problem of initial state dilution by searching for a different intermediate state in neutral HfF that could be addressed using 312–320 nm light, so that when combined with the second photon at 355 nm, would only allow the creation of $^1\Sigma^+$ ions. Unfortunately, most of the transitions identified in the target wavelength range originated from the $\nu = 1$ vibrational level of the $X^2\Delta_{3/2}$ state in neutral HfF, which meant that the two-photon Rydberg autoionizing states still lie above multiple ionization thresholds. Thus, we stuck to the autoionization scheme with the 308 nm and 355 nm lasers. In retrospect, and as shown in Section 6.3, having the additional HfF^+ population in three different vibronic states turned out to be a useful feature in understanding photodissociation spectroscopy!

6.2.2 Lasers, lasers and more lasers

As outlined at the start of this chapter, there is a need to search for HfF^+ states in two frequency regions: repulsive/predissociating states above 50000 cm^{-1} and bound states below 40000 cm^{-1}. To avoid performing a two-dimensional search for states, we needed to increase our chances of successfully accessing multiple molecular states by shining as many lasers as possible onto the ions. The lasers we had at our disposal were the following: the fundamental and second harmonic light from the SIRAH Precision Scan tunable dye laser, all four harmonics of the Nd:YAG laser (1064 nm, 532 nm, 355 nm, 266 nm), 308 nm and 769 nm (previously used for LIF). Overlapping 8 laser beams, most of which possess pulse energies of ~ 1 mJ, over such a wide range of wavelengths turned out to be a non-trivial task. Fig. 6.3 shows a layout of the optics used to combine all 8 laser beams using dichroic mirrors, for the particular case where the wavelength range of the Precision Scan dye laser in the fundamental was 547–581 nm (using Pyrromethene 580

dissolved in ethanol as the dye gain medium). Dichroic mirrors (see Table 6.1) instead of beam splitters were preferred in the optical setup so as to minimize loss of laser pulse energy. Since the laser beams are propagating collinearly through the vacuum chamber, the successful attainment of a LIF signal meant that the lasers are overlapped with the trapped ions.

Since the Nd:YAG laser used to generate 355 nm light and pulse-amplify 308 nm light for photoionization was also used to pump the tunable pulsed dye laser, the lasers used for photoionization and photodissociation fired at the same time. Care had to be taken to match the lasers' path lengths so that the laser beams are temporally overlapped when they traverse the ion cloud. The presence of the photodissociation lasers at the time of photoionization, however, is unwelcome: two-photon ionization from 266 nm, for instance, could dominate the ionization process so much that the HfF^+ ions could be formed with initial population spread across an even larger number of vibronic states. Shutters were therefore used to gate out any laser other than the 308 nm and 355 nm lasers during photoionization. Given the 10 Hz repetition rate of the Nd:YAG laser, the photodissociation is then carried out only after the ions have been trapped for 100 ms.

Table 6.1: Specifications of dichroic and broadband mirrors used to overlap laser beams of different wavelengths for photodissociation.

Optic	Reflected λ (nm)	Transmitted λ (nm)	Damage Threshold
MPQ-245-390	245–390		0.92 J/cm^2, 10 ns at 532 nm
LWP-45-Rp-266-Tp-308	258–274	>308	10 J/cm^2, 20 ns, 20 Hz
LWP-45-Rp-300-Tp-355	291–309	>355	10 J/cm^2, 20 ns, 20 Hz
LWP-45-Rp-355-Tp-515	345–365	>515	10 J/cm^2, 20 ns, 20 Hz
LWP-45-Rp-532-Tp-607	516–548	>607	10 J/cm^2, 20 ns, 20 Hz
SWP-45-Rp-780-Tp-633	757-803	600–685	10 J/cm^2, 20 ns, 20 Hz
BBDS	350–1100		1 J/cm^2 at 355 nm
BSR31	355	532/1064	4 J/cm^2, 20 ns, 20 Hz
BSR15	1064	532	10 J/cm^2, 20 ns, 20 Hz
DMLP567	380–550, 532, 1064	584–700	2 J/cm^2
DMLP900	400–872	932–1300	1.21 J/cm^2 at 532 nm

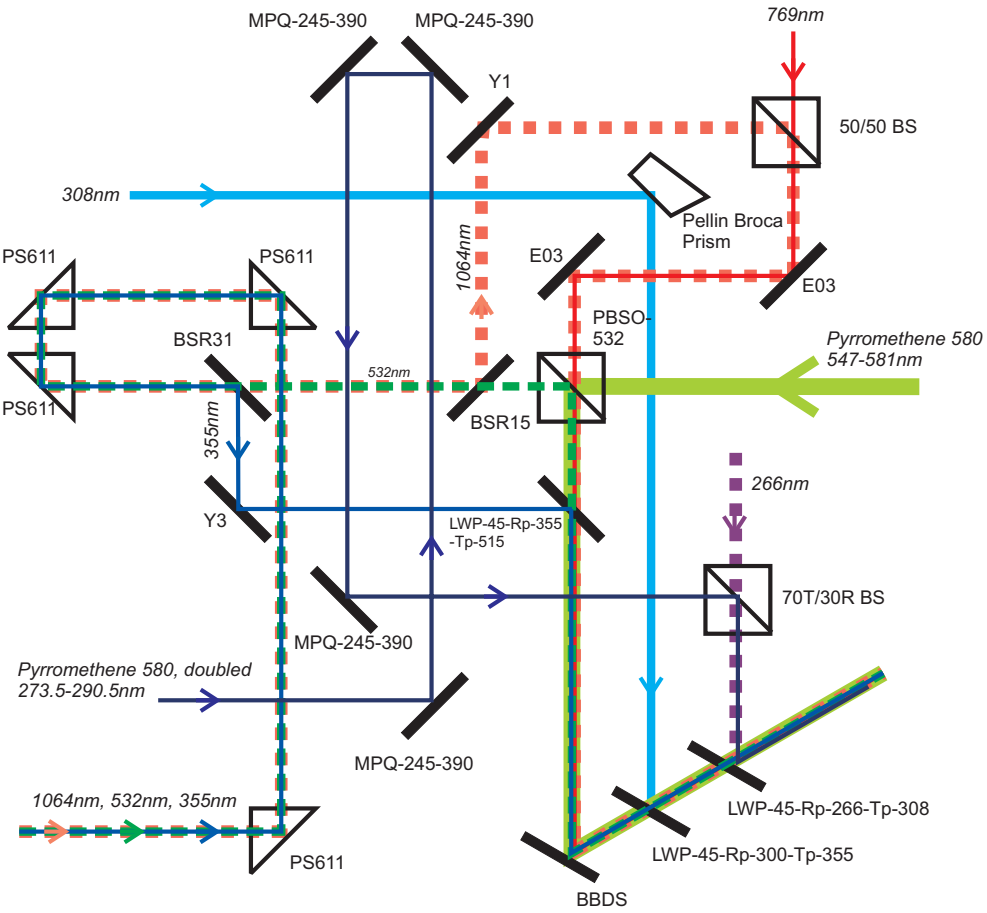

Figure 6.3: Layout of optics used to overlap 8 laser beams (wavelengths in italics) in a search for photodissociation transitions. Table 6.1 gives a list of specifications for most of the optics shown.

6.2.3 Hf^+ detection

For photodissociation to occur, the combination of laser frequencies needs to be higher than the bond dissociation energy. On the other hand, if too high a dissociation potential is accessed, the dissociation products (notably Hf^+) can fly away with a kinetic energy so large and in such a near-isotropic manner, that the detection efficiency on a MCP located along a given direction is diminished. The MCP detection can be improved by using the trap electrodes to give the ions a big velocity 'kick' $v_{kick,x}$ towards the MCP — big enough to overwhelm the velocity v_{PD} inherited from photodissociation. The angle subtended by the two velocities should be smaller than the angle subtended by the MCP (9 mm radius of active area, 11.6 cm from the ion trap center) (see Fig. 6.4a):

$$\frac{v_{PD,y}}{v_{kick,x}} \leq \frac{0.9}{11.6} = 0.08\,, \tag{6.4}$$

$$\text{where} \quad \frac{1}{2}m_{\mathrm{Hf}}\left(v_{PD,x}^2 + v_{PD,y}^2 + v_{PD,z}^2\right) = \frac{3}{2}m_{\mathrm{Hf}}v_{PD}^2 = \frac{1}{10}\left(U^* - D_{R\to\infty}\right)\,. \tag{6.5}$$

For a 'kick' velocity of 5500 m/s, Eqs. (6.4) and (6.5) predict that we can access dissociation potentials as high as 41000 cm^{-1} above $D_{R\to\infty}$.

A higher 'kick' velocity not only increases the range of energies over which we can detect dissociation potential curves, but also tends to increase the mass resolution between the dissociated Hf^+ ions and the remaining HfF^+ ions, both of which get ejected at the same time. This is because a higher 'kick' velocity maps the HfF^+ ion cloud width onto a narrower distribution in arrival time (see Fig. 6.4b), and the well separated ion peaks provide a good level of discrimination between any dissociated Hf^+ signal ions and the tail of the HfF^+ distribution.

Besides ions from the HfF^+ distribution contaminating the Hf^+ signal, the photodissociation signal to noise ratio can be reduced due to two sources of background: 1. the photodissociation lasers can ionize residual background gases to give ions that show up at all times on the MCP, including the time window corresponding to the Hf^+ signal; 2. the photoionization lasers can off-resonantly ionize Hf to give Hf^+ (henceforth referred to as "aboriginal" Hf^+), which remains trapped for the entire duration until the photodissociation lasers fire. To remove the background ions created by

the photodissociation lasers, we can trap any dissociated Hf^+ ions for a short time before ejecting the ion cloud onto the MCP, thereby separating the dissociation signal in time from the promptly ionized gases. Specifically, the additional post-dissociation trap duration T_{trap} should be chosen so that the energetic Hf^+ ions can be focused onto the MCP over their flight time to the detector T_{det} (Fig. 6.4c). For ions in a trap of secular frequency ω and oscillation amplitude y_0, the focusing condition is expressed as a zero net displacement in the transverse direction $\hat{y}$:

$$\begin{aligned} y + \dot{y}T_{det} &= y_0 \sin(\omega T_{trap}) + \omega y_0 T_{det} \cos(\omega T_{trap}) = 0\,, \\ \tan(\omega T_{trap}) &= -\omega T_{det}\,, \\ T_{trap} &= \frac{1}{\omega}\left(-\tan^{-1}(\omega T_{det}) + \pi\right)\,. \end{aligned} \tag{6.6}$$

While typical trap frequencies lie in the range of (2π)3–6 kHz, the trap frequencies in all three directions are ramped up to the same value of (2π)13 kHz just before photodissociation, so as to squeeze the ion cloud and allow for better spatial overlap with the dissociation laser beams. For $T_{det} = 21$ μs and $\omega = (2\pi)13$ kHz, the post-dissociation trap wait time according to Eq. (6.6) is then $T_{trap} = 0.026$ ms. Since the ions can be ejected from the trap only after an integer number of trap RF cycles to avoid imaging the RF micromotion velocity, T_{trap} is chosen to be a multiple of the refocusing time 0.026 ms and $(2\pi)/\omega_{rf}$, which, in the case of $\omega_{rf} = (2\pi)50$ kHz, ends up giving $T_{trap} = 0.1$ ms.

To reduce the aboriginal Hf^+ ions created by the photoionization lasers (in particular, 355 nm), one can operate the ion trap in a regime that is stable for HfF^+ but unstable for Hf^+ up to the time of dissociation. Alternative to ramping the trap to a different set of $\{a, q\}$ parameters, we can 'kick' the ion cloud twice (along $\hat{x}$) during the trap cycle to 'hide' the promptly created Hf^+ ions under the HfF^+ distribution when the ion cloud is ejected after dissociation (see Fig. 6.5). The first 'kick' sets both HfF^+ and Hf^+ ions sloshing in the trap at frequencies differing by 10% (for $a \ll q$, the trap frequency is approximately proportional to q and therefore inversely proportional to the ion mass). After some time T_{hide}, the two ion species dephase in their slosh motion such that a second 'kick' removes (adds to) the momentum imparted by the first 'kick' for the HfF^+ (Hf^+) ions.

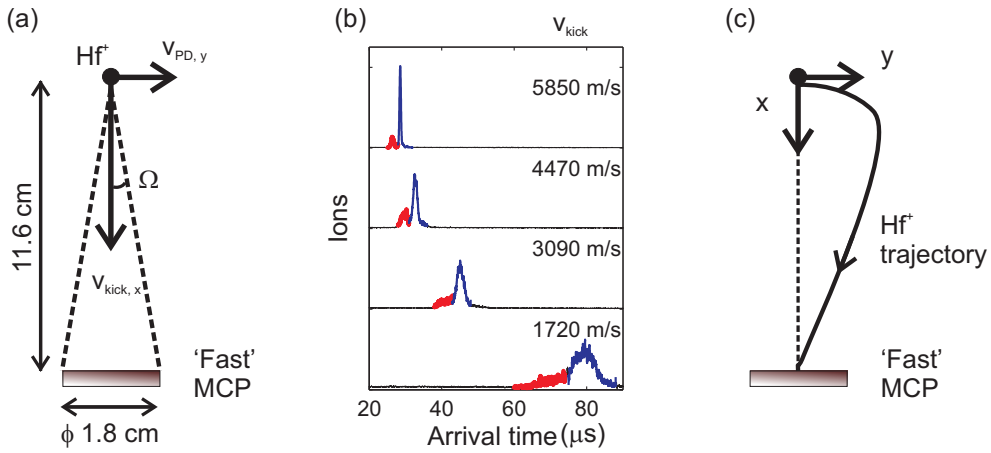

Figure 6.4: (a) To be fully captured by the MCP detector (subtending a solid angle Ω from the ion cloud), the Hf^+ ions need to be ejected towards the MCP with a longitudinal velocity $v_{kick,x}$ that is large compared to their transverse velocity $v_{PD,y}$. (b) Arrival time of Hf^+ (red) and HfF^+ (blue) ions on the 'fast' MCP: the faster the ejection velocity v_{kick}, the shorter the arrival time and the better resolved the two ion species. This data is taken by simulating the presence of Hf^+ and HfF^+ ions in the trap by ionizing both neutral Hf atoms and HfF molecules. (c) Trajectory of the Hf^+ ion cloud when ejected from the trap after a refocusing time T_{trap}, so that the Hf^+ ions are focused onto the MCP.

The HfF^+ ion cloud subsequently becomes stationary while the Hf^+ ions' center-of-mass sloshes with an even greater amplitude, until the trapped ions are ejected at T_{trap} after photodissociation, at which time the Hf^+ ions should be initially moving along $-\hat{x}$ and eventually catch up with the arrival of HfF^+ on the MCP. Using the double 'kick' method, we reduced the background Hf^+ ions by a factor of 4. Nevertheless, the application of the double 'kicks' suffered from reproducibility issues due to interference on the ion trap voltages from nearby laser shutters, so we eventually discarded the procedure and lived with the small amount of aboriginal Hf^+ background.

6.3 Photodissociation spectroscopy of HfF^+

6.3.1 An initial disappointment

When we first begun to look for photodissociation lines, the 10 mJ 266 nm laser immediately started photoionizing the background gas to give 2–5 'Hf^+' ions per shot. The photodissociation signal-to-noise ratio would have been only 0.1 if our initial photodissociation efficiency was 1%. Thus, we temporarily removed the 266 nm laser from the photodissociation sequence and scanned through the wavelength range afforded by using Pyridine 2 in the tunable pulsed dye laser (691–751 nm in the fundamental). This dye, in combination with the other fixed wavelength lasers, would allow us to access a sum frequency range of 49000–58000 cm^{-1} if using a two-photon transition and 67000–77000 cm^{-1} with a three-photon transition. This scan yielded no photodissociation signal, which was somewhat discouraging.

Given that the HfF^+ bond dissociation energy was ≈ 52000 cm^{-1}, we would have been hoping to hit either a predissociating state below 60000 cm^{-1} with two on-resonant photons or a predissociating/repulsive state above 60000 cm^{-1} with three on-resonant photons. Both situations required us to be at least 'doubly lucky'. On the other hand, if we were able to employ the 266 nm laser, we could access states above 60000 cm^{-1} with two photons, and if the predissociating/repulsive state there was broad enough, we could potentially access it even if one of the two photons was at a fixed wavelength! It was therefore necessary to solve the problem of background ionization by 266 nm,

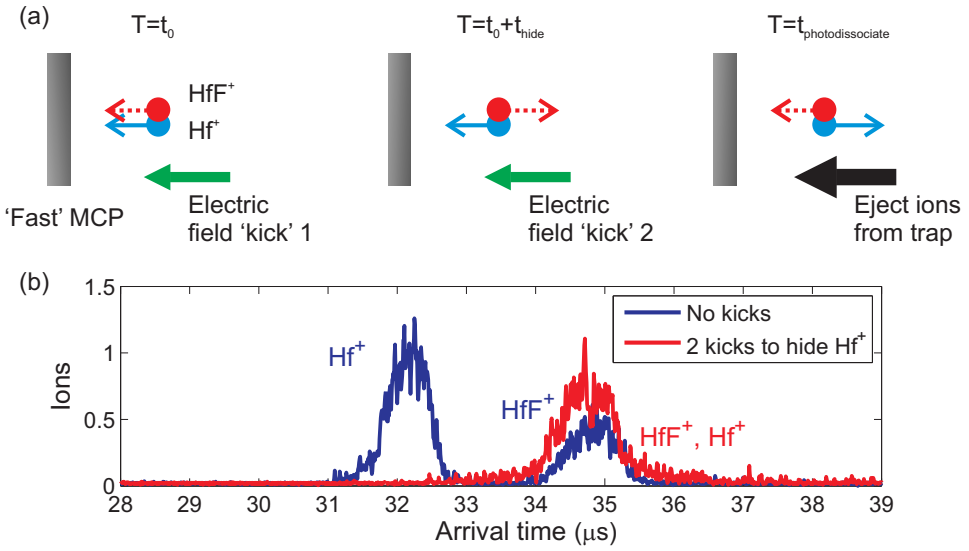

Figure 6.5: Hiding aboriginal Hf^+ ions. (a) A pair of velocity 'kicks' is applied to the ions at times t_0 and $t_0 + t_{hide}$, which are chosen such that the Hf^+ and HfF^+ ions are moving in phase and out of phase relative to each other, respectively. In this way, the HfF^+ ions remain stationary whereas the Hf^+ ions oscillate with an even larger velocity after the second 'kick'. When the photodissociation lasers fire, the Hf^+ ions should be moving away from the detector, so that they eventually arrive the MCP at the same time as the heavier HfF^+ ions. (b) Two oscilloscope traces depicting the arrival of Hf^+ and HfF^+ with (red) and without (blue) the pair of 'kicks'. Without the 'kicks', the bump at earlier (later) time indicates the arrival of Hf^+ (HfF^+). With the 'kicks', both ion species arrive at the same time. This data is recorded with the Hf^+ and HfF^+ ions created by ionizing both neutral Hf atoms and HfF molecules.

so that we could include the 266 nm laser without hurting our signal to noise ratio.

Ions produced by the 266 nm laser turned out to obey the following characteristics: 1. they were produced regardless of whether HfF neutral molecules were being created in the source chamber; 2. they could be trapped for several hundred milliseconds; 3. when ejected onto the 'fast' MCP, their arrival time was 30 times broader than the arrival time window of the Hf^+ ions, corresponding either to a wide range of masses or a very diffuse cloud of trapped ions. Based on these observations, we concluded that the ions came from background gases introduced into the vacuum chamber during the trap assembly (also affectionately termed "isogreasanol"), and could be decreased by baking the vacuum chamber. Indeed, after baking the ion trap setup to 200° over two days, the background ionized gas decreased by an order of magnitude, and we were poised to retackle photodissociation.

6.3.2 HfF^+ lines galore!

To increase the chances of accessing high-lying dissociative states with two on-resonant photons, we changed the gain medium for the tunable pulsed dye laser to Pyrromethene 580 (fundamental wavelength range 547–581 nm). This allowed us to access frequencies as high as 69000-74000 cm^{-1} with either two tunable 34500–37000 cm^{-1} photons (for 1+1 REMPD) or a tunable 31400–36400 cm^{-1} photon and a fixed 37600 cm^{-1} (266 nm) photon (for 1+1' REMPD). To our pleasant surprise, we found several HfF^+ transitions in the frequency range 32500–36500 cm^{-1}, made by a UV photon from the frequency-doubled output of the tunable dye laser. The fact that we can detect the HfF^+ transitions by counting Hf^+ indicates that we are hitting at least one dissociating state. The dissociating state(s) could be accessed by either the fixed 266 nm or a second tunable (> 32900 cm^{-1}) photon, which means that the state lies above 70500 cm^{-1}.

Fig. 6.6 shows a summary of the HfF^+ transitions found in the vicinity of 35000 cm^{-1}, scanned using both Pyrromethene 580 and Pyrromethene 597 as the gain medium of the tunable dye laser. The gap in the spectrum is due to Wood's anomaly, which is a grating configuration that causes the dye laser to stop lasing in that wavelength region for a 1800 lines/mm grating.

Since many of the transitions at 35000 cm^{-1} come from two 32900–36500 cm^{-1} photons accessing a dissociating state, the intensities of transitions shown in Fig. 6.6 reflect a convolution of both the photodissociation resonance (which is almost surely not saturated by the second photon) and the variation in gain of the tunable dye laser; in particular, the pulse energy is diminished in the vicinity of the Wood's anomaly. The assignment of vibronic bands is aided by the initial population of HfF^+ ions in three different vibronic states: using the known spacing between the three initial vibronic states [16], we can identify transitions between the same upper state at > 30000 cm^{-1} and one of the three lower vibronic states, as indicated by the line markers in Fig. 6.6. Some of the isolated transitions that remain unidentified may come from upper states that have allowed transitions only to either the $^1\Sigma^+$ or $^3\Delta_1$ state, but not both.

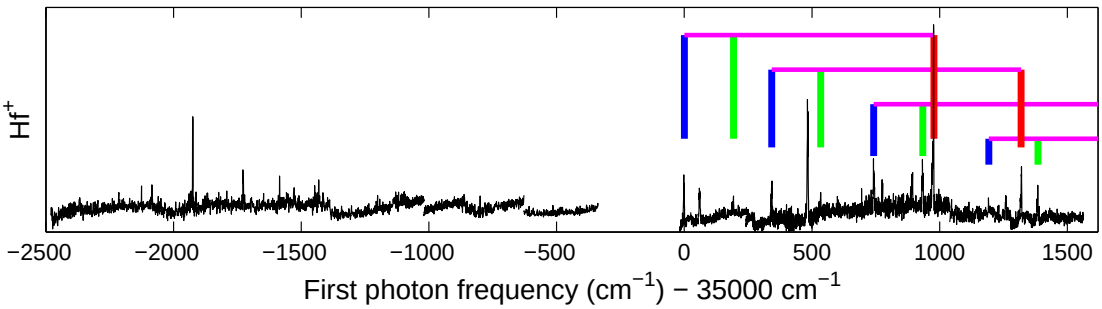

Figure 6.6: REMPD spectroscopy of HfF^+ transitions at 32500–36500 cm^{-1}, detected by photodissociating HfF^+ into Hf^+ and F. The gap in the spectrum is due to Wood's anomaly of the laser grating that causes a loss in laser intensity. Transitions that have been identified as originating from the $^1\Sigma^+(\nu'' = 0)$,$^1\Sigma^+(\nu'' = 1)$ and $^3\Delta_1(\nu'' = 0)$ lower states to excited states at > 30000 cm^{-1} are denoted by red, green and blue vertical lines, respectively. Vertical lines connected by a horizontal magenta line belong to transitions terminating on the same upper vibronic state.

To identify the individual rotational lines of a given vibronic band, we tried to reduce the pulse energy of the first photon (provided by the tunable dye laser) to avoid power broadening the rotational lines. However, since the tunable dye laser was sometimes also responsible for providing the second photon in photodissociation, a lower dye laser pulse energy also reduced the overall photodissociation signal, making it more difficult to discern different rotational lines. Instead of lowering the dye laser pulse energy, a narrowband continuous wave laser at 13002 cm^{-1} tuned to

resonance of one of the rotational lines in the $^1\Pi_1 \leftarrow^1 \Sigma^+(0,0)$ transition was used to first optically pump away ions from a given $^1\Sigma^+(\nu''=0, J'')$ lower state before photodissociating the HfF^+ ions. The presence of the continuous wave laser would leave a depletion gap in the vibronic band at ≈ 35000 cm^{-1}, which can in turn be identified as a rotational line of that band. Fig. 6.7 shows the rotational lines identified using such depletion spectroscopy for a vibronic band at 35975 cm^{-1}. The lower state rotational constant was fixed to be the known value for the $^1\Sigma^+(\nu''=0)$ state, i.e. 0.305 cm^{-1} [16]. The upper state rotational constant was then identified to be 0.269 cm^{-1}, and the lack of a Q branch indicated that the upper state has $\Omega'=0$.

6.3.3 Nature of photodissociating state at 72000 cm^{-1}

While having one tunable dye laser allowed us to perform REMPD spectroscopy of HfF^+ intermediate states, a scan of HfF^+ states above the bond dissociation energy could be carried out only with two tunable lasers. Fig. 6.8a shows a spectrum of the dissociating states at 72000 cm^{-1}, measured by tuning the first photon (70 μJ) to resonance with the vibronic band at 35976 cm^{-1} and then scanning the second photon ($\approx$1 mJ). Care was taken to tune the second photon off-resonance from transitions at 36000 cm^{-1} (see Fig. 6.8b) to avoid artificially enhancing the dissociation process arising from the more intense second photon addressing multiple rotational levels. The plotted Hf^+ ions are taken to be the difference between chopping the first photon on versus off, to account for any variations in the background ionization process with the second photon's frequency. To our surprise, there is structure in the dissociation resonance at 72000 cm^{-1}, which can indicate that:

(1) the intermediate state at 36000 cm^{-1} is at a high-lying vibrational level, and is mapped onto the dissociation resonance using the reflection approximation for a purely repulsive curve, or

(2) the dissociating state at 72000 cm^{-1} is a predissociating state whose structure comes from one or more avoided crossings, or

(3) some combination of the above reasons.

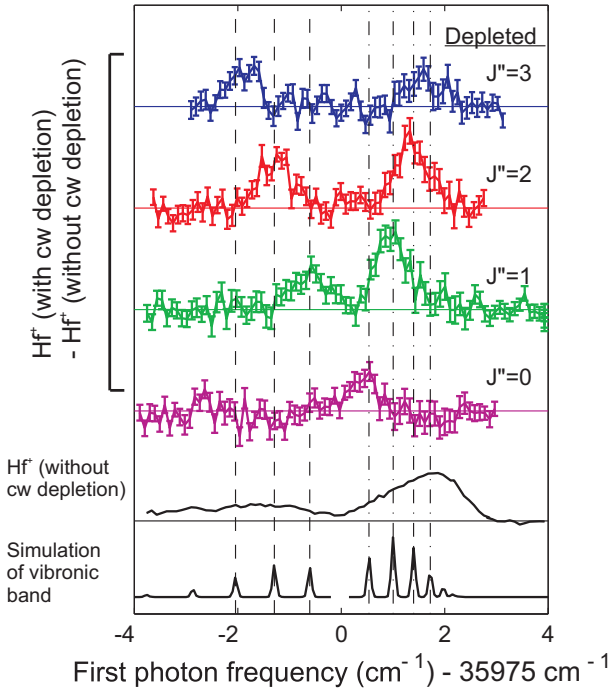

Figure 6.7: Depletion spectroscopy of the $\Omega' = 0 \leftarrow^1 \Sigma^+$ vibronic band at 35975 cm^{-1} (shown as the unresolved, thick black line in the second lowest panel). To resolve the individual rotational lines, the vibronic band is scanned over in the presence of a depletion laser driving a particular rotational transition of the $^1\Pi_1 \leftarrow^1 \Sigma^+$ band, and the difference in Hf^+ with and without the depletion laser is plotted as the colored lines with error bars. The thin black line (bottom panel) denotes the simulated vibronic band with its R branch on the right (dot-dashed vertical lines) and P branch on the left (dashed vertical lines).

To truly understand the nature of the dissociating states, more spectroscopy work — specifically, more scans of the dissociation resonances and a better understanding of the intermediate states at 35000 cm^{-1} — needs to be done. Nevertheless, the goal of preforming photodissociation is not to understand the high-lying states of HfF^+, but to use dissociation as an efficient detection tool for the states involved in the eEDM search. One way to efficiently carry out photodissociation is to look for the dissociation resonance with the largest cross section, which involves a non-trivial two-dimensional search for HfF^+ states with two tunable lasers dedicated for dissociation. The other method is to use the fourth harmonic of a Nd:YAG laser at 266 nm to access the second dissociation transition. In the latter case, even if the dissociation cross section is small, we can maximize the dissociation efficiency by saturating the second transition with higher pulse energy. The latter scheme is much easier to implement than using two tunable lasers, and is hence employed as the method of dissociation for the remainder of this thesis.

6.4 Photodissociation as a readout tool

6.4.1 Saturation of dissociation transition

Fig. 6.9 shows the saturation curve, which is a plot of photodissociation efficiency versus pulse fluence, for the dissociation resonance accessed by saturating the $\Omega' = 0 \leftarrow^1 \Sigma^+$ transition at 35975 cm^{-1} with the first photon and varying the pulse fluence F (i.e. pulse energy for a given beam area) of 266 nm as the second photon. Each point on the saturation curve is taken to be the difference in Hf^+ ions counted with the first photon present versus absent, so as to remove the effects of a more intense 266 nm pulse more efficiently ionizing the background gas. The saturation curves were recorded for two different 266 nm beam waists. For the bigger beam waist ($w_0 = 5.0$ mm), the saturation curve (open circles) is mostly linear. For the smaller beam waist ($w_0 = 3.3$ mm), the Hf^+ counts (open triangles) clearly saturate above 50 mJ/cm^2 but to a smaller value of ion counts, due to laser overlap with a smaller fraction of the ion cloud. Each saturation curve is fit to a single exponential $A(1-\exp(-F/F_S))$, where F_S is the saturation fluence. The single exponential is only

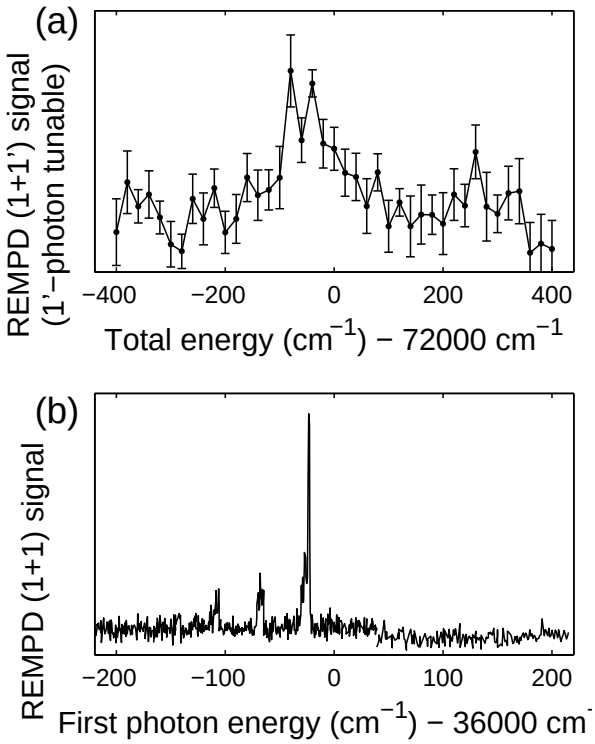

Figure 6.8: (a) Dissociation resonance accessed by two photons of total energy 71600–72400 cm^{-1}, recorded by tuning the first photon to 35976 cm^{-1} and scanning the frequency of the second photon. When scanning the dissociation resonance in (a), care was taken to step cleanly over any one-photon transitions shown in (b). (b) HfF^+ transitions accessed by a single photon of energy 35800–36200 cm^{-1}.

an approximate functional form due to complicating overlap details between the dissociating lasers and the ion cloud. As a sanity check, the linear slopes of the two curves at small pulse fluence differ by a ratio of 2.4, which is comparable to the ratio of the 266 nm beam areas in the two cases. The saturation data indicates that as long as the ion cloud is smaller than the dissociation laser beams, the dissociation transition can be saturated with the 266 nm pulse fluence being > 50 mJ/cm^2.

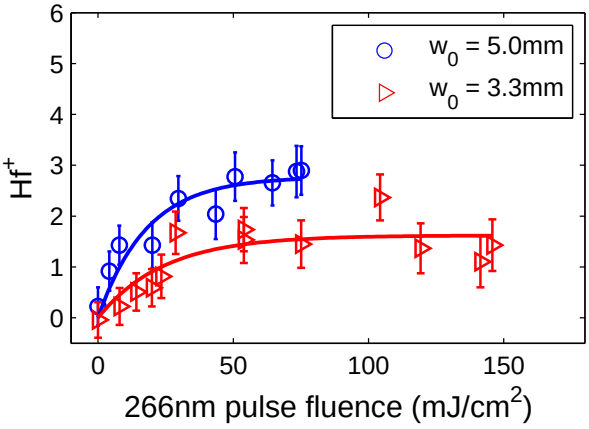

Figure 6.9: Saturation of the 1+1' photodissociation transition with 266 nm laser pulse energy. Two different beam waists were used for the 266 nm laser: (blue circles) $w_0 = 5.0$ mm and (red triangles) $w_0 = 3.3$ mm. The saturation behavior is fit to a single exponential $A(1-\exp(-F/F_S))$. The smaller exponential amplitude for the smaller beam waist is due to a less complete spatial overlap between the 266 nm laser and the ion cloud.

6.4.2 Efficiency of photodissociation

Saturating the dissociation transition does not necessarily guarantee that all the HfF^+ ions in a single rovibronic state will be dissociated. Competition could arise between the photodissociation process and radiative decay of the dissociating state down to a lower state of HfF^+, such that the photodissociation efficiency saturates with laser pulse energy to a value that is $< 100\%$. To understand the maximum achievable photodissociation efficiency for the repulsive curve accessed by the 266 nm laser, we first ensured that both (1+1') REMPD photons are saturating their respective transitions, and that their beam waists are large enough so that spatial overlap with the ion cloud

will not be an issue. We then reverted to creating HfF^+ ions with a well-defined rotational state distribution, i.e. by autoionizing neutral HfF such that 35% of the HfF^+ is formed in the $J = 0$ rotational state of the ground vibronic level (shown in Chapter 3). The total HfF^+ ion number with and without the photodissociation lasers were then recorded, and we made sure that the MCP detector was not saturated to reflect accurate ion numbers. The loss in HfF^+ was 30% that of the HfF^+ ions in a single rovibronic state without dissociation, indicating that the photodissociation efficiency is 30%. On the other hand, the HfF^+ number loss was the same as the Hf^+ ion number detected, indicating that the detection efficiency of dissociated Hf^+ ions is as high as 100%. The overall efficiency of photodissociation as a state readout technique is therefore 30%, which is likely to be limited by competition with other processes like spontaneous emission. The photodissociation efficiency of 30%, nevertheless, is two orders of magnitude higher than that of LIF!

Chapter 7

Stimulated Raman transfer into $^3\Delta_1$

The statistical sensitivity of an eEDM measurement is proportional to the square root of the number of ions making the eEDM transition. An improvement to the statistical sensitivity can come from a higher state detection efficiency, as offered by photodissociation over LIF, or from a larger initial population of ions in a particular $|J, m_J, \Omega\rangle$ level of the $^3\Delta_1(\nu = 0)$ state. In Chapter 3, we have shown that as many as 30% of the autoionized HfF^+ can be populated in a given $|J, m_J\rangle$ level of the ground $^1\Sigma^+(\nu'' = 0)$ state using optical-optical double-resonance autoionization. The autoionization technique can in principle be extended to form $^3\Delta_1(\nu = 0)$ ions. One such example was the use of 308 nm + 355 nm as ionization lasers in the photodissociation experiments. The Rydberg states accessed by the ionization lasers, however, underwent either vibrational autoionization to form $^3\Delta_1$ ions or electronic autoionization to form $^1\Sigma^+$ ions (i.e. the ion core of the Rydberg state was in a different electronic state from the final ion formed). Electronic autoionization is undesirable because it dilutes the ion population amongst multiple vibronic states. It is plausible to embark on a search for a Rydberg state that only vibrationally autoionizes into the $^3\Delta_1(\nu = 0)$ state, yet this effort requires a clean understanding of the molecular orbital composition of both the Rydberg states and the neutral HfF intermediate states at $\approx$30000 cm^{-1} — a rather daunting task for a molecule of which very little is known in general! Even in the best case scenario where only vibrational autoionization is present, several rotational-hyperfine states of the $^3\Delta_1$ will still be populated besides the desired $|J = 1, F = 3/2\rangle$ state. Additional lasers will then be needed to clean out population in the unwanted states.

An alternative to autoionizing directly into $^3\Delta_1$ is the stimulated Raman population transfer of ions from $^1\Sigma^+$ to the $^3\Delta_1$ state. The excited state $^3\Pi_{0+}(\nu' = 1)$ at 11115 cm^{-1} has been shown to have a strong electronic dipole moment and Franck-Condon overlap to both the $^1\Sigma^+$ and $^3\Delta_1$ states [16, 63]. The three levels form a Λ-type system (Fig. 7.1), of which the two lower levels $|1\rangle$ and $|3\rangle$ couple to $|2\rangle$ via lasers of Rabi frequencies Ω_1 and Ω_3 respectively, but not directly to each other. Ions can therefore be autoionized first into the $^1\Sigma^+$ state with a significant fraction in a given $|J, m_J\rangle$ level, and then transferred via a Raman process to the $^3\Delta_1$ state. The stimulated Raman transfer process can be adequately described using three-level physics — a coherent process with potentially a huge efficiency for quantum sate manipulation! The physics and results of stimulated Raman transfer are described in this chapter.

7.1 Basics of stimulated Raman transfer

In the rotating wave approximation, the Hamiltonian for the three-level system as illustrated in Fig. 7.1 is described by the following matrix in the basis of states $|1\rangle, |2\rangle$ and $|3\rangle$:

$$H = \frac{1}{2}\begin{pmatrix} 0 & \Omega_1 & 0 \\ \Omega_3 & 2\Delta - i\gamma & \Omega_3 \\ 0 & \Omega_1 & 2\delta \end{pmatrix}, \tag{7.1}$$

where Δ is the one-photon detuning from the excited state, δ is the two-photon detuning, and Ω_1, Ω_3 are the Rabi frequencies of the lasers coupling $|2\rangle \leftarrow |1\rangle$ and $|2\rangle \rightarrow |2\rangle$, respectively. Eq. (7.1) assumes that the ions that have decayed out of $|2\rangle$ (at a rate γ) completely leave the three-level system. For the $^3\Pi_{0+}(\nu' = 1, J' = 1)$ state, the probability of decaying back to either the $^1\Sigma^+(\nu'' = 0, J'' = 0)$ state or the $^3\Delta_1(\nu = 0, J = 1)$ state is less than 10% each. So, the Hamiltonian given by Eq. (7.1) remains an adequate description. Had it been otherwise, the master equation approach should be used instead of modeling the decay as an imaginary term in the Hamiltonian.

If the two-photon resonance condition is fulfilled ($\delta = 0$), an eigenstate of the Hamiltonian is

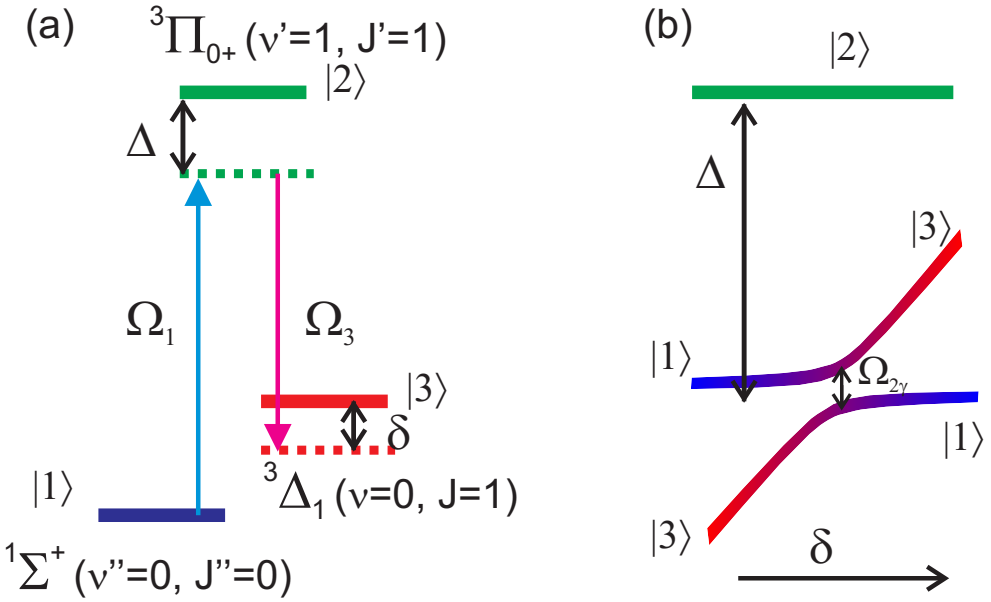

Figure 7.1: (a) 'Bare' states used in the stimulated Raman transfer of population from $|1\rangle$ to $|3\rangle$ via adiabatic elimination of $|2\rangle$. The bare states are addressed by lasers of Rabi frequencies Ω_1 and Ω_3 and of detunings Δ and δ from the one-photon and two-photon transitions, respectively. (b) Three-level system shown as "dressed" states; where the two-photon detuning δ is zero, the dressed states are symmetric and antisymmetric superpositions of the bare states $|1\rangle$ and $|3\rangle$. The point of closest separation in the avoided crossing is given by the two-photon Rabi frequency $\Omega_{2\gamma}$. Individual ions are transferred from $|1\rangle$ to $|3\rangle$ as their velocities (and hence Doppler shifts) sweep through zero with their secular motion in half a trap cycle.

the dark state $|\psi_d\rangle$, which does not couple to the decaying excited state $|2\rangle$:

$$|\psi_d\rangle = \frac{1}{\sqrt{\Omega_1^2 + \Omega_3^2}} \left(\Omega_3 |1\rangle - \Omega_1 |3\rangle\right) . \tag{7.2}$$

Coupling to the dark state is one way of enabling population transfer from $|1\rangle$ to $|3\rangle$ without loss, by first turning on the laser coupling Ω_3 and then ramping on Ω_1 while Ω_3 is adiabatically turned off. This technique has been very successful for the coherent population transfer of Feshbach molecules to their ground state [60]. However, $|\psi_d\rangle$ is no longer an eigenstate once $\delta \neq 0$, as is the case for the eEDM experiment with trapped ions possessing two-photon Doppler widths of 3 MHz.

Instead of coupling to $|\psi_d\rangle$, the population transfer with HfF^+ ions can be carried out using adiabatic elimination. Namely, the two transfer lasers are far-detuned from resonance to $|2\rangle$, such that the off-resonant scattering rate from $|2\rangle$ is slow compared to the time it takes to perform the transfer:

$$\begin{aligned} \gamma_{sc}(\Delta) &= \frac{\gamma}{2} \frac{I/I_0}{1 + I/I_0 + (2\Delta/\gamma)^2} \\ &\approx \frac{\gamma}{2} \frac{I}{I_0} \left(\frac{\gamma}{2\Delta}\right)^2 \text{ for large } \Delta . \end{aligned} \tag{7.3}$$

Applying the Schrödinger equiation to the Hamiltonian from Eq. (7.1) and with the state expressed as $|\psi\rangle = c_1 |1\rangle + c_2 |2\rangle + c_3 |3\rangle$, we obtain:

$$i\dot{c_1} = \frac{\Omega_1}{2} c_2 , \tag{7.4a}$$

$$i\dot{c_2} = \frac{\Omega_1}{2} c_1 + (\Delta - i\frac{\gamma}{2}) c_2 + \frac{\Omega_3}{2} c_3 . \tag{7.4b}$$

$$i\dot{c_3} = \frac{\Omega_3}{2} c_2 + \delta c_3 . \tag{7.4c}$$

With adiabatic elimination, the population in $|2\rangle$ is unchanged over time, i.e. $\dot{c_2} = 0$. The population dynamics in the states $|1\rangle$ and $|3\rangle$ can then be described as $i|\dot{\psi'}\rangle = H_{2\gamma} |\psi'\rangle$, where $|\psi'\rangle = c_1 |1\rangle + c_3 |3\rangle$, and

$$H_{2\gamma} \approx \frac{1}{2} \begin{pmatrix} \frac{\Omega_1^2}{2\Delta} & \Omega_{2\gamma} \\ \Omega_{2\gamma} & \frac{\Omega_3^2}{2\Delta} + 2\delta \end{pmatrix} , \tag{7.5}$$

$$\text{where } \Omega_{2\gamma} = \frac{\Omega_1 \Omega_3}{2\Delta} . \tag{7.6}$$

The two-photon effective Hamiltonian $H_{2\gamma}$ is the same as that for a two-level system with Rabi frequency $\Omega_{2\gamma}$ connecting the two states $|1\rangle$ and $|3\rangle$. Fig. 7.1b shows the dressed state picture for the three-level system with adiabatic elimination, where $|1\rangle$ and $|3\rangle$ are connected by an avoided crossing and the frequency separation between the two crossings at the point of closest approach is given by $\Omega_{2\gamma}$. The two-photon detuning plotted on the horizontal axis needs to be swept (over time T_{sweep}) slowly compared to $(\Omega_{2\gamma}/2)^2$ to fulfill the adiabatic condition for efficient population transfer from $|1\rangle$ to $|3\rangle$. More generally, the probability of adiabatically following the dressed eigenstate is given by the Landau-Zener formula:

$$P_{LZ}\left(|1\rangle \rightarrow |3\rangle\right) = 1 - \exp\left(-2\pi \frac{(\Omega_{2\gamma}/2)^2}{2\delta/T_{sweep}}\right) . \tag{7.7}$$

In the JILA eEDM experiment, the ions at 20 K experience one-photon Doppler shifts of $\pm(2\pi)30$ MHz. At some point during a half-trap cycle, each individual ion moves from positive to negative velocities (or vice versa) and sweeps through the two-photon detuning of $\pm(2\pi)3$ MHz in doing so. (The two-photon detuning of the Λ-system is about one-tenth that of the one-photon Doppler shift because the difference in frequency between the two transitions is one-tenth of any one of the transition frequencies.) Therefore, the stimulated Raman transfer is simply performed by leaving both co-propagating transfer lasers on simultaneously for a half-trap cycle ($T_{sweep} = \pi/\omega_{trap}$). As long as $\Omega_{2\gamma}$ is large enough to fulfill the adiabatic condition, the Raman transfer will be efficient (>50%). However, where $\Omega_{2\gamma}$ is small, the transfer lasers will have to be left on for multiple half-trap cycles. In subsequent half-trap cycles, the population transfer is no longer fully coherent, i.e. ions can also be transferred back from $|3\rangle$ to $|1\rangle$, so that over time the population equilibrates to 50% in either $|1\rangle$ or $|3\rangle$. All this assumes that the population in $|2\rangle$ is small due to the adiabaticity of the transfer process.

7.2 Estimation of Raman transfer parameters

7.2.1 Strategy

Eq. (7.7) describes the Raman transfer efficiency that can be accomplished for a given set of Rabi frequencies, one-photon detuning, two-photon detuning and sweep time. Several of these crucial parameters were not yet experimentally established before we started building the Raman transfer experiment, namely: the lifetime of the $^3\Pi_{0+}$ excited state, which sets an upper limit on T_{sweep}, and the Rabi frequencies for both transitions $\{\Omega_1, \Omega_3\}$. The Rabi frequency Ω_i is related to laser intensity I_i by the following:

$$I_i = \frac{1}{2}\epsilon_0 c {E_i}^2 = \frac{1}{2}\epsilon_0 c \left(\frac{\hbar\Omega_i}{\langle 2 |\mathbf{d}| i\rangle} \right)^2, \tag{7.8}$$

where $\langle 2 |\mathbf{d}| i\rangle$ is the rovibronic transition dipole matrix element between $|2\rangle$ and $|i\rangle = |1\rangle, |3\rangle$. In the limit of infinite laser intensity or negligible Doppler shift, the Raman transfer efficiency can be as high as 100%. However, as mentioned at the end of Section 7.1, the two-photon Doppler shift is $\pm(2\pi)3$ MHz. Additionally, since the laser power is finite and the ions are spread across a 3 mm 2σ-radius cloud, the Raman transfer laser intensity is limited. It is therefore important to first estimate the $^3\Pi_{0+}$ lifetime and the Rabi frequencies that can be achieved with reasonable laser intensities. The main unknowns related to the lifetime and Rabi frequencies are the rovibronic transition dipole matrix elements $\langle 2 |\mathbf{d}| i\rangle$. Specifically, the electronic components of these transition dipole matrix elements $\left\langle {}^3\Pi_{0+} |\mathbf{d}| {}^1\Sigma^+ \right\rangle$ and $\left\langle {}^3\Pi_{0+} |\mathbf{d}| {}^3\Delta_1 \right\rangle$ require more work to be determined, since the vibrational and rotational dipole matrix elements can be easily calculated from the vibrational wavefunction overlap and Clebsch-Gordan coefficients.

Unfortunately, of the HfF^+ data available to us, none are directly related to the transition dipole matrix elements we need to calculate:

(1) Transitions to the $^3\Pi_{0+}$ state have been identified spectroscopically by performing velocity modulation spectroscopy in a discharge tube at ≈850 K, but the density of populations is not normalized, making an absolute measurement of the transition dipole matrix elements

impossible. On the other hand, it is plausible to extract the relative ratio of the relevant transition dipole matrix elements from the spectroscopic intensities.

(2) Petrov et. al. had directly calculated $\left\langle {}^3\Pi_{0+} \left| \mathbf{d} \right| {}^1\Sigma^+ \right\rangle$ and $\left\langle {}^3\Pi_{0+} \left| \mathbf{d} \right| {}^3\Delta_1 \right\rangle$ from ab-initio theory [63], but given the large uncertainty in the other ab-initio results (e.g. transition frequencies), we would prefer to extract the *absolute* transition dipole matrix elements from experiment. Nevertheless, it is interesting to note that the ratio of $\left\langle {}^3\Pi_{0+} \left| \mathbf{d} \right| {}^1\Sigma^+ \right\rangle$ to $\left\langle {}^3\Pi_{0+} \left| \mathbf{d} \right| {}^3\Delta_1 \right\rangle$ reported in [63] falls within 30% of that extrapolated from the velocity modulation spectroscopy data, so we also use the theoretical ratio of dipole matrix elements to guide our estimations.

(3) LIF experiments of HfF^+ ions have yielded both the lifetime of the excited state and saturation fluence of the LIF transition, but the LIF transition is that between ${}^1\Sigma^+$ and ${}^1\Pi_1$. The lifetime and saturation fluence measurements provide independent ways to estimate $\left\langle {}^1\Pi_1 \left| \mathbf{d} \right| {}^1\Sigma^+ \right\rangle$, but neither of the two methods yield a transition dipole matrix element connecting to the ${}^3\Pi_{0+}$ state.

Given the above data and constraints, the strategy to estimate $\left\langle {}^3\Pi_{0+} \left| \mathbf{d} \right| {}^1\Sigma^+ \right\rangle$ and $\left\langle {}^3\Pi_{0+} \left| \mathbf{d} \right| {}^3\Delta_1 \right\rangle$ is as follows: we first calculate $\left\langle {}^1\Pi_1 \left| \mathbf{d} \right| {}^1\Sigma^+ \right\rangle$ in two ways using the two LIF measurements of lifetime and of saturation fluence; the extent to which the two extracted dipole matrix elements agree with each other gives us some measure of faith in the accuracy of our LIF measurements. We then relate $\left\langle {}^1\Pi_1 \left| \mathbf{d} \right| {}^1\Sigma^+ \right\rangle$ to $\left\langle {}^3\Pi_{0+} \left| \mathbf{d} \right| \psi_{el,i} \right\rangle$ using the ratios of dipole matrix elements available from both the velocity modulation spectroscopy data and Petrov et. al.ś calculations. Finally, we account for vibrational and rotational wavefunction overlaps to obtain the total rovibronic transition dipole matrix elements $\langle 2 \left| \mathbf{d} \right| i \rangle$, with which we estimate the ${}^3\Pi_{0+}$ state lifetime and Raman transfer Rabi frequencies.

7.2.2 Estimation of $\langle {}^1\Pi_1 |\mathbf{d}| {}^1\Sigma^+\rangle$ from an LIF measurement of the $^1\Pi_1$ lifetime

We first present one of two ways to estimate the transition dipole matrix element $\langle {}^1\Pi_1 |\mathbf{d}| {}^1\Sigma^+\rangle$, i.e. from an LIF measurement of the $^1\Pi_1$ decay lifetime. The $^1\Pi_1$ is most likely to decay to either $^1\Sigma^+$ or $^3\Delta_2$, as indicated by the electronic transition dipole matrix elements given in Table 7.1 [64, 63]. The observed decay rate is then the sum of decay rates to the individual lower electronic and vibrational states:

$$\frac{1}{\tau({}^1\Pi_1, \nu'=0)} \approx \sum_{\nu''} \frac{1}{\tau({}^1\Pi_1, \nu'=0 \rightarrow {}^1\Sigma^+, \nu'')} + \frac{1}{\tau({}^1\Pi_1, \nu'=0 \rightarrow {}^3\Delta_2, \nu'')}\,, \tag{7.9}$$

$$\text{where} \quad \frac{1}{\tau({}^1\Pi_1, \nu'=0 \rightarrow \psi_{el,i}, \nu'')} = \frac{2e^2}{3\epsilon_0 hc^3}\omega^3 \left|\langle \nu'=0|\nu''\rangle \langle {}^1\Pi_1 |\mathbf{r}| \psi_{el,i}\rangle\right|^2 . \tag{7.10}$$

In Eq. (7.10), ω refers to the radial frequency difference between the $^1\Pi_1(\nu'=0)$ and $\psi_{el,i}(\nu'')$ levels (see Table 7.2 for a table of electronic energies and [4] for a list of vibrational energies). Due to diminishing Franck-Condon factors, only the first four vibrational levels of the lower electronic state are summed over in Eq. (7.9).

To measure the lifetime of the $^1\Pi_1(\nu'=0)$ state, the decay of fluorescence photons was measured on a photomultiplier tube as a function of delay time after firing the LIF laser. Fig. 7.2 shows the measured lifetime of the $^1\Pi_1(\nu'=0)$ state to be 1.15(4) μs. The measured lifetime is close to the predicted lifetime of 0.86 μs calculated from the transition dipole matrix elements $\langle {}^1\Pi_1 |\mathbf{d}| \psi_{el,i}\rangle$ in Table 7.1. If the relative values of the transition dipole matrix elements are to be trusted, the dipole matrix elements only need to be scaled by an overall factor of 0.87 to match the measured lifetime, which gives $\langle {}^1\Pi_1 |\mathbf{d}| {}^1\Sigma^+\rangle = 0.48\ e\ a_0$.

Table 7.1: Calculated transition dipole matrix elements (in ea_0) between states of HfF^+ given by the corresponding row header and column header [64]. If denoted by an asterisk, that value is obtained from Reference [63].

	$^1\Sigma^+$	$^3\Delta_1$	$^3\Delta_2$	$^3\Delta_3$	$^1\Delta_2$	$^3\Pi_{0+}$	$^3\Pi_1$	$^3\Pi_2$
$^1\Pi_1$	0.55	0.03	0.18	0*	0.021*	0.002*	0.135*	-0.006*
$^3\Pi_{0+}$	0.15	0.27	0*	0*	0*			

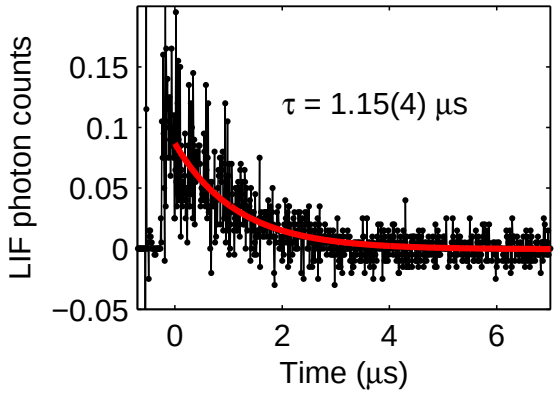

Figure 7.2: Lifetime of the $^1\Pi_1(\nu' = 0)$ state measured using LIF.

Table 7.2: Measured and calculated electronic energies (in cm^{-1}) of ground and excited states in HfF^+. By default, the reported values are measured by Cossel et. al. [16]. If denoted by a dagger sign, the reported value was measured by Barker et. al. [4]. If denoted by an asterisk, that value was calculated by Petrov et. al. [63].

$^1\Sigma^+$	$^3\Delta_1$	$^3\Delta_2$	$^3\Delta_3$	$^1\Delta_2$	$^3\Pi_{0+}$	$^3\Pi_1$	$^1\Pi_1$	$^3\Phi_2$
0	977	$2166^\dagger$	$3951^\dagger$	11519^*	10402	10895	13002	13933

7.2.3 Estimation of $\left\langle {}^1\Pi_1 \left| \mathbf{d} \right| {}^1\Sigma^+ \right\rangle$ from LIF measurements of the saturation fluence

The dipole matrix element $\left\langle {}^1\Pi_1 \left| \mathbf{d} \right| {}^1\Sigma^+ \right\rangle$ can also be estimated from measurements of the LIF saturation fluence, $\mathcal{F} = h\nu/\sigma$, where ν is the transition frequency and σ is related to the integrated cross section $\sigma_0 = \int \sigma(\omega) d\omega$:

$$\sigma_0 = \frac{\pi\omega}{3g_1\epsilon_0\hbar c} \left| \left\langle \nu' = 0 | \nu'' = 0 \right\rangle \left\langle {}^1\Pi_1 \left| \mathbf{d} \right| {}^1\Sigma^+ \right\rangle \right|^2 S_{J',J''}{}^2 \,, \tag{7.11}$$

where g_1 is the degeneracy of the lower state and $S_{J',J''}{}^2$ is the rotational line intensity given by the Hönl-London factor. (Note that among the different rotational lines that can be probed, the $R(0)$ line gives $g_1/S_{J',J''}{}^2 = 1$ whereas the $Q(n)$ lines give $g_1/S_{J',J''}{}^2 = 2$, which is consistent with our observation that the saturation fluence for the $R(0)$ line is half that of the $Q(1)$ or $Q(2)$ line.)

To obtain σ_0 from σ, we assume the ions are Doppler-broadened with a Doppler width of $\nu^\sigma_{\mathrm{dopp}} = (2\pi)$ 30 MHz. Since the Gaussian profile shares the same area as a top-hat profile of the same amplitude and of a top-hat full width $\nu^{\mathrm{TH}}_{\mathrm{dopp}} = 2\sqrt{2}\nu^\sigma_{\mathrm{dopp}}$, we can make the approximation

$$\sigma_0 = \sigma \nu^{\mathrm{TH}}_{\mathrm{dopp}} \,. \tag{7.12}$$

Combining Eqs. (7.11) and (7.12), the electronic transition dipole matrix element is related to the observed saturation fluence via

$$\left\langle {}^1\Pi_1 \left| \mathbf{d} \right| {}^1\Sigma^+ \right\rangle = \frac{1}{\left\langle \nu' = 0 | \nu'' = 0 \right\rangle} \sqrt{3\epsilon_0 c\hbar^2 \nu^{\mathrm{TH}}_{\mathrm{dopp}} \frac{g_1}{\pi \mathcal{F} S_{J',J''}{}^2}} \,. \tag{7.13}$$

The observed saturation fluence from LIF studies was $\mathcal{F} = 0.52$ $\mu\mathrm{J/cm}^2$ for the $R(0)$ line ($g_1 = 1$), from which we determined $\left\langle {}^1\Pi_1 \left| \mathbf{d} \right| {}^1\Sigma^+ \right\rangle = 0.35$ e a_0. This electronic transition dipole moment

is 40% smaller than that estimated in Section 7.2.2, but is nevertheless on the same order of magnitude.

7.2.4 Estimation of $^3\Pi_{0+}$ lifetime and Rabi frequencies for Raman transfer

To obtain the transition dipole matrix elements $\langle {}^3\Pi_{0+} |\mathbf{d}| {}^1\Sigma^+, {}^3\Delta_1 \rangle$ from $\langle {}^1\Pi_1 |\mathbf{d}| {}^1\Sigma^+ \rangle$, we can use the following methods:

(1) Measure the relative intensities of the $^1\Pi_1 \leftarrow {}^1\Sigma^+$, $^3\Pi_{0+} \leftarrow {}^1\Sigma^+$ and $^3\Pi_{0+} \leftarrow {}^3\Delta_1$ vibronic bands as observed in velocity modulation spectroscopy [16], and then account for the Franck-Condon overlaps to get only the relative magnitudes of electronic dipole matrix elements. The relative electronic dipole matrix elements are then scaled by an overall factor to match the estimated dipole matrix elements of $\langle {}^1\Pi_1 |\mathbf{d}| {}^1\Sigma^+ \rangle$ from either Sections 7.2.2 or 7.2.3. Such scaling assumes a certain temperature distribution of electronic levels in the velocity modulation discharge tube setup, for which there is unfortunately no self-consistent check.

(2) Use the dipole matrix elements provided by Petrov and Titov in Table 7.1, but scale them by an overall factor to match $\langle {}^1\Pi_1 |\mathbf{d}| {}^1\Sigma^+ \rangle$ from either Sections 7.2.2 or 7.2.3.

From the electronic transition dipole matrix elements and Franck-Condon overlaps, the lifetime of the Raman transfer excited state $^3\Pi_{0+}$ can be estimated using the same formulas as Eqs. (7.9) and (7.10) but substituting for the lower electronic levels $\psi_{el,i} = {}^1\Sigma^+, {}^3\Delta_1$. Further, the transfer laser Rabi frequencies Ω_i can be calculated from a given laser intensity I_i by inverting Eq. (7.8). More explicitly,

$$\Omega_i = \langle {}^3\Pi_{0+} |\mathbf{d}| \psi_{el,i} \rangle \langle \nu' | \nu'' = 0 \rangle \left| \mathcal{S}^{F' J' m'_F \Omega'}_{F'' J'' m''_F \Omega''} \right| \frac{1}{\hbar} \sqrt{\frac{2I}{\epsilon_0 c}} \quad , \tag{7.14}$$

where

$$\left|\mathcal{S}^{F'J'm'_F\Omega'}_{F''J''m''_F\Omega''}\right| = \sqrt{(2F'+1)(2F''+1)(2J'+1)(2J''+1)} \begin{Bmatrix} J'' & F'' & I \\ F' & J' & 1 \end{Bmatrix} \begin{pmatrix} F' & 1 & F'' \\ -m'_F & m'_F - m''_F & m''_F \end{pmatrix} \begin{pmatrix} J' & 1 & J'' \\ -\Omega' & \Omega' - \Omega'' & \Omega'' \end{pmatrix} \quad (7.15)$$

The choice of rotational and hyperfine levels to be used for the population transfer warrants some careful consideration. In ^{180}Hf^{19}F$^+$, the nuclear hyperfine number is $I = 1/2$, so each m_J level is further split into two m_F levels. To measure the eEDM transition frequency, the ions need to be populated in the state $|F = 3/2, J = 1, m_F = 3/2, \Omega = 1\rangle$. Given our ability to populate as many as 30% of the HfF$^+$ in $|J'' = 1, m''_J = -1, \Omega'' = 0\rangle$ of the $^1\Sigma^+$ ground state and assuming equal population in each m''_F sub-level of the $|m''_J = -1\rangle$ state, we can populate 15% of the HfF$^+$ in $|F'' = 3/2, J'' = 1, m''_F = 3/2, \Omega = 0\rangle$. The path that yields the strongest two-photon rotational amplitude $\mathcal{S}^{|2\rangle}_{|1\rangle}\mathcal{S}^{|3\rangle}_{|2\rangle}$ is then provided by the transitions $^1\Sigma^+$ ($|F'' = 3/2, J'' = 1, m''_F = 3/2, \Omega'' = 0\rangle$) $\rightarrow$ $^3\Pi_{0+}$ ($|F' = 1/2, J' = 0, m'_F = 1/2, \Omega' = 0\rangle$) $\rightarrow$ $^3\Delta_1$ ($|F = 3/2, J = 1, m_F = 3/2, \Omega = 1\rangle$), which can be made by a σ^--polarized photon followed by a σ^+-polarized photon. This transfer scheme works well only if the quantization axis is fixed, as is often the case in atomic physics experiments to be either the direction of laser propagation or the direction of an external magnetic or electric field.

In the eEDM experiment, the externally applied electric field used to polarize the molecule has to be constantly rotating to keep the ions trapped. The quantization axis, which is set by the electric field, is therefore constantly rotating as well. This means that even though 15% of the HfF$^+$ can be autoionized into a single m''_F level when the electric field is aligned with the direction of laser propagation, the different m''_F levels will be remixed as the quantization axis rotates. Since the minimum time required for the Raman transfer, which is half a trap cycle, translates to multiple rotation cycles ($\omega_{rot} \gg \omega_{trap}$), the fraction of ions occupying any one of the six m''_F levels in $J'' = 1$ will be time-averaged to one-sixth of the total population in the $J'' = 1$ level. From Chapter 3, we showed that the autoionization process gave 60% yield in the $J'' = 1$ level, which means that

the fraction of ions in a single $|J''=1, m_F''\rangle$ state is only 10%. On the other hand, the same autoionization line, accessed through an intermediate state of the opposite parity, can yield 35% of the HfF^+ in the $J''=0$ state, where the $J''=0$ only has two m_F'' levels. As many as 17.5% of the HfF^+ can therefore be populated in one of the two m_F'' levels in $(F''=1/2, J''=0)$. Due to parity selection rules, the ${}^3\Pi_{0+}(J'=0) \leftarrow {}^1\Sigma^+(J''=0)$ transition is forbidden. The best case scenario is then to first make a $R(0)$ transition on the upward transfer leg (Ω_1) and then a $Q(1)$ transition on the downward transfer leg (Ω_3). For a single Raman transfer leg, the rotational amplitude $|\mathcal{S}|$ is then calculated by first summing over the rotational line intensities to the different unresolved final states and averaging over the number of initial states, and then taking the square root of that quantity.

Table 7.3 summarizes the ${}^3\Pi_{0+}(\nu'=1)$ lifetime and Rabi frequencies Ω_1, Ω_3 for reasonable transfer laser intensities of 1 W/cm^2. The electronic transition dipole matrix elements $\langle {}^3\Pi_{0+} |\mathbf{d}| \psi_{el,i}\rangle$ displayed in the table are extrapolated from the average of the two values for $\langle {}^1\Pi_1 |\mathbf{d}| {}^1\Sigma^+\rangle$ as calculated in Sections 7.2.2 and 7.2.3.

Table 7.3: Electronic transition dipole matrix elements $\langle {}^3\Pi_{0+} |\mathbf{d}| \psi_{el,i}\rangle$, lifetime of ${}^3\Pi_{0+}(\nu'=1)$, and Rabi frequencies Ω_1, Ω_3 that can be achieved with a 1 W/cm^2 laser. With the help of (a) relative intensities measured in velocity modulation spectroscopy or (b) relative dipole matrix elements presented in Table 7.1, the transition dipole matrix elements $\langle {}^3\Pi_{0+} |\mathbf{d}| \psi_{el,i}\rangle$ are estimated from the average value for $\langle {}^1\Pi_1 |\mathbf{d}| {}^1\Sigma_0\rangle$ as calculated in Sections 7.2.2 and 7.2.3. The Rabi frequencies Ω_1 and Ω_3 are calculated for the transition ${}^3\Pi_{0+}(\nu'=1, J'=1) \leftarrow {}^1\Sigma^+(\nu''=0, J''=0)$ and ${}^3\Pi_{0+}(\nu'=1, J'=1) \rightarrow {}^3\Delta_1(\nu=0, J=1)$ respectively.

	(a)	(b)
$\langle {}^3\Pi_{0+} \|\mathbf{d}\| {}^1\Sigma^+\rangle\,(ea_0)$	0.116	0.114
$\langle {}^3\Pi_{0+} \|\mathbf{d}\| {}^3\Delta_1\rangle\,(ea_0)$	0.164	0.204
$\tau({}^3\Pi_{0+}, \nu'=1)(\mu\text{s})$	15	16
$\Omega_1/(2\pi)$ (MHz)	2.5	2.5
$\Omega_2/(2\pi)$ (MHz)	2.1	2.7

7.3 Experiment setup

To perform stimulated Raman transfer to the $^3\Delta_1$ state via the $^3\Pi_{0+}(\nu' = 1)$ excited state, the transfer lasers for the upward and downward leg need to be tuned to 899.7 nm and 986.4 nm, respectively. The 899.7 nm home-built laser is the output of a 1.5 W tapered amplifier injected by light from an external cavity diode laser (ECDL), while the 986.4 nm laser is a Toptica DL Pro laser, which is also an ECDL seeding a 2 W tapered amplifier. Both the home-built and Toptica laser have extended mode-hop-free tuning ranges offered by feeding forward the ECDL grating position (via the piezoelectric stack's control voltage) onto the diode current [22].

The two transfer lasers need to have their relative frequencies stabilized to much better than the inverse of the time the ions take to traverse the adiabatic crossing (illustrated in Fig. 7.1b), which is typically

$$\frac{1}{T_{transfer}} = \frac{2\,\omega_{trap}\,\delta}{\pi\Omega_{2\gamma}} \approx 2 \times 10^5\,\mathrm{s}^{-1}\,. \tag{7.16}$$

The High Finesse WS7 wavemeter that is used to measure the absolute wavelengths of the two transfer lasers only has an accuracy on the order of 10 MHz. To stabilize the lasers to a maximum relative linewidth of $\ll 30$ kHz, the 899.7 nm and 986.4 nm lasers are locked to an optical cavity of finesse 1500 and 3000 for the two wavelengths respectively. The details of the cavity lock setup are beyond the scope of this thesis and will be discussed in Kevin Cossel's thesis. Briefly, to center the desired laser frequencies on a cavity resonance (free spectral range = 1.3 GHz), the laser frequencies are offset by AOMs before sending them through the cavity: the 899.7 nm laser is offset by a double-passed acousto-optical modulator (AOM) at 2×260 MHz, and the 986.4 nm laser is first offset by a 800 MHz AOM and then a double-passed AOM at 2×200 MHz. Each laser is then locked using a Pound-Drever-Hall lock [21]. The linewidth of a single locked laser is measured to be 10 kHz, which is also an upper bound on the relative frequency jitter between the two lasers.

In a search for the two-photon resonance ($\delta = 0$), we scanned the transfer laser frequencies by tuning the frequencies of the double-passed AOMs while keeping the lasers locked to the cavity. The long-term stability of the cavity, enabled by placing the cavity in a sealed and evacuated vacuum

chamber that is temperature stabilized to 0.01°C, was good enough such that the two-photon resonance line (shown in Section 7.5) drifted by less than 100 kHz over two weeks.

The two transfer lasers are switched on and off using AOMs as shutters before being fiber-coupled to the ion trap setup. Light from both lasers is then directed onto the ions through the top electrode/light pipe of the ion trap. The axial direction of laser propagation was chosen so as to be insensitive to the circular micromotion from the application of a rotating field in the radial plane, which can cause the ions to exhibit Doppler widths as large as $\sigma_D = (2\pi)480$ MHz. To achieve reasonably high Rabi frequencies ($> (2\pi)4$ MHz), the 150 mW transfer lasers are telescoped down to a beam waist of $w = 1$ mm. The spatial overlap between the smaller transfer laser beam waist and the ion cloud was improved by ramping the trap frequencies in the radial directions up to $(2\pi)11$ kHz, which squeezed the ions to a radial width of $\sigma_i = 0.8$ mm. The axial trap frequency was simultaneously ramped down to $\omega_{trap} \equiv \omega_z = (2\pi)0.85$ kHz, which not only cooled the ions to give a smaller axial Doppler width (also the two-photon detuning δ), but also increased the sweep time for the transfer T_{sweep}, making the Raman transfer occur more efficiently as described by Eq. (7.7).

To detect the ion number in either the $^1\Sigma^+$ state or the $^3\Delta_1$ state, we employed the UV doubled output of a pulsed dye laser to provide the first photon and 266 nm (provided by the same Nd:YAG pumping the dye laser) as the second photon to access the dissociating state. The first photon of the dissociation laser was tuned to resonance between the relevant lower state and the upper state $[35.97]\Omega' = 0$, where the spectroscopic constants for the upper state have been characterized in the previous chapter. At a pulse energy of 100 μJ and a linewidth of 0.12 cm^{-1}, the first dissociation photon is sufficient to resolve individual rotational states but not providing any finer resolution (e.g. it cannot address individual hyperfine or Ω-doublet levels). This level of resolution turns out to be a convenient feature in performing spectroscopy of the $^3\Delta_1$ level (Section 7.5), where the dissociation laser frequency does not have to be changed in order to access different hyperfine or parity levels.

7.4 Rabi frequency calibration

Before performing the stimulated Raman transfer, we are interested in a direct measurement of the Rabi frequency for a given applied laser intensity, to provide both a check against the Rabi frequency estimates presented in Section 7.2 and to obtain a better sense of our success with Raman transfer. For such a Rabi frequency calibration, only one of the two transfer lasers is used and is tuned to resonance between the relevant lower state $|i\rangle$ and the upper state $|2\rangle$.

Using a laser of some measured intensity, the efficiency of transferring ions from $|i\rangle$ to $|2\rangle$ in a half-trap cycle T_{sweep} is given by the Landau-Zener probability:

$$P_{LZ}\left(|i\rangle \rightarrow |2\rangle\right) = 1 - \exp\left(-2\pi \frac{(\Omega_i/2)^2}{2\Delta/T_{sweep}}\right) . \tag{7.17}$$

Eq. (7.17) is now derived for a two-level Hamiltonian, written in the $\{|i\rangle, |2\rangle\}$ basis as

$$H_i = \frac{1}{2}\begin{pmatrix} 0 & \Omega_i \\ \Omega_i & 2\Delta \end{pmatrix} , \tag{7.18}$$

where Ω_i is the one-photon Rabi frequency (to be determined) and Δ is the one-photon Doppler shift. The analytical result with Δ calculated from the standard deviation of a Gaussian-distributed velocity spread is very similar to the numerical result obtained by thermally averaging over the whole velocity distribution.

Once populated in $|2\rangle$, the ions spontaneously decay quickly compared to a half-trap cycle, so that in subsequent half-trap cycles, the ions are not transferred from $|2\rangle$ back to $|i\rangle$. The probability of decay in a single half-trap cycle can then be cleanly determined by leaving on the transfer laser for multiple half-trap cycles and measuring the exponential time constant τ_i for the ions to be depleted from state $|i\rangle$:

$$\frac{N_{^1\Sigma^+}(t)}{N_{^1\Sigma^+}(t=0)} = e^{-t/\tau_1} = \left[1 - P_{LZ}\left(|i\rangle \rightarrow |2\rangle\right)\right]^{t/T_{sweep}} \tag{7.19}$$

from which we can determine the Rabi frequency:

$$\begin{aligned} \exp\left(-\frac{t}{\tau_i}\right) &= \exp\left(-\frac{t}{T_{sweep}} 2\pi \frac{(\Omega_i/2)^2}{2\Delta/T_{sweep}}\right) \\ \Rightarrow \quad \Omega_i &= \sqrt{\frac{4\Delta}{\pi\tau_i}} \end{aligned} \tag{7.20}$$

The Rabi frequency calibration method assumes that the ion cloud is well-overlapped with the laser, so that there are no ions on the laser beam periphery that can take a longer time to move through the laser radially and be depleted less efficiently. To avoid the spatial overlap issue, the laser beam is expanded to three times the ion cloud width. The fact that the Rabi frequency is decreased with a larger beam waist is immaterial for this experiment because we are only interested in calibrating the Rabi frequency as a function of laser intensity.

As a sanity check, we first performed the Rabi frequency calibration on the $^1\Pi_1(\nu' = 0, J' = 1) \leftarrow {}^1\Sigma^+(\nu = 0, J = 1)$ LIF transition, for which the dipole matrix element has already been estimated from two prior LIF measurements. Fig. 7.3a shows the number of $^1\Sigma^+$ ions depleted as a function of the trap time for a diode laser intensity of 0.49 mW/cm^2. The depletion in ion number is read out as the difference in $^1\Sigma^+$ ions photodissociated with and without the LIF laser. The depletion follows an exponential decay, from which the Rabi frequency is extracted using Eq. (7.20). Fig. 7.3b is a plot of the Rabi frequency versus the laser electric field $E = \sqrt{2I/(\epsilon_0 c)}$, from which the slope yields the combined rovibronic dipole matrix element to be 0.098(13) $e\ a_0$. Accounting for the vibrational and rotational dipole matrix elements, the measured electronic dipole matrix element is $\left\langle {}^1\Pi_1 \left| \mathbf{d} \right| {}^1\Sigma^+ \right\rangle = 0.23(3)\ e\ a_0$, which is 2.1 and 1.5 times smaller than that estimated from LIF lifetime and saturation fluence measurements respectively.

Although the sanity-check experiment did not agree with previous estimates particularly well, we proceeded with the same method of Rabi frequency calibration for the $^3\Pi_{0+}(\nu' = 1, J' = 1) \leftarrow {}^1\Sigma^+(\nu = 0, J = 0)$ upward leg of the Raman transition. Fig. 7.3c shows the summary plot of Rabi frequency versus 899.7 nm laser electric field, and the slope gave a combined rovibronic dipole matrix element to be $\langle 2 \left| \mathbf{d} \right| 1 \rangle = 0.065(9)\ e\ a_0$. The combined rovibronic matrix element is the most relevant for the stimulated Raman transfer experiment; expressed in a more practical manner, the measured rovibronic matrix element would give $\Omega_i = (2\pi)2.3(3)$ kHz for an intensity of 1 W/cm^2. On the other hand, one might again be curious about how the measured electronic dipole matrix element compares against the estimated values in Table 7.3. In this case, the electronic dipole matrix element is measured to be 0.08(1) $e\ a_0$, which is comparable to the estimated values.

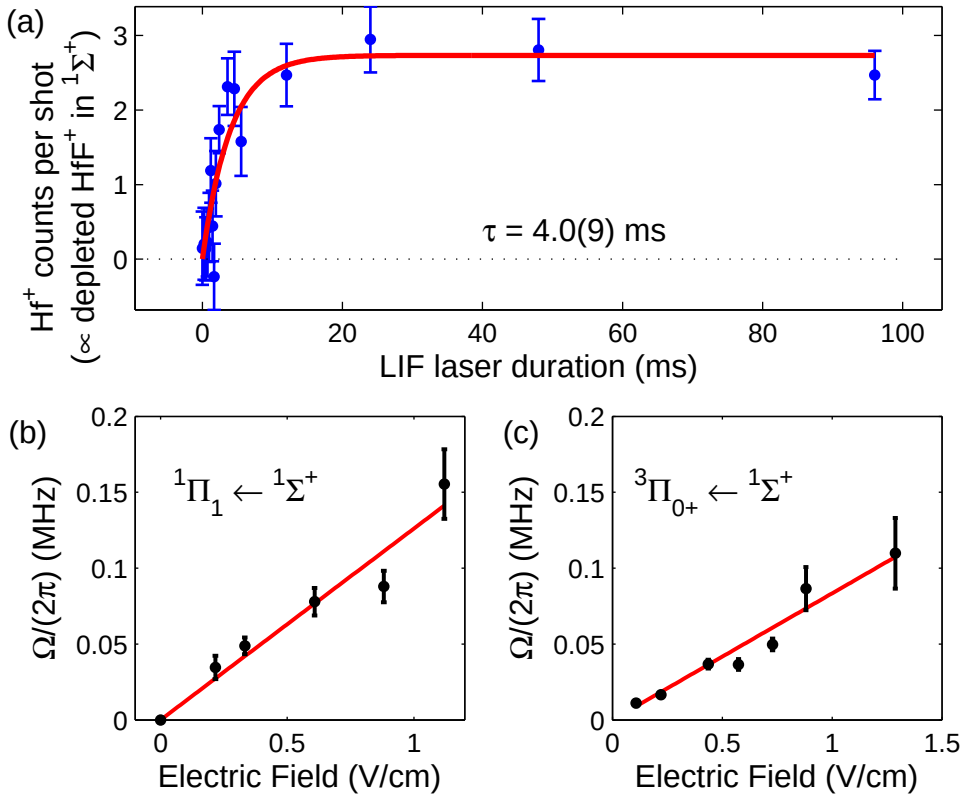

Figure 7.3: (a) Number of HfF^+ ions transferred out of the $^1\Sigma^+$ state (detected as the difference in dissociated Hf^+ counts with and without the LIF laser) as a function of LIF laser duration, where the LIF laser is tuned to resonance with the $^1\Pi_1(\nu' = 0, J' = 1) \leftarrow {}^1\Sigma^+(\nu'' = 0, J'' = 1)$ transition. For this data, the Doppler width (one-photon detuning Δ) was anomalously large at 120 MHz. Nevertheless, the decay time constant of 4.0(9) ms, which is measured for a particular LIF laser intensity of 0.49 mW/cm^2, can be converted to a LIF laser Rabi frequency of $(2\pi)0.078(9)$ MHz and plotted as a single point in (b). (b) Plot of Rabi frequency versus laser electric field for the $^1\Pi_1(\nu' = 0, J' = 1) \leftarrow {}^1\Sigma^+(\nu'' = 0, J'' = 1)$ LIF transition. The slope gives the rovibronic transition dipole moment to be 0.098(13) $e\ a_0$. (c) Plot of Rabi frequency versus laser electric field for the $^3\Pi_{0+}(\nu' = 1, J' = 1) \leftarrow {}^1\Sigma^+(\nu'' = 0, J'' = 0)$ transition. The slope gives the rovibronic transition dipole moment to be 0.065(9) $e\ a_0$.

In principle, we should also be able to extend the Rabi frequency calibration technique to Ω_3, where the lower state is the $^3\Delta_1$ state. Prior to attempting the stimulated Raman transfer, we populated the $^3\Delta_1$ by using a 355 nm photon as the second photon in autoionization. However, the exponential depletion process was measured to be very noisy with the $^3\Delta_1$ state regardless of the laser intensity, and we were unable to trust the Rabi frequency obtained; one possible reason was a low number of HfF^+ ions that autoionized into the $^3\Delta_1$ level. On the other hand, after performing the stimulated Raman transfer, we were able to cleanly deplete $^3\Delta_1$ ions by sending a on-resonant 986.4 nm laser onto the ions through one of the trap *radial* directions with the rotating bias field turned on at $\omega_{rot} = (2\pi)253$ kHz. This side-depletion laser (also expanded to ensure full overlap with the ions) was only strobed on with a duty cycle of 20% when the rotating field is pointing along the direction of propagation of the laser. In this case, the one-photon detuning was dominated by the Doppler shift of the circular micromotion to be $(2\pi)480$ MHz and $T_{sweep} = 2\pi/\omega_{rot}$. By measuring the exponential decay time constant to be 0.89(2) ms for a 70 mW/cm^2 beam, we determined the rovibronic dipole matrix element to be $\langle 2 |\mathbf{d}| 1\rangle = 0.04(1)\ e\ a_0$, or that we should expect a Rabi frequency of $2(\pi)1.4(4)$ MHz per mW/cm^2 of laser. The measured rovibronic dipole matrix element in turn implied an electronic dipole matrix element of 0.11(3) $e\ a_0$, which is about 1.7 times weaker than that in Table 7.3.

7.5 Results of stimulated Raman transfer

7.5.1 Spectroscopy of hyperfine levels in $^3\Delta_1(\nu = 0, J = 1)$

Having obtained a rough calibration of the Rabi frequencies, we attempted to perform the stimulated Raman transfer, with the HfF^+ ions created only in the $^1\Sigma^+(\nu'' = 0)$ state, of which 35% were formed in the $J'' = 0$ level. To search for the two-photon resonance ($\delta = 0$), the 899.7 nm laser frequency was fixed to be red-detuned from the $|2\rangle \leftarrow |1\rangle$ transition by $\Delta = (2\pi)80$ MHz, while the 986.4 nm laser was scanned in frequency. The photodissociation laser was tuned to read out HfF^+ ions in the $^3\Delta_1(J = 1)$ state and no rotating bias field was applied. Fig. 7.5a shows the

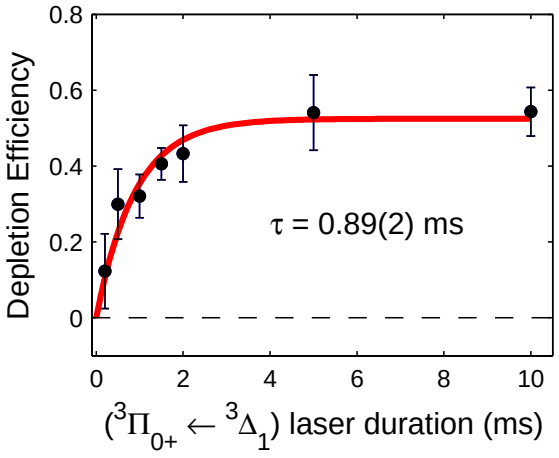

Figure 7.4: Depletion efficiency of the $^3\Delta_1$ HfF^+ ions as a function of the 986.4 nm side-depletion laser duration, where the 986.4 nm laser of intensity 70 mW/cm^2 is tuned to resonance with the $^3\Pi_{0+}(\nu' = 1, J' = 1) \leftarrow {}^3\Delta_1(\nu = 0, J = 1)$ transition. The decay time constant of 0.89(2) ms implies a rovibronic dipole matrix element of 0.04(1) $e\ a_0$.

number of $^3\Delta_1$ ions dissociated into Hf^+ ions as a function of the 986.4 nm laser frequency. The two signal peaks are the two hyperfine levels of the $^3\Delta_1(J = 1)$ state: $F = 1/2$ and 3/2 (Fig. 7.5b). (The signal for the frequency region in between the two peaks has been measured to be zero in other data sets not shown.) The hyperfine splitting is measured to be E_{HF} =46.5(2) MHz, which lies in the range of the theoretical estimate of 33.9–58.1 MHz [62].

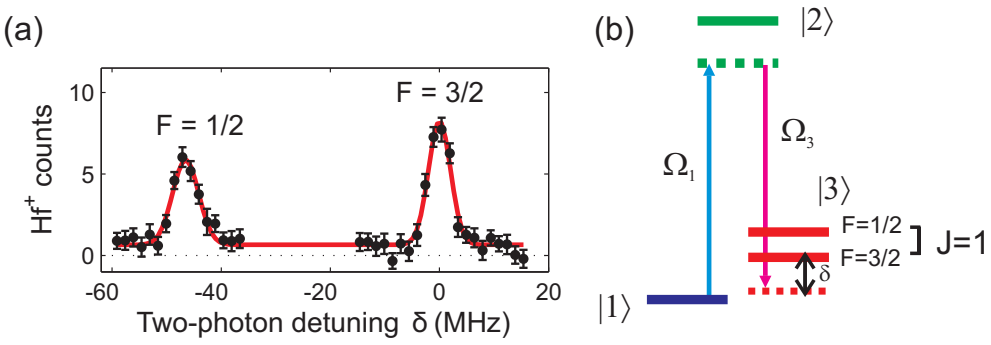

Figure 7.5: (a) Hyperfine spectroscopy of the $^3\Delta_1(\nu = 0, J = 1)$ state. (b) Bare states used in the stimulated Raman transfer, with the $^3\Delta_1(J = 1)$ hyperfine levels explicitly denoted.

To figure out the Raman transfer efficiency, we tuned the photodissociation laser to detect the number of HfF^+ ions depleted from the $^1\Sigma^+(J'' = 0)$ state when the Raman transfer is performed. Fig. 7.6a shows the dissociated Hf^+ signal as a function of transfer time, measured without any transfer lasers (black crosses), and with the 899.7 nm laser turned on but with (blue dots) and without (red open circles) the 986.4 nm laser. Both lasers are tuned to the two-photon resonance for transfer to the $^3\Delta_1(F = 3/2)$ level. In the absence of any transfer lasers, the HfF^+ ion number remains roughly constant at N_0. With the 899.7 nm laser only, the number of HfF^+ ions (N_1) decreases slowly over time due to off-resonant optical pumping of the HfF^+ ions out of the $^1\Sigma^+(J = 1)$ state into other rovibronic states. With both transfer lasers, the HfF^+ ions (N_2) are depleted more quickly, and the efficiency of depleting $^1\Sigma^+$ ions, $\eta = (N_1 - N_2)/N_1$, saturates to 53(3)% in several half-trap cycles (Fig. 7.6b). Since some of the ions depleted by off-resonant optical pumping ($N_0 - N_1$) are ions that would have also undergone stimulated Raman transfer with both lasers, the Raman transfer efficiency is bounded to be between 53(3)% and $(N_0 - N_2)/N_0$ = 67(2)% after

multiple half-trap cycles.

The fact that the multiple half-trap cycles are needed to saturate the Raman transfer efficiency means that the population of ions in the $^3\Delta_1$ level comes from equilibrating with the ion population in the initial $^1\Sigma^+$ level. The expected efficiency of ions transferred can then be given by the ratio of degenerate states in the final $^3\Delta_1$ level to the total number of states involved. More explicitly, there are two $|m_F''\rangle$ states in the initial $^1\Sigma^+$ level, and eight $|F = 3/2, m_F\rangle$ states and four $|F = 1/2, m_F\rangle$ states in the final $^3\Delta_1$ level.The ratio of degenerate states is then $\mathcal{R} = 8/(8+2) = 0.8$ or $4/(4+2) = 0.67$ for the $F = 3/2$ and $1/2$ final states, respectively. However, parity selection rules dictate that in the absence of any electric fields mixing the $^3\Delta_1$ states of opposite parity, there are only four $F = 3/2$ and two $F = 1/2$ states available for the Raman transfer, which changes the ratio of final states to total states to $\mathcal{R}$ =$4/(4+2) = 0.67$ or $2/(2+2) = 0.5$ respectively (Fig. 7.7a). In the absence of the rotating bias electric field, it is not clear the extent to which the trapping fields are able to mix the states of opposite parity (Fig. 7.7b), so the transfer efficiency, barring any technical issues, is expected to be in the ranges of 0.67–0.8 and 0.5–0.67 for the $F = 3/2$ and $1/2$ levels. In any case, $\mathcal{R}$ is consistently higher for the $F = 3/2$ hyperfine level, which accounts for the slight increase in ions transferred to the $F = 3/2$ level over the $F = 1/2$ level as observed in Fig. 7.5a.

7.5.2 Stark spectroscopy with a rotating bias field

In the absence of an external bias electric field, the $^3\Delta_1$ states of opposite parity, separated by ω_{ef}, are given by: $|-\rangle = (|\Omega = +1\rangle - |\Omega = -1\rangle)/\sqrt{2}, |+\rangle = (|\Omega = +1\rangle + |\Omega = -1\rangle)/\sqrt{2}$, where '+'/'−' denote the total parity of the state. With the rotating bias electric field strong enough to mix the states of opposite parity, Ω becomes a good quantum number and the m_F levels undergo a linear Stark splitting in the molecular frame:

$$E_S = -m_F\,\Omega\,\gamma_F\,d_{mf}\mathcal{E}_{rot} + E_F \quad (\text{assume } d_{mf}\mathcal{E}_{rot} \gg \omega_{ef})\,, \tag{7.21}$$

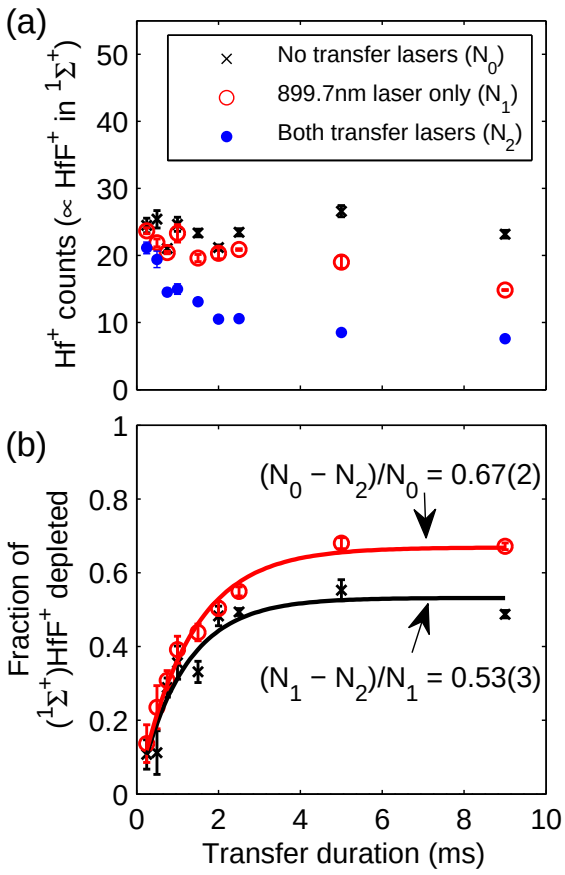

Figure 7.6: (a) HfF^+ ions (detected as dissociated Hf^+) as a function of transfer laser duration for the cases of (blue dots) both transfer lasers present, (red open circles) 899.7 nm laser present only, and (black crosses) no transfer lasers. The 899.7 nm laser causes a slow off-resonant optical pumping of HfF^+ out of the $^1\Sigma^+$ state over time. The presence of both transfer lasers depletes the $^1\Sigma^+$ ions more quickly. (b) Fraction of HfF^+ ions depleted from the $^1\Sigma^+$ state, determined from the data shown in (a) as either (red) $(N_1 - N_2)/N_1$ or (black) $(N_0 - N_2)/N_0$. The depletion fraction, which is expected to be the same as the transfer fraction, saturates after a few milliseconds of transfer time.

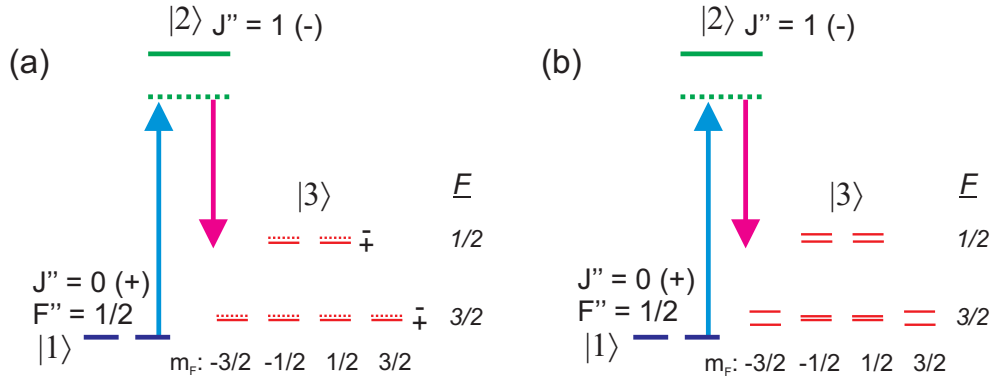

Figure 7.7: Bare states involved in the stimulated Raman transfer with their parities denoted as '+' or '−'. (a) In the absence of an external electric field, the $^3\Delta_1$ energy levels are states of well-defined parity: $|\pm\rangle = (|\Omega = +1\rangle \pm |\Omega = -1\rangle)/\sqrt{2}$. Parity selection rules dictate that only $- \leftrightarrow +$ transitions are allowed, so only the $|+\rangle$ states of the $^3\Delta_1$ manifold can be populated. (b) In a weak electric field that is still sufficient to mix states of opposite parity without giving rise to a large Stark shift, all 12 states of the $^3\Delta_1$ may be populated in Raman transfer.

where E_F is the offset for a given hyperfine level, d_{mf} is the molecular frame dipole moment and γ_F is a geometric g-factor accounting for how the total angular momentum couples to the electric field (analogous to the magnetic g-factor for an external magnetic field) [45]:

$$\gamma_F = \frac{F(F+1) + J(J+1) - I(I+1)}{2F(F+1)J(J+1)}\,. \tag{7.22}$$

For $F = 3/2$ and $1/2$, $\gamma_F = 1/3$ and $2/3$, respectively.

Fig. 7.8a shows the spectrum of Stark-shifted levels taken by scanning the 986.4 nm laser with a rotating bias electric field of 16 V/cm present. As expected from E_S being proportional to $m_F\Omega$, the two hyperfine levels $F = 3/2$ and $1/2$ yield four and two Stark-split levels, respectively. However, the Stark levels on the red-detuned side of the hyperfine level tend to be diminished in intensity relative to the blue-detuned side. This is because the rotating field is ramped back down to zero shortly before firing the photodissociation laser and ejecting the ions from the trap, so that the large rotating field will not cause the ejected ions to be deflected away from the MCP detector. The ramping down of the electric field adiabatically transforms the m_F levels from states of good Ω back to states of good parity. On the other hand, the photodissociation laser is tuned to resonance with the $[35.97]\Omega' = 0(J' = 1) \leftarrow {}^3\Delta_1(J = 1)$ transition. Since the upper $\Omega' = 0$ state has no Ω-doubling, each rotational level has a fixed parity $(-1)^{J'}$, so parity selection rules dictate that only the ${}^3\Delta_1\,|+\rangle$ levels can make a transition to the excited $(J' = 1)\,|-\rangle$ level. The intensities of the blue-detuned Stark levels are non-zero because the residual trapping fields induce a small amount of mixing between the $|+\rangle$ and $|-\rangle$ levels. Based on the above explanation, we would expect that if we repeated the Stark spectroscopy with the bias electric field ramped down but with the photodissociation laser tuned to access the $(J' = 2)\,|+\rangle$ excited state, parity selection rules would similarly cause the red-detuned Stark levels to be diminished in intensity compared to the blue-detuned ones. Indeed, this prediction matched the intensities of Stark levels detected using a $R(1)$ photodissociation line as shown in Fig. 7.8b.

To measure equal intensities for the Stark-shifted levels on both sides of a given hyperfine level, we carried out the Stark spectroscopy with the rotating bias field ramped down at a later

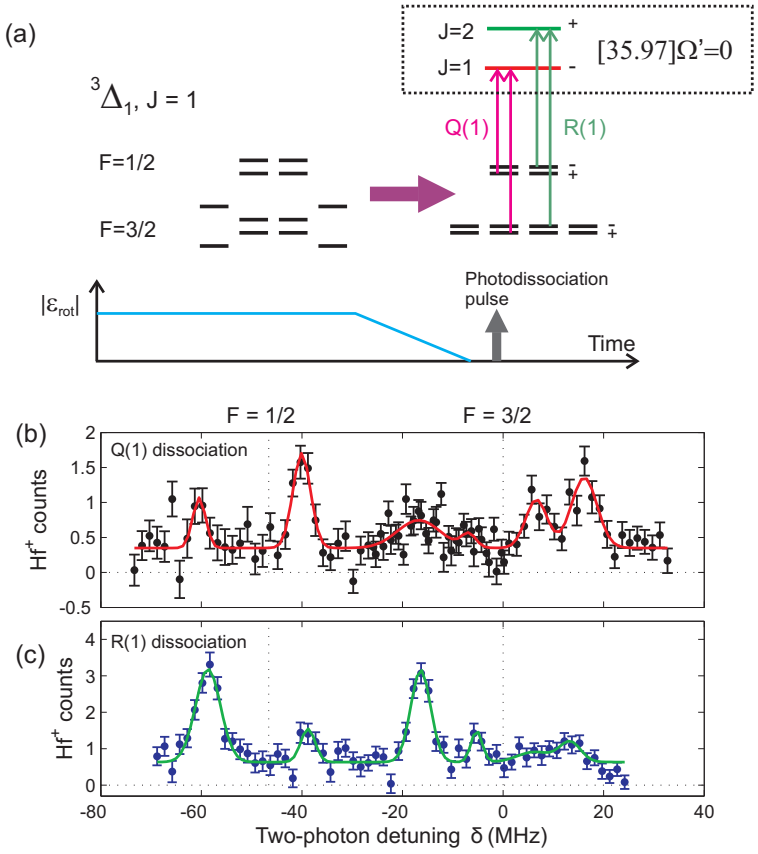

Figure 7.8: (a) Spectroscopy of the Stark-shifted $m_F\Omega$ levels in the $^3\Delta_1(J = 1)$ level with a rotating bias electric field. The $F = 1/2$ and $3/2$ levels split into two and four levels, respectively. (a) The rotating field magnitude is always ramped down to zero before the photodissociation laser pulse is applied, such that the Stark levels are transformed back to states of good parity. The photodissociation laser can be tuned to either a (b) $Q(1)$ or a (c) $R(1)$ transition. For the $Q(1)(R(1))$ dissociation transition, detection of the $|-\rangle$ ($|+\rangle$) parity states is less efficient.

time, chosen to be large enough to mix states of opposite parity but small enough to not induce a large deflection kick on the ions when they are ejected. The Stark spectrum was then measured with three different bias field magnitudes: 22.4 V/cm, 16 V/cm and 8 V/cm (Fig. 7.9a–c). The bias electric field magnitudes are determined from numerical calculations in SIMION. In accordance with Eq. (7.21), the Stark levels grew farther apart with larger electric fields. However, at large enough electric fields such that the Stark splitting between adjacent levels of a single hyperfine level is comparable to the hyperfine splitting, the $||m_F| = 1/2\rangle$ states for each hyperfine level will start to mix, and the Stark splittings are modified to give:

$$\begin{aligned} & E_S(F = \frac{3}{2}, m_F\Omega = \pm\frac{1}{2}) \\ = \; & \frac{1}{2}\left(E_{HF} \mp \frac{d_{mf}\mathcal{E}_{rot}}{2}\right) - \frac{1}{2}\sqrt{\left(\frac{d_{mf}\mathcal{E}_{rot}}{6} \mp E_{HF}\right)^2 + 2\left(\frac{d_{mf}\mathcal{E}_{rot}}{3}\right)^2} + E_{F=\frac{3}{2}} \qquad (7.23a) \\ & E_S(F = \frac{1}{2}, m_F\Omega = \pm\frac{1}{2}) \\ = \; & \frac{1}{2}\left(-E_{HF} \mp \frac{d_{mf}\mathcal{E}_{rot}}{2}\right) + \frac{1}{2}\sqrt{\left(\frac{d_{mf}\mathcal{E}_{rot}}{6} \mp E_{HF}\right)^2 + 2\left(\frac{d_{mf}\mathcal{E}_{rot}}{3}\right)^2} + E_{F=\frac{1}{2}} \qquad (7.23b) \end{aligned}$$

(Note that the original appearance of these equations in [45] had some typographical errors, which have now been fixed in this thesis.) The $|m_F| = 3/2$ stretch states remain unperturbed by the hyperfine mixing. Fig. 7.9d is a plot contrasting the linear Stark splittings given by Eq. (7.21) (dashed lines) against the Stark shifts accounting for the mixing between hyperfine levels as described by Eq.(7.23) (solid lines). The measured Stark spectra peak positions from Figs. 7.9a–c are also plotted as a function of bias electric field magnitude in Fig. 7.9d, and are shown to follow the solid curves, especially at larger electric fields. Using Eq. (7.23), we determined the molecular frame dipole moment of HfF^+ in the $^3\Delta_1$ state to be 1.54(1) $e\ a_0$, which turned out to be very close to the value of 1.50 $e\ a_0$ predicted by Petrov et. al. [63].

With the ability to populate two $^3\Delta_1(\nu = 0)\,|F, J, m_F, \Omega\rangle$ quantum states by tuning the Raman transfer lasers to a particular two-photon resonance, we are now poised to consider various schemes for implementing Ramsey spectroscopy to measure the eEDM-sensitive transition.

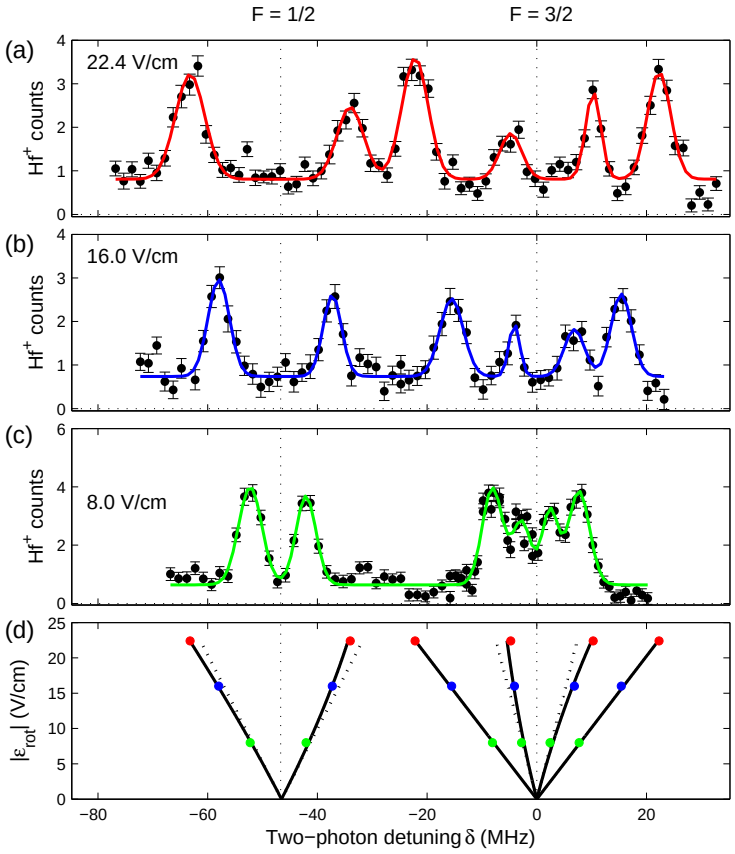

Figure 7.9: Stark spectroscopy of the $^3\Delta_1(\nu = 0, J = 1)$ state with a rotating bias field of (a) 22.4 V/cm, (b) 16.0 V/cm and (c) 8.0 V/cm/ (d) The Stark-shifted peak positions are plotted as a function of rotating electric field magnitude as colored dots. The dashed lines are the linear Stark shifts from Eq. (7.21) and the solid lines are the Stark shifts including perturbation effects as described in Eq. (7.23).

Chapter 8

Ramsey spectroscopy of the eEDM-sensitive transitions [50]

Over the length of this thesis, we have progressed from conducting HfF^+ vibronic spectroscopy with initial theoretical uncertainties of 100 THz to resolving Stark splittings in a given rovibronic-hyperfine state at the 10 MHz level using a rotating bias field. We have already managed to isolate and populate only two $|m_F, \Omega\rangle$ levels by tuning the Raman laser frequencies to access only one of the Stark manifolds. To measure the eEDM, we need to first measure the energy splitting between the two $|m_F, \Omega\rangle$ levels within a Stark manifold using Ramsey spectroscopy, and then repeat the frequency measurement for the other eEDM-sensitive transition. At this stage, we only need three remaining experimental tools to perform the Ramsey spectroscopy:

(1) a way to prepare the ions in only one of the two $|m_F, \Omega\rangle$ levels,

(2) a magnetic field that is co-rotating with the bias electric field, and

(3) a method for imposing a coherence between $|m_F = +3/2\rangle$ and $|m_F = -3/2\rangle$.

This chapter[1] describes the physics and implementation of Ramsey spectroscopy of trapped HfF^+ molecular ions in rotating bias electric and magnetic fields. The Ramsey spectroscopy, which is the first demonstration of coherent spectroscopy of trapped ions with a rotating quantization axis, yields a measurement of the magnetic g-factor for the $^3\Delta_1$ state, which has been previously estimated to be small but never measured. From the magnetic g-factor data, we obtain a preliminary limit on the eEDM and provide an estimate of the attainable statistical uncertainty for the

[1] Much of this chapter will be appearing in Reference [50].

eEDM with current parameters. Finally, this chapter closes with an outlook for the JILA eEDM experiment.

8.1 $^3\Delta_1$ levels with rotating bias fields

In the presence of a constantly rotating quantization axis, adjacent projections (i.e. $\Delta m = \pm 1$) of an angular momentum onto the quantization axis become mixed as viewed in the laboratory frame that is outside of the rotating frame. For instance, for a spin-1/2 particle, the eigenstate projections of the spin changes from $\{|\pm z\rangle\}$ to $\{\pm\frac{1}{2}\left(|z\rangle - \frac{\sin\theta}{\cos\theta\pm 1}|-z\rangle\right)\}$ as the quantization axis rotates by an infinitesimal polar angle θ. Similarly, for a constantly rotating bias electric field (which acts as the quantization axis), adjacent m_F levels of the $^3\Delta_1(\nu = 0, J = 1, F = 3/2)$ state become mixed. In the case of states $|a\rangle$ and $|b\rangle$ (and similarly, $|c\rangle$ and $|d\rangle$) separated by a three-photon transition as illustrated in Fig. 8.1a, the eigenstates are $\{(|a\rangle \pm |b\rangle)/\sqrt{2}\}$ ($\{(|c\rangle \pm |d\rangle)/\sqrt{2}\}$) under a rotating bias electric field, where the energy splitting Δ between the eigenstates is given by

$$\Delta \propto \omega_{ef}\left(\frac{\omega_{rot}}{d_{mf}\mathcal{E}_{rot}}\right)^3. \tag{8.1}$$

Δ is the same as $\omega^{u/\ell}$ for the case of $B = 0$. The exponent of 3 in Eq. (8.1) comes from the fact that three photons are needed to couple $m_F = 3/2 \leftrightarrow -3/2$, whereas the ω_{ef} term is present to provide a coupling between states of $\Omega \leftrightarrow -\Omega$, which must also be overcome for the three-photon transition to occur.

So far, the above physics is valid in the absence of a magnetic field. In the presence of a magnetic field co-rotating with the bias electric field, the m_F levels can be interchangeably referred to as either Stark or Zeeman levels. Where there is a magnetic field B_{rot} large enough to provide a Zeeman shift that can overwhelm the energy splitting Δ, the eigenstates then resume to be $\{|a\rangle, |b\rangle\}$. The full spectrum of the levels in the uppermost Stark manifold of the $^3\Delta_1(F = 3/2)$ state in the presence of rotating electric and magnetic fields is given by the avoided crossing depicted in Fig. 8.1b, where the asymptote of the avoided crossing is the Zeeman shift for each of the two

stretch states, $\pm(3/2)g_F\mu_B B_{rot}$.

In accordance with Eq. (1.7), the eEDM measurement would then correspond to a Ramsey spectroscopy measurement of the frequency splitting between the two levels at some finite $\pm B_{rot}$ (shown as two vertical arrows in Fig. 8.1b) for both the upper and lower Stark manifolds. Sitting on the side of a Ramsey fringe at a given time, one can detect a small shift in the frequency (due to the eEDM) as a shift in fringe position (Fig. 8.1c). However, the ability to sit on the side of a Ramsey fringe requires knowledge of the Ramsey fringe frequency, or in other words, knowledge of the spectroscopic constants Δ and g_F defining the avoided crossing, neither of which has been experimentally determined until this thesis work.

While Eq. (8.1) gives a qualitative understanding for Δ, the g-factor for the $^3\Delta_1$ state can be estimated as follows [45]:

$$g_F = \gamma_F\big[\,((g_L+g_r)\Lambda + (g_S+g_r)\Sigma)\,\mathrm{sign}(\Omega) - g_r J(J+1)\big] - g_I\kappa_F\,, \tag{8.2}$$

where g_L and g_S are the orbital and spin g-factors, and g_r and g_I are the rotation and nuclear spin g-factors. g_r and g_I are small as they are on the order of the ratio of electron mass to molecular mass, i.e. $m_e/m_{mol} \sim 10^{-3}$. In the $^3\Delta_1$ state, $\Lambda = \pm 2$ and $\Sigma = \mp 1$ whereas $g_L = 1$ and $g_S = 2 + \alpha/\pi + \mathcal{O}\big((\alpha/\pi)^2\big)$, such that there is a near cancellation of the orbital and spin magnetic moments and the overall g-factor becomes very small. On the other hand, spin-orbit mixing, which is predominant in heavy molecules, may cause the $^3\Delta_1$ state to contain admixtures of other states, such that the cancellation of the orbital and spin magnetic moments is not as complete, giving a bigger g-factor. In any case, the relatively small g-factor is one of the chief advantages of the $^3\Delta_1$ state, because it reduces the sensitivity of the eEDM transitions to stray magnetic fields. An experimental determination of the g-factor requires the implementation of a rotating magnetic field, which is described in the following section.

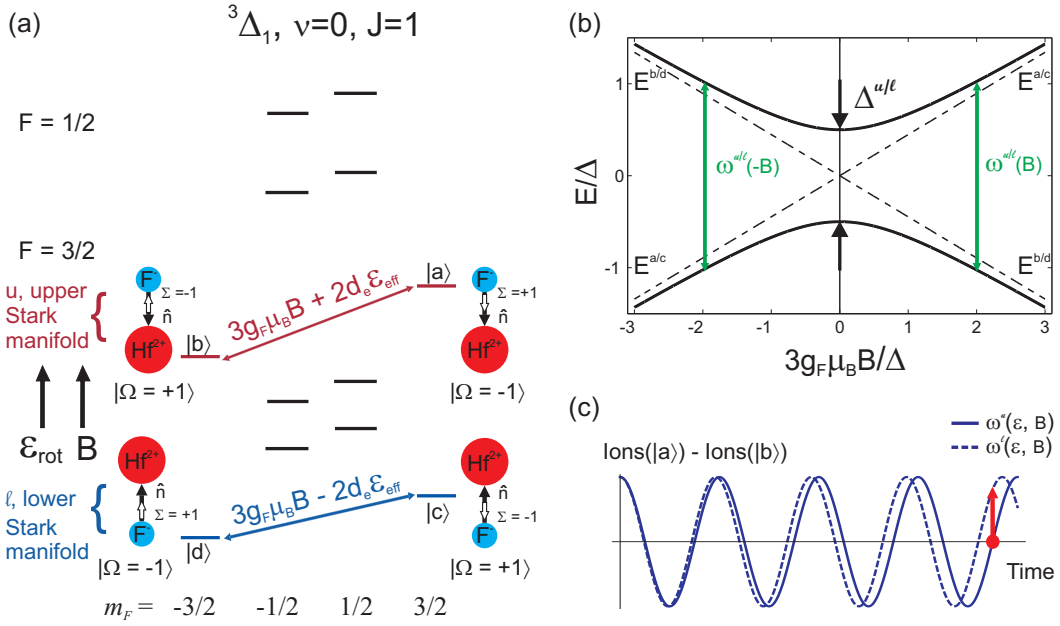

Figure 8.1: (a) (Reproduced from Fig. 1.5) HfF^+ energy levels in the $^3\Delta_1, \nu = 0, J = 1$ state in the presence of an external electric and magnetic field, where the eEDM-sensitive transitions are between states $|a\rangle$ and $|b\rangle$ and between states $|c\rangle$ and $|d\rangle$. (b) In the presence of a rotating quantization axis, $|a\rangle$ and $|b\rangle$ (similarly, $|c\rangle$ and $|d\rangle$) are coupled to each other and form an avoided crossing as a function of magnetic field. At the center of the avoided crossing (i.e. no magnetic field), the eigenstates are equal superpositions of the stretch states of the same Stark manifold, e.g. $\{|0\rangle, |1\rangle = (|a\rangle \pm |b\rangle)/\sqrt{2}\}$ for the upper Stark pair. The vertical green arrows denote the eEDM-sensitive transition frequencies. (c) Ramsey fringes measured for the upper (solid) and lower (dashed) Stark manifolds. The eEDM signal is proportional to the amount by which the Ramsey fringe moves when sitting on the side of a fringe.

8.2 Experimental tools

8.2.1 Rotating magnetic field

To implement a rotating magnetic field, one can imagine running AC currents up and down the fin electrodes in a way as to create a rotating magnetic field that is aligned parallel or anti-parallel to the rotating bias electric field. A simpler approach to mock up B_{rot} is by installing a static radial magnetic field gradient using a pair of anti-Helmholtz coils: Fig. 8.2a shows a 3-dimensional view of the coils and B field lines relative to the fin electrodes, and Fig. 8.2b depicts the top view of the ion trap with the radial B field gradient. To understand how the static B field gradient, in combination with the rotating electric field, gives rise to a rotating magnetic field, consider the magnetic field lines sampled by a HfF^+ ion undergoing circular micromotion at the rotating field frequency ω_{rot} as illustrated in Fig. 8.2b. At time 0, $\vec{\mathcal{E}}_{rot}$ points along $\hat{x}$ and since $\vec{r}_{rot} \propto -\vec{\mathcal{E}}_{rot}$, the molecular ion starts out on the left side of the micromotion circle. The magnetic field sampled by the molecular ion points in the direction $-B(r_{rot})\hat{x} + B_{static}(\vec{R})\hat{y}$, where $B(r_{rot})$ is the magnitude of magnetic field at the radius of circular micromotion r_{rot} from the trap center. $B_{static}(\vec{R})$ is the magnetic field at the center of the micromotion circle ($\vec{R}$). A quarter rotation cycle later, $\vec{\mathcal{E}}_{rot}$ points along $\hat{y}$ while the magnetic field sampled by the ion points along $(-B(r_{rot}) + B_{static}(\vec{R}))\hat{y}$. Over the course of a rotation cycle, then, the magnetic field experienced by the ions can be decomposed into a spatially-dependent but time-invariant component $B_{static}(\vec{R})$ and a time-varying component $\vec{\mathcal{B}}_{rot}(t) = \vec{\nabla}B \cdot \vec{r}_{rot}$ that rotates with the bias electric field, either in phase or 180° out of phase (depending on whether the magnetic field lines point radially inward or outward). By definition, B_{rot} is positive if it lies parallel to $\mathcal{E}_{rot}$. $\vec{B}_{static}(\vec{R})$ is a function of the ions' secular displacement within the trapping volume, but for any given instant in time, all the ions experience identical B_{rot}. The variation in $\vec{B}_{static}(\vec{R})$ across the ion cloud is of little concern, since the rotating quantization axis makes us primarily sensitive to the rotating component of the magnetic field.

Fig. 8.2c shows a photograph of the anti-Helmholtz coils installed to produce the magnetic

field gradient. Each coil (mean radius 135.9 mm) is made by winding 3 layers of 13 turns of 2.66 mm-diameter square copper wire. The anti-Helmholtz pair produces a radial gradient of 0.08254 G/cm for 1 A of current. The coils are driven by a Kepco BOP 20-20M bipolar power supply, whose output can be externally controlled by an analog input voltage to provide up to ± 20 A of current. As shown in Fig. 8.2c, the coils are situated outside the trap chamber, which means that time-varying changes to the magnetic fields are impeded by eddy currents in the large aluminum mirrors originally designed for fluorescence collection in the trap. The eddy currents dissipate on the time scale of 20 ms (Fig. 8.2d), which means that any ramps in the magnetic coil currents need to take much longer than 20 ms so that the actual trap fields can follow the current drive.

8.2.2 Optical pumping

In order to perform Ramsey spectroscopy, the ions must be initialized in only one of the two $|m_F, \Omega\rangle$ levels. As explained in Chapter 7, the usual atomic physics trick of preferentially populating the molecular ions in one of the two stretch states using circularly-polarized light does not work due to the combination of the quantization axis rotating and the need for Raman transfer lasers to propagate perpendicular to the plane of rotation. The following scheme, however, does work: after the Raman lasers populate the ions in both $|m_F, \Omega\rangle$ levels of a Stark manifold, a circularly-polarized optical pumping laser (henceforth referred to as the 'depletion' laser) tuned to resonance with the $^3\Pi_{0+}(J' = 1) \leftarrow {}^3\Delta_1(J = 1)$ transition is used to deplete the ions in one of the two stretch states. The depletion laser is aligned along the same beam path as the ionization and dissociation lasers, and is stroboscopically turned on with a duty cycle of 20% whenever the quantization axis lies parallel to the direction of laser propagation. The depletion laser is picked off from the 986 nm transfer laser and sent through two acousto-optic modulators as intensity switches that are aligned to ensure no depletion laser light is incident on the ions when the quantization axis has rotated by 180°. Due to the reduced depletion laser intensity and large Doppler shift associated with v_{rot}, as many as 250 rotation cycles may be needed to fully deplete the ions from one of the stretch states (say, $|b\rangle$), leaving the ions in only $|a\rangle$. To change the handedness of the depletion

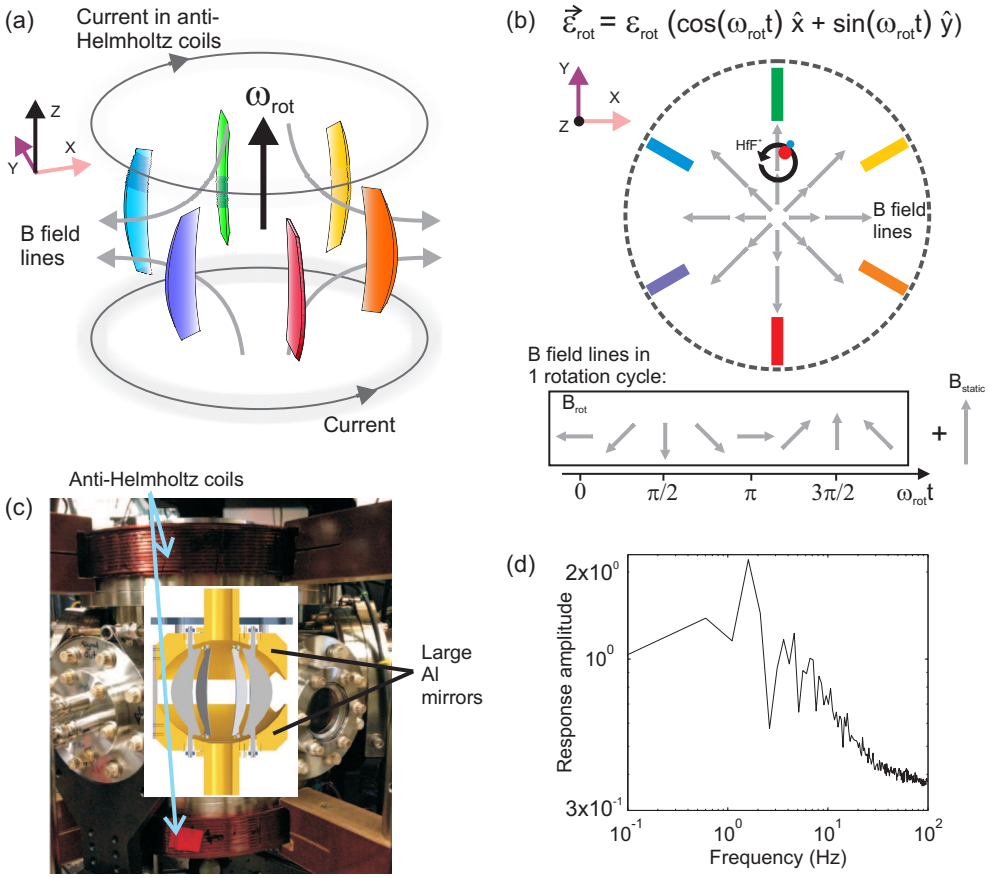

Figure 8.2: (a) 3-dimensional schematic of the fin electrodes and anti-Helmholtz magnetic field coils, which create a radial magnetic field gradient shown by the gray arrows. (b) Top view of the ion trap showing the fin electrodes and magnetic field lines in the plane of rotation. A molecular ion undergoes circular micromotion at ω_{rot} and samples the magnetic field lines that can be decomposed into $B_{rot}(t) + B_{static}$. For the case depicted with the B field lines pointing outwards radially, B_{rot} is 180° out of phase from $\mathcal{E}_{rot}$, i.e. $B_{rot} < 0$. (c) Photograph of the anti-Helmholtz coils. (d) The response of the magnetic field gradient in the trap center to any changes in the coil current is impeded by eddy currents in the large aluminum trap mirrors on the time scale of 20 ms.

laser polarization, one can simply offset the timing of the depletion laser pulses such that the laser light is only present when the quantization axis is anti-aligned to the direction of depletion laser polarization. In the rest of this chapter, the sequence of 250 depletion pulses (or however many are needed for full depletion) is referred to as a 'depletion laser strobe-sequence'.

8.3 Ramsey spectroscopy at $B = 0$

We now embark on experimentally mapping out the avoided crossing depicted in Fig. 8.1b. The first step is to understand the avoided crossing splitting at the point of closest approach Δ by performing Ramsey time-of-flight spectroscopy in the absence of any magnetic fields. The Ramsey sequence is as follows: after populating ions in a single Stark manifold (say, both $|a\rangle$ and $|b\rangle$ incoherently in the upper Stark manifold u), the ions in state $|b\rangle$ are optically pumped away with a σ^+-polarized depletion laser strobe-sequence. The remaining ions in $|a\rangle$ can then be expressed as populating a superposition of the two eigenstates $\{|0\rangle, |1\rangle \equiv (|a\rangle \pm |b\rangle)/\sqrt{2}\}$, i.e. $|a\rangle = (|0\rangle + |1\rangle)/\sqrt{2}$. In other words, the depletion strobe-sequence is equivalent to performing a $\pi/2$-pulse on the ions, the physics of which is analogous to the following: a beam of unpolarized light, sent through a *gedanken* σ^+-polarizer, becomes σ^+-polarized, which is also a linear combination of horizontal and vertical linear polarizations. A variable wait time T ensues, during which the relative phase between the states $|0\rangle$ and $|1\rangle$ freely evolves as $e^{-i\omega^u T}$, due to $|0\rangle$ and $|1\rangle$ being the eigenstates under the rotating electric and magnetic fields. The $\pi/2$-pulse is then applied again with a σ^+-polarized depletion laser and the Hf^+ ions detected upon firing the dissociation laser only come from those remaining in state $|a\rangle$. The number of ions remaining in $|a\rangle$ is related to the argument of the free evolution phase as follows: at $\omega^u T = 2n\pi$ (where n is an integer), there is no change in the ion number for $|a\rangle$ between the first and second $\pi/2$-pulse. Conversely, after $\omega^u T = (2n+1)\pi$, all the ions initially in $|a\rangle$ would have been transferred into $|b\rangle$, giving maximal depletion signal with the second $\pi/2$-pulse. In general, the change in ion signal in $|a\rangle$ between the first and second $\pi/2$-pulse is proportional to $(1 - \cos(\omega^u T))$. The above Ramsey sequence can be repeated using σ^--polarized light for the second $\pi/2$-pulse, which makes the dissociation laser sensitive to a change

in ion population in state $|b\rangle$. The difference between the two chops (differing in the helicity of the second $\pi/2$-pulse) then provides the relative change in ion population between states $|a\rangle$ and $|b\rangle$, which is proportional to the relative phase between the two states accumulated during T. To normalize for any drifts in ion number at a given wait time T, the ion number is also recorded without any $\pi/2$ pulses applied. The combination of these chops give the fractional difference in ion population between states $|a\rangle$ and $|b\rangle$ as a function of the free evolution time T, and is shown as a Ramsey fringe in Fig. 8.3b.

Fig. 8.3c shows the zero-magnetic-field Ramsey fringe frequencies plotted as a function of rotating bias electric field magnitude for both Stark manifolds $\{|a\rangle, |b\rangle\}$ and $\{|c\rangle, |d\rangle\}$. For a given $\mathcal{E}_{rot}$, the average of the two fringe frequencies is inversely proportional to $\mathcal{E}_{rot}^3$ (Fig. 8.3d), as predicted by Eq. (8.1) for a three-photon transition. On the other hand, the slight frequency difference $\delta\Delta$ between the two Stark manifolds comes from interactions with the $F' = 1/2$ hyperfine level, i.e. the upper Stark manifold is further repelled from the $F' = 1/2$ levels than the lower Stark manifold. Since the $m_F = \pm 3/2$ states are connected to the $m'_F = \pm 1/2$ states in the $F' = 1/2$ manifold through a one-photon transition, the frequency difference $\delta\Delta$ is proportional to the ratio of the Stark shift to the hyperfine energy difference $((d_{mf}\mathcal{E}_{rot})/E_{HF})^1$, and akin to the expression for Δ, $\delta\Delta$ is also proportional to $1/(d_{mf}\mathcal{E}_{rot})^3$. More precisely, perturbation theory on the Hilbert space of 12 $|F, m_F, \Omega\rangle$ sub-levels in the $^3\Delta_1(J = 1)$ rotational state yields the following expressions [54]:

$$\Delta = \frac{1}{2}\left(\Delta^\ell + \Delta^u\right) = 27\omega_{ef}\left(\frac{\omega_{rot}}{d_{mf}\mathcal{E}_{rot}}\right)^3, \tag{8.3}$$

$$\delta\Delta = \frac{1}{2}\left(\Delta^\ell - \Delta^u\right) = \frac{81}{8}\omega_{ef}\left(\frac{\omega_{rot}}{d_{mf}\mathcal{E}_{rot}}\right)^3\left(\frac{d_{mf}\mathcal{E}_{rot}}{E_{HF}}\right). \tag{8.4}$$

The lines shown in Fig. 8.3c–e come from a simultaneous fit to Δ, $\delta\Delta$, Δ^ℓ and Δ^u using Eqs. (8.3)–(8.4), and the data gives good agreement with perturbation theory. The sole fit parameter, $\omega_{ef}/(2\pi)$, is determined to be 830(50) kHz, which is a more precise value for the zero-field splitting between states of opposite parity compared to its previous estimate of 740 kHz, where the latter has been obtained by extrapolating from $\omega_{ef}/(2\pi)$ observed in high-lying rotational levels of HfF^+

in a discharge tube [16].

8.4 Ramsey spectroscopy at $B \neq 0$

Having understood the avoided crossing splitting at the point of closest approach, we now turn to measuring g_F. In principle, g_F can be determined by performing Ramsey spectroscopy in the same way as described in Section 8.3 but with a finite magnetic field gradient applied throughout the Ramsey sequence. However, as B_{rot} gets larger, the Ramsey fringe contrast decreases because the eigenstates at larger B_{rot} are more similar to the m_F stretch states and the depletion laser strobe-sequence behaves less like a $\pi/2$-pulse. With a lower fringe contrast, the fringe frequency is more difficult to determine.

There is a simple modification to the Ramsey sequence in Section 8.3 that can still yield fringes of relatively high contrast. Starting with no magnetic field, the depletion laser strobe-sequence is used to create an equal superposition of $|a\rangle$ and $|b\rangle$. The magnetic field gradient is then ramped on, held a finite value for the free evolution time T, and finally ramped back down to zero for the second depletion laser strobe-sequence acting as the $\pi/2$-pulse. The main problem with the magnetic field ramps is the fact that eddy currents in the ion trap occur on a time scale significant to the coherence time of the Ramsey fringes. In order for the magnetic field at the trap center to reliably follow the expected field values from driving currents, the magnetic field ramps then have to occur on the time scale slower than that of the eddy currents, which means that after accounting for two magnetic field ramps, there is hardly any free evolution time that one can afford to wait for before the Ramsey fringe contrast diminishes due to decoherence. In a future iteration of the eEDM experiment, designed to avoid large eddy currents (e.g. by removing the aluminum mirrors from the ion trap), one can revisit this idea of ramping the magnetic field, in which case one only has to be careful to account for the ramps affecting the initial phase of the Ramsey fringe.

Another method of performing the Ramsey $\pi/2$-pulses uses the fact that the avoided crossing splitting Δ depends strongly on the rotating electric field magnitude. Fig. 8.4a shows the avoided crossing for two values of $\mathcal{E}_{rot}$. The Ramsey sequence is carried out as follows (Fig. 8.4b): at a given

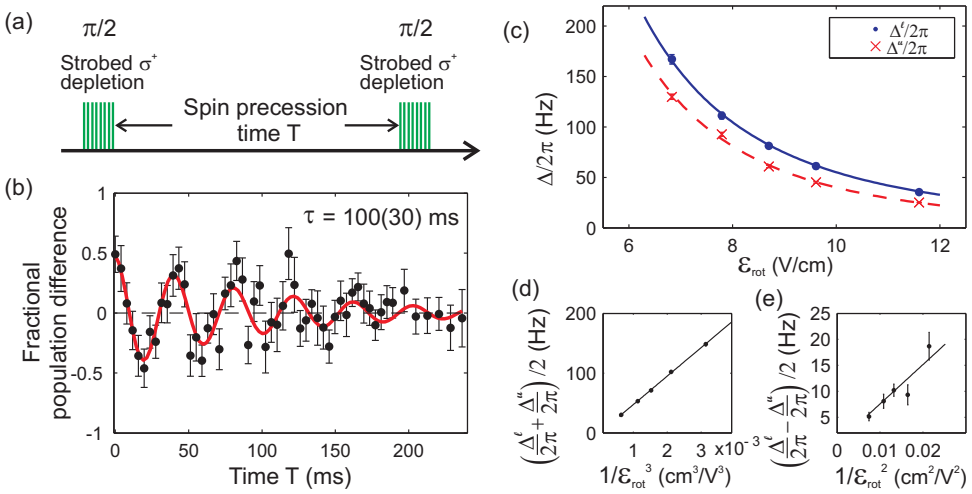

Figure 8.3: (a) Ramsey sequence performed to measure the zero-B-field splitting Δ, where the depletion laser strobe-sequence acts as a $\pi/2$-pulse. (b) Sample Ramsey fringe recorded at $B = 0$, where the fractional population difference $(N_a - N_b)/(N_a + N_b)$ is plotted as a function of the free evolution time T. The fit fringe frequency is $\Delta = (2\pi)24.5(5)$ Hz. (c) Plot of $\Delta/(2\pi)$ as a function of $\mathcal{E}_{rot}$ for both the upper (red crosses) and lower (blue dots) Stark manifolds. (d) The mean value of Δ for the two Stark manifolds is inversely proportional to $\mathcal{E}_{rot}^3$, which is in agreement with Eq. (8.3). (e) The difference in Δ for the two Stark manifolds follows that predicted by Eq. (8.4). The lines in (c–e) are simultaneous fits of the data to Eqs. (8.3) and (8.4), with the zero-electric-field splitting ω_{ef} as the only fit parameter.

applied magnetic field gradient, we first populate, say, the upper Stark manifold, and then apply a σ^+-polarized depletion laser strobe-sequence such that the ions are only left in state $|a\rangle$. The rotating electric field magnitude is subsequently jumped down to a lower value, which increases the avoided crossing splitting so that the ions in state $|a\rangle$ are projected onto a basis of eigenstates that are nearly equal superpositions of $|a\rangle$ and $|b\rangle$. After waiting for a short time, the rotating electric field magnitude is increased back to its original value, such that the total duration of any changes in the electric field corresponds to a $\pi/2$-pulse. The ions are allowed to evolve freely in time T, and the same $\pi/2$-pulse is repeated to project the ions back into either state $|a\rangle$ or $|b\rangle$, which can be read out using the circularly polarized depletion laser and dissociating the remaining HfF^+ ions.

The Ramsey fringe frequencies obtained from applying the above electric-field-ramp sequence are plotted for several different magnetic field gradients in Fig. 8.4c. The avoided crossing is mapped out for both the upper and lower Stark manifolds, and the data for each Stark manifold is fit to the following function:

$$\frac{\omega^{u/\ell}}{2\pi} = 2\sqrt{\left(\frac{\Delta^{u/\ell}}{2(2\pi)}\right)^2 + \left(\frac{3}{2}\mu_B g_F^{u/\ell}(r_{rot}\cdot\nabla B - B_{offset}^{u/\ell})\right)^2}\,, \tag{8.5}$$

where the radius of circular micromotion $r_{rot} = 0.22$ mm for a rotating electric field magnitude of 11.6 V/cm during the free evolution wait time. The second order Zeeman effect is negligible at the level of $\lesssim 10^{-2}$ compared to the linear Zeeman effect for our experimental parameters. The fit parameters yielded $\Delta^u = 25(1)$ Hz and $\Delta^\ell = 36(1)$ Hz, which are in good agreement with that expected from Eqs. (8.3)–(8.4). The magnetic field offsets fit to $B^u_{offset} = 0.15(11)$ mG and $B^\ell_{offset} = 0.02(9)$ mG, although lower offsets have been obtained when considering a subset of Ramsey fringe data taken within a short time window of each other. One source of contribution to B_{offset} comes from currents driven up and down the fin electrodes to provide the rotating voltages:

$$I_{rot} = V_{rot}\,\omega_{rot}\,C_{fin}\,, \tag{8.6}$$

$$B_{offset} = 3\frac{\mu_0 I_{rot}}{2\pi r_{fin}}\,, \tag{8.7}$$

where I_{rot} is the current for a single fin, V_{rot} is the amplitude of the rotating voltage, C_{fin} is the capacitance between two oppositely placed fin electrodes and $r_{fin} = 4$ cm is the distance between

the trap center and any given fin. The factor of 3 in Eq. (8.7) is a geometrical factor accounting for the fact that the six fin electrodes are spaced 60° apart and adjacent fins are driven out of phase by 60°. The total capacitance of a single fin (without its SHV-feedthroughs) is measured within the assembled ion trap to be 32 pF, which is likely to be dominated by the capacitance between the fin and aluminum mirror at the two points of closest approach. Using an estimated capacitance of 5 pF between opposite fins, for a rotating electric field of 11.6 V/cm or $V_{rot} = 75$ V, B_{offset} is calculated to be 0.089 mG, which is about the same as that measured. This effort should be quite stable and thus readily cancelled.

Finally, the fit of the avoided crossing yields the magnetic g-factors $|g_F^u| = 0.00306(1)$ and $|g_F^\ell| = 0.00305(1)$. Both magnetic g-factors are measured to be very small and within a factor of two of that predicted by Eq. (8.2), which means that there is little state mixing from other levels into the $^3\Delta_1$ state. The reported error on the g-factors ($\delta g_F = 10^{-5}$) is only the statistical error. We have yet to estimate the systematic error on g_F, which is likely to be dominated by the uncertainty on the value of $\mathcal{E}_{rot}$. The upper and lower Stark manifolds are expected to exhibit a slight difference in g_F due to three contributions, which are briefly listed as the following [45]:

(1) Centrifugal distortion terms in the zero-electric-field Hamiltonian, giving a parity-dependent g_F,

(2) Perturbations to the $|m_F, \Omega\rangle$ levels from $\mathcal{E}_{rot}$ mixing adjacent rotational levels, in which case one gets

$$\delta g_F = \frac{9 d_{mf} \mathcal{E}_{rot}}{40 B_e} g_F \,, \quad \text{and} \tag{8.8}$$

(3) Perturbations to the $|m_F, \Omega\rangle$ levels from the rotating quantization axis coupling m_F levels between the two hyperfine states (i.e. between $|F = 3/2, m_F = \pm 1/2\rangle$ and $|F' = 1/2, m'_F = \pm 1/2\rangle$):

$$\delta g_F = \frac{\sqrt{6}}{\gamma^2_{F=3/2}} \frac{\omega^2_{rot}}{d_{mf} \mathcal{E}_{rot} E_{HF}} g_F \,. \tag{8.9}$$

Since there is an electric field of 11.6 V/cm applied, the first contribution is negligible. The second and third contributions are calculated to be 1.8×10^{-6} and 4.1×10^{-6} respectively, which are so far

in agreement with the (crude) measured difference. One should note that by mapping out the whole avoided crossing as shown in Fig. 8.4c, neither the difference in g-factors nor B_{offset} is measured in a manner optimal for high precision. Instead, one should chop quickly between four sets of Ramsey fringes taken at some finite $\pm\nabla B$ and for both the upper and lower Stark manifolds in order to determine δg_F and B_{offset} more precisely.

8.5 Sign of magnetic g-factor

So far, the application of Ramsey spectroscopy to determine the magnetic g-factor only yields the magnitude of g_F, but not its overall sign: regardless of whether the ions in $|a\rangle$ (or $|c\rangle$) absorb from or emit energy into the rotating magnetic field, the $\cos(\omega^u T)$ signal remains unchanged. The sign of g_F is important especially if a non-zero electron EDM has been measured, as it is also related to the sign of the non-zero eEDM. Even if a finite eEDM has not yet been measured, determining the sign of g_F involves a cute piece of physics that is not necessarily encountered in many physics experiments: Berry's phase. One may think that Berry's phase, which would add a systematic shift to the eEDM-sensitive transitions, is unavoidable for our experiment due to the constant rotation of trapped molecular ions. The demonstration of our understanding of Berry's phase through an experiment such as measuring the sign of the g-factor is therefore a fantastic reason on its own to perform such an experiment!

To understand how Berry's phase may be used to determine the sign of g_F, let us first take a step back and revisit the Hamiltonian with a rotating quantization axis $\vec{\mathcal{F}}$ that has been tilted away from the plane of rotation by an angle $\alpha = (\pi/2) - \theta$ (Fig. 8.5a) [45, 57]:

$$H_{dressed} = H_0 - \vec{d}_{mf} \cdot \vec{\mathcal{E}}_{rot} + H_{rot}\,, \tag{8.10}$$

$$\text{where} \quad H_{rot} = -\omega_{rot}\left(\cos(\theta)F_z - \sin(\theta)F_x\right)\,. \tag{8.11}$$

θ is the polar angle, whereas F_z and F_x are the projections of the quantization axis onto the $\hat{z}$ and $\hat{x}$ axes. The Berry's phase accumulated from the tilt of the quantization axis away from the

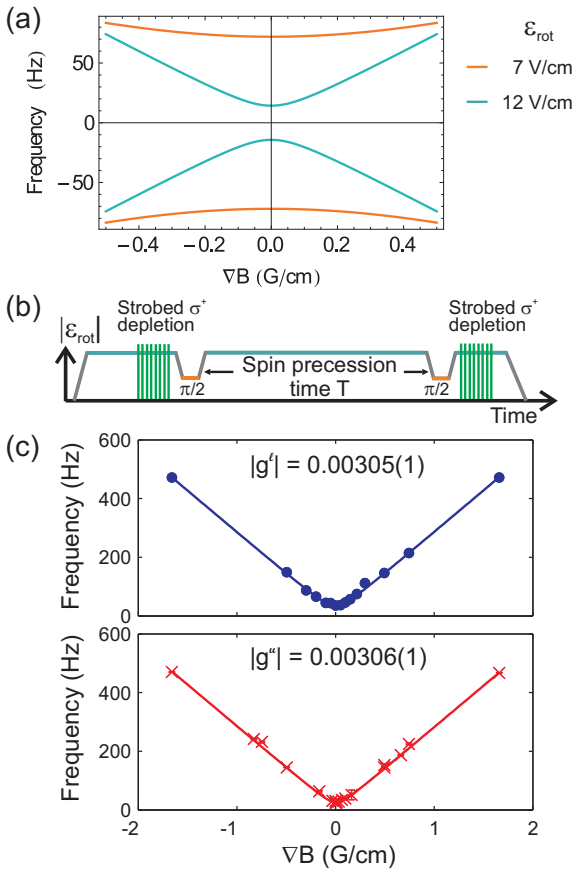

Figure 8.4: (a) Theory curves for the avoided crossing as a function of the rotating magnetic field (mocked up using ∇B), plotted for two different values of $\mathcal{E}_{rot}$. (b) Ramsey sequence performed to measure the magnetic g-factor. The $\pi/2$-pulses are ramps in $\mathcal{E}_{rot}$, which can change the eigenstate at some finite magnetic field from, say, $\approx |a\rangle$ to $\approx (|a\rangle - |b\rangle)/\sqrt{2}$. (c) The avoided crossing is experimentally mapped out for both the lower (blue dots) and upper (red crosses) Stark manifolds. The slopes of the avoided crossing give $|g_F^\ell| = 0.00305(1)$ and $|g_F^u| = 0.00306(1)$.

horizontal plane of rotation then gives rise to an energy shift

$$E_{Berry} = -m_F \omega_{rot} \sin(\alpha) \approx -m_F \omega_{rot} \alpha \,. \tag{8.12}$$

For HfF^+ ions confined to the plane of rotation, $E_{Berry} = 0$. However, the trapped ions also undergo axial oscillations, such that the quantization axis (electric field) can be tipped away from the plane of rotation, introducing a Berry's phase. Considering only states $|a\rangle$ and $|b\rangle$ and ignoring any contributions to their energies from an eEDM, the Hamiltonian in the state basis $\{|a\rangle, |b\rangle\}$ then becomes

$$H = \begin{pmatrix} \frac{3}{2} g_F \mu_B B_{rot} + \frac{\omega_{max}}{2} \cos(\omega_z t) & \frac{\Delta}{2} \\ \frac{\Delta}{2} & -\frac{3}{2} g_F \mu_B B_{rot} - \frac{\omega_{max}}{2} \cos(\omega_z t) \end{pmatrix}, \tag{8.13}$$

where $\omega_{max} = -m_F \omega_{rot} (\mathcal{E}_{z,max}/\mathcal{E}_{rot})$ is the Berry's phase picked up from the tilt of the quantization axis $(\mathcal{E}_{z,max}/\mathcal{E}_{rot})$ and where $\mathcal{E}_{z,max}$ is the maximum axial electric field experienced by the ions as they oscillate away from the plane of rotation ($z = 0$).

For a cloud of ions oscillating about the $z = 0$ plane with a random initial phase in the axial direction, the Berry's phase accumulated by some ions oscillating above the plane of rotation cancels out that accumulated by ions oscillating below the plane of rotation, such that the overall Berry's phase is zero. On the other hand, if the entire ion cloud is oscillating, say, in the region $z > 0$, the ions can accumulate an overall Berry's phase, which, depending on the relative orientations of the quantization axis (electric field) and the magnetic field, can shift state $|a\rangle$ up or down in addition to the Zeeman shift (with the opposite Berry's phase shift for $|b\rangle$). For $\omega_{max} \cos(\omega_z t) > 0$, the two terms dominating the energies of states $|a\rangle$ and $|b\rangle$ (i.e. $(3/2) g_F \mu_B B_{rot}$ versus $(\omega_{max}/2) \cos(\omega_z t)$) will have the same sign if $g_F B_{rot} > 0$, so that the two levels are further split apart with the Berry's energy shift (and vice versa if $g_F B_{rot} < 0$).

Experimentally, to determine the sign of g_F, we carried out the same Ramsey sequence as described in Section 8.4 but with an additional 'kick' applied to the ions along the axial direction before performing the first $\pi/2$-pulse. The axial frequency was lowered to $(2\pi)0.8$ kHz, such that the ions would be moving in only the upper half region $z > 0$ in the first 625 μs. According to Eq. (8.13), such an upward kick to the ions yields $\omega_{max} > 0$, and the accumulated Berry's phase

would shift the Ramsey fringe frequency to be larger or smaller depending on the sign of g_F. The experiment can then be repeated with the ions kicked down into the region $z < 0$ to make sure that the Ramsey fringe shifts in the opposite direction compared to the chop with the upward kick. Fig. 8.5d shows the Ramsey fringes obtained with the ions kicked into $z > 0$ (blue dots) and also into $z < 0$ (red crosses), for the case where $B_{rot} > 0$. Relating the fringe phase shift observed in the first 625 μs (shaded region on the plot) to Eq. (8.13), one can therefore determine the sign of the g-factor.[2] As an additional sanity check, the two chops are repeated, this time with an outward radial magnetic field gradient, i.e. $B_{rot} < 0$. As expected, the Ramsey fringe phase shifts are now reversed compared to that plotted in Fig. 8.5d for the kicks in the two axial directions, as the relative sign between $g_F B_{rot}$ and $\omega_{max}\cos(\omega_z t)$ has flipped.

One should note that there is at least one other alternative method for measuring the sign of g_F: one can instead measure the Stark splitting between adjacent m_F levels in both the presence and absence of a rotating magnetic field, by first populating state $|a\rangle$ using the Raman transfer lasers and depletion strobe-sequence, and then applying RF photons to couple $|a\rangle$ to its adjacent state $|F = 3/2, m_F = 1/2, \Omega = -1\rangle$. For $\mathcal{E}_{rot} = 16$ V/cm, the Stark splitting is 10.5 MHz, which means that to determine the sign of g_F by recording a 100 Hz shift on the RF transition, $\mathcal{E}_{rot}$ needs to be stable to 10^{-5} , which is plausible but no mean feat to achieve.

8.6 A preliminary eEDM measurement and some implications for sensitivity to systematics

Returning to the avoided crossing mapped out in Section 8.4, we can combine the Ramsey fringe frequencies recorded at some finite $\pm\nabla B$ and for both the upper and lower Stark manifolds as the terms in the 'four-way chop' described in Eq. (1.7) to give a preliminary limit on the eEDM: $|d_e| < 10^{-25}$ e cm. A serious measurement of the eEDM would involve sitting on the side of a Ramsey fringe and looking at a shift of the Ramsey fringe position for any given chop, as

[2] At the time of thesis submission, we still have not yet reached a consensus on the sign of the g-factor. However, the method of determining the sign by kicking the ions and observing the subsequent Ramsey fringe phase shift remains on a fairly solid foundation. The final consensus on the sign of the g-factor will be reported in Reference [50].

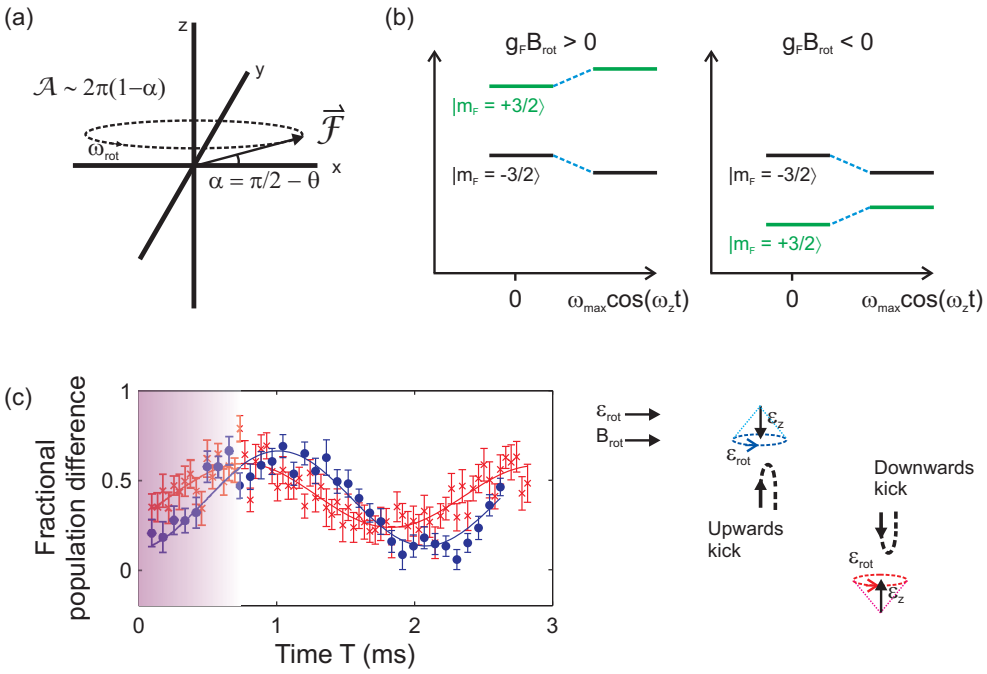

Figure 8.5: (a) (Adapted from [45]) The tipping of the rotating quantization axis $\vec{\mathcal{F}}$ away from the plane of rotation by the angle α introduces a non-zero Berry's phase that is proportional to the solid angle $\mathcal{A}$. (b) If $g_F B_{rot} > 0$, the $|m_F = \pm 3/2\rangle$ levels in the absence of Berry's phase are Zeeman-shifted so that $|m_F = 3/2\rangle$ lies above $|m_F = -3/2\rangle$ in energy. With Berry's phase providing $\omega_{max}\cos(\omega_z t) > 0$, however, the two Zeeman levels are split further apart. Conversely, if $g_F B_{rot} < 0$, the $|m_F = -3/2\rangle$ level is higher in energy, but with Berry's phase giving $\omega_{max}\cos(\omega_z t) > 0$, the $|m_F = -3/2\rangle$ level is lowered slightly whereas the $|m_F = 3/2\rangle$ state is raised, causing the two Zeeman levels to have a smaller splitting. (d) Ramsey fringes recorded with the molecular ions undergoing a finite Berry's phase as they are either kicked upwards (blue dots) or downwards (red crosses) from the plane of rotation. The shaded region corresponds to half an axial trap oscillation, which is also the time over which the ions are only in the $z > 0$ (or $z < 0$) region and where the phase shifts of the Ramsey fringes are of interest. This data is recorded with $B_{rot} > 0$, such that the observed phase shifts for the two kicks yield $g_F < 0$.

opposed to recording the entire fringe. For imperfect $\pi/2$-pulses, the initial phase of the Ramsey fringe may be less well-understood, which means that in addition to sitting on only a side of the Ramsey fringe, we may also have to measure the initial phase of the fringe. These chops would have to be performed with a 'blind' offset added to each frequency measurement so that the experimenters will not be biased towards a particular eEDM value [36]. The final reported eEDM value is then given by the offset combined with the statistical uncertainty and systematic uncertainty: $d_e = (d_e^{offset} \pm \delta d_e^{stat} \pm \delta d_e^{syst})$.

As mentioned at the beginning of this thesis, δd_e^{stat} is inversely proportional to the figure-of-merit, which is in turn proportional to the effective electric field, coherence time and square root of the number of spin-flip transitions detected. The potentially long coherence time offered by trapped molecular ions over neutral molecules is one of the chief advantages of the JILA eEDM experiment. In Fig. 8.6a, we show that we can currently achieve coherence times longer than 150 ms, which is approximately two orders of magnitude higher than all other molecule eEDM experiments that offer a similarly large effective electric field. The long coherence time of 150 ms, combined with $\mathcal{E}_{eff} = 24$ GV/cm and 4 spin-flips detected per shot at a repetition rate of 1 Hz, puts our present statistical uncertainty at $\delta d_e^{stat} = 2.2 \times 10^{-28}$ e cm/$\sqrt{\text{day}}$. Further, the 100-times higher resolution provided by the narrower spin-flip transition linewidth means that we are less sensitive to systematic effects that distort the lineshape. The source of decoherence beyond 150 ms is presently a topic of investigation, and preliminary studies point to ion-ion interactions as a plausible factor, although a more detailed study needs to be performed to sort through the different decoherence sources. The ultimate goal we wish to achieve for the coherence time is the rovibronic lifetime of the $^3\Delta_1(\nu = 0, J = 1)$ state, which has been measured to be as long as 1.6(4) s (Fig. 8.6b). With a longer coherence time, both our statistical uncertainty and sensitivity to systematics can be further lowered.

Returning to the (coarse) measurements of $\delta\Delta$ and δg_F obtained in Sections 8.3 and 8.4, we examine the implications of these quantities for potential systematics in an eEDM measurement. As explained in Reference [45], the most important contributions to a systematic effect that could

survive the four-way chop are quantities that influence ω^u and ω^ℓ separately, e.g. δg_F and $\delta\Delta$. Firstly, for a given δg_F, a systematic shift from any stray rotating magnetic fields or magnetic field gradients would be reduced by $\delta g_F/g_F$ after the four-way chop:

$$\omega^{u/\ell}(\mathcal{E}_{rot}, B_{rot}+B_{rot}^{stray})+\omega^{u/\ell}(\mathcal{E}_{rot}, -B_{rot}+B_{rot}^{stray}) = 6g_F^{u/\ell}\mu_B B_{rot}^{stray} \pm 2d_e\mathcal{E}_{\mathit{eff}}, \tag{8.14}$$

$$\begin{aligned}&\Big[\omega^u(\mathcal{E}_{rot}, B_{rot}+B_{rot}^{stray})+\omega^u(\mathcal{E}_{rot}, -B_{rot}+B_{rot}^{stray})\Big]\\ &-\Big[\omega^\ell(\mathcal{E}_{rot}, B_{rot}+B_{rot}^{stray})+\omega^\ell(\mathcal{E}_{rot}, -B_{rot}+B_{rot}^{stray})\Big]\\ &= 12\delta g_F\mu_B B_{rot}^{stray}+4d_e\mathcal{E}_{\mathit{eff}}.\end{aligned} \tag{8.15}$$

Further, B_{rot}^{stray} can be reduced by compensating for it with a non-chopped rotating magnetic field B_{rot}^{shim}. The combination of B_{rot}^{shim} and our theoretical values for δg_F is expected to put our eEDM systematic sensitivity below 10^{-28} e cm. Secondly, $\delta\Delta$ gives rise to a systematic shift if a chop in B_{rot} causes a change in $\mathcal{E}_{rot}$ by $\delta\mathcal{E}_{chop}$:

$$\begin{aligned}&[\omega^u(\mathcal{E}_{rot}+\delta\mathcal{E}_{chop}, B_{rot})-\omega^u(\mathcal{E}_{rot}-\delta\mathcal{E}_{chop}, -B_{rot})]\\ &-\Big[\omega^\ell(\mathcal{E}_{rot}+\delta\mathcal{E}_{chop}, B_{rot})-\omega^\ell(\mathcal{E}_{rot}-\delta\mathcal{E}_{chop}, -B_{rot})\Big]\\ &= 8\frac{\delta\Delta}{\Delta}\eta\delta\mathcal{E}_{chop}\\ &\approx 3\left(\frac{d_{mf}\mathcal{E}_{rot}}{E_{HF}}\right)\eta\delta\mathcal{E}_{chop}\,.\end{aligned} \tag{8.16}$$

where η is the analog of the sensitivity of $\omega^{u/\ell}$ to $\mathcal{E}_{rot}$ as g_F is to B_{rot}:

$$\eta^{u/\ell} \equiv \frac{\partial\omega^{u/\ell}}{\partial\mathcal{E}_{rot}}\Big|_{\mathcal{E}_{rot}^0, B_{rot}} = \frac{(\Delta^{u/\ell})^2}{g_F^{u/\ell}\mu_B B_{rot}\mathcal{E}_{rot}}\,. \tag{8.17}$$

For $\mathcal{E}_{rot} = 11.6$ V/cm, $B_{rot} = 15$ mG and a plausible value of $\delta\mathcal{E}_{chop} = 100$ μV/cm, $\eta = (2\pi)1.6$ Hz/(V/cm) and the remainder systematic shift given by Eq. (8.16) is estimated to be $(2\pi)0.25$ mHz, which is at the 5×10^{-30} e cm level.

8.7 Conclusions and outlook

By the end of this thesis, we have developed all the techniques required to perform an eEDM measurement: the quantum state preparation is accomplished by first autoionizing neutral HfF

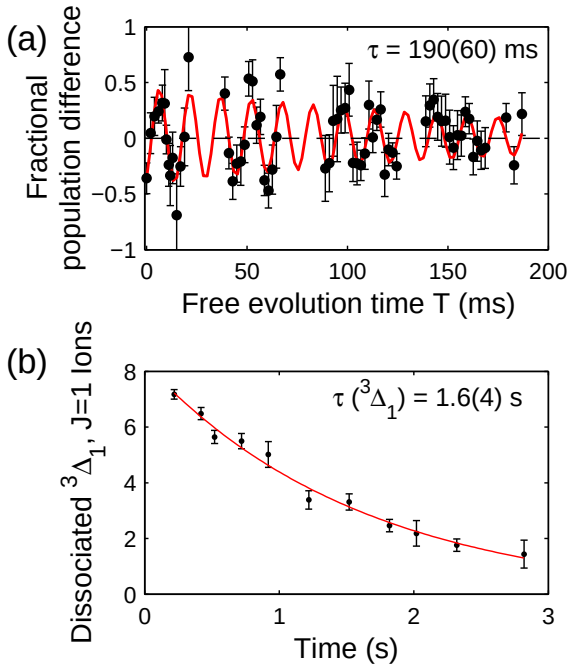

Figure 8.6: (a) The coherence time for the Ramsey spectroscopic measurement of an eEDM-sensitive transition frequency is presently limited to about 200 ms. (b) Decay of the number of dissociated $^3\Delta_1(\nu = 0, J = 1)$ HfF^+ ions as a function of trap time. The coherence time is not limited by the rovibronic lifetime of the $^3\Delta_1(\nu = 0, J = 1)$ state, which we have measured to be as long as 1.6(4) s.

molecules into the true electronic ground state $^1\Sigma^+$, and then performing a Raman transfer of the HfF^+ molecular ions into the desired $^3\Delta_1$ quantum states, while the efficient state detection is achieved by rotational-state-resolved photodissociation. In the meantime, the ions remain trapped in a RF Paul trap of a novel design and are subject to rotating bias electric and magnetic fields. The rotating electric bias field is unique to our ion trap experiment and has not been utilized in any other RF Paul traps. We have provided the first demonstration of coherent Ramsey spectroscopy of ions in a rotating bias field, where the $\pi/2$-Ramsey-pulses are implemented by ramping the rotating electric field.

For the eEDM measurement, the combination of Ramsey fringes taken at opposite magnetic fields and with different sublevels of the $^3\Delta_1$ state gives $|d_e| < 10^{-25}$ e cm, and our present numbers for the coherence time and spin-flip transitions detected put our statistical sensitivity at $\delta d_e^{1\sigma} < 2.2 \times 10^{-28}$ e cm$/\sqrt{\text{day}}$. The sources of decoherence remain to be understood and the coherence time to be improved, after which a full systematic evaluation of the eEDM will be carried out, with the goal of achieving $|d_e| < 10^{-29}$–10^{-28} e cm. Besides performing the four-way chop that adds to the eEDM signal, other chops that can serve as sanity checks include chopping the polarization of the depletion laser for the first or second strobe-sequence and chopping the sign of rotation $\omega_{rot} \rightarrow -\omega_{rot}$. Unlike other eEDM experiments where the direction of electric field is applied by a pair of parallel plates can be reversed, the direction of electric field cannot be chopped in the same sense for the JILA eEDM experiment. The electric field direction is in effect always "inward" with respect to the circular motion. However, chopping for systematics from motional magnetic fields arising from $\vec{\mathcal{E}} \times \vec{v}$ can be easily performed by reversing the sign of rotation, whereas for beam experiments, the same chop requires building a second source of molecules symmetrically about the electric field plate setup. With Kevin Cossel and Matt Grau leading the charge on the coherence time experiments, I am confident that the systematic evaluation will proceed speedily, and I look forward to a new limit on the eEDM coming forth from the ion trap setup!

In the longer term, we have plans to switch from HfF^+ to ThF^+, a molecular ion that shares many of the advantages offered by HfF^+, except that ThF^+ is better: firstly, $\mathcal{E}_{eff} \approx 90$ GV/cm [55],

which is three times higher than that of HfF^+, and secondly, the $^3\Delta_1$ state is likely to either be the true electronic ground state or no more than 315 cm^{-1} above the ground state [5]. In either of those cases, the $^3\Delta_1$ level is likely to be more long-lived than the present lifetime of the $^3\Delta_1$ level in HfF^+. Unfortunately, the issues with using ThF^+ are the same as they were for HfF^+ six years ago: more spectroscopic information about ThF^+ (as well as neutral ThF) needs to be obtained, from which the quantum state preparation and state detection schemes have to be worked out. Dan Gresh has revived the frequency-comb-enhanced velocity-modulation spectroscopy technique for ThF^+ in a discharge tube, with which he has started to observe some ThF^+ transitions. Hopefully, in the near future, sufficient ThF^+ transitions can be identified and the discharge tube setup can be converted into a second ion trap experiment for ThF^+ state manipulation. With HfF^+ and ThF^+ experiments running in parallel, the JILA eEDM effort is an exciting one to watch, especially if a nonzero eEDM is detected!

Returning to the coherent spectroscopy on trapped HfF^+ molecular ions in a rotating bias field, it is tempting to think about the rotating bias field technique in the context of the larger molecular ion community. Many molecular ion experiments are built [89] either to carry out precision spectroscopy (e.g. on simple molecules like HD^+ to test ab-initio theory [10] and to look for time-variation in the mass ratios m_e/m_p [77]) or to use the additional levels provided by the rotational and vibrational degrees of freedom to perform quantum information processing [79]. With the exception of Penning trap experiments [85, 58], these molecular ion experiments tend to under-utilize the electric dipole moment of molecular ions despite its importance as both a test of ab-initio calculations and as a degree of freedom in isolating particular Stark-Zeeman quantum states for quantum information experiments. The application of a rotating bias field in a RF Paul trap is a general technique that brings out the advantages of polar molecules while still preserving the simplicity of an ion trap, and can have an impact on others in the molecular ion community beyond those interested in an electron electric dipole moment search.

Bibliography

[1] A. G. Adam, W. S. Hopkins, and D. W. Tokaryk. J. Mol Spectrosc., 225:1, 2004.

[2] T. Aoyama, M. Hayakawa, T. Kinoshita, and M. Nio. Phys. Rev. Lett., 99:110406, 2007.

[3] T. Aoyama, M. Hayakawa, T. Kinoshita, and M. Nio. Phys. Rev. D, 77:053012, 2008.

[4] B. J. Barker, I. O. Antonov, V. E. Bondybey, and M. C. Heaven. J. Chem. Phys., 134:201102, 2011.

[5] B. J. Barker, I. O. Antonov, M. C. Heaven, and K. A. Peterson. J. Chem. Phys., 136:104305, 2012.

[6] N. V. Barkovskii, V. I. Tsirel'nikov, A. M. Emel'yanov, and Yu. S. Khodeev. Teplofiz. Vysok. Temper., 29:474, 1991.

[7] S. M. Barr. Int. J. Mod. Phys. A, 8:209, 1993.

[8] D. J. Berkeland, J. D. Miller, J. C. Bergquist, W. M. Itano, and D. J. Wineland. J. Appl. Phys., 83:5025, 1998.

[9] W. Bernreuther and M. Suzuki. Rev. Mod. Phys., 63:313, 1991.

[10] U. Bressel, A. Borodin, J. Shen, M. Hansen, I. Ernsting, and S. Schiller. Phys. Rev. Lett., 108:183003, 2012.

[11] J. M. Brown, J. T. Hougen, K. P. Huber, J. W. C. Johns, I. Kopp, H. Lefebvre-Brion, A. J. Merer, D. A. Ramsay, J. Rostas, and R. N. Zare. J. Mol. Spectrosc., 55:500, 1975.

[12] C. L. Callender, P. A. Hackett, and D. M. Rayner. J. Opt. Soc. Am. B, 5:1341, 1988.

[13] J. H. Christenson, J. W. Cronin, V. L. Fitch, and R. Turlay. Phys. Rev. Lett., 13:138, 1964.

[14] E. D. Commins. Annu. Rev. Nucl. Part. Sci., 62:133, 2012.

[15] E. D. Commins, J. D. Jackson, and D. P. DeMille. Am. J. Phys., 75:532, 2007.

[16] K. C. Cossel, D. N. Gresh, L. C. Sinclair, T. Coffey, L. V. Skripnikov, A. N. Petrov, N. S. Mosyagin, A. V. Titov, R. W. Field, E. R. Meyer, E. A. Cornell, and J. Ye. Chem. Phys. Lett., 546:1, 2012.

[17] R. Das, C. Y. Wu, A. G. Mihill, E. D. Poliakoff, K. S. Wang, and V. McKoy. J. Chem. Phys., 101:5402, 1994.

[18] D. DeMille, F. Bay, S. Bickman, D. Kawall, D. Krause Jr., S. E. Maxwell, and L. R. Hunter. Phys. Rev. A, 61:052507, 2000.

[19] D. R. Denison. J. Vac. Sci. Tech., 8:266, 1971.

[20] L. F. Dimauro and T. A. Miller. Chem. Phys. Lett., 138:175, 1987.

[21] R. W. P. Drever, J. L. Hall, F. V. Kowalski, J. Hough, G. M. Ford, A. J. Munley, and H. Ward. Appl. Phys. B: Lasers and Optics, 31:97, 1983.

[22] S. Dutta, D. S. Elliott, and Y. P. Chen. Appl. Phys. B, 106:629, 2012.

[23] S. Eckel, P. Hamilton, E. Kirilov, H. W. Smith, and D. DeMille. Phys. Rev. A, 87:052130, 2013.

[24] B. Efron and R. J. Tibshirani. An Introduction to the Bootstrap. Chapman and Hall, 1994.

[25] U. Fano. Phys. Rev. A, 2:353, 1970.

[26] U. Fano and J. H. Macek. Rev. Mod. Phys., 45:553, 1973.

[27] A. Fujii, T. Ebata, and M. Ito. J. Chem. Phys., 88:5307, 1988.

[28] A. Fujii, T. Ebata, and M. Ito. Chem. Phys. Lett., 161:93, 1989.

[29] P. K. Ghosh. Ion Traps. Oxford Science Publications, 1995.

[30] M. Grau, A. Leanhardt, H. Loh, L. C. Sinclair, R. P. Stutz, T. Yahn, and E. A. Cornell. J. Mol Spectrosc., 272:32, 2012.

[31] C. H. Greene and Ch. Jungen. Adv. At. Mol. Phys., 21:51, 1985.

[32] D. R. Guyer, L. Hüwel, and S. R. Leone. J. Chem. Phys., 79:1259, 1983.

[33] D. Hanneke, S. Fogwell, and G. Gabrielse. Phys. Rev. Lett., 100:120801, 2008.

[34] A. Hansson and J. K. G. Watson. J. Mol. Spectrosc., 233:169, 2005.

[35] G. Herzberg. Molecular Spectra and Molecular Structure: I. Spectra of Diatomic Molecules. Van Nostrand Reinhold Company, 1950.

[36] J. J. Hudson, D. M. Kara, I. J. Smallman, B. E. Sauer, M. R. Tarbutt, and E. A. Hinds. Nature, 473:493, 2011.

[37] Ch. Jungen and O. Atabek. J. Chem. Phys., 66:5584, 1977.

[38] S. Kakar, H. C. Choi, and E. D. Poliakoff. J. Chem. Phys., 97:6998, 1992.

[39] D. M. Kara, I. J. Smallman, J. J. Hudson, B. E. Sauer, M. R. Tarbutt, and E. A. Hinds. New J. Phys., 14:103051, 2012.

[40] J. J. Kay, D. S. Byun, J. O. Clevenger, X. Jiang, V. S. Petrović, R. Seiler, J. R. Barchi, A. J. Merer, and R. W. Field. Can. J. Chem., 82:791, 2004.

[41] J. J. Kay, S. L. Coy, B. M. Wong, C. Jungen, and R. W. Field. J. Chem. Phys., 134:114313, 2011.

[42] J. J. Kay and R. W. Field. To be published.

[43] J. W. Keller, W. T. Hill III, D. L. Ederer, T. J. Gil, and P. W. Langhoff. J. Chem. Phys., 87:3299, 1987.

[44] I. B. Khriplovich and S. K. Lamoreaux. CP Violation Without Strangeness: Electric Dipole Moments of Particles, Atoms and Molecules. Springer, 1997.

[45] A. E. Leanhardt, J. L. Bohn, H. Loh, P. Maletinsky, E. R. Meyer, L. C. Sinclair, R. P. Stutz, and E. A. Cornell. J. Mol. Spectrosc., 270:1, 2011.

[46] J. Lee, E. R. Meyer, R. Paudel, J. L. Bohn, and A. E. Leanhardt. J. Mod. Opt., 56:2005, 2009.

[47] J. P. Lees, V. Poireau, V. Tisserand, et al. Phys. Rev. Lett., 109:211801, 2012.

[48] H. Lefebvre-Brion and R. W. Field. The Spectra and Dynamics of Diatomic Molecules. Elsevier Academic Press, 2004.

[49] D. Leibfried, R. Blatt, C. Monroe, and D. Wineland. Rev. Mod. Phys., 75:281, 2003.

[50] H. Loh, K. C. Cossel, M. Grau, K.-K. Ni, J. L. Bohn, E. R. Meyer, J. Ye, and E. A. Cornell. In preparation.

[51] H. Loh, R. P. Stutz, T. S. Yahn, H. Looser, R. W. Field, and E. A. Cornell. J. Mol. Spectrosc., 276:49, 2012.

[52] H. Loh, J. Wang, M. Grau, T. S. Yahn, R. W. Field, C. H. Greene, and E. A. Cornell. J. Chem. Phys., 135:154308, 2011.

[53] L. P. Maguire, S. Szilagyi, and R. E. Scholten. Rev. Sci. Instrum., 75:3077, 2004.

[54] E. R. Meyer and J. L. Bohn. Private communication.

[55] E. R. Meyer and J. L. Bohn. Phys. Rev. A, 78:010502(R), 2008.

[56] E. R. Meyer, J. L. Bohn, and M. P. Deskevich. Phys. Rev. A, 73:062108, 2006.

[57] E. R. Meyer, A. E. Leanhardt, E. A. Cornell, and J. L. Bohn. Phys. Rev. A, 80:062110, 2009.

[58] B. J. Mount, M. Redshaw, and E. G. Myers. Phys. Rev. A, 85:012519, 2012.

[59] T. Nagata, A. Nakajima, T. Kondow, and K. Kuchitsu. Chem. Lett., 16:1911, 1987.

[60] K.-K. Ni, S. Ospelkaus, M. H. G. de Miranda, A. Pe'er, B. Neyenhuis, J. J. Zirbel, S. Kotochigova, P. S. Julienne, D. S. Jin, and J. Ye. Science, 322:231, 2008.

[61] H. Park, D. J. Leahy, and R. N. Zare. Phys. Rev. Lett., 76:1591, 1996.

[62] A. N. Petrov, N. S. Mosyagin, T. A. Isaev, and A. V. Titov. Phys. Rev. A, 76:030501(R), 2007.

[63] A. N. Petrov, N. S. Mosyagin, and A. V. Titov. Phys. Rev. A, 79:012505, 2009.

[64] A. N. Petrov and A. V. Titov. Private communication.

[65] V. S. Petrović and R. W. Field. J. Chem. Phys., 128:014301, 2008.

[66] E. D. Poliakoff, H. C. Choi, R. M. Rao, A. G. Mihill, S. Kakar, K. Wang, and V. McKoy. J. Chem. Phys., 103:1773, 1995.

[67] E. D. Poliakoff, J. L. Dehmer, D. Dill, A. C. Parr, K. H. Jackson, and R. N. Zare. Phys. Rev. Lett., 46:907, 1981.

[68] E. D. Poliakoff, J. L. Dehmer, A. C. Parr, and G. E. Leroi. J. Chem. Phys., 86:2557, 1987.

[69] M. Pospelov and A. Ritz. Ann. Phys., 318:119, 2005.

[70] M. E. Pospelov and I. B. Khriplovich. Sov. J. Nucl. Phys., 53:638, 1991.

[71] B. C. Regan, E. D. Commins, C. J. Schmidt, and D. DeMille. Phys. Rev. Lett., 88:071805, 2002.

[72] P. G. H. Sandars. Phys. Lett., 14:194, 1965.

[73] P. G. H. Sandars. Phys. Lett., 22:290, 1966.

[74] P. G. H. Sandars. Phys. Rev. Lett., 19:1396, 1967.

[75] P. G. H. Sandars. Atomic Physics, 4:71, 1975.

[76] L. I. Schiff. Phys. Rev., 132:2194, 1963.

[77] S. Schiller and V. Korobov. Phys. Rev. Lett., 71:032505, 2005.

[78] R. E. Scholten. Rev. Sci. Instrum., 78:026101, 2007.

[79] D. I. Schuster, L. S. Bishop, I. L. Chuang, D. DeMille, and R. J. Schoelkopf. Phys. Rev. A, 83:012311, 2011.

[80] M. J. Seaton. Rep. Prog. Phys., 46:167, 1983.

[81] L. C. Sinclair. Development of frequency comb velocity-modulation. PhD thesis, University of Colorado at Boulder, 2010.

[82] L. C. Sinclair, K. C. Cossel, T. Coffey, J. Ye, and E. A. Cornell. Phys. Rev. Lett., 107:093002, 2011.

[83] R. P. Stutz. Towards measuring the electron electric dipole moment using trapped molecular ions. PhD thesis, University of Colorado at Boulder, 2010.

[84] I. Teper, Y.-J. Lin, and V. Vuletić. Phys. Rev. Lett., 97:023002, 2006.

[85] J. K. Thompson, S. Rainville, and D. E. Pritchard. Nature, 430:58, 2004.

[86] A. V. Titov. Private communication, 2012.

[87] A. C. Vutha, W. C. Campbell, Y. V. Gurevich, N. R. Hutzler, M. Parsons, D. Patterson, E. Petrik, B. Spaun, J. M. Doyle, G. Gabrielse, and D. DeMille. J. Phys. B, 43:074007, 2010.

[88] W. C. Wiley and I. H. McLaren. Rev. Sci. Instrum., 26:1150, 1955.

[89] S. Willitsch. Int. Rev. Phys. Chem., 31:175, 2012.

[90] J. Xie and R. N. Zare. Chem. Phys. Lett., 159:399, 1989.

[91] J. Xie and R. N. Zare. J. Chem. Phys., 93:3033, 1990.

[92] J. Ye and T. W. Lynn. Adv. Atom. Mol. Opt. Phys., 49:1, 2003.

[93] J. Ye, L.-S. Ma, and J. L. Hall. J. Opt. Soc. Am. B, 15:6, 1998.

[94] R. N. Zare. Angular Momentum: Understanding Spatial Aspects in Chemistry and Physics. John Wiley and Sons, 1998.

[95] H. Zhang, R. McConnell, S.Ćuk, Q. Lin, M. H. Schleier-Smith, I. D. Leroux, and V. Vuletić. Phys. Rev. Lett., 109:133603, 2012.

[96] R. Zhao, I. M. Konen, and R. N. Zare. J. Chem. Phys., 121:9938, 2004.